Time Domain Reflectometry Imaging

- a new moisture measurement technique for industry and soil science

---

A thesis

submitted in partial fulfilment

of the requirements for the Degree of

Doctor of Philosophy

in Soil and Physical Sciences

at

Lincoln University

by

I. M. Woodhead

Lincoln University

2001

Declaration: Prior Publication of Parts of this Thesis

Parts of this thesis have been (i) presented or to be presented at international conferences and included in the conference proceedings, (ii) published in refereed journals and (iii) printed in non-refereed publications.

(i) Conference presentation and proceedings

Woodhead, I., Buchan, G., Kulasiri, D. 1999. Modelling TDR response in heterogeneous composite materials, *Third Workshop on Electromagnetic Wave Interaction with Water and Moist Substances,* Athens, Georgia
(includes parts of Chapters 2, 3 and 6)

Woodhead, I., Buchan, G., Kulasiri, D. 2001. Non-invasive measurement of moisture distribution using TDR, *Fourth Workshop on Electromagnetic Wave Interaction with Water and Moist Substances,* Weimar, Germany (accepted for oral presentation, May 15, 2001)
(includes parts of Chapters 2 and 4)

(ii) Published in refereed journals

Woodhead, I, Buchan G, Kulasiri D, Christie, J. 2000. A new model for the response of TDR to heterogeneous dielectrics. *Subsurface Sensing Technologies and Applications*, 1:473-487
(includes parts of Chapters 2, 3 and 6)

Woodhead, I. M., Buchan, G. D., Kulasiri, D. 2001. Pseudo 3-D moment method for rapid calculation of electric field distribution in a low loss inhomogeneous dielectric. *IEEE Transactions on Antennas and Propagation,* 49:1117-1122
(includes parts of Chapters 2, 3 and 6)

(iii) Other publications

Woodhead, I. M., Buchan, G. D. 1996. Determination of moisture content profiles in composite materials using dielectric computed tomography. In *WISPAS*
(includes parts of Chapters 1 and 2)

Woodhead, I. M., Buchan, G. D. 2000. Non-invasive determination of subsurface moisture distribution. In *WISPAS*
(includes parts of Chapters 2, 3, and 4)

Abstract of a thesis submitted in partial fulfilment of the requirements for the degree of Doctor of Philosophy

Time Domain Reflectometry Imaging

- a new moisture measurement technique for industry and soil science

by I.M. Woodhead

This thesis describes the theoretical and practical aspects of a new technique for quantitative, non-invasive and non-destructive imaging of the near-surface moisture content distribution of composite materials. The technique relies on the alteration by a nearby composite material, of the propagation velocity of an electromagnetic pulse along a parallel transmission line, through distortion of the evanescent field. A set of measurements taken at different relative positions of the transmission line and composite material are, in conjunction with a forward model describing propagation velocity on the line, inverted to provide the image of moisture content distribution. Development of the technique, called 'Time Domain Reflectometry Imaging' (TDRI), involved four steps:

1. Instrumentation to obtain a set of measurements of propagation times;
2. A forward model;
3. An inverse procedure; and
4. Conversion of a calculated permittivity distribution to a moisture distribution.

Critical to the success of the inverse method is a set of measurements of propagation velocity that provide pico-second propagation time accuracy, and are sufficiently linearly independent to enable discrimination of the permittivity of each discretised cell within the composite material. Using commercial time domain reflectometry (TDR) instruments, a switched reference measurement, waveform subtraction and intersecting waveform tangents, sufficient timing accuracy has been achieved.

The forward model was developed using the moment method. The advantage of such an integral equation method is that recalculation is not required when changing the impressed field. Hence for a particular model of the composite material's moisture distribution, just one execution of the forward model provides predicted propagation velocities for all positions of the transmission line. A new pseudo 3-D variant of the volume integral equation approach was

developed to suit the 2-D transmission line, and resulted in a 100 fold reduction in memory use, and a greater than 10 fold reduction in execution time. The forward solution uses the telegrapher's equation to predict propagation velocity from an arbitrary permittivity distribution surrounding the line.

Inversion of the measured data was accelerated by the use of three novel tactics: a rapid electric field surrogate for the Jacobian; a dynamic method of determining the conjugate gradient weighting factor; and a new blocking technique that accelerated the convergence of buried cells that have only a small influence on propagation velocity.

The final TDRI step is a numerical model to translate both the *a priori* moisture distribution data to a permittivity distribution, and conversely the solution permittivity distribution to moisture content. A dielectric model based on an earlier model of Looyenga was adapted to include both the different characteristic of tightly held water, and the Debye relaxation of free water. The intention was a model with applicability to a range of composite materials. It was tested with data for soil, bentonite clay and wood, and except for one free parameter, model parameters were set by measurable physical properties of the host material.

Validation of the models and the inversion process was achieved by a combination of a self-consistency test, comparison with published data, and measurement.

Keywords: time domain reflectometry imaging, moment method, integral equation, pseudo 3-D, tomography, conjugate gradient, blocking, dielectric, model.

Preface

A great deal of mankind's scientific endeavour has hinged on the exploration of unknown regions. Galileo pioneered the use of instruments to extend vision to greater distances, and around 1590 Janzen invented the microscope to probe regions too small to be viewed unaided. In earlier times, the exploration of the interior of objects that were opaque to visible light, was often restricted to destructive invasive techniques such as dissection, or in the case of the human body, autopsy. However the groundbreaking discovery of Röntgen waves (or X-rays) provided a tool to enable the exploration of new regions, particularly in medicine. This breakthrough by the use of an indirect visualisation tool used a portion of the electromagnetic spectrum to which body tissue was not opaque, and thus enabled non-invasive and non-destructive examination of the interior of the human body.

Today, non-invasive and non-destructive probing of the interior of objects or subsurface regions ranges from seismo-acoustic investigations for geological purposes and the mapping of the surface of Venus by radar from an orbiting craft, to Positron Emission Tomography (PET) used for producing high quality images of the interior of the human body. Much of the progress that has been driven by the medical 'industry' has resulted in technology that is too expensive for other than research or medical requirements. However alternative probing technologies are suitable for other applications including the detection of buried land mines, examination of leachate plume invasion in the vadose zone, and the measurement of near-surface soil moisture from orbiting satellites. The work described in this thesis has the aim of adding a further probing technique, primarily for industrial use.

1. Imaging moisture content distribution

The aim of the work described here is to develop techniques to non-invasively generate an image of moisture content distribution using the dielectric properties of a composite material. It uses the very high frequency and microwave regions of the electromagnetic spectrum as a probing signal to determine moisture content profiles. The new method of imaging moisture content distribution will be referred to as time domain reflectometry imaging (TDRI) since it uses the evanescent field of a parallel transmission line (PTL) to probe one face of the composite material, for example the top of a block of cheese or the flat face of a stick of lumber or a soil surface. Movement of the PTL over the face provides a set of readings of propagation velocity. Then tomographic inversion techniques are applied to produce an image of the permittivity distribution *and hence moisture content distribution* within the material. This thesis describes how three disparate components of research and their respective technological developments are combined to form a measuring system. The components that make up the system are: development of numerical modelling techniques for time domain reflectometry (TDR); application of non-linear tomographic inversion to the model output; and the refinement of techniques for accurately measuring the propagation velocity of an electromagnetic pulse.

The ideas and impetus for this research arose in part from earlier work by the author in developing techniques for measuring spatially averaged moisture content in soil and timber. While average moisture content over a region is an extremely useful and commonly required parameter for a range of applications, a measure of the moisture *distribution* was deemed to have considerable added value in several industries (eg dairy, timber, roading) and research areas (eg soil physics). The work described here will be continued by the author, who will have the opportunity to investigate at least some of the suggestions for future work made in §7.2.

2. Objectives and achievements

The work described here involved: study of the relevant background theory; critical review of relevant literature; original development; adaptation and refinement of appropriate algorithms, techniques and equipment; and comparison of results with alternative measurement techniques. When appropriate, a pragmatic approach was adopted, so that exploration of paths that were not necessary for the rigorous yet focussed direction of the research, was avoided.

The objective of this research was to develop the theory and techniques to show that TDRI, a new technique, could be used for non-invasive, non-destructive measurement of moisture content distribution in composite materials. This objective was met.

Achievements made in the course of this research, and directly related to the work include:

- Development of the TDRI concept
- Establishment of a new pseudo 3-D moment method (MM) modelling technique
- Adaptation of the MM to modelling TDR response to an inhomogeneous dielectric distribution
- Development of a new blocking technique to speed convergence of a non-linear, iterative inversion process
- Refinement of high speed TDR measurement techniques
- Configuration of Looyenga's dielectric model to account for a distinct bound water phase and dielectric relaxation
- Presentation at two international conferences (Woodhead et al., 1999; Woodhead et al., 2001), two refereed journal papers (Woodhead et al., 2000; Woodhead et al., 2001), two research notes (Woodhead and Buchan, 1996; Woodhead and Buchan 2000), presentation of a seminar to the geophysical inversion group at the University of British Columbia (1999), presentation of two seminars at Lincoln University, and a seminar on TDRI at the Process Tomography Centre, University of Manchester Institute of Science and Technology (2001).

3. Thesis layout

Part one of this thesis (Chapters 1 and 2) contains an introduction and critical review of the different techniques and technologies relevant to the work. Part two describes the contribution from the original theoretical and experimental work that comprise the focus and contribution of this research.

Part I (Introductory material and literature review)

Chapter 1 introduces the need for, and use of techniques that can non-destructively measure the interior of objects or materials to reveal the interior moisture content distribution. The capability to non-destructively measure moisture content distribution is placed in an industrial context by examples from several industries. The TDRI concept is also introduced.

Chapter 2 reviews modelling techniques to describe the dielectric properties of composite materials containing water, particle surface influences and relaxation processes. Then numerical methods for modelling TDR with a heterogeneous permittivity distribution along with cell size and shape considerations, the choice of basis functions, and convergence are reviewed. Finally, iterative inversion techniques, alternatives for the sensitivity matrix, and the conjugate gradient method are included in a review of relevant inversion techniques.

Part II (Research/contribution)

In Chapter 3, the MM is adapted to the nonlinear problem of determining the propagation velocity on a PTL buried within an inhomogenous dielectric material. Hence it forms the forward model for TDRI. The work includes adaptation of the MM to the forward model, development of a rapid, pseudo 3-D MM, comparison of several field integration techniques, and self-validation of the resultant model.

Chapter 4 describes the basis of the inverse solution method along with details of the software that implements the inverse solution method. Since the technique of tomographic reconstruction involves choosing a starting dielectric distribution, and then iteratively correcting the distribution using the forward calculation, the technique may employ either real measurements as is the overall thrust of the research, or artificial measurements generated using the forward calculation from an arbitrary dielectric distribution. The latter process is used to evaluate and refine the inversion technique and parameters, and to validate the process. The conjugate gradient inversion method chosen for this work is described, as are a rapidly calculated Jacobian, and a new blocking technique to rapidly improve the convergence of buried cells. Last, a procedure to quantify the ill-posedness of a measured data set is formulated.

Chapter 5 is concerned with the adaptation of the Looyenga dielectric model to include bound water and relaxation components. The new model is partially validated against measured data from the literature, and then inverted for use by TDRI.

Chapter 6 describes details the measurement systems used to validate the forward model, and the results are discussed in relation to the precision of the instrumentation and possible modelling errors. Next, the entire TDRI system is evaluated using measurements on a wood phantom. The measured data are analysed, processed to form images of dielectric and hence moisture content distribution, compared with the actual moisture distribution, and then errors are discussed.

Conclusions and recommendations for further work make up Chapter 7. It includes a summary of the important findings and developments that have been combined to form the TDRI technique. Suggestions for future refinement and development of the work are also proposed.

4. Acknowledgements

I wish offer sincere appreciation for the support, guidance and encouragement of my supervisors, Associate Professor Graeme Buchan and Professor Don Kulasiri.

I also acknowledge support from management and staff at Lincoln Ventures Ltd, Lincoln University, and by staff from the Soil and Physical Sciences Group, Lincoln University, and the Applied Computing, Mathematics and Statistics Group, Lincoln University

Special thanks are due to my wife Merryl for her encouragement and patience, and to daughters Josie and Rochelle.

I acknowledge the response, interest and suggestions of Brent Clothier, John Holdem, Rick Keam and Clarke Topp when, at the formative stages of this PhD, feedback was sought on a number of possible research directions.

Finally, I wish to acknowledge the support by the New Zealand Foundation for Research Science and Technology, who through the Public Good Science Fund made it possible to time-share my part-time PhD studies with my full-time employment, and to funding by the NZ Lottery Grants Board that provided the Tektronix 1502C TDR to the Soil and Physical Sciences Group, Lincoln University.

Ian Woodhead
April 2001

Contents

List of Figures

List of Tables

Glossary

1. Abbreviations

CG	Conjugate gradient
DE	Differential equation
EFIE	Electric field integral equation
EM	Electromagnetic
EPA	Environmental Protection Agency (of USA)
FD	Finite difference (numerical solution method)
FEM	Finite element method
IE	Integral equation (numerical solution method)
MFIE	Magnetic field integral equation
MI	Microwave imaging
MM	Moment method
PDF	Probability distribution function
PTL	Parallel transmission line
RAM	Random access memory
RMS	Root mean square
R^2	Correlation coefficient
SAR	Specific absorption rate (of EM radiation by human body)
TD	Time domain
TDR	Time domain reflectometry
TDRI	Time domain reflectometry imaging
TE	Transverse electric
TEM	Transverse electromagnetic mode
VHF	Very high frequency
VIE	Volume integral equation
VNA	Vector network analyser (frequency domain measuring instrument)

2. Roman symbols

a	Diameter of transmission line rods (m)
b	Spacing of transmission line rods (m)
bw	Bandwidth (Hz)
c	Velocity of light (3×10^8 m/s)
C	(a) Capacitance (F)
	(b) Capacitance per unit length of transmission line (F/m)
C_d	Covariance matrix of the data space d
C_m	Covariance matrix of the model space m

D	Electric displacement (C/m^2)
d	The data space of the general inverse solution
d_{obs}	Observed data set (measurements)
$\boldsymbol{E}$	Electric field (N/C)
$\boldsymbol{E}_i$	Impressed electric field (N/C)
$\boldsymbol{E}_P$	Electric field due to polarisation (N/C)
eps	Floating point accuracy
$\boldsymbol{G}$	A Green's function
g	The forward transfer function of the general inverse solution
G	The forward model (in matrix form)
$\boldsymbol{H}$	Magnetic field intensity (A/m)
h	A correction used in iterative improvement
J	Jacobian, first derivative of a data set
J_a	Approximation to the Jacobian J
K	Linear function transforming $\boldsymbol{P}$ to $\boldsymbol{E}$, $\boldsymbol{K} = [K]$ is the scattering matrix
k	'Constant' used for characteristic line integration
k_a	Apparent dielectric constant (as measured by TDR)
L	Capacitance per unit length of transmission line (F/m)
l	1-D integration path
m	The model space of the general inverse solution
m_{prior}	*A priori* model
$\boldsymbol{P}$	Polarisation (C/m^2)
P	(a) Probability (b) Porosity or volume fraction of inclusions
q	Electric charge (C)
r	3-D space dimension (generally, $\underset{\sim}{r} = \underset{\sim}{x} + \underset{\sim}{y} + \underset{\sim}{z}$)
R	(a) Resistance per unit length of transmission line (Ω/m) (b) Rank of a matrix
S	Objective function
T	Temperature (°C)
t_p	Propagation time (s)
t_r	Rise time (s)
U	Energy (of electric field, J)
V	Volume fraction of inclusion (in Looyenga dielectric model)
v_p	Propagation velocity (m/s)
Z_0	Characteristic impedance of a transmission line (Ω)
Z_t	Terminating impedance of a transmission line (Ω)

3. Greek symbols

α	(a) 'Shape factor' for Looyenga (and other) dielectric models
	(b) Weighting factor in conjugate gradient method
β	Empirically-determined fitting factor for generic dielectric model
χ	Electric susceptibility
δ	(a) The Dirac delta function
	(b) A perturbation
ε_0	Permittivity of free space (8.5×10^{-12} F/m)
ε'	Real (in phase) permittivity (F/m)
ε''	Imaginary (out of phase) permittivity (F/m)
ε_b	Relative permittivity of ice-like, bound water
ε_h	Relative permittivity of host material (dry soil particles, dry wood, etc)
ε_r	Relative permittivity (dielectric constant)
ε_m	Relative permittivity of mixture (resultant for generic dielectric model)
ε_w	Relative permittivity of water
ε_∞	High frequency (for a particular relaxation) relative permittivity
Φ	Electric potential (J/C)
Γ	Reflection coefficient
λ	(a) Wavelength (m)
	(b) Tikhonov regularisation constant
μ	(a) Permeability (H/m)
	(b) Mean
μ_0	Permeability of free space ($4\pi\times10^{-7}$ H/m)
μ_r	Relative permeability
η	Condition number of a matrix
θ_g	Gravimetric water content (kg/kg)
θ_0	Initial or *a priori* moisture content (m^3/m^3)
θ_t	Transition (bound-to-free) volumetric water content (m^3/m^3)
θ_v	Volumetric water content (m^3/m^3)
ρ	(a) Dry bulk density (kg/m^3)
	(b) Charge density (C/m)
σ	Conductivity (S/m)
τ	Relaxation time (s)
ω	Angular frequency (Hz)

Chapter 1

Introduction

This chapter introduces several industrial situations where non-invasive and non-destructive measurement of the internal moisture content distribution or the internal structure of a composite material, has demonstrable value. In each case, the information could be provided by time domain reflectometry imaging (TDRI) that utilises electromagnetic (EM) probing techniques, in conjunction with a dielectric model that relates the material's dielectric properties to its moisture content. Next, various techniques for non-invasive and non-destructive imaging of materials will be described in purely qualitative terms. This is followed by an outline of the TDRI method developed in this research, and how it differs from alternative techniques. While the focus of this research has been on mapping the internal moisture distribution of composite materials, the technique developed has uses for other material properties that are reflected in electrical and dielectric properties.

1.1 Uses for measurement of moisture distribution

Determination of moisture content is of vital interest to a wide range of disciplines and industries. The range of materials is also diverse and includes soil, cereals, dairy products and timber. However, beyond a measure of the mean moisture content over a prescribed volume, moisture content *profiles* are of interest. Distribution of moisture affects such crucial physical and biological processes as drying stresses in timber, solute transport and biological organism behaviour in soil, uniformity of dye absorption in textiles, and the quality of many food products. The capability to characterise moisture gradients or profiles is important in controlling drying processes in materials such as timber (Zeff pers comm., 1995) and textiles, or to characterise moisture content profiles that arise in soil due to drainage, plant water uptake or capillarity (Hillel, 1980). Hence a method of non-invasive, non-destructive measurement of moisture profiles would find application in many areas.

A good example is the timber drying industry. Kiln drying aims to provide a client with timber that has a uniform moisture distribution, such as a mean moisture content of 10% by weight. As timber dries a moisture gradient is established between the surface and centre of the timber, and rapid drying such as within a kiln generates steep moisture gradients. Ideally, the gradients would be monitored during the drying process to enable limiting gradients at crucial periods (for example early in the drying process) to limit the extent of cracking and checking of the timber, yet maintain sufficiently large gradients for rapid drying and hence acceptable kiln throughput. Once the surface of the timber is somewhat drier than the target moisture content, a very high humidity condition is formed to reintroduce moisture to the surface of the timber. This has the aim of partially reversing the gradient formed during drying and hence accelerating the trend towards uniform, equilibrium moisture content. A measure of the moisture content

gradient is demonstrably useful to this industry (Zeff pers comm., 1995) to control the drying rate and to optimise the rehumidifying stage. After drying, boards undergo "remanufacturing" to form the final product. This may comprise some or all of the following processes: planing, sawing, shaping, gluing, sanding and finishing with a protective coating. Timber moisture content affects both the ease of applying the above processes, and the final quality. In those processes where a significant amount of the wood material is removed, an initially uniform moisture content distribution is desirable to avoid reducing the dimensional stability of the product. After drying has been completed, a sorting phase based on moisture content distribution would enable rejection of boards which are outside an acceptable moisture content range or which have a large moisture gradient. High moisture content could lead to future moisture loss through the surface, with detrimental impacts on the quality of the remanufacturing processes.

Another example is in the cheese making industry. In a commercial cheese plant, saturated curd is fed onto a slowly moving draining belt. The whey drains through the belt, aided by chopping the curd with rotating knives spaced at intervals along the belt. Near the end of the belt and prior to being fed to a press, salt is applied to the drained curd to cause curd shrinkage (and consequential release of further whey and reduction in moisture content), provide flavour enhancement, and enhance the shelf life of the product. One measure of the final cheese quality is the salt-to-moisture ratio, an indication of the keeping qualities of the cheese (Morison pers com., 1994). The ratio is affected by the moisture content of the curd prior to salting (itself variable since it is affected by both milk composition and the curd cooking process), and management of the ratio within fine tolerances is a goal of the cheese maker. A measure of the moisture content gradient on a cheese bed prior to salting would provide the cheese maker with both an indication of the uniformity of the curd as well as its mean moisture content, hence permitting better control over the crucial salt-to-moisture ratio. In making cheddar cheese, the salted and drained curd is compressed under gravity in Wincanton towers, cut into large blocks and sealed in polythene for packaging and dispatch as a bulk cheese product. Once the blocks of cheese are sealed, there is no further opportunity for moisture exchange with the atmosphere, and over time the cheese moisture content gradients will equilibrate to the mean moisture content. However since the actual moisture content affects maturation, quality may be adversely affected by significant variation in moisture content. Hence a measure of the moisture distribution would enable isolation of blocks with unacceptably high gradients to be withheld or downgraded (Bruce pers comm., 1997; van der Sanden pers comm., 1999).

Sapstain is a fungal disease of felled but unpeeled logs. The fungus grows in a region of timber above a moisture content of 20%. When logs are transported long distances, the natural drying of the logs generates a zone of ideal conditions for sapstain growth, and the region slowly recedes into the log as drying progresses. Consequently, sapstain may ultimately affect a significant portion of the log. While avoidance may include wetting logs to ensure the upper moisture content limit for sapstain growth is always exceeded, a measure of the moisture beneath the bark would provide industry with a better management and research tool (Price pers comm., 1997).

A further application relates to the development of potholes within chip seal road surfaces. Research is still under way to provide full understanding of the influences and processes that cause the initial breakdown in a bitumen chip road surface. However it is well known that once the initial degradation of the seal has commenced, water seepage into the subsurface or basecoarse zone reduces its the mechanical and load-bearing properties. The basecoarse softening renders the area more susceptible to further damage to the seal from road traffic, so allowing the ingress of additional water. An ideal solution to this difficulty could be realised by a vehicle equipped with the capability to map the moisture distribution over the road surface, and thus detect the onset of the conditions contributing to pothole formation. Early, preventative and more economical maintenance procedures could then be implemented.

Examples of other industrial and research uses for non-invasive imaging techniques (not necessarily the detection of moisture content distribution) include:

- determining the internal structure of animals or fish (eg breeding or quality investigation)
- performing clinical diagnostics
- medical research applications
- examination of insect behaviour in fruit
- development of bruises and fungal infections in fruit
- study of water infiltration or surface evaporation in soil columns
- understanding temporal development of plant root mats
- characterising drying processes in timber
- examining structural characteristics of sawn timber
- monitoring spalling development in reinforced concrete
- determining aggregate distribution in concrete
- exploring the internal structure or make up of rare or antique objects.

1.2 Permittivity as a surrogate for moisture content

Water has several distinctive properties that may be used for measurement of moisture content in composite materials. One is that the bond angle of 104.47 degrees (Franks, 1972) between the hydrogen atoms, combines with the differing electronegativity of the hydrogen (2.1) and oxygen (3.5) atoms to result in a large polar moment. The strong polar nature of water contributes to its large relative permittivity (ε_r) of approximately 80 compared to that of most dry biological and natural materials for which ε_r is generally in the range 2 to 5 (Nelson, 1973; Kent, 1987). This large contrast enables dielectric measurements of composite materials to form a useful indirect measurement of volumetric moisture content (θ_v). In practice, ε_r is a curvilinear function of the θ_v, whose curvature is dependent on the composite material, its texture, and its porosity which influence the interaction of the composite material with water.

ε_r arises primarily from polar molecules that store energy by elastic rotation, but contributions are also made by elastically altering bond angles, and intra-atomic contributions that are dominated by distortion of electron distribution. In the absence of an electric field, a polar

substance such as water has permanent dipole moments that are randomly distributed so that no net polarisation is present. The conductivity of the material and any conducting inclusions (eg dissociated water) dispersed within the material contribute to the dielectric loss of the mixture. The total permittivity ε comprises a real component ε' that represents the real or energy storage component of the permittivity, and ε'' the orthogonal or imaginary component that results from the conduction current contributed to by conductivity and other forms of dielectric loss. Where j is $\sqrt{-1}$,

$$\varepsilon = \varepsilon' - j\varepsilon'' \tag{1.1}$$

Many methods of determining ε' are usefully employed for determining θ_v of composite materials. However where ε'' is large in comparison with ε', the measurement becomes inaccurate (Leschinik and Schlemm, 1999). Consequently, the choice of measurement frequency range when measuring ε' is crucial since many loss processes are frequency dependent.

1.3 Time domain reflectometry imaging (TDRI)

Use of ε_r with imaging techniques has in many cases, provided the means to image moisture content distribution. Imaging may be categorised according to how the images are used. Frequently, visualisation is the requirement and it is sufficient to provide contrast between different materials and aspects of the image. However, in many industrial applications and in TDRI for moisture measurement, the imaging must be quantitative. Appendix 1 provides a qualitative comparison of the common techniques, along with TDRI.

TDRI is believed to be a new technique for quantitative imaging of θ_v distribution. The probing signal comprises the lateral evanescent field of a parallel transmission line (PTL), generated by TDR equipment, but could similarly comprise the evanescent field at the end of an open circuited transmission line. A set of TDR measurements that comprise readings for different positions of the PTL in relation to the nearby composite material (Figure 1.1) is inverted to obtain a representation of the actual ε_r distribution of the composite material. The PTL is moved over a grid in the x-y plane to resolve the simple 2-D ε_r distribution. In this case where ε_r is assumed invariant in the z direction, TDRI resolves ε_r of the cuboid cells of length equal to that of the PTL (300 mm for example). The measurement of θ_v distribution across sawn lumber is an application where this assumption of longitudinal uniformity is reasonable. However, in the cheese example described above, resolution in the third dimension would be required. In this case, a second set of measurements taken with the PTL moving over a grid in the y-z plane would be required to provide the additional data required to resolve the unknown ε_r distribution. The use of the evanescent field of the PTL as the probing signal results in the one device (the PTL) forming both the source and receiver for TDRI.

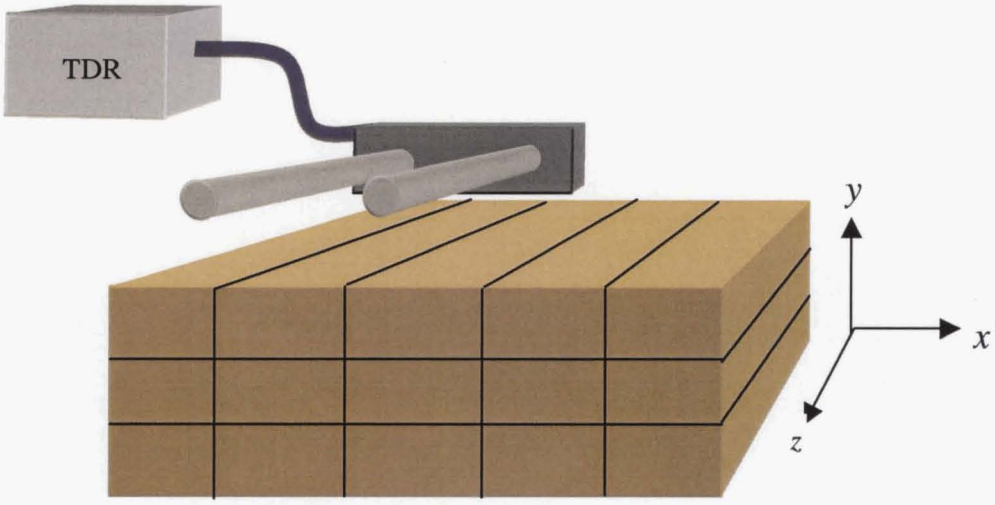

Figure 1.1 Typical implementation of TDRI showing the PTL over the composite material.

The principal departure of the TDRI measurement procedure from current tomographic practice, is the use of the lateral, evanescent field of the PTL as the EM probing signal, and hence TDRI differs from microwave imaging, the existing technique that is most similar. This use of the evanescent field of a PTL imparts several advantages:

1. Since the propagation is guided, scattering does not significantly reduce the signal level as occurs with microwave imaging (Jofre et al., 1990).

2. Use of the lateral electric field of a travelling wavefront results in a spatial resolution that is not inherently limited by the wavelength λ of the propagating wave. In travel time tomography the smallest resolvable feature size is generally of the order of 3λ (Berryman, 1991), and for diffraction tomography, both amplitude and phase of the scattered signal must be measured. In TDRI, resolution is limited by the sensitivity of the measuring apparatus.

3. The measured parameter is the travel time of the signal, a parameter that is in principle easy to measure and less affected by noise than a direct measure of the amplitude of scattered propagation as required for diffraction tomography. Microwave imaging commonly requires a measure of both the amplitude and phase of the scattered signal to adequately solve the inverse problem (Johnson et al., 1996). However TDRI requires a very high measurement resolution (resolve < 1 ps) and this impacts on the depth resolution of the measurement system. All these factors are discussed further in Chapters 4, 5 and 6.

Since the analysis method assumes transverse electromagnetic mode (TEM) propagation, the width of the PTL must be small compared with the wavelength λ, so a practical penetration depth limit is approximately 100 mm with current instrumentation and measurement frequencies. These factors too will be discussed in later Chapters.

Chapter 2

Literature Review

Since time domain reflectometry imaging (TDRI) is a technique that draws on methods across several disciplines, this literature review is divided into four sections representing the key elements of the technique as described in §1.3. Initially, a review is made of dielectric mixing models since the model is required for TDRI when translating the *a priori* or initial estimate of the volumetric moisture content (θ_v) distribution to a distribution of relative permittivity (ε_r) used by the inversion process, and subsequently for translating the solution back to θ_v. Next, the crucial aspect of time domain reflectometry (TDR) measurement is reviewed, followed by a brief exploration of the spatial sensitivity of a parallel transmission line (PTL) to a surrounding ε_r distribution. Numerical modelling techniques that contribute to the forward problem of predicting the propagation velocity (v_p) on a PTL, buried in an arbitrary ε_r distribution are then reviewed. The last section is a review of suitable inversion techniques that use physical measurements and a solution to the forward problem, to provide a predicted ε_r distribution.

2.1 Dielectric mixing models

The use of dielectric properties as an indirect measure of θ_v is widely accepted across a range of disciplines such as the natural sciences (eg soil), food engineering (eg fish, food powders), timber processing (on-line measurement of medium density fibreboard), and agriculture (barley within a silo). In this section, relevant theoretical and practical aspects of dielectric mixing models to predict the dielectric properties of moist composites are reviewed. Dielectric modelling is important to this work since it represents the 'reality component', whereby dielectric properties are translated to the desired knowledge of θ_v of the composite material.

Dielectric mixing models aim to quantify the influence of a range of physical properties on ε_r of a material, although the model may take the form of $\varepsilon_r(\theta_v, \textit{other parameters})$ or $\theta_v(\varepsilon_r, \textit{other parameters})$. Figure 2.1 (Torgovnikov, 1993) provides an insight into ε_r of wood, demonstrating the strong, non-linear dependence of ε_r on both frequency and θ_v.

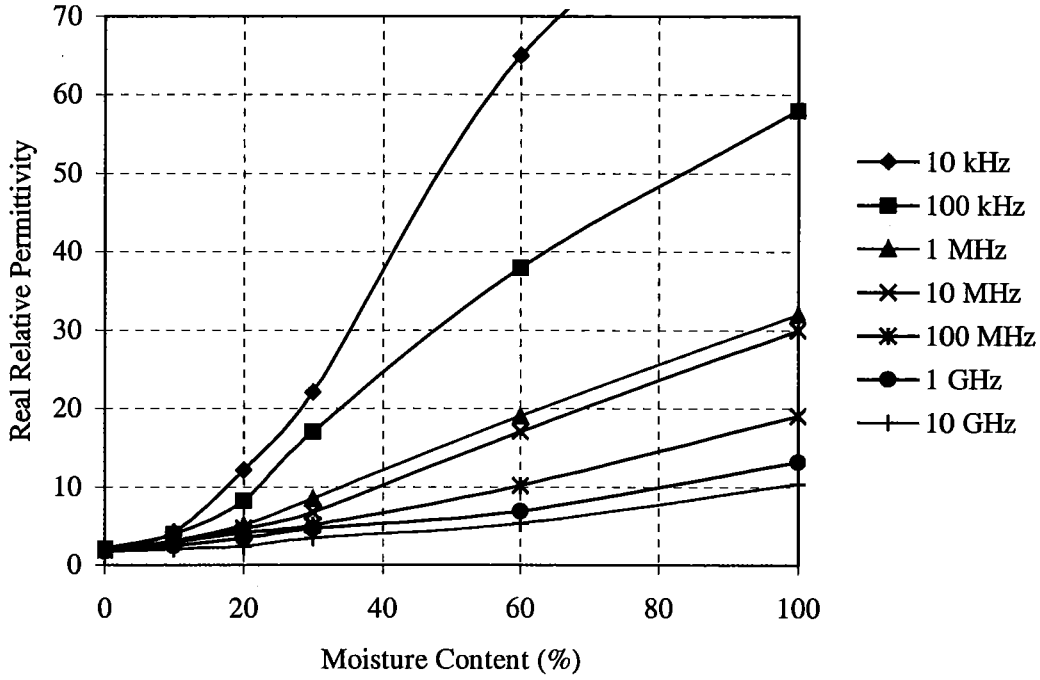

Figure 2.1 Dielectric properties of an unnamed wood species (Torgovnikov, 1993).

Recently, there has been a lot of activity in modelling the dielectric properties of soil as a function of θ_v, so much of the material reviewed here applies primarily to soil models. Although the properties of soil differ from cellulose or collagen-based materials from the aspects of particle size range and biological passivity, there are many similarities in response and the principles are transferable across materials. This arises from the large disparity between ε_r of water (~80) and that of most composite materials (3-5).

Many dielectric mixing models apply to a restricted range of parameters, particularly the particle shape and size distribution within the composite material, and the measurement frequency. These two factors are sufficiently influential that their impact will be reviewed prior to discussing dielectric modelling.

2.1.1 Surface effects

Torgovnikov (1993) pointed out that the stable bonding of wood cellulose with monomolecular moisture results in an insignificant contribution to ε_r and loss tangent in the θ_v range 0 to 4-6%. The effect is largely due to the interaction between water molecules and nearby surfaces of the wood, in particular the binding to cellulose.

Water held in close proximity to surfaces such as clay particles forms a monolayer of water molecules that have dielectric properties similar to those of bound water (Wang and Schmugge, 1980). Since the particle size range of soil components varies from less than 1 μm for clay particles to 2 mm for sand (Hillel, 1980), there has been significant interest in addressing the

dielectric properties of monomolecular layers and their effect on measurements of θ_v using dielectric techniques. The large range of surface area to volume ratios for different soil types significantly influences the dielectric behaviour of different soils, particularly at low θ_v (Wang and Schmugge, 1980; Wang, 1980). Hence it is observed that the change in ε_r with the introduction of small quantities of water to dry soil particles is small. In their dielectric models, Wang and Schmugge (1980) employ a transition water content (θ_t) denoting a change from a slowly increasing ε_r with water content to a more rapid increase. θ_t increases with surface area ratio, being highest for clay (typically 0.19 V/V) and lowest for sand (typically 0.017 V/V for coarse-grained soils). From the presented data, the transition at θ_t is apparent in the data for clay, but indistinct for loam and sand. Dirksen and Dasberg (1993) suggested that the apparent dielectric behaviour of tightly bound water may be calculated from the specific surface (area) and assumed a monomolecular layer with $\varepsilon_r = 3.2$ for bound water. As an alternative to specific surface, they state that the hygroscopic water content is a good estimate of bound water fraction.

Or and Wraith (1999) calculated the approximate effective ε_r of water near a solid surface to be respectively 6, 32 and 80 for the first, second and subsequent monomolecular layers. They also pointed out that the surface or bound water makes less contribution to ε_r than bulk water, yet is indistinguishable to standard (sic) thermo-gravimetric measurement techniques. Presumably, drying at progressively higher temperatures would allow extraction of information relating to the quantity and binding energy of bound water.

Similar effects have been noted with other materials. From a study of the proteins haemaglobin, albumin and collagen, Kent and Meyer (1984) observed that ε_r of sorbed water, even in the loosely held multilayer states, differed from that of bulk water (~80). Takashima (1962) demonstrated that ε_r of ovoalbumin crystals was close to unity until the adsorbed water increased to 17 %, whereupon there was a notable increase.

Charged double layers have reportedly resulted in low frequency ε_r in excess of 1000 (Schwan et al., 1962). Although not strictly a surface effect, elevation of ε_r by the Maxwell-Wagner effect can be evaluated using the shperical inclusion model of Schwan et al. (1962). The model indicates that an order of magnitude increase in ε_r may occur at $\theta_v > 40$ % (with a corresponding relaxation time of 10^{-7} s at a solution conductivity of 0.01 S/m). Either of these effects could contribute to the low frequency elevation of ε_r apparent in Figure 2.1.

2.1.2 Frequency effects

Bound water exhibits relaxation at a lower frequency than bulk water (Dobson et al., 1985; Hastead, 1973), and hence a dielectric loss mechanism within the frequency range used for soil water measurement (hence less than the 16 GHz relaxation frequency of bulk water). Wang (1980) pointed out that the log of the relaxation time is proportional to the activation energy. Yagihara et al. (1999) demonstrated that the relaxation strength and frequency of water molecules within the calcium silicon hydrate of mortar both decrease as curing proceeds. The relaxation frequency changed from approximately 1 MHz after 33 days to 100 Hz after 4 years,

as the quantity of free water decreased. Hoekstra and Doyle (1970) observed relaxation frequencies around 1 GHz for film water on Na-montmorillonite clay and γ-aluminium oxide, and attributed this to breakage of hydrogen bonds between adjacent water molecules in a thin film. They contend that this is supported by the activation energies of approximately 25 kJ/mole at microwave frequencies (which are similar to the energy of hydrogen bonds of approximately 21 kJ/mole reported by Brown, 1968).

2.1.3 Purely empirical dielectric models

One approach to providing a translation from ε_r to θ_v of a composite material is the pragmatic application of just one measured parameter, real ε_r. This method relies on the overwhelming ε_r of water and hence its volume fraction. For example the empirical equation of Topp et al. (1980) for soil, provides a useful relationship over a wide range of soil conditions, from loams to sand and for water content from 0.05 to 0.5 (White and Zegelin, 1995; and others). Topp's equation utilises the *apparent* in-phase or lossless permittivity k_a measured by TDR:

$$\theta_v = -5.3\times10^{-2} + 2.92\times10^{-2} k_a - 5.5\times10^{-4} k_a^2 + 4.3\times10^{-6} k_a^3 \qquad (2.1)$$

This model has been used extensively for soil applications and, with alteration of the coefficients, also provides a useful basis for other materials such as coal (Zegelin, 1995 pers. comm.; White and Zegelin, 1995). Numerous authors have pointed out the departure of Topp's model for clay soils, all soils at low θ_v, and for high porosity peat soils at high θ_v. In referring to the influence of bound water, White and Zegelin (1995) remarked that Topp's equation makes no assumption about ε_r of soil water. This viewpoint appears difficult to justify since instead of accounting for the varying quantities of bound water for different soil types, Topp's equation applies a curvilinear function that assumes a smaller (but invariant) ε_r contribution when θ_v is small. A useful summary of TDR-based empirical models and their departures in various soils is presented by Jacobsen and Schjonning (1995). These data indicated that good prediction of θ_v with mineral soils, was obtainable over the range 2 to 36 %, and at dry bulk densities of around 1350 and 1550 kg/m^3. The Topp equation provided a total root mean square (RMS) error of 2.21 % using 4 mineral soils. Jacobsen and Schjonning (1993) obtained an RMS error of 0.96% using ten mineral soils and an empirical equation that included *a priori* information in the form of percentages of clay and organic matter.

Alharthi and Lange (1987) introduced a two step model that defines θ_v as:

$$\theta_L = 0.128(\sqrt{\varepsilon} - A) \quad \text{and} \quad \theta_H = 0.011\varepsilon + \frac{0.32}{A^3} \qquad (2.2)$$

where θ_L and θ_H are respectively the calculated results for low and high water content values, and A is 1.59 for sandy and clayey loams. These forms were obtained by inversion and simplification of the Hannai-Bruggeman equation (Hannai, 1968 cited in Alharthi and Lange, 1987):

$$\theta = \left(\frac{\varepsilon_c - \varepsilon_s}{\varepsilon_w - \varepsilon_s}\right)\left(\frac{\varepsilon_w}{\varepsilon_c}\right)^{\frac{1}{3}} \tag{2.3}$$

where ε_c represents the composite permittivity, ε_s the soil permittivity, and ε_w the permittivity of water.

The model assumes roughly spherical particles, and uses an empirically derived, soil-type dependent constant A. Model output was shown to agree well with measurements for a sandy soil and for a complex soil, although there was no indication of performance with a clay soil. Presumably an alternative shape factor A would need to be determined empirically for soil particles that do not conform to the assumption of near-spherical particles.

Bartley et al. (1999) used an artificial neural network (feed forward, back propagation) to determine θ_v of wheat using eight frequencies in the range 10 to 18 GHz. The neural network was trained using three sets of measured parameters: ε_c, amplitude data from transmission coefficients, and both phase and amplitude transmission coefficients. The correlation coefficients obtained (R^2) were 0.992, 0.982 and 0.993 respectively for θ_v and density ranges of 10.6 to 19.2 % and 0.72 to 0.88 g/cm^3 respectively. Seventy points were used to train the system.

Empirical models do not directly account for measurement frequency. The soil models referred to above, generally use the Tektronix 1502 time domain reflectometer (TDR), and the resulting waveforms are normally analysed using a dedicated software package (Or et al., 1998). Hence although the highest frequencies tend to be most influential on the maximum slope of the returned edge and thus dispersion change with θ_v (Or and Rasmussen, 1999), the effect is to some extent incorporated within the model. It is apparent that at high θ_v, dielectric loss causes a dispersion that influences the accuracy. For example Jacobsen and Schjonning (1995) used the formulation of Roth et al (1992) with 9 mineral soils to obtain an RMS error of 3.57 %, and with different coefficients obtained an RMS error of 15.9 % for 7 organic soils. Similarly they evaluated the coefficients of Dasberg and Hopmans (1992) to obtain RMS errors of 2.9 % and 8.53 % for sandy loam and clay loam respectively. The clays and organic components in the soil are expected to confer more dielectric loss than the mineral component. Note that the forms of Roth et al. (1992) and Dasberg and Hopmans (1992) were not optimised for the soils chosen by Jacobsen and Schjonning (1995), although others have observed that empirical equations are best suited to coarse-grained soils.

2.1.4 Physically-based models

Dielectric mixing models inevitably make simplifying assumptions about many of the loss and combinatorial parameters that are involved in the make-up of a composite material. For example the earlier models attributed to Bötcher (1952) and Bruggeman (1935), were synthesised from a simple but general theoretical basis, that of packed spherical particles. Looyenga (1965) used a different approach that was in principle, independent of the shape of the particles. A general two-phase model is:

$$\varepsilon_m = [\varepsilon_h^{\alpha} + P(\varepsilon_{inc}^{\alpha} - \varepsilon_h^{\alpha})]^{\frac{1}{\alpha}} \tag{2.4}$$

where ε_m, ε_h, and ε_{inc} are respectively the complex ε_r of the mixture, the host and the inclusion, and P is the volume fraction of the inclusions. Looyenga (1965) derived this equation with $\alpha = 1/3$. While quite severely constrained by the assumptions, idealistic models such as the above frequently provide useful relationships (Campbell, 1990). However, they are most applicable to situations with narrow ranges of both particle size and shape, and where accuracy requirements are not too stringent. To represent composite materials more accurately, additional parameters need to be incorporated, and in stark contrast to the above empirical models, most require *a priori* information about the host material and the nature of the water inclusion.

Wobschall (1977) described a semi-disperse model where in soil, the water is considered to be in part the dispersed material, and in part the dispersing medium. He also incorporated three forms of water: crevice water, water dispersed in films over soil particles, and non-dispersed or bulk water. The model was tested with frequencies to 100 MHz. Dobson et al. (1985) and Hallikainen et al. (1985) pointed out the impracticality of determining the Wobschall parameters and instead configured a model that used more easily measured parameters. These included the dry solids fraction, the film water fraction in the double layer, the bulk water, and air. These were combined in the de Loor (1968) four component model:

$$\varepsilon_m = \varepsilon_s + \sum_{i=1}^{3} \frac{V_i}{3}(\varepsilon_i - \varepsilon_s) \sum_{j=1}^{3} \frac{1}{\left[1 + A_j \left\{ \left(\frac{\varepsilon_i}{\varepsilon_b} \right) - 1 \right\}\right]} \tag{2.5}$$

where ε_s and ε_i are the relative permittivities of the host and inclusions, ε_b the effective relative permittivity near boundaries, A_j the depolarisation ellipsoid factors that relate to the shape of the soil particles (de Loor, 1968), and V_i the volume fractions of the inclusions. The model, which was tested over the range 1.4 to 18 GHz, also predicted the imaginary component of ε_r. The authors noted that for good accuracy, bound water should be treated as a distinct component of the mixture. This aspect was also pointed out by Hallikainen et al. (1985) in a related paper and was previously emphasised by Wang (1980), and Wang and Schmugge (1980). At 0.3 GHz and >1 GHz, Wang (1980) showed how the influence of water relaxation coupled with the differing surface area factors and hence bound water fractions between sands and clays, demanded a parameter representing bound water. He usefully related the bound water fraction to wilting point to provide a practically obtainable parameter for this purpose.

The so-called α model (mistakenly attributed by Dirksen and Dasberg (1993) to Birchak et al. (1974)) was considered by Dirksen and Dasberg (1993) to be inferior to the Maxwell-de Loor model. The reason cited was the textural influence on the empirically defined and soil specific α.

Wang and Schmugge (1980) employed a linear model with parameters that included an empirically determined factor γ representing the quantity of initially absorbed water:

$$\varepsilon = \theta_v \varepsilon_x + (P - \theta_v)\varepsilon_a + (1 - P)\varepsilon_r \tag{2.6}$$

where ε_x is the permittivity of the initially absorbed water, P is the porosity of the dry soil, and ε_a and ε_r are the relative permittivities of the air and solids fractions. ε_x is defined by:

$$\varepsilon_x = \varepsilon_i + (\varepsilon_w - \varepsilon_i)\frac{\theta_v}{\theta_t}\gamma \tag{2.7}$$

where ε_i is the relative permittivity of ice, representing the bound water fraction, ε_w that of water, and θ_t the transition moisture content discussed earlier. A further free parameter altered ε'' as a function of θ_v^2, and the data from measurements at 5 GHz were fitted to both ε' and ε''. Notable in the work of Wang and Schmugge (1980) was the quantitative correlation between wilting point and both γ and θ_t. They also reported on the prediction of wilting point from the sand and clay fractions of soil, hence providing two possible avenues for defining γ and θ_t. Although the work was aimed at the higher frequencies used for remote sensing, there appears to be little application of the results to TDR-based models. Indeed White and Zegelin (1995) noted that textural influence was limited to $\theta < 0.15$, adding that some 'bound water' may not be measured by oven drying, and Grewal and Buchan (1991) noted the retention of adsorbed water in soil after drying at 105 °C. Certainly within host materials such as celluloses, it is considered that some water is retained after drying at 105 °C (Keey, 1998).

Jacobsen and Schjonning (1995) also compared the output from several 3 and 4 phase models with experimental data for the soils used above for evaluating the empirical models. While the models that included those of Dobson et al. (1985) and Dirksen and Dasberg (1993), do not perform any better than the above empirical formulations, they are more prescriptive. The 4 phase models do not include any fitting or optimisation parameters, although like the above 2 phase model, the 3 phase models include a term α that has been derived empirically.

2.1.5 Other model classifications

Ansoult et al. (1985) used a stochastic approach where the probability of finding air, water or a host particle in the immediate vicinity of a point charge, was used to predict ε_r. The input parameters were the prescribed volume fractions of air, water and solids, and the number of degrees of freedom u ascribed to the model. Friedman (1997) refined that model to eliminate

the necessity for u, which was not considered to have physical meaning. Then, without use of the empirical fitting factor u, close agreement with Topp's equation was obtained.

2.2 TDR measurements

TDRI requires accurate measurement of propagation time on a PTL. Measurements may be made in the frequency domain using a vector network analyser (VNA) for example, and then converting to the time domain (TD) using a Fast Fourier Transform (FFT) or Laplace transform (Hager, 1994). However, direct measurement in the TD is commonly used for TDR, and is appropriate for TDRI in the first instance since picosecond measurements of propagation time t_p in the frequency domain require specialist equipment (VNA) and error correction techniques such as time gating.

Two-port TD measurements were pioneered by Fellner-Feldegg (1969, 1972). The essence of the technique is to impose a known time-varying voltage to the test material and record the resultant time-dependent response. The imposed voltage (frequently a step function) must contain all frequencies of interest, and have a known frequency distribution to permit full characterisation of the material. The TD data are frequently transformed back to the frequency domain for presentation of the material's spectral characteristics. Typically, the test material either terminates a transmission line or forms part of the dielectric surrounding a PTL to which the time-varying voltage is applied, and either arrangement could be used for TDRI. The returned signal contains the TD data.

When the test material terminates a transmission line, the reflection coefficient Γ (a complex quantity), which is defined as the ratio of the reflected to incident voltage, is a measure of the terminating impedance. The dielectric properties may be resolved by use of:

$$\Gamma = \frac{Z_t - Z_o}{Z_t + Z_o} \tag{2.8}$$

where Z_t is the (unknown) terminating impedance, and Z_o is the impedance of the transmission line. The real component of Z_t can be resolved from the steady state or long-term value of Γ, and the imaginary component of Z_t by the time varying value of Γ. Calibration is a critical aspect of the above measurement process. The coaxial probe that terminates the transmission line is used to couple the line to the material being measured (Sheen and Woodhead, 1999). First, a model of the complex impedance of the probe (with the material to be measured) is required to extract the dielectric properties of the material from the complex Γ. Then, measurements using reference materials are used in the model to predict the unknown properties (Cole et al. 1980, Kraszewski et al. 1983, Mashimo et al. 1987, Hager 1994, Stuchly et al. 1982, Misra 1987). Operation over a wide frequency and complex ε_r range requires a detailed model (Sheen and Woodhead, 1999).

When the test material forms the dielectric of the transmission line (which would normally be a PTL), simpler relationships govern the prediction of ε_r from measured parameters if radiation can be ignored (§3.1.2). If the PTL and material are lossless, the propagation velocity v_p, of a voltage step on the line is related to ε_r of the material. Given a lossless PTL of unit length:

$$v_p = \frac{1}{\sqrt{\mu_0 \mu_r \varepsilon_0 \varepsilon_r}} \tag{2.9}$$

where μ_0, is the permeability of free space, μ_r the relative permeability of the material, and ε_0 the permittivity of free space. μ_r is very close to one for most insulating materials. Thus in practice for a lossless PTL and dielectric material, v_p is a direct measure of ε_r. For example v_p in bulk water ($\varepsilon_r \approx 80$) is about 9 times slower than in vacuum or air ($\varepsilon_r \approx 1$). Note that regarding the measurement process as lossless is a common and often reasonable assumption (Topp et al., 1980).

Where losses are not negligible, v_p is dependent on both the real and imaginary components of ε_r and PTL parameters, and due to dissipation of energy, the attenuation on the line is no longer zero. Furthermore, apart from the special case of a distortionless line, v_p and attenuation become functions of frequency. Consequently, frequency distortion or dispersion and amplitude distortion alter the shape of the transmitted edge, as indicated by the influence of soil water conductivity on the risetime (t_r) of a TDR signal (Ferre et al., 1999). Figure 2.2 shows a typical TDR trace, where the label 'start' denotes where the signal encounters the balun that changes the unbalanced signal from the measuring instrument to a balanced signal for the PTL. The point of reflection is usually determined from the intersection of tangents to the minimum and maximum slopes around the returned edge (Wraith and Or, 1999). In a lossy material the returned edge becomes less distinct, and may impact on edge detection algorithms (Wraith and Or, 1999). The tangent method is commonly used for measurements in soil, and was demonstrated by van Germert (1973). The limitations of the method will be explored further in §6.4.

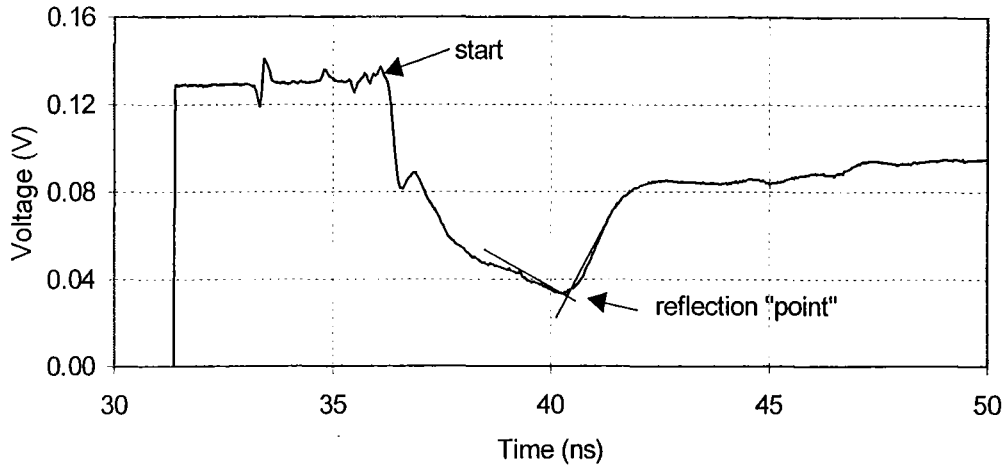

Figure 2.2 Typical TDR waveform for soil. The 'start' point denotes the time when the voltage step encounters the balun, and the tangent lines illustrate determination of the reflection point.

For conventional TD measurement of θ_v in soil for example, a TDR instrument such as the Tektronix 1502C (pulse amplitude 0.3V into 50 Ohms, pulse risetime $\leq$ 200 ps, and measurement accuracy the greater of 133 ps or 1% of reading) is used to both generate and measure the TD signal. A balun was typically used to couple the unbalanced 50 Ohm signal to the balanced PTL, but recently direct coupling to a central signal rod and two or three surrounding grounded rods (Zegelin et al., 1989) has been used for simplicity and enhanced performance at higher θ_v and/or conductivity. With either method there are inevitable impedance differences between the 50 Ohm signal from the Tektronix 1502, and the moisture-dependent impedance of the transmission line, but Hook and Livingstone (1995) reported no difficulties with such mismatches. Spaans and Baker (1993) compared the performance of several balun winding arrangements in a range of soil conditions, and recommended baluns tightly wound with several turns (for isolation) of 0.127 mm enamelled wire on small Ni-Zn ($\mu_r = 100$) cores. Although a 1:1 balun provided good performance for conductivity measurement (better matching at higher θ_v and conductivity), the Guanella-type 1:4 balun provides better matching at the higher impedances (near the 300 Ohms free space value) that will typify TDRI.

2.3 A forward model

We now review the literature related to methods for calculating v_p on a PTL near or embedded in, an arbitrary ε_r distribution. First, we discuss the relative benefits and disadvantages of integral equation (IE) and differential equation (DE) methods, and hence the reasons for choosing an IE approach for this work. Then pragmatic aspects of the moment method (MM) such as solution stability and accuracy will be reviewed.

Eqn (2.9) quantifies propagation velocity for a lossless, isotropic, homogeneous ε_r distribution surrounding the PTL. Ferre et al., (1996) showed that TDR provides a good approximation to the average of any longitudinal variation in θ_v since it has a near square root relationship with ε_r. However the lateral sensitivity is not a linear function of distance from the PTL, so lateral variations are not integrated linearly. Knight (1992) used small perturbations within the lateral plane to show that the spatial weighting function was proportional to the electric field energy density, in turn proportional to the square of the local electric field. He then derived analytically, an approximate lateral sensitivity weighting function that assumed an almost uniform ε_r distribution. This work provided a theoretical basis for comparison with earlier empirical means of determining the spatial sensitivity (Baker and Lascano, 1989; Baker, 1991).

Initially, we will impose four simplifying conditions on a PTL embedded in an inhomogeneous dielectric:

1. The PTL rods have zero resistance (usually true (§3.1.2) but see §6.3).
2. The material surrounding the PTL has permeability μ_0 (the lossless, free space value).
3. $\varepsilon_r(x, y)$ surrounding the PTL is a function of the transverse coordinates (x, y) only, ie ε_r has no z dependence.
4. ε_r is lossless at the measurement frequency, hence allowing the use of quasi-static analysis (see §3.2). This condition, typical for many soils and timber for example, applies to the method chosen for solving the forward problem and does not form an inherent limitation of TDRI.

2.3.1 Modelling the sensitivity of a parallel transmission line

With the problem constrained by conditions 1-3 above, the capacitance C of the line and hence v_p, may be considered to be purely a function of ε_r and line geometry (Figure 2.3):

$$v_p = f(C) = f(a, b, \varepsilon(x, y)) \tag{2.10}$$

where f incorporates the line geometry (described by line diameter a and spacing b) and ε_r, itself a function of the rectangular space coordinates x and y. Hence the objective is to find the form of f so that v_p may be determined from $a, b, \varepsilon_r(x, y)$.

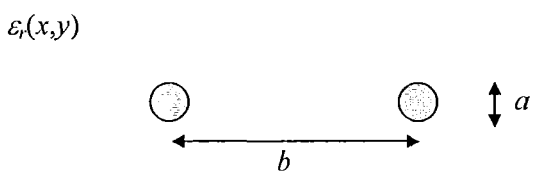

Figure 2.3 Physical arrangement of the PTL, where a is the diameter and b the spacing of the PTL rods, and $\varepsilon_r(x,y)$ describes the relative permittivity of the surrounding region.

Including condition 4 above, and using potential theory (Ramo et al., 1993):

$$\nabla \cdot \nabla \Phi = \nabla \cdot (-\frac{\boldsymbol{D}}{\varepsilon}) \tag{2.11}$$

where Φ is the electric potential and $\boldsymbol{D}$ the electric displacement (or electric flux density). In rectangular coordinates, and for an inhomogeneous permittivity $\varepsilon_r(x,y)$, Maxwell's first equation $\nabla \cdot \boldsymbol{D} = \rho$ becomes;

$$\nabla \cdot (\varepsilon_0 \varepsilon_r(x,y) \nabla \Phi) = -\rho \tag{2.12}$$

In this application, the domain of Eqn (2.12) may include the source and sink of electric flux (the PTL).

Two commonly used methods for solving the inhomogeneous dielectric problem are DE methods that include finite difference (FD) and finite element methods (FEM), and IE techniques such as the MM. Numerical approaches involve a discretisation stage where the differential or integral transforms are represented by discrete steps or summations. Appendix 3 provides equivalent DE and IE forms for the potential on a PTL.

FD methods (eg Binns et al., 1992) have been used for a range of potential field problems, and use a rectangular grid to discretise the region of interest. An approximate solution to the potential function is defined at each mesh node by expressing the potential function as a difference equation, expressed in terms of the potential at the neighbouring nodes. The Taylor representation of the derivatives is commonly truncated so that terms in h^2 and higher (where h is the mesh size) are ignored. The FD scheme generates a system of equations with a sparse, banded coefficient matrix, since the potential at each mesh node is represented in terms of the nearest neighbours.

The FEM (eg Binns et al., 1992) represents the potential within an element, in turn defined by a basis function over the area of the element, in terms of the potential values at the vertices of the elements. Triangular elements are commonly used, and enable better modelling of complex shapes than the rectangular grids of the FD method, and easily accommodate increased accuracy by the addition of nodes at the mid points of each boundary segment. Further, the mesh size may be altered over the problem domain to provide higher resolution in areas of particular interest. Galerkin methods (identical weighting and basis functions) are frequently used for solving the potential function within each element.

FEM's for the class of problem described by Eqn (2.12) are fast and applicable to 2-D, but since boundary conditions must be included, they often require the calculations to extend beyond the region of interest, to cover the entire domain of the problem. This generally means calculating to a boundary selected so that the influence of the boundary field on the result is small, and then imposing boundary conditions (typically Dirichlet boundary conditions where

the electric field potential $\Phi(r) = 0$). Although the DE methods result in the construction of a large matrix spanning the problem domain, the matrix is banded thus allowing the use of sparse matrix solution methods.

A general IE solution to Eqn (2.12) is (Appendix 3):

$$\begin{aligned} -\nabla\Phi(r) &= \boldsymbol{E}(r) \\ &= \frac{1}{\varepsilon(x,y)} \iiint_{region} \boldsymbol{G}(r)\rho(x,y)\,dr \end{aligned} \tag{2.13}$$

where r is a 3-space dimension, $\boldsymbol{G}(r)$ is a Green's function that incorporates the boundary conditions, and $\rho(x,y)$ is the charge density. Eqn (2.13) is a Fredholm integral equation of the first kind, and inherently ill-posed (Tsukerman, 1997) since any steep gradient in the homogeneous term ($\boldsymbol{E}(r)$ in this case) can only arise through near singular values of the kernel $\boldsymbol{G}(r)$ or the function $\rho(x,y)$. Here, $\boldsymbol{G}(r)$ has so-called $1/r$ or self-term singularities where the field and source points coincide so that $r = 0$. Methods for solving Eqn (2.13) circumvent the ill-posedness by the use of techniques such as the Galerkin method that approximate the ill-posed form (Tsukerman, 1997), in a similar manner to the approximate or discrete representations of the DE methods. IE methods generally produce smaller scattering matrices than the DE methods, but are full (Glisson, 1989) compared to the banded matrices that typify DE formulations (Binns et al., 1992). In addition, IE methods used with inhomogeneous dielectric distributions require a volume integral equation (VIE) approach and hence calculation in 3-D, even if there is invariance in one direction. In 1984, Spiegel noted that FD methods were finding increased use, although this trend has not continued for EM modelling (Appendix 4 outlines the generalised scattering for the EM problem, in contrast to the quasi-static modelling applicable to TDRI). He also noted that FD methods have a smaller solution matrix but there is a need to extend the modelled region, so the benefit depends on the particular application. Tsai et al. (1986) remarked that the FEM is more appropriate for modelling bounded regions such as waveguides. Spiegel (1984) referred to the then current capability of up to 100,000-cell simulation, and separately referred to the EPA "man model" (human body model) of 15,000 cells with 1000 allocated to the body. He concluded that larger systems could be realistically modelled using FD techniques.

IE methods have been employed for 3-D EM modelling because of their better numerical efficiency (Weaver et al, 1995), but FD methods are now being increasingly used due to the concept of staggered grids (Weidelt, 1995), and the flexible topology of the FEM allows it to accurately model complex shapes (Binns et al., 1992). However, IE methods continue to be used for 3-D EM modelling for homogeneous problems and when the Green's functions may be easily calculated. For example, Xiong et al. (1995) emphasised the better accuracy and efficiency of IE methods, despite the broader generality of DE methods. The differences are more blurred for quasi-static problems such as for the inhomogeneous dielectric problem for TDRI. In general, IE methods have advantages of better handling of boundary conditions (they are defined within the IE) so only the anomalous region needs to be solved. The numerical efficiency tends to be worse however, particularly for large numbers of cells or elements.

Although the matrix requiring inversion in IE methods is generally smaller, it is full, unlike the banded matrix of the FD and FEMs (Ramo et al., 1994).

IE methods are particularly well suited to applications where the region of interest is bounded by free space, since under these circumstances, calculations need only be performed inside the anomalous region, hence reducing the scale of the problem. Further, where the impressed field is altered in amplitude, position or distribution, the matrix that forms the system of equations is unchanged. It may also be observed that even when the electrical properties of the medium are altered, only diagonal elements of the matrix are affected; the off diagonal elements only depend on the geometry of the anomalous region. These features have a significant benefit in this instance where the modelling forms part of tomographic inversion, and where the forward calculation is repeated using the same physical properties of the region, but with an altered impressed field.

Solving IEs numerically follows a discretisation and summation procedure, and the most common technique is the MM. Harrington (1968) provides an abstract description of the method, and outlines its application to static modelling the polarisation in an inhomogeneous ε_r distribution. The method is extended to provide a solution to the TDR problem in §3.3. We now turn to practical aspects of the method that affect accuracy and convergence.

2.3.2 Accuracy of numerical solutions of the IE

A crucial aspect of any numerical technique is the solution accuracy. Errors are induced in the MM solution by:

- truncation of the approximation by a series (Eqn 3.49)
- discretisation errors in representing the zone of interest by aggregated cells of fixed geometry
- finite order basis functions that describe the (in this case) field in each cell
- approximations in defining the Green's function $G(r)$ in Eqn (2.13)
- numerical errors from a poorly conditioned scattering matrix.

These aspects are aptly demonstrated by recent efforts in developing the 'man model', used for predicting specific absorption rates (SAR) of humans who are exposed to EM energy. Modelling the human form requires VIE techniques, and errors arise due to poor representation of shape, fine internal features, and the large contrast of electrical properties between different zones such as between bone and arteries. What is fascinating about this field of study is the issue of validation. Measurement of field strength within the body is very difficult due to the minuscule signals involved, quite apart from limited access to internal regions. Hence, much of the discussion on SAR modelling involves analysis of convergence, comparison with more simply validated models, and conjecture. Tsukerman (1997) commented that MM surface formulations provide good convergence of integral characteristics (Galerkin methods are applicable to both DE and IE formulations). However, convergence is not generally uniform so errors are variable in the spatial domain.

2.3.3 Choice of basis functions

A common approach to the MM is to employ constant or pulse basis functions, that provide a unity weighting in the addressed cell, and zero elsewhere (Harrington, 1968). However this does impact on accuracy since the field (the methods are applicable to the solution of all potential fields) is constant within each cell, so any changes in field magnitude and/or direction must occur at cell boundaries and hence be abrupt. Approaches that use less constraining basis functions will assist the model accuracy, although with an attendant increase in complexity and degrees of freedom. For example to obtain improved accuracy, Tsai et al. (1986) used 3-D linear basis functions to describe the field in each cell in a MM EM scattering problem for the man model. Their modified Galerkin method used analytic integrations over spheres approximating cell volumes, thereby eliminating the $1/r$ singularity in the self-term. However, the method required larger matrices and more unknowns per cell, thus posing a significant trade-off between the accuracy of field calculation over each cell and the total number of cells. The convergence issue and the consequential reduced accuracy resulting from the approximations by the pulse basis functions were also noted by Spiegel (1984).

Qian and Boerner (1995) noted that the use of higher order basis functions can reduce the discretisation required for acceptable convergence. They compared constant, linear and quadratic basis functions in a 1-D EM scattering problem using an IE method, and showed significant improvement of linear basis functions over the constant basis functions, but little further improvement with the quadratic form. However, a distinct advantage noted was that the coarser discretisation allowed larger cell sizes and hence more accurate numerical treatment of the Green's function singularity. This singularity (Appendix 4) does not occur with the quasi-static modelling described in §3.5.

In describing the MM solution for a man model, Hagmann et al. (1978) discussed the use of interpolants to improve the convergence and hence accuracy. They initially showed improved convergence using a simplified and easily verified 1-D problem with quadratic interpolants. The methodology was then applied using a set of application rules, to the 3-D case for a Cartesian mesh. The new approach provided an estimated improvement in error of nearly 50% for the SAR man model with 512 cells. They also demonstrated an interpolation method for use with non-uniform or arbitrarily positioned cells that used the field in adjacent cells to represent more accurately the field in each cell.

Massoudi et al. (1984) investigated the convergence and distribution of SAR in a man model and concluded that the Galerkin method with linear basis functions produced better results than pulse basis functions. In response, Hagmann (1985) remarked that pulse basis functions were only appropriate where the field varied slowly over the volume of the cell. He noted that for a cubic model, the errors at the edges and corners where the field varied strongly could introduce significant error. Further, where two adjacent cells had dissimilar dielectric properties but similar electric field strengths, a jump in the electric flux density both at, and normal to, the cell boundary is required. This could be resolved by the charge density on the surface of each cell,

as calculated by Hohmann (1975). Hagmann also remarked that at low frequencies, a pulse basis function represents the field as more like a sphere than a cube, and hence the change in the SAR with subdivision reported by Massoudi et al. (1984) was due to a move from the rounded man model to one with corners. Massoudi et al. (1985) then reiterated that sufficiently accurate results had not been obtained with pulse basis functions.

It is apparent that the deficiencies of the pulse basis functions are well recognised, and are most apparent in the inevitable jump in the field at cell boundaries. However, because of the unknown SAR of the man model, the errors are difficult to quantify. Massoudi et al., (1984) noted that when comparing formulations with the SAR for the man model, the SAR distribution needs to be considered as well as the average since the SAR can vary by 8:1 in adjacent cells of the man model. Alternatives to the pulse basis function such as the rooftop method (Schaubert et al., 1984) or linear basis functions can also satisfy the need for different field values on different faces of the cell (to match adjacent cells). The approach advanced by Xiong et al. (1995) who used a volume integral for the induced currents and a surface integral for the charge term, produced the correct jump in the normal component of each cell's field without introducing fictitious surface charges.

Galerkin's method has been widely accepted as providing solutions that are superior to non-Galerkin formulations (Peterson et al., 1996). Wang (1991) noted that using Galerkin's method in the MM provides a near-exact solution if the basis functions are orthogonal and complete in representing the unknown potential function over the spatial domain of an homogeneous permittivity. Tsukerman (1997) commented that Galerkin discretisation acts as regularisation, and that mesh size is a regularisation parameter. Wang (1991) also noted that Galerkin solutions have the highest accuracy given set numerical constraints, allow superior handling of singularities and that reciprocity is preserved if basis functions are real valued or if a symmetric inner product is used.

However, contrary to the above observations, Peterson et al. (1996) with subsequent support from Dudley (1997) showed that Galerkin solutions do not always provide results that are more accurate. Peterson et al. (1996) constructed an electric field integral equation (EFIE) solution to scattering of a plane wave by an infinite conducting cylinder. They discovered that in general, increasing the order of the basis or testing functions improved accuracy, seemingly regardless of violating the Galerkin equality. Clearly, there remains further work in this field to further quantify the advantages of the Galerkin method. It would be useful to replicate the comparison by Peterson et al. (1996) but by reformulating the problem in terms of an integral quantity such as capacitance, which Tsukerman (1996) stated is excellently handled by the MM. This approach is likely to reveal further insights, since the IE defining the field due to a charge distribution results in the linear operator $-\varepsilon \nabla^2$ that is self-adjoint (Harrington, 1968) and hence automatically ensures reciprocity. However, the questions remain: under what non-Galerkin conditions does reciprocity fail, and what is the impact on the solution accuracy?

2.3.4 Cell shape and size

Cell shape and size affect model accuracy, particularly at boundaries. Cubic cells are convenient to use with MM solutions and Cartesian coordinates, but are less well suited than polyhedra to fit smooth and curved boundaries. Tsai et al. (1986) used triangular patches to model the surface charge term and cubes for volume integration applied to a MM solution to the EM scattering problem for an arbitrary dielectric. Good agreement was obtained with the Mie (Mie and van Bladel, 1963) analytical solution for a dielectric sphere. In considering the convergence and distribution of SAR in a man model at 27 MHz, Massoudi et al. (1984) observed that subdividing buried cells or surface cells where the field was parallel to the surface, had little impact on accuracy. However cell subdivision at an edge or corner and where the surface was perpendicular to the field, caused a considerable change in the predicted field in the immediate vicinity, although little effect on the average SAR. Hagmann (1985) remarked that there is little point in cell subdivision to improve edge accuracy, unless the edge is also altered in shape (such as by the addition of intermediate cells) to better reflect the shape of the modelled object.

Guo et al. (1993) compared the results from numerical modelling with the Mie result for scattering by a dielectric sphere. They concluded that field errors are mostly due to the geometric difference between the dielectric sphere and its discretised model, and that the error due to volume mismatch dominated over the shape mismatch error. This was observed to be consistent with the variation of field error with discretisation. They tried border smoothing by setting the boundary cells at half the border ε_r, but this was unsuccessful in reducing the oscillatory nature of field error with discretisation. Consequently, they advised smoothing the geometry rather than ε_r. Tsai et al. (1986) also remarked on the difficulty of providing an exact solution for the scattering problem. In their application of determining the fields inside the human body, they used an IE method solved by a MM similar to that described by Harrington (1968). The IE was discretised and solved with a modified Galerkin method whereby the cells were approximated by spheres and the weighting function was used to satisfy the IE over the sphere rather than the cell. Guo et al. (1993) chose a similar approach in deriving the Green's function within each cell by integrating over the cell, and then representing the cubic cell by a sphere of equivalent volume.

Schaubert et al. (1984) used tetrahedral cells in a VIE, MM solution to the EM scattering problem, and noted that the accuracy was comparable with cubic cells, but that the approach provided greater geometric flexibility.

2.3.5 Wavelength considerations

An important consideration when formulating the model of a physical system is the size of the scatterer and its sub sections or cells in relation to the wavelength of the illuminating source. Glisson (1989) remarked that IE methods fail when the wavelength is small compared with the size of scatterer, and that failure also occurs at internal resonance frequencies. Guo et al. (1993) noted without recourse to other work, that the cell dimensions must be less than, say,

one quarter wavelength (λ), and Ghodgaonkar et al. (1983) also stated that the cell size should be less than $\lambda/4$. However Zhou and Shafai (1997) claim that for the EM scattering problem and using a MM VIE method, the cell size should be no more than $\lambda/10$ to ensure good far-field prediction. Hagmann (1981) in proposing tests for convergence with dielectric slabs, provided an upper bound for the useable cell size such that $l < \sqrt{6}\,|k|^{-1}$ where l is the side length of the cell and $|k|$ is the magnitude of the propagation vector in the scatterer. When using a magnetic field integral equation (MFIE) method, Peterson and Klock (1988) noted that a maximum cell density of 100 per square λ (that is a cell length no more than $\lambda/10$) was required to achieve good accuracy of internal fields. TDRI uses the evanescent field of the PTL so is not subject to the above constraints.

2.3.6 Convergence and execution considerations

Given an appropriate selection of basis functions and cell size and shape for a MM IE solution, a method may fail or perform poorly due to an insufficient number of cells to adequately represent the physical model, in turn demanding larger scattering matrices. Xiong (1992) used an iterative approach to the solution, thereby avoiding the necessity to store all the large scattering matrix in memory at one time. The anomalous region was divided into substructures and other substructures were treated as excitations. The procedure was then equivalent to solving the scattering matrix by block solution methods, keeping just one substructure in memory at any time. The advantages cited included the property that the condition number for a substructure was less than that for the entire matrix, computation time was lower, and the method was adaptable to parallel processing. In a similar vein, Wang (1991) remarks on an iterative scheme for solution by a conjugate gradient (CG) method, and which handles an order of magnitude more cells than the direct method. However he notes that the iterative solution does not permit storage and reuse of the scattering matrix, although it would appear that the approach used by Xiong (1992) does not have this drawback. Wang also noted that unless ill posed, the direct and iterative MM produce equivalent results, so there is a one-to-one correspondence between the two processes.

Spiegel (1984) referred to the successive discretisation approach where the whole model is solved, and then a sub area is solved at higher resolution using the sub area boundary conditions defined by the initial coarse model. He also noted that the symmetry of the man model allows a reduction in the number of cells used.

Guo et al. (1993) formulated the IE scattering matrix for vector EM fields in and around an arbitrary dielectric object, and noted that the scattering matrices are dependent only on the geometry of the problem. This meant they could be computed off-line (ie not at compute time), hence greatly speeding the calculation process. Although somewhat obscure, it appears that a significant feature was to store a set of calculations that depended on the relative positions of the field and source points. To save memory space, these were only retrieved as required during calculation.

Chew et al. (1997) examined various methods for solutions to EM problems that provide rapid solutions, and pointed out that wavelets could be used to sparsify the dense matrices of electrostatic and low frequency EM problems.

Convergence may fail in EFIE methods with large values of complex ε_r. Peterson and Klock (1988) suggested that the fictitious charges referred to earlier with the pulse basis functions may be responsible for the instability with larger values of ε_r. They noted instability of the EFIE model of Richmond (1966) for cylinders of $\varepsilon_r = 4 - j100$ and $\varepsilon_r = 75 - j300$, and for ε_r exceeding approximately 10. An alternative formulation using a MFIE method overcame the instability.

2.4 The generalised inverse problem

The forward problem describes, in general, the transfer function between known input parameters, and initially unknown output parameters. In the case of the corresponding inverse problem, the output parameters are known, and one or more of the forward problem's input parameters are required. Here, inverse problems and their solution methods are reviewed with emphasis on non-linear problems, since TDRI is non-linear (Appendix 2).

The inverse solution may be described by:

$$m = g^{-1}(d) \tag{2.14}$$

where m is a set of model parameters (the model space and in this case comprise values of ε_r), g describes the forward transfer function and includes reliance on other parameters such as PTL geometry and fundamental constants, and d is a set of observations (the data space and in this case refer to reading of t_p). In this case the problem is discretised so that g is represented by a matrix that performs a translation from the model space to the data space. A unique solution requires knowledge of both the nature of g and sufficient independent observations d. While there are numerous methods of solving inverse problems, the choice depends on the nature of the problem and the number of unknowns. Specifically, impediments to providing a satisfactory solution include:

- non-unique solutions (eg insufficient observations)
- measurement noise and hence uncertainty in the data d
- non-linearity of the transfer function g
- incomplete understanding of the transfer function g or its inverse.

The above deficiencies are frequently manifested by a poorly conditioned matrix g so that even if a solution to Eqn (2.14) is obtained, it is likely to be inaccurate and will be very sensitive to small perturbations in the data. Wang (1991) noted that a matrix is ill-conditioned if the inverse of the condition number approaches the floating point precision. However, it is likely

that the above indicators of a poorly conditioned matrix g will become evident well before the condition number gets sufficiently small that g is singular.

2.4.1 Ill-posed problems

When there are insufficient observations d to fully define the model parameters m, the inverse problem is considered under-determined or ill posed, and a unique solution will not be obtained. However Ellis and Oldenburg (1994) pointed out that in such cases, a convergent solution may be obtained by including *a priori* data in the form of previously known values or introduced constraints. Wexler et al. (1985) in describing impedance-computed tomography pointed out the necessity of using as many voltage measurements as pixels to prevent divergence and negative conductivities. Introducing *a priori* data in the form of conductivity constraints are likely to have improved the inversion process and relaxed the required number of measurements.

Since measurement noise or uncertainty further adds to the ill posedness of an inverse problem, additional *a priori* data may be added to the observation set to improve the stability and precision of the solution. These *a priori* data are usually in the form of known boundary conditions or introduced constraints, such as in the present case where ε_r of a sample material cannot be less than one and is most unlikely to exceed 87 (ε_r of liquid water at zero Celsius). The *a priori* data may also take the form of a general requirement such as the selection of the smoothest or flattest solution.

The introduction of *a priori* data suggests a Bayesian approach, which formalises the process of refining preconceived notions of a state of nature by using experimental data or observations. When applied to probability or frequency distributions that more typically represent inverse problems, Bayes theorem may be written (Tarantola, 1987):

$$f(m \mid m_p) = f(m)\frac{f(m_p \mid m)}{\int f(m_p \mid m) f(m) \quad dm} \tag{2.15}$$

In this case, $f(m \mid m_p)$ is the conditional probability distribution of m given $f(m_p)$. When applied to an under-determined inverse problem, $f(m \mid m_p)$ would refer to the probability distribution of the solution set m of Eqn (2.14) given the *a priori* data m_p. The probability density function (PDF) $f(m)$ is improved by the *a priori* information encapsulated in the remaining terms on the right of Eqn (2.15), or in true Bayesian tradition, may alternatively refer to the improvement of *a priori* knowledge by the observed data (Bhattacharyya and Johnson, 1977). In the inverse problem described here, $f(m)$ encapsulates all the *a priori* knowledge and constraints that the solver wishes to apply to the solution in the form of an estimate of the solution PDF. Having observed the experimental evidence m, the solver calculates $f(m_p \mid m)$, the PDF of the *a priori* data for given m, and finally, $f(m \mid m_p)$. While Bayesian ideas are generally somewhat contentious, they do assist in resolving underdetermined problems that are otherwise intractably short of information (Ellis and Oldenberg, 1994). However the approach

assumes that the distribution is known or at least has a known PDF, and perhaps more importantly, that the moments of the PDF are known. It may be necessary to either assume that the PDF is Gaussian and hence accept the consequential outliers that may arise if the true distribution is broader, or avoid the PDF approach and exclude a measure of the solution accuracy.

The formal approach to inverse problem theory described by Tarantola (1987) assumes that the state of knowledge of a data set is best described by the moments of a probability distribution. Again, the difficulty that arises is to determine whether the uncertainties may be considered Gaussian. Commonly, data are derived from instruments that measure physical parameters, and to Tarantola's consternation (Tarantola, 1987), instrument manufacturers do not usually provide a statistical analysis of errors when specifying instrument performance. Rather it would appear that many instrument errors would not fit Gaussian distributions, since the errors are frequently dominated by non-linearities, and systematic temperature and temporal dependencies. These influences would not normally be parameterised in the random sampling that would verify an instrument's error distribution, although assigning a PDF to the instrument reading error is useful for less well-defined or measurable reading-dependent errors. One example of a non-PDF instrument error is in the Tektronix 1502 time domain reflectometer that has a reading-dependent error due to tiny ripples near each end of a ramp function that is used as a voltage to time converter (Hook, 1995). A further example is the Hewlet Packard HP34401A digital voltmeter where the error is specified (after one year from calibration) as ± 0.004 % of reading, plus ± 0.0007 % of the full scale, plus 0.0005 % of reading per °C outside the range 23 ± 5°C, plus 0.0001 % of full scale per °C outside the range 23 ± 5°C. These specifications provide error limits in the form of reading and scale-dependent errors and environment (temperature) dependent errors, but no parameterisation of a PDF. Similar specifications in the form of timebase drift limits were specified for the HP5313A timer/counter, but an earlier (10-year-old) HP54121T sampling oscilloscope did provide moments of a PDF when specifying timebase accuracy. In this case, the average error was specified as 0.4 ps with standard deviation of 1.82 ps from a sample size of 274 measurements across 8 instruments. Despite the timebase specification, there was no similar PDF specified for the amplitude or x measurement (an oscilloscope is a 2-D, x-t measuring instrument), so a composite PDF describing the measurement errors for measurement of analogue signals cannot be generated from the manufacturers' specifications.

For large data sets that represent the observations d, the central limit theorem may be applied and random sampling used to approximate a Gaussian distribution. However, if the number of data are small the only options are to either assume a PDF, or avoid the Bayesian approach and instead provide an inverse solution that is not augmented by a confidence interval or other measure of the solution accuracy.

Again referring to Gaussian PDF's, Tarantola (1987) comments on the common and sometimes unjustified use of least squares formulations, and recommends examining the data residuals and qualitatively assessing the inversion results. This forms a useful approach for situations where the Gaussian assumptions are violated, and serves as a check on the inversion process.

However, this approach dictates that human intervention is required in the inversion process, a principle aired by others in the case of under-determined problems (Ellis and Oldenburg, 1994). Where the Gaussian assumption is invalid, Tarantola also advocates considering the use of long-tailed distributions such as the chi-squared or Cauchy PDF's, since they provide a more robust inverse solution that is relatively insensitive to a small number of distant outliers. Despite the above, much of the content of Tarantola (1987) is devoted to least squares methods, perhaps indicative of the maturity of the approach and the shortage of good methodology for handling non-Gaussian distributions with a small number of data. Consequently, it would appear that the only viable approach is to employ non-parametric methods for error analysis. Clearly, this is an area of ongoing research work.

In a similar vein to insufficient data d, failure of the inverse solution may be ascribed to insufficient knowledge of the nature of the physical system described by g. This is typified by a poorly convergent, unstable or non-monotonic forward solution (which as in the case described here may itself be an inverse problem). These uncertainties are ideally described by a PDF around the forward modelisation g, although careful analysis of the model may be required. The uncertainty inherent in most pragmatic models that mathematically describe our view of physical systems (eg dielectric models in §2.1) includes approximations to the true transfer functions, as well as exclusion of parameters that may have only a small or perhaps unknown influence. The model g may then be ascribed a PDF Θ, and in the case of an exact theory or perfect confidence in the forward function,

$$\Theta(d \mid m) = \delta(d - g(m)) \tag{2.16}$$

where δ is the Dirac delta function. More commonly, a PDF describing $d|m$ will be Gaussian or comprise some other known distribution that includes both the uncertainty in d and g, so that

$$\Theta(d \mid m) = \Psi(d - g(m)) \tag{2.17}$$

where Ψ is a known PDF comprising $\Psi_1(d) \bigcap \Psi_2(g(m))$ and where Ψ_1 and Ψ_2 are known PDF's of d and $g(m)$ respectively. Tarantola also noted that provided both the data errors and model errors were Gaussian, they could be combined, even for non-linear inverse problems. Alternatively, where the errors from either d or g are assumed small or known to be small compared to the other, then Ψ_1 or Ψ_2 could be represented by the Dirac delta function, δ.

Given knowledge of the PDFs as above, Tarantola (1987) states that the most general solution to the inverse problem is revealed by the underpinning relation:

$$\sigma(d,m) = \frac{\rho(d,m)\Theta(d,m)}{\mu(d,m)} \tag{2.18}$$

where $\sigma(d,m)$ is the PDF that represents the final or *a posteriori* state of information, $\rho(d,m)$ is the *a priori* PDF, $\Theta(d,m)$ is the theoretical PDF that represents the physical correlations between d and m (as explained by g), and $\mu(d,m)$ is the state of null information.

The latter is incorporated to normalise $\Theta(d,m)$ with respect to units of measurement. As commented earlier, the PDF's may frequently be unknown, and so an "exact" result may be calculated by the inversion process, but little will be known about how representative the solution is of the physical system for which the solution is sought.

2.4.2 Linearity

Linearity is a crucial determinant of inverse problem classification since it impacts on the methodology that may be used to provide a solution. Suitable classifications are:

1. **Linear.** These inverse problems are defined by the characteristic that the data are linearly dependent on the model parameters (Zhdanov, 1993), and may be solved by one of several direct methods (Tarantola, 1987). X-ray tomography is an example of the application of linear inverse techniques, since the attenuation along a ray path is essentially independent of the attenuation elsewhere.
2. **Weakly Nonlinear.** This classification applies to problems that are successfully solved by linearising the transfer function g around some *a priori* data and solving directly as for the linear case. Examples of weakly nonlinear problems are given below.
3. **Nonlinear.** Nonlinear problems require iterative solutions since there is no known method of projecting forward to a solution for a general, and perhaps very non-linear, problem. Methods for solving non-linear inverse problems are inevitably iterative (Berryman, 1991), and there are numerous variants of the optimisation techniques that may be used to converge to a solution.
4. **Strongly Nonlinear.** A further class of inverse problem arises where g is severely non-linear and hence characterised by multi-valuedness and disparate solution spaces. This class of problem, epitomised by the travelling salesman problem (the shortest circuit of numerous cities is required, and the problem is characterised by many local minima), is atypical of physical systems that instead tend to adhere to better-behaved functions. Monte Carlo methods that include stochastic elements for controlling search direction and/or step length are generally required to solve severely non-linear problems (Tarantola, 1987).

The forward problem for TDRI is non-linear (Appendix 2), and so the remainder of the review on methodology for solving inverse problems will focus on the non-linear class of problems that need to be solved iteratively. Prior to that we briefly review the approach to solving weakly nonlinear problems, using a method that linearises a non-linear problem to allow resolution as if it were linear, since the method has been used to solve some tomography problems.

2.4.3 Weakly nonlinear problems

Assuming a linear $g(m)$, a first order Taylor development around a perturbation δm is:

$$g(m+\delta m) = g(m) + J(\delta m) \tag{2.19}$$

where J is the first derivative or Jacobian. Then applying Eqn (2.19) to an inverse problem that is nearly linear, and recasting in terms of m_{prior}, where $\delta m = m - m_{prior}$, we may obtain an approximate form:

$$g(m) \approx g(m_{prior}) + J(m - m_{prior}) \tag{2.20}$$

where J is the Jacobian near m_{prior}. Thus Eqn (2.20) linearises the problem around m_{prior}. This approach is also attributed to Born for wavefield problems (Tarantola, 1987). An estimate for m may then be obtained as for strictly linear problems by:

$$m \approx m_{prior} + J^{-1}\left(d - g(m_{prior})\right) \tag{2.21}$$

where $d - g(m_{prior})$ is the distance between the actual data and the data that would be generated by m_{prior}. Then using the Moore-Penrose pseudo inverse for J gives:

$$m \approx m_{prior} + (J^T J)^{-1} J^T \left(d - g(m_{prior})\right) \tag{2.22}$$

and incorporating weighting matrices to quantify uncertainty in d and m_{prior} gives (Tarantola, 1987):

$$m \approx m_{prior} + \left(J^T C_d^{-1} J + C_m^{-1}\right)^{-1} J^T C_d^{-1}\left(d - g(m_{prior})\right) \tag{2.23}$$

where C_d is the covariance matrix for the data, and C_m the covariance matrix for m_{prior}. The covariance matrices provide the opportunity to weigh individual data elements according to their error (if known), so that for example, C_d could be used to account for variations in accuracy with reading, such as occurs with the Tektronix 1502C. Clearly, the linearised method is only appropriate if either m_{prior} is close to the solution, or g is almost linear.

Despite the limitations and assumptions, various researchers have used a linearisation approach, usually to speed inversion since only one step is required to arrive at a solution. Smith et al. (1995) described an electrical impedance tomography system for clinical use, using 16 electrodes fed from a 5 mA, 20 kHz current source. To achieve high-speed inversion for real time viewing, a linear reconstruction algorithm was used to form measurements from just the real component of the measured impedance. Back projection was applied along the equipotentials that would have arisen from a uniform impedance distribution. In acknowledging the violation of linearity assumptions, the authors noted that only the normalised difference between a reference image and the current image was inverted, and was claimed to provide a more robust inversion procedure. In contrast with this approach, Wexler et al. (1985) described an impedance tomography system where the conductivity distribution was progressively refined for consistency with the (measured) boundary conditions using least squares minimisation. Although the system was used in a laboratory tank where properties were more predictable than the torso images by Smith et al. (1995), the presented images used

64 electrodes instead of the 16 used by Smith et al. (1995), and the images appeared better defined and more representative of the real structures. However, Bones (1981) points out that the inverse problem for recovering the internal structures from surface measurements on a torso is inherently underdetermined, and that *a priori* data are required.

Xie et al. (1991) described a capacitance tomography method using a FEM forward solution with 12 capacitive elements positioned radially around a pipe. The inverse problem was solved using linear back projection of capacitance calculated from line integration of potentials. As with the system described by Smith et al. (1995), this qualitative imaging system demanded a rapid inversion method.

Jofre et al. (1990) described linearised reconstruction for 2.45 GHz diffraction tomography. The inverse solution provided a contrast resolution of 1%, with a reconstruction algorithm comprising the Born approximation followed by double convolution to allow subsequent linear reconstruction. An absolute ε_r was not obtained due to scale (wavelength to pixel ratio) and high contrasts that impacted on the assumptions of the Born approximation. When used for quantitatively imaging a human arm, the high contrast and size compared with the 122 mm wavelength (2.45 GHz) used, constrained the method so that the ε_r range between bone and muscle, 8 and 50 respectively, was compressed to between 65 and 92. Pichot et al. (1985) described their active microwave imaging (diffraction tomography) using MM for the forward solution and what appears to be a linearised (with 2-D Fourier Transform) ray tracing method for image reconstruction. In describing inversion of scattered microwave data, Jofre et al. (1990) used the Born approximation that assumes that the scattering perturbs the illumination so that the field within the anomalous region was approximated by the incident field.

Borup et al. (1992) commented that the Born and Rytov (first order approximation of the Ricatti equation) methods are fast, but are not good enough for the high contrast that human tissue presents to ultrasonic propagation. Mackie and Madden (1993) commented similarly on the usually very nonlinear nature of the electrical properties of materials. However, Torres Verdin et al. (1995) described an extended Born approximation for 2-D inversion of electrical conductivity data. The method was reportedly little slower than the Born or Rytov approximations, but provided much more realistic results. It ignored the higher order terms in the Green's tensor, but instead focussed on the terms where the field-source distance was small.

For induced polarisation data, Oldenburg and Li (1994) compared linear and nonlinear methods but preferred to use a linearisation method instead of the non-linear approach of Ellis and Oldenburg (1994) since it was more rapid. However, they recognised that the non-linear approach gave the most accurate results. It is clear from the presented data, that the underdetermined nature of the problem constrained the results so that the images from the non-linear method were not greatly improved over the linearised approach. However, it would seem that when striving for quantitative inversion with a better conditioned problem such as TDRI, the improvement in accuracy from the non-linear method would be more marked than with the imprecise, smoothed results demonstrated by the induced polarisation inversion.

2.4.4 Non-linear problems

The method described above linearised g around m_{prior}. Alternatively, the problem may be linearised just in the region of the solution estimate, and iterative methods used for solution. This method is applicable to a broad range of problems from the linear (trivial) to very nonlinear problems such as those involving electrical properties (Mackie and Madden, 1993). Pichot et al. (1997) also comment that microwave inverse scattering is strongly nonlinear and illposed if quantitative imaging is required. Hence, although there are numerous variants on the optimisation process, avoiding linearisation over a possibly large portion of the model space by just using linearisation around the solution estimate and then iterating, appears most appropriate. For example, Chew and Wang (1990) described reconstruction of a 2-D ε_r distribution illuminated by a plane wave and with multiple receivers, much like an X-ray CT scanner. They showed that for noise-free cases, their distorted Born method was superior to the Born iterative method, not so for noisy cases. The method was a solution to:

$$E_z^s(x,y) = \iint_s G(\rho-\rho',\varepsilon_r^b)k_0^2\varepsilon_r E_z(x',y')dx'dy' \tag{2.24}$$

where ε_r^b was the background permittivity, k the free space propagation vector $\omega\sqrt{\varepsilon_0\mu_0}$ (Hagmann 1978), and $G(\rho-\rho',\varepsilon_r^b)$ the solution to:

$$\nabla_s^2 G(\rho-\rho',\varepsilon_r^b) + k_0^2\varepsilon_r^b(x,y)G(\rho-\rho',\varepsilon_r^b) = -\delta(\rho-\rho') \tag{2.25}$$

In their iterative Born method, the Green's function G was unchanged during iteration, whereas the distorted Born method updated G at each iteration, recognising the change in ε_r^b.

The remainder of the review on methodology for solving inverse problems will focus on the non-linear class of problems that may be solved iteratively. A typical procedure for providing an iterative solution to the inverse problem is provided by the following steps.

1. Select an objective function that indicates when the solution method has been completed.
2. Select an appropriate method of updating the solution.
3. Select a provisional solution set such as our *a priori* information.
4. Solve the forward problem to calculate a trial data set.
5. Use trial data to calculate the objective function and exit if stopping criteria met.
6. Compute a search direction and step length.
7. Update the provisional solution.
8. Loop to Step 4.

2.4.5 The objective function

The objective function (or misfit function) provides a measure of the completeness of the inversion process. The result is also frequently used as a measure of the misfit when updating

or refining the trial solution (Step 6 in the above sequence). A stopping criterion for the inverse solution iteration may be:

- a target value for the objective function (ie a true minimisation problem)
- the rate of change of the objective function (for example when it has fallen below a preselected value or proportion of the model solution)
- the number of iterations has reached a preselected limit
- a combination of the above.

In its basic form, the objective function S is just the residual, a measure of the deviation of the model solution from the observed data.

$$S = g(m) - d \tag{2.26}$$

A dilemma that arises in selecting an objective function is the weighting to apply to individual data elements. For example Mackie and Madden (1993) applied weighting in the form of log parameterisation to ensure positiveness, remove bias, and to reduce the scale when inverting magnetotelluric data.

Eqn (2.26) uses the L_1 norm ($\|x\|_1 = \sum_{i=1}^{n} x_i$) where each element x_i of vector space with dimension n, has equal weighting and so robustly handles outliers (Tarantola, 1987). More commonly and because of its straight forward application, the L_2 norm ($\|x\|_2 = \sqrt{\sum_{i=1}^{n} x_i^2}$) is used and provides more weighting to elements where the difference between data and the model is greater. This is appropriate where the PDF's of the model and the data are known to be Gaussian, but if there are systematic errors or the PDF is a long-tailed distribution for example, too much weight may be applied to elements that are best discounted. The general L_p norm is defined as (Tarantola, 1987):

$$\|x\|_p = \left[\sum_{i=1}^{n} \frac{|x^i|^p}{(\sigma^i)^p} \right]^{\frac{1}{p}} \tag{2.27}$$

where σ is a positive constant with the same dimension as x, is used to eliminate the dimensionality of the norm. Clearly, we have the choice of applying a greater weight to larger discrepancies ($p > 1$) or a smaller weight ($p < 1$). This magnitude-related weighting may be combined with a further Bayesian approach that chooses, in a prior sense, arbitrary weighting for elements of the objective function, based on a known or assumed PDF of the model or data. This is conveniently incorporated into an L_2 norm so that the misfit function of Eqn (2.26) becomes:

$$S = (g(m) - d)' C_d^{-1} (g(m) - d) \tag{2.28}$$

Lastly, we may introduce *a priori* data into the objective function, and choose the weighting between the data misfit and the *a priori* knowledge of the system to further influence the outcome of a solution based on our understanding of the nature of the problem. Ellis and Oldenburg (1994) discussed this in relation to an under-determined geophysical DC conductivity (σ) problem and applied a large weighting to the *a priori* data. They took the view that for such ill-posed geophysical problems, the appropriate solution method was to consider the solution to comprise *a priori* information, constrained by the measured data. In the DC σ case, *a priori* data in the form of a partially known σ distribution and an estimated background σ were used to generate a provisional model. The *a priori* data comprised a smooth σ variation, a known region of high σ, and a known background σ. These data were also used to construct a weight matrix before incorporating the constraints comprising the measured data, and minimising the objective function using Lagrange multipliers. The result of this approach was to provide realistic results and avoid the smoothest or so-called flattest model that minimised the difference in predicted parameters. Ellis (1995) also emphasised the futility of solving an ill-posed or underdetermined problem without employing *a priori* data. Under these circumstances, an apparently good fit as might have been indicated by statistical measures, could be far from a realistic model of the (in this case) subsoil σ distribution. Indeed, several quite different solutions might fit the data.

Zhdanov (pers comm. 1999) also referred to the inadequacy of the smoothest model in many situations, and of the necessity to include as much *a priori* information as possible. Ellis (1995) remarked that any under-determined problem requires regularisation which in turn demands *a priori* data. However the point needs to be made that any form of constraint such as requiring a maximally smooth solution is Bayesian and the constraints should be as rigorously justified as other known data since they influence the solution.

2.4.6 Regularisation

Regularisation is a process generally attributed to Tikhonov (1977), and enables, by the addition of *a priori* data, the solution of ill-posed problems. The ill-posedness is manifested by ill-conditioned solution matrices that preclude resolving the problem, or at best result in an unstable solution. Unstable solutions may also arise from measurement noise, and regularisation will assist in providing a stable solution. For example, consider the objective function $S = d - g(m)$. If the problem is underdetermined, there will be fewer d than $g(m)$ so S will be rank deficient, hence there will be several m satisfying the objective function. The regularisation procedure adds a stabilising functional so that the resultant is of full rank. Tikhonov regularisation is accomplished by the weighted sum of *a priori* data to the misfit function so that in general:

$$S = \phi(m,d) + \lambda\xi(m) \tag{2.29}$$

where ϕ is a misfit function such as the S of Eqn (2.28), and ξ a stabilising function, normally dependent on just the model, and sometimes called the side constraint when referring to

Tikhonov regularisation. λ is the Tikhonov constant that may be any positive real number. Side constraints include:

1. the common approach of seeking a maximally smooth or flat solution set (which may be accomplished by minimising a data norm, typically the L_2 norm)
2. minimising the residual between the model and the *a priori* data
3. the L_1 norm of the gradient or the L_2 norm of the biased gradient in a total variation approach (Portniaguine and Zhdanov, 1999)
4. a function that allows solutions with discontinuous properties by capping their contribution to the side constraint (Portniaguine and Zhdanov, 1999)
5. a thresholding method that penalises steep gradients that have small amplitude (Pichot et al., 1997)
6. known d values that may be included as optimisation constraints
7. a combination of the above.

Methods 3 to 5 are intended to overcome the blurred, indistinct, and often unrealistic images that often arise when using a data norm as the side constraint, by allowing gradient perturbations consistent with overall smoothness.

Ellis and Oldenburg (1994) used regularisation when inverting 2-D geophysical resistivity data. The initial model was made consistent with *a priori* data by forming a model space misfit, and was then combined with the data misfit and solved by linearising around the model and iterating. Thus, their objective function comprised:

$$S = \phi_m + \mu(\phi_d - \phi_d^*) \tag{2.30}$$

where ϕ_m was the model space misfit, μ the Lagrange multiplier, ϕ_d the data misfit, and ϕ_d^* the χ^2 data misfit. The misfits were weighted L_2 norms, and minimisation comprised a Taylor expansion about a perturbation δ_m to allow solving for δ_m and hence adjusting μ to obtain the target ϕ_d^* at each iteration. The approach emphasised the *a priori* data in underdetermined problems, and recognised that regularisation forced inclusion of *a priori* data, even the common requirement for maximum flatness.

Mackie and Madden (1993) chose the maximum likelihood method where the objective function was the weighted sum of the variances of the model error and of the *a priori* model:

$$(A_k^H R_d^{-1} A_k + R_m^{-1})^{-1} \Delta m_k = A_k^H R_d^{-1}(d - g(m_k)) + R_m^{-1}(m_0 - m_k) \tag{2.31}$$

where A was the sensitivity matrix, d the observed data, m the model, g the mapping of m into the data space, R_d the data covariance, R_m the model covariance, m_0 the *a priori* model, and Δm the change to the model. They used log parameterisation to ensure positivity and reduce the range of the conductivity data.

Pichot et al. (1997) in describing an edge-preserving regularisation method, regularised independently, the real and imaginary components of the susceptibility.

$$S = \phi + \sum_x \sum_y \lambda_r^2 \varphi\left(\frac{\left\|\mathrm{Re}(\nabla\chi_{xy})\right\|}{\delta_r}\right) + \sum_x \sum_y \lambda_i^2 \varphi\left(\frac{\left\|\mathrm{Im}(\nabla\chi_{xy})\right\|}{\delta_i}\right) \tag{2.32}$$

Here, ϕ was the misfit function, λ the regularisation parameter, φ the regularising function, $\nabla\chi$ the discrete gradient, and δ was a threshold parameter. φ was bimodal depending on the size of $\nabla\chi$. It was either linear or "underlinear" when $\nabla\chi$ was large thus ensuring edge preservation, but to adequately smooth homogeneous areas, φ was quadratic when $\nabla\chi$ was small. The effect was to penalise discrete gradients that were smaller than δ, so tending to suppress noise while allowing steep gradients.

2.4.7 Updating the solution

The iterative solution described in §2.4.4 may be considered an optimisation problem in which an initial *a priori* data set is repeatedly updated with the aim of minimising the objective function, or at least a linear combination of the objective function and the side constraint that forms a regularised objective function. Hence numerous methods such as described by Gill (1981), Conte and de Boor (1981) and Press et al. (1992) may be employed for updating the model, and those commonly used for non-linear inverse problems are derivatives of Newton's method, but also include heuristically-inclined alternatives such as simulated annealing and neural networks. Here, we briefly review the CG approach. Note that Press et al. (1992), in an introduction to their presentation of methods for solution of multidimensional optimisation problems, provide a very useful navigation aid to choosing an appropriate method, but caution that there are no "recipe" approaches, particularly if good performance is required.

Press et al. (1992) pointed out that there is little to choose between the CG and quasi-Newton methods – a CG method has been chosen for this work. The method has the goal of avoiding the pitfall of the steepest descent method, which may make numerous small steps in different directions when converging to a minimum of the function. The steepest descent method uses the correction:

$$h = -\alpha G(x_n) \tag{2.33}$$

where α is a weighting factor. The slow convergence is caused by the steepest descent algorithm adopting a new descent direction that is normal to the current contour and hence normal to the previous direction of travel. In the CG method, information is carried forward from previous iterations to point in a direction that is conjugate to previous directions. This is quite simply achieved by a regularisation process (Zhdanov, 1993) which uses a gradient that is a linear combination of the previous gradient and the freshly calculated one. Hence:

$$h = -\alpha\left[G(x_n) - \beta G(x_{n-1})\right] \tag{2.34}$$

where

$$\beta = \frac{\|G(x_n)\|^2}{\|G(x_{n-1})\|^2} \tag{2.35}$$

Press et al. (1992) advise the use of the Polak-Ribière formulation, which is claimed to provide advantages where g is not well approximated by a truncation of Eqn (2.20) to a quadratic representation. The Polak-Ribière formulation provides an alternative calculation for β:

$$\beta = \frac{\|G(x_n)\| \|G(x_n) - G(x_{n-1})\|}{\|G(x_{n-1})\|^2} \tag{2.36}$$

Pichot et al., (1997) used the Polak-Ribière CG direction in their microwave diffraction work to direct inversion that used least squares minimisation and regularisation. Mackie and Madden (1993) described 3-D CG inversion of magnetotelluric data, and described the CG relaxation method that avoids the calculation of the sensitivity by relying on the one forward modelling per iteration to quantify the effect of the sensitivity and provide substantial savings in computation time for large 3-D problems.

Borup et al. (1992) used CG methods for inversion of ultrasonic data since they provided fewer artefacts than algebraic reconstruction techniques (and presumably other methods that assume linearity). Although not strictly monotonic, they found that the bi-conjugate gradient method gave better convergence than CG, in turn better than the algebraic reconstruction technique (ART) for diffraction tomography, and generally better accuracy than a linearised ray tracing from the Born approximation. Mackie and Madden (1993) employed a relaxation approach using two nested loops, the inner being a CG relaxation iteration that avoided the necessity for matrix inversion at each iteration of the outer loop.

2.4.8 Jacobian and Hessian

The Jacobian and the Hessian (Fréchet derivatives), respectively the matrices of first and second derivatives of the data, are used in inverse solution methods to control the direction of iteration to minimise the objective function. Their calculation is frequently the most computationally intensive step of an inversion process. FD techniques are typically used to determine the derivatives, so the Jacobian for example will require two forward calculations for each partial derivative element, and the Hessian three. Clearly, accuracy is of concern, particularly for the Hessian. Farqhuarson (pers comm. 1999) considered that Jacobian inaccuracy could be tolerated, and Zhdanov (pers comm. 1999) stated that in general, an approximation to the Jacobian that enabled a rapid calculation, was beneficial. However, Hessian accuracy is critical (Zhdanov pers comm., 1999), but not required for many optimisation methods, including the CG method.

The impact of inaccurate Jacobian is dependent on the methodology and nature of the problem. Linear or linearised approaches are clearly critically dependent on Jacobian accuracy since this directly affects both the distance and the heading of the single step from the solution estimate to the actual solution, so the impact is directly calculable and dependent on the distance between the estimate and the solution. The situation is not so clear cut with iterative methods since the process converges to a solution so that as the distance between the trial solution and the actual solution (as quantified by the misfit function) reduces, Jacobian errors have less impact. However, if the errors in the Jacobian are large or the allowable step length is large, divergence may result. There is clearly a judgement call between a solution method that employs small step length, an inaccurate Jacobian and many iterations, and one that expends additional effort (and hence processing time) on producing a more accurate Jacobian that then allows a larger step size and fewer iterations. The first option is more conservative and less likely to fail due to divergence where the Jacobian is insufficiently accurate. On the other hand, computation of the forward solution and hence the Jacobian through FD methods can be very costly in computation time (Ellis, 1995).

There are several approaches to obtaining the Jacobian and these include:

1. The FD approach. While this requires an evaluation of the forward model for each cell. As noted above, this may be costly, especially for large, 3-D models.

2. In a derivative of the above, Torres Verdin et al. (1995) described an extended Born approximation, that could be used to provide an approximate Jacobian. Although the application was for 2-D inversion of electrical σ data, the method has broader applicability.

3. Ellis (1995) described an approximation to the Jacobian for 3-D conductivity EM inversion that was the product of the primary electric field and the magnetic Green's dyad:

$$\boldsymbol{G} = \int_{\tau} \Gamma^{H} \boldsymbol{E}_{i} \delta\sigma \, d\tau \tag{2.37}$$

   where Γ^{H} is the magnetic Green's dyad that describes the spatial influence of sources due to the primary or incident EM field $\boldsymbol{E}_i$, on the field in the region, and $\delta\sigma$ is the σ perturbation. The function was calculated in the EM σ implementation of the Born approximation method described below, so did not incur the penalty of additional calculation.

4. Farqhuarson and Oldenburg (1995) described an exact adjoint equation method of determining sensitivity:

$$\boldsymbol{G} = \int_{\tau} \boldsymbol{E}_{x} \cdot \boldsymbol{E}_{i} \psi \, d\tau \tag{2.38}$$

   where $\boldsymbol{E}_x$ is the x-coordinate of the auxiliary or adjoint field in $d\tau$ due to the excitation $\boldsymbol{E}_i$, and ψ is the basis function for the problem. Although exact, the method is approximately 20 times faster than the FD method for the 2.5-D and 3-D examples given.

5. Farqhuarson and Oldenburg (1995) also described a variant on the above in which the approximate Jacobian was derived by approximating the adjoint field $\boldsymbol{E}_x$ by that constrained by a homogeneous halfspace or layered halfspace. All field points in each layer then had the same adjoint field. Example inversions using the approximation demonstrated their adequacy and were approximately two orders of magnitude faster than the exact adjoint field method.

6. Mackie and Madden (1993) reported on the use of the field values from one iteration to form an estimate of the field gradient for the next iteration. They reduced forward modelling by utilising reciprocity to calculate the sensitivity just once for each frequency (all sources were 'on') in the initial iteration. Thereafter, the result of the previous iteration was used.

Clearly, there are opportunities to use Jacobian approximations, and the dramatic savings in computational effort attainable (eg method 5 above) mean that for any non-linear problem where computation time is an issue, approximations should be considered. Unless the approximations are poor in terms of either accuracy or savings in computation time compared with exact methods, they will result in more rapid inversion.

2.5 Discussion

2.5.1 Dielectric modelling

TDRI has the potential to be used for θ_v moisture content measurement in a range of composite materials, and requires dielectric models to suit each of the target composite materials. While this could be achieved by several empirical models, each calibrated for a particular material, the performance of physically-based models has been demonstrably superior. Although Jacobsen and Schjonning's (1995) third order polynomial fit to their data was better than that from any of the empirical or physically-based models, it was a 'hindsight calibration' using all available data, so would not necessarily fit new data. Further, empirical models can only compensate for components of surface or frequency influences that have a direct relationship with θ_v. For example, a bound water fraction that changes with particle size or shape distribution cannot be represented by an empirical model, and would be expected to have a significant impact on model accuracy at low θ_v. Notwithstanding the above, Topp's (1980) empirical model has provided good results across a range of coarse-grained soils, in which surface effects have less influence than fine-grained soils.

A generic, physically based model for use by TDRI in a range of composite materials, would use parameters to cater for differences between the physical properties that influence ε_r. Hallikainen et al. (1985) pointed out that many of the influential properties are difficult to measure, but it is apparent, particularly from the work of Dirksen and Dasburg (1993), that the most significant relate to the dielectric properties and volume fraction of the adsorbed water.

The use of just θ_t as a parameter appears a practical compromise. As pointed out by Wang and Schmugge (1980), it is correlated with wilting point so is potentially measurable in soils. In other materials, it could be determined empirically, or presumably determined from a measure of water activity. It will be shown in §5.2 that a bimodal model using θ_t adheres significantly better to the properties of Bentonite, a fine-grained swelling clay, than that of Dirksen and Dasburg (1993).

From the literature, it is evident that ε_r and volume fraction of the bound water fraction are important considerations for modelling ε_r of composite materials. Wang and Schmugge (1980) emphasised the importance for soils, and although other host materials have a smaller *range* of particle size, they will be similarly affected for all but the largest particle sizes. For example the mean particle size of flour is typically 20 μm and the tracheids in timber are typically 5 by 40 μm (Keey, 1998). Most materials including those based on cellulose (plants) and collagen (animals) also include sites for hydrogen bonding that will attach to water molecules and hence impart a lower ε_r than that of free or bulk water.

Three relaxation processes in the practical TDR frequency range of 100 MHz to 3 GHz suggest the necessity to incorporate frequency in a TDRI dielectric model. These are liquid water (16 GHz), bound water (1 GHz for Na-montmorillonite clay, Hoekstra and Doyle (1970)), and the Maxwell Wagner effect (up to 500 MHz, Hilhorst (1998)). The effect of liquid water relaxation is only likely to be important for situations where the high frequencies are not significantly attenuated, such as for a short PTL or for low θ_v. Further, bound water relaxation is only likely to be a significant influence at low θ_v since it affects the strength of the bound water contribution.

The maximum relaxation frequency of Maxwell Wagner loss in practical situations was noted by de Loor (1968) to be 1 MHz, yet Hilhorst (1998) indicated that in the presence of plate-like host particles, the Maxwell Wagner effect is apparent to 500 MHz. To resolve the apparent contradiction between the above authors, the spherical inclusions model derived by Schwan et al. (1962) was evaluated for a typical composite material. The model predicts the relaxation time τ:

$$\tau = \varepsilon_0 \left[\frac{2\varepsilon_1 + \varepsilon_2 - v_2(\varepsilon_2 - \varepsilon_1)}{2\sigma_1 + \sigma_2 - v_2(\sigma_2 - \sigma_1)} \right] \tag{2.39}$$

where σ_1 refers to the host conductivity, σ_2 to that of the dispersed conducting particles, and v is the volume fraction. The assumed properties were a non-conductive host with $\varepsilon_r = 3$ and $\sigma = 0$, and a water inclusion with $\varepsilon_r = 80$, and the water σ and volume fraction or θ_v were left as free variables. Although Hastead (1973) cautioned that the formulations were strictly for low θ_v, Campbell (1988) remarked that they give useful indications with θ_v up to at least 40 %. Using the model of Schwan et al. (1962), the author observed Maxwell Wagner effects with relaxation times of the order of 10^{-8} s, supporting the contention of Hilhorst (1998) that effects are apparent to 500 MHz. Short relaxation times occur when σ of the water inclusion is large ($\sigma \sim 0.1$ S/m), and results in a significant elevation of ε_r ($\Delta\varepsilon_r > 10$) for $\theta_v > 30$ %, and

hence a significant change due to relaxation. This is in quite stark contrast to Campbell (1988) who in a similar approach considered as negligible, the calculated impact of the Maxwell-Wagner effect for typical soils. However closer examination of Campbell's analysis revealed that σ_1 and σ_2 had mistakenly been interchanged, so that σ of the inclusion (water) had been allocated a zero value. Thus while Campbell contended that the dispersion exhibited in his measurements of the dielectric properties of several soils was due to conduction or ion transport alone, it would appear more likely to have been a combination of ion transport and the Maxwell-Wagner effect. However, although the Maxwell Wagner effect would be apparent at frequencies to 500 MHz as claimed by Hilhorst, the model of Schwan et al. (1962) indicates that the effects will be negligible at frequencies above 100 MHz unless σ is high. This is not expected for TDRI.

Two additional aspects should also be considered. Where the composite or its inclusions result in a significant loss component at the measurement frequency, a measure of the imaginary ε_r and inclusion in the model is important (Campbell, 1988). However for TDRI as described here, a low loss material will be assumed, a reasonable assumption for many materials at the typical 1 GHz measurement frequency (§3.2), so this factor will not be considered.

The last influence that has been frequently been assumed small (at least in the case of most soil models) is temperature. ε_r of bulk water has a temperature coefficient of approximately -0.005 $^{\circ}C^{-1}$, however many relaxation processes, including those of tightly-held water, exhibit either positive or negative temperature coefficients. Wraith and Or (1999) postulated that two opposing temperature coefficient processes within soils were responsible for the varied responses reported in the literature. In the first instance, it would seem appropriate to account for the temperature coefficient of free water when constructing a dielectric model.

It is interesting to note that many physically based models employ free parameters that are chosen and configured to take account of particular physical properties, but the parameter coefficients are determined empirically. A good example of this is the author's (unpublished) development of instrumentation and a model to measure θ_v of timber during kiln drying. Several parameters such as timber density, temperature distribution, transmission line spacing and others were introduced since they were theoretically related to particular measurements and properties of the TDR style waveforms. All the measurements were then combined using least squares minimisation from calibration trials that intentionally explored the boundaries of timber properties and drying conditions.

2.5.2 Measurement of propagation velocity

A TDR instrument is appropriate for TDRI since it both generates and measures the propagating voltage step. Although dispensing with the balun has become popular for measurements in soil, the resulting evanescent field will be smaller than with a PTL, and somewhat more difficult to model. Hence, despite the effect of the balun on limiting frequency response (discussed further in §6.3), it is more appropriate for TDRI, at least for this initial development phase.

A further constraint on the balun when used for TDRI, is presentation of a near-perfectly balanced signal to the PTL (discussed further in §6.3), and good isolation from ground. The comparisons of Spaans and Baker (1993) suggest that this would be achieved by the Guanella, 1:4 balun with additional 1:1 isolation balun. However this arrangement must be tempered with the requirement for fast risetimes (through low inductance baluns) to achieve accurate time measurement.

A consistent reference measuring point such as the start point of Figure 2.2 is also required for accurate timing of t_p. For TDRI, this must be at the beginning of the PTL, and not an earlier arbitrary point as used for TDR in soil, since a high accuracy is required, and v_p prior to the beginning of the active or measured region of the PTL may not be constant. Hook et al. (1992) employed diode switches on the PTL to enable measurement of t_p between the diode switches, and was reported to improve waveform accuracy when using long connecting cables and for conductive soils. The author devised a similar technique in 1987 (unpublished) for a soil moisture meter that is now in commercial production. Use of a similar differencing technique is likely to cancel consistent errors when measuring t_p for TDRI. Hook and Livingston (1995) quantified the timing errors in the Tektronix 1502C timebase and noted that particular measurement near the ends of the timebase ramp, that is near multiples of 50 ns, are less accurate than the centre, and that linearity of the ramp limited accuracy elsewhere. It is expected that the latter error would be reduced by a differencing technique.

2.5.3 The forward problem

In contrast to the EM scattering approach required when illuminating an object with a plane wave, quasi-static modelling is appropriate for guided propagation, since under the constraints of low loss, and an evanescent or non-propagating field such as that surrounding a PTL, the problem may be posed as Eqn (2.13) and solved numerically. The dimensionality is critical in choosing the method that will be employed. For an isotropic, homogeneous ε_r distribution, the IE method may be constrained to 2-D, and formulated in terms of surface charges. However an inhomogeneous or anisotropic ε_r distribution requires a VIE method. This forms a further contrast with DE methods that may, assuming an invariant third dimension, use a 2-D solution. However, we will show in §3.7, a new pseudo 3-D VIE method that provides the benefits of a 2-D approach, and which retains the IE benefit that the scattering matrix is unaffected by altering the impressed field.

Cell shape and size are somewhat interdependent in that an inappropriate shape, such as the cube that is most appropriate for Cartesian coordinates, may be compensated for to some extent by decreasing cell size. For TDRI, cubic cells are most appropriate for materials such as timber and cheese, and are also suitable for a continuous medium such as soil. However the field distribution over each cell is not uniform as pulse basis functions assume, and although errors may be reduced by the use of smaller cells, matching the cell size to the PTL rod size does simplify the modelling.

Model accuracy is governed by the extent or graininess of the discretisation, the accuracy of representing the polarisation field in the cell, and the error from assuming a constant impressed field over the cell. Hence, where the field has a strong gradient, accuracy is usefully improved by reducing cell size, but at the expense of increased execution time. By more accurately integrating the field in each cell, the calculation time is likely to increase, but may be more than compensated for by the increased granularity that may then be tolerated (Tsai et al., 1986). In the case of TDRI with materials such as soil and wood, it is expected that the spatial rate of change of ε_r would be less than 1 mm^{-1} (ie $\Delta\varepsilon_r < 10$ between adjacent 10 mm cells used in §6.6). This rate of change is much less than the sharp variations typical of the man model.

Consequently, cubic cells are most appropriate for TDRI, and if increased accuracy is required, use of higher order basis functions is most appropriate.

2.5.4 The inverse problem

The conventional approach has been to employ least squares for calculating the objective function. However it is apparent that Gaussian weighting for the objective function is disadvantageous for inconsistent data sets (that do not lead to a unique solution even if fully determined) since it results in a 'levelling' of the errors, whereas a longer tailed distribution would be expected to be more tolerant. This approach may have advantages over regularisation with a maximally flat solution for example, since that penalises all measured data, not just those that differ most from the predicted set.

There is a trade-off with Tikhonov regularisation in that although we may be confident of the accuracy of our model and data and hence the residual norm, some of this information must be forfeited (ie λ not large) to obtain regularisation. For this work, the unknown, anomalous region of the space probed by the PTL rods, may in principle be probed from three of its four sides, although for convenience in industrial measuring situations, access from just one side of the material is preferable. Consequently, we may provisionally state that the problem is at worst moderately under-determined, considering that known constraints such as bounding values, maximum expected spatial and temporal rates of change of the measured parameter, and spatial monotonocity provide sufficient *a priori* data for stable convergence to a solution. We note here that temporal rates of change do not appear to have been used in the past for *a priori* data. However, where a temporal sequence of reconstructed images is to be produced, physical and pragmatic limitations applying to differences between successive snapshots will provide additional *a priori* data, albeit with attendant difficulties for incorporation with other data

To provide an objective function that incorporates regularisation, we may combine Eqn (2.28) and Eqn (2.29), so that:

$$S = \frac{1}{1+\lambda}\left[(g(m)-d)' C_d^{-1} (g(m)-d) + \lambda (m-m_{prior})' C_m^{-1} (m-m_{prior})\right] \qquad (2.40)$$

where the (m - m_{prior}) term represents the distance between the first estimate or *a priori* data vector and the current solution m. It too is weighted, in this instance by the confidence in m_{prior} that is encapsulated in the covariance matrix C_m.

Since the forward solution is computationally demanding, minimal calculation effort for the Jacobian is required, and an electric field approximation is likely to suffice. There is clear consensus that Jacobian accuracy is not too critical. Indeed, with a quite nonlinear problem, an approximate Jacobian has a narrower domain over which it is close to the true Jacobian, so accuracy could be expected to have less impact on the number of iterations than with a weakly nonlinear problem.

Chapter 3

A Forward Model for Time Domain Reflectometry Imaging

Here, a full forward model for the time domain reflectometry imaging (TDRI) problem is developed and verified. Initially, a model of the parallel transmission line (PTL) will be formulated and then the moment method (MM) will be adapted to model the resulting field from a given relative permittivity (ε_r) distribution. The composite model will then be applied to the standard equation for a low-loss PTL to predict the propagation velocity v_p.

3.1 Overview and justification

In Chapter 1, the concept was introduced of employing the evanescent field of a PTL to probe a composite material and thereby enable generation of images of the distribution of volumetric moisture content (θ_v). Fig 1.1 showed the arrangement of the equipment that employs a moveable PTL near the composite material with unknown θ_v distribution. Readings of v_p, recorded for different relative positions of the PTL and the composite material, are then processed to recover information on the θ_v distribution. The required processing involves three steps, solutions to the forward and inverse problems, and application of a dielectric model. These may be defined respectively as:

- Calculate the v_p on a PTL near or embedded in an arbitrary ε_r distribution.
- Determine the ε_r distribution around a PTL given a series of measurements of v_p.
- Translate a given ε_r distribution within a composite material to θ_v distribution.

The first step is a definition of the TDRI forward problem and its solution, and forms the objective of the work described in this chapter.

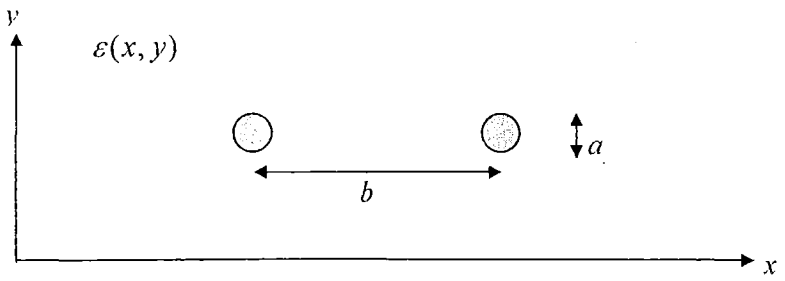

Figure 3.1 Physical arrangement of transmission line.

3.1.1 Methodology

In Appendix 2 it is shown that v_p is not a linear function of the ε_r distribution, and then in §2.3.1 that a MM integral equation (IE) solution method is appropriate for solving TDRI. The main steps in solving the forward problem are:

- Calculate the quasi-static field of a PTL.
- Determine the anomalous field distribution (using the MM).
- Integrate the field between the PTL rods to obtain the potential difference.
- Calculate the line capacitance and use the transmission line formula to calculate v_p.

3.1.2 Practicalities

Prior to describing the forward solution, the issue of spatial resolution will be briefly discussed in the context of the wavelength-resolution conflict that is a factor in microwave imaging (MI). Then TEM propagation on a PTL is described in relation to wavelength (λ), and longitudinal integration issues are addressed.

While there appears little prior art in the use of TDRI, several groups of researchers (Pichot et al., 1985; Johnston et al., 1996) are currently investigating the use of microwave diffraction imaging and ground penetrating radar (GPR). A key aspect of these approaches, where a plane wave is launched into the medium and the scattered wave is detected, is that the resolution is dependent on λ of the probing signal. The Rayleigh limit for resolution is $\lambda/2$ and although the attainable resolution is normally about 3λ (Berryman, 1991), diffraction techniques that also extract phase information from the scattered signal enable resolution near the Rayleigh limit. Super resolution (beyond the Rayleigh limit) employs the evanescent field (Devaney, 1992) although there is some promise for super resolution beyond this limit (Bertero, 1992). In the case of TDRI, the probing signal is the evanescent field from guided TEM propagation that may be fully described by a quasi-static approach (Ramo et al., 1993), and hence *resolution in the transverse plane is not limited by wavelength.* The reason for the difference between the two methods is that in contrast to TDRI, MI relies on resolving ε_r in the direction of propagation, and the Rayleigh limit restricts the information that may be extracted.

For TEM propagation, radiation losses become significant when the transverse dimensions of the PTL are of the order of λ. For $\lambda = 60$ mm (equal to the PTL rod spacing b, in Figure 3.1), the frequency is 5 GHz, corresponding to a pulse risetime t_r of 70 ps where the bandwidth is taken to be $0.35/t_r$ (Brazee,1968). Hence frequency components of this order will become attenuated during propagation.

In principle, higher order modes where the transverse field around a PTL has additional nodes to those at the PTL rods may exist. However, the effect of these is to cause some additional dispersion, and since the amplitude is also likely to be small on lines with spacing much greater than λ, the effects may be neglected (Ramo et al., 1993).

In the approach that is used here, the assumption is made that the anomalous region is lossless. In practice, and as described in §3.2, it will suffice that the conductivity $\sigma << \omega\varepsilon$, where ω is the angular frequency. This is equivalent to $\sigma << 0.6$ S/m in a typical TDR measurement situation where the frequency component that is measured is 1 GHz, and ε_r of the material surrounding the transmission line is 10, representing a θ_v of approximately 20 %.

The other aspect of departure from an ideal transmission line is resistive loss in the PTL rods. Ramo et al. (1993) point out that even when considering the skin effect resistance of a PTL, the real or loss component of impedance (resistance) within the conductor is usually small compared with the imaginary or inductive component (ie $R << \omega L$ where R and L are respectively the distributed resistance and inductance per unit length of PTL).

3.2 Propagation velocity on a transmission line

Providing the geometry of the PTL is appropriate ($\lambda > b$), quasi-TEM propagation occurs on the PTL with inhomogeneous transverse ε_r distribution. Assuming that ε, conductivity σ and permeability μ are independent of time, the two Maxwell equations that describe EM wave propagation may be written as:

$$\nabla \mathbf{x} \boldsymbol{E} = -\mu \frac{\partial \boldsymbol{H}}{\partial t} \tag{3.1}$$

$$\nabla \mathbf{x} \boldsymbol{H} = \sigma \boldsymbol{E} + \varepsilon \frac{\partial \boldsymbol{E}}{\partial t} \tag{3.2}$$

The right hand side of Eqn (3.2) comprises the conduction current due to σ of the propagating medium, and the displacement current due to ε', the energy storage or real component of ε.

Now consider TEM propagation along a PTL, where the transverse plane is described by the x and y Cartesian coordinates and the longitudinal coordinate is z. In the case of a guided EM wave propagating with zero loss, the z component of both $\boldsymbol{E}$ and $\boldsymbol{H}$ is zero. Then considering the x-z plane, it may be shown (Ramo et al., 1993) that:

$$\frac{\partial^2 \boldsymbol{E}_x}{\partial z^2} = \mu\varepsilon \frac{\partial^2 \boldsymbol{E}_x}{\partial t^2} \tag{3.3}$$

Solutions of Eqn (3.3), the 1-D wave equation, lie on characteristic curves (Williams, 1980) defined by:

$$\frac{dz}{dt} = \frac{1}{\sqrt{\mu\varepsilon}} \tag{3.4}$$

$v_p = \frac{dz}{dt}$ is independent of the time rate of change of E, and hence independent of the slope of a voltage pulse, or equivalently its frequency spectrum as represented by a Fourier series.

Consider the case where the medium has a small loss. Provided $\sigma << \omega\varepsilon$, the conduction current contribution in Eqn (3.2) may be ignored, and Eqn (3.3) adequately describes the wave propagation. This condition is equivalent to $\sigma << 0.6$ S/m in a typical TDR measurement situation where the measured frequency component is 1 GHz, and ε_r of the material surrounding the transmission line is 10, representing a θ_v of approximately 20%. ε may be replaced by $\varepsilon' - j\frac{\sigma}{\omega}$. It can be shown that v_p in the low-loss case is adequately represented by a truncated series expansion:

$$v_p \approx \frac{1}{\sqrt{\mu\,\varepsilon\left(1 + \frac{\sigma^2}{8\varepsilon^2\,\omega^2}\right)}} \tag{3.5}$$

In considering loss in the axial direction, it may be shown (Ramo et al., 1993) that even when considering the skin effect resistance of a PTL, the real or loss component (resistance) within the conductor is small compared with the imaginary or inductive component (i.e. $R << \omega L$ where R and L are respectively the distributed resistance and inductance per unit length of the PTL). The consequence of the small real loss in the axial direction is negligible contribution to the integral of $\boldsymbol{E} \cdot \boldsymbol{dl}$ (along a path between the PTL rods that defines the line voltage) by the axial magnetic field and negligible contribution to the transverse magnetic field by the displacement current. The negligible axial components of $\boldsymbol{E}$ and $\boldsymbol{H}$ enable the use of Eqn (3.3) to describe the TEM propagation with low-loss ε, and quasi-static analysis to represent the transverse fields.

3.3 A solution to the forward problem

Initially, we define a region in which a solution is sought, and ascribe particular EM properties, although the solution that will be derived may also apply to more general regions. The region is a Hilbert space (a linear vector space with inner product), defined by 3-D Cartesian coordinates (x, y, z represented by r). Throughout the region and beyond, the permeability is the lossless, free space value μ_0, and outside the region, ε is the lossless, free space value ε_0. The region includes an impressed electric field that is fully defined by the quasi-static EM field of a PTL that is enclosed within the region (ie there is no other macroscopic electric field either from an external source or an internal permanent polarization field). For the immediate solution, we further constrain the properties of the region and the PTL to have zero or very small loss. Hence:

1. the PTL rods have zero or near-zero resistance (true for typical rods)
2. ε within the region is lossless, or at least tan δ is small (true for many composite materials).

With the problem constrained as above, the capacitance of the PTL and hence its characteristic and non-dispersive v_p, may be considered to be purely functions of ε and PTL geometry (Figure 3.1);

$$v_p = f(a,b,\varepsilon(r)) \tag{3.6}$$

where f is a function of the line geometry (described by line diameter a and spacing b) and of ε, itself a function of the 3-D Cartesian space coordinate r. Eqn (3.6) describes the forward problem, and the objective is to find the form of f so that v_p may be determined from a, b, and $\varepsilon(r)$.

Given an impressed electric field $\boldsymbol{E}_i(r)$ in the region defined above with arbitrary $\varepsilon(r)$, the total resultant electric field distribution $\boldsymbol{E}(r)$ is:

$$\boldsymbol{E}(r) = \boldsymbol{E}_i(r) + \boldsymbol{E}_p(r) \tag{3.7}$$

$\boldsymbol{E}_p(r)$ is the polarization field that is generated by those parts of the region with non-zero susceptibility and in response to $\boldsymbol{E}_i(r)$. Hence, where the polarization of the region is defined by $\boldsymbol{P}(r)$ and since:

$$\boldsymbol{E}(r) = \frac{\boldsymbol{P}(r)}{\varepsilon_0 \chi(r)} \tag{3.8}$$

then

$$\frac{\boldsymbol{P}(r)}{\varepsilon_0 \chi(r)} = \boldsymbol{E}_i(r) + \boldsymbol{E}_p(r) \tag{3.9}$$

or

$$\begin{aligned} -\boldsymbol{E}_i(r) &= \boldsymbol{E}_p(r) - \frac{\boldsymbol{P}(r)}{\varepsilon_0 \chi(r)} \\ &= K(\boldsymbol{P}) \end{aligned} \tag{3.10}$$

Here, K is a linear operator acting on the polarization $\boldsymbol{P}$, $\boldsymbol{E}_i$ the external impressed field and $\chi(r)$ is the electric susceptibility ($\varepsilon_r(r) - 1$). The polarization region may now be discretised, and following the MM (Harrington, 1968), we calculate the matrix of polarization vectors $\boldsymbol{P}(\mathrm{r})$:

$$[K][\boldsymbol{P}] = -[\boldsymbol{E}_i] \tag{3.11}$$

so that

$$[\boldsymbol{P}] = -[K]^{-1}[\boldsymbol{E}_i] \tag{3.12}$$

In practice, back-solving for $\boldsymbol{P}$ using Gaussian elimination is more efficient than calculating the inverse (Press et al., 1992) although when calculating for several $\boldsymbol{E}_i$, it is more efficient to calculate $[K]^{-1}$ once. To extract the vector of electric field strengths we utilize Eqn (3.8) so that:

$$[\boldsymbol{E}] = \left[\frac{\boldsymbol{P}(r)}{\varepsilon_0 \chi(r)}\right] \tag{3.13}$$

The PTL voltage is obtained by a line integral over a suitable integration path l between the rods:

$$V = \int_{rod1}^{rod2} \boldsymbol{E}(r) \cdot d\boldsymbol{l} \tag{3.14}$$

or in discretised form:

$$V = \sum_{rod1}^{rod2} [\boldsymbol{E}] \Delta l \tag{3.15}$$

where $[\boldsymbol{E}]\Delta l$ is the projection of $\boldsymbol{E}$ on line element Δl. The capacitance per unit length of the PTL is

$$C = \frac{q}{V} \tag{3.16}$$

where q is the charge per unit length of the PTL used to define the impressed field. Finally, to calculate v_p, C is substituted in the telegrapher's equation for a lossless PTL:

$$\begin{aligned} v_p &= \frac{1}{\sqrt{LC}} \\ &= \sqrt{\frac{\pi}{C\mu \cosh^{-1}\left(\frac{b}{a}\right)}} \end{aligned} \tag{3.17}$$

Here L is the inductance per unit length, and a and b are respectively the diameter and spacing of the PTL rods. In the above derivation of v_p, the remaining unknowns comprising the impressed field $\boldsymbol{E}_i$ and the polarization field $\boldsymbol{E}_p$ will now be determined.

3.4 The field of a parallel transmission line

As outlined by Magnusson (1965), the electric and magnetic field components on a PTL with TEM propagation are in phase with the current (which can be assured as in this case, where for a PTL, $b << \lambda$). Further, even though there may be small resistive loss in the conductor material, the TEM assumption remains a very good representation of line behaviour (Ramo et al., 1993), and since the current contribution arising from dielectric loss is normal to the PTL, it does not affect TEM assumptions.

One approach to calculating the field of a PTL is to assume line charges. It is appropriate to ignore the proximity effect (calculated below) that explains the misalignment between the centre of each rod and each geometric centre of the bipolar field distribution, in turn arising from the non-uniform charge distribution on each rod resulting from the proximity of the other. Under this assumption, the field may be derived as follows.

Consider a Cartesian space with $\varepsilon_r = 1$, two line charges $\pm q$ per unit length, and a field point p (where the field strength is to be quantified).

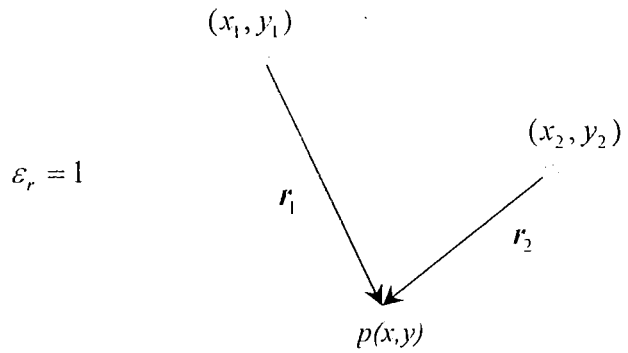

Figure 3.2 Cartesian geometry of a PTL for calculation of the impressed field, $\boldsymbol{E}_i$.

From Figure 3.2 we define:

$$r_1 = \hat{x}(x - x_1) + \hat{y}(y - y_1) \tag{3.18}$$

$$r_2 = \hat{x}(x - x_2) + \hat{y}(y - y_2) \tag{3.19}$$

and

$$\|r_1\| = \sqrt{(x - x_1)^2 + (y - y_1)^2} \tag{3.20}$$

$$\|r_2\| = \sqrt{(x-x_2)^2 + (y-y_2)^2} \tag{3.21}$$

By field superposition and the field from a line charge (Kip, 1963), the Cartesian components of the electric field at p are:

$$E_x = \frac{\hat{x}\rho}{2\pi\varepsilon_0}\left(\frac{(x-x_1)}{\|r_1\|^2} - \frac{(x-x_2)}{\|r_2\|^2}\right) \tag{3.22}$$

and

$$E_y = \frac{\hat{y}\rho}{2\pi\varepsilon_0}\left(\frac{(y-y_1)}{\|r_1\|^2} - \frac{(y-y_2)}{\|r_2\|^2}\right) \tag{3.23}$$

where ρ is the charge per unit length on each line.

However, the proximity effect does alter the effective centre of the PTL rods from the geometric centre, and may be quantified by (Grivet, 1976):

$$d = \sqrt{b^2 - a^2} \tag{3.24}$$

where d is the electrical rod spacing, and a and b are respectively the rod diameter and physical rod spacing. For the analyses appropriate to the work here, where the ratio $b:a$ has been chosen as 10:1, the proximity effect is quite small (with a uniform ε_r, $d = 0.995\,b$).

For the specific case of the above line charges and field point lying on a rectangular grid within a Cartesian coordinate system, the above general form of the field distribution may be alternatively formulated (Figure 3.3).

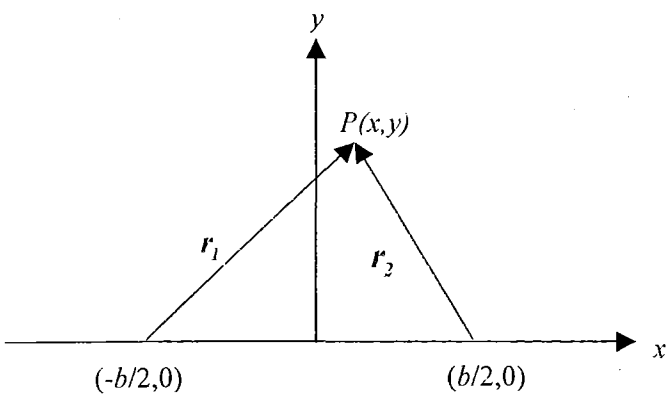

Figure 3.3 Cartesian geometry for a PTL on a rectangular grid.

$$\boldsymbol{r}_1 = \hat{x}(x + \frac{b}{2}) + \hat{y}y \tag{3.25}$$

$$\boldsymbol{r}_2 = \hat{x}(x - \frac{b}{2}) + \hat{y}y \tag{3.26}$$

For a line charge density ρ,

$$\begin{aligned} \boldsymbol{E} &= \frac{1}{2\pi\varepsilon_0}\left(\frac{-\rho\hat{\boldsymbol{r}}_1}{|\boldsymbol{r}_1|} + \frac{\rho\hat{\boldsymbol{r}}_2}{|\boldsymbol{r}_2|}\right) \\ &= \frac{1}{2\pi\varepsilon_0}\left(\frac{-\rho\boldsymbol{r}_1}{|\boldsymbol{r}_1|^2} + \frac{\rho\boldsymbol{r}_2}{|\boldsymbol{r}_2|^2}\right) \end{aligned} \tag{3.27}$$

so that

$$\boldsymbol{E}_x = \frac{\hat{x}}{2\pi\varepsilon_0}\left(\frac{-\rho\left(x+\frac{b}{2}\right)}{\left(x+\frac{b}{2}\right)^2 + y^2} + \frac{\rho\left(x-\frac{b}{2}\right)}{\left(x-\frac{b}{2}\right)^2 + y^2}\right) \tag{3.28}$$

$$\boldsymbol{E}_y = \frac{\hat{y}}{2\pi\varepsilon_0}\left(\frac{-\rho y}{\left(x+\frac{b}{2}\right)^2 + y^2} + \frac{\rho y}{\left(x-\frac{b}{2}\right)^2 + y^2}\right) \tag{3.29}$$

where the lines have charge densities of $+\rho$ and $-\rho$ C/m, and $\hat{x}$ and $\hat{y}$ are unit (dimensionless) vectors.

If the dielectric medium is inhomogeneous, the total electric field is distorted from the above, but the above may be used as the impressed field $\boldsymbol{E}_i$ from which the anomalous or resultant field is calculated.

3.5 Determination of the polarization field

The polarization of a discretised zone or cell within a dielectric material may be represented by a dipole at its geometric centre (Harrington, 1968), quantified by the dipole moment $\boldsymbol{P} = \hat{r}ql$ where q is the dipole charge magnitude and l the separation distance (Figure 3.4).

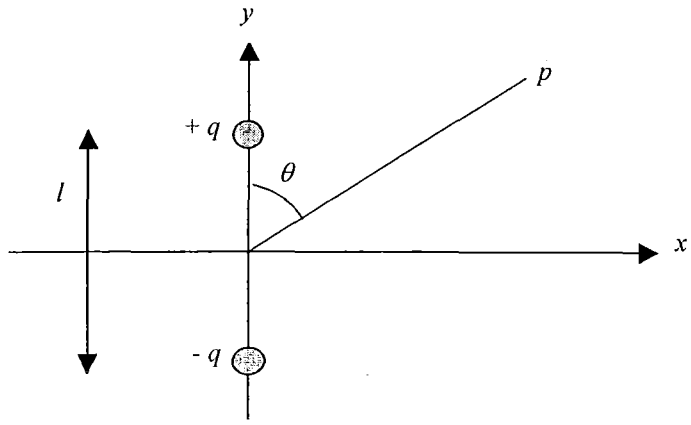

Figure 3.4 Cartesian geometry for calculation of the field of a dipole.

From Plonsey and Collin (1961), the total potential Φ due to a dipole resulting from the superposition of the field from one charge of the dipole, and the Taylor expansion of the opposite charge, a distance l from the first is:

$$\Phi = -\frac{\partial}{\partial z}\left(\frac{q}{4\pi\varepsilon_0 r}\right)l + \frac{1}{2!}\frac{\partial^2}{\partial z^2}\left(\frac{q}{4\pi\varepsilon_0 r}\right)l^2 + \textit{higher order terms} \tag{3.30}$$

Then since

$$\frac{\partial}{\partial z}\left(\frac{1}{r}\right) = \frac{-z}{r^3} \tag{3.31}$$

and

$$\frac{\partial^2}{\partial z^2}\left(\frac{1}{r}\right) = \frac{-1}{r^3}\left(1 - \frac{3z^2}{r^2}\right) \tag{3.32}$$

hence

$$\Phi = \frac{ql}{4\pi\varepsilon_0 r^3}\left(z - \frac{l}{2} + \frac{3lz^2}{2r^2}\right) + \textit{higher order terms} \tag{3.33}$$

and since $z = r\cos\theta$ and $\boldsymbol{P}\cos\theta = \boldsymbol{P}\cdot\hat{\boldsymbol{r}}$:

$$\Phi = \frac{\boldsymbol{P}\cdot\hat{\boldsymbol{r}}}{4\pi\varepsilon_0 r^2}\left(1 - \frac{l}{2r\cos\theta} + \frac{3l\cos\theta}{2r} + \textit{higher order terms}\right) \tag{3.34}$$

Frequently, $l << r$ so that all but the first term vanishes.

In most dielectric materials, there is no net polarization until it is imposed by an external or impressed field. When applied to this quasi-static electric field problem, the MM may be considered as the summation in each cell, of the electric field contributions due to the polarization in all other cells. Cubes are a convenient cell shape for a Cartesian coordinate system and are used here, but cells with trapezoidal (Schaubert and Meaney, 1986) or hexagonal cross-sections are viable but less convenient alternatives (§2.3.4).

The following derivation of Eqn (3.45), a dyadic representation of the field due to a source polarization, builds on the description by Harrington (1968). Consider the influence of a portion (U) of polarized material on the potential at point f. The total polarization of U can be represented by a dipole at the centre of the region, and with dipole moment $\boldsymbol{P}$ (Figure 3.5).

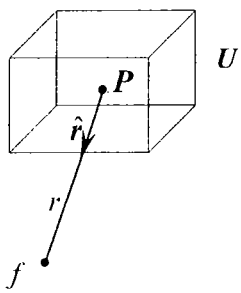

Figure 3.5 Geometry of a region of polarization within a polarized material.

From electrostatic theory, the potential at f is (Kip, 1969):

$$\begin{aligned} \Phi_f &= \frac{1}{4\pi\varepsilon_0}\frac{\boldsymbol{P}\cdot\hat{\boldsymbol{r}}}{r^2} \\ &= \frac{1}{4\pi\varepsilon_0}\frac{\boldsymbol{P}\cdot\boldsymbol{r}}{r^3} \end{aligned} \tag{3.35}$$

where $\hat{\boldsymbol{r}}$ is a unit vector pointing from the centre of U to f. The electric field is $\boldsymbol{E}_f = -\nabla\Phi_f$ and using the superposition theorem, the total field at s due to contributions from all field points is:

$$\boldsymbol{E}_f = \int_{all\ U} -\nabla\cdot\frac{1}{4\pi\varepsilon_0}\frac{\boldsymbol{P}\cdot\boldsymbol{r}}{r^3}dv \tag{3.36}$$

Since the region is a linear vector space (was previously defined as a Hilbert space):

$$\boldsymbol{E}_f = -\frac{1}{4\pi\varepsilon_0}\nabla \int_{all\ U} \frac{\boldsymbol{P}\cdot\boldsymbol{r}}{r^3} dv \tag{3.37}$$

The region may then be discretised to obtain the required $\boldsymbol{E}_P$ of Eqn (3.10):

$$\begin{aligned}\boldsymbol{E}_P &= \boldsymbol{E}_f \\ &= -\frac{1}{4\pi\varepsilon_0}\nabla \sum_{all\ U} \frac{\boldsymbol{P}\cdot\boldsymbol{r}}{r^3}\Delta v\end{aligned} \tag{3.38}$$

where Δv is the volume of each subregion or cell, U. Since

$$\begin{aligned}\hat{\boldsymbol{r}} &= \frac{\boldsymbol{r}}{r} \\ &= \frac{x+y+z}{r}\end{aligned} \tag{3.39}$$

it follows that:

$$\nabla\frac{\boldsymbol{P}\cdot\boldsymbol{r}}{r^3} = \nabla\frac{\boldsymbol{P}\cdot(x+y+z)}{r^3} \tag{3.40}$$

and since $\frac{dr}{dx} = \frac{x}{r}$ and $x = x\hat{\boldsymbol{x}}$, the partial derivatives of Φ are:

$$\Phi_x = \frac{\boldsymbol{P}}{4\pi\varepsilon_0 r^5}\cdot\left(\hat{x}(r^2-3x^2) - \hat{y}3xy - \hat{z}3xz\right) \tag{3.41}$$

$$\Phi_y = \frac{\boldsymbol{P}}{4\pi\varepsilon_0 r^5}\cdot\left(\hat{x}3yx - \hat{y}(r^2-3y^2) - \hat{z}3yz\right) \tag{3.42}$$

$$\Phi_z = \frac{\boldsymbol{P}}{4\pi\varepsilon_0 r^5}\cdot\left(\hat{x}3zx - \hat{y}3zy - \hat{z}(r^2-3z^2)\right) \tag{3.43}$$

Since for Cartesian coordinates, $\nabla\Phi = \hat{x}\Phi_x + \hat{y}\Phi_y + \hat{z}\Phi_z$, the electric field at f due to polarization at a source s, in dyadic form is:

$$\boldsymbol{E}_f = \frac{-\boldsymbol{P}}{4\pi\varepsilon_0 r^5}\cdot\begin{bmatrix}\hat{x}\hat{x}(r^2-3x^2) - \hat{x}\hat{y}3xy - \hat{x}\hat{z}3xz \\ -\hat{y}\hat{x}3yx + \hat{y}\hat{y}(r^2-3y^2) - \hat{y}\hat{z}3yz \\ -\hat{z}\hat{x}3zx - \hat{z}\hat{y}3zy + \hat{z}\hat{z}(r^2-3z^2)\end{bmatrix} \tag{3.44}$$

In calculating this expression, r is the distance between a field point f and source point s, defined as $r = \sqrt{x_{fs}^2 + y_{fs}^2 + z_{fs}^2}$, where x_{fs}, y_{fs} and z_{fs} are the relative distances between the source and field points in each direction of the 3-D Cartesian space. Hence the total field at f due to all polarizations in U is:

$$\boldsymbol{E}_f = \sum_{all\ U} \left(\frac{-\boldsymbol{P}}{4\pi\varepsilon_0 r^5} \cdot \begin{bmatrix} \hat{x}\hat{x}(r^2 - 3x^2) - \hat{x}\hat{y}3xy - \hat{x}\hat{z}3xz \\ -\hat{y}\hat{x}3yx + \hat{y}\hat{y}(r^2 - 3y^2) - \hat{y}\hat{z}3yz \\ -\hat{z}\hat{x}3zx - \hat{z}\hat{y}3zy + \hat{z}\hat{z}(r^2 - 3z^2) \end{bmatrix} \right) \tag{3.45}$$

Matrix K in Eqn (3.12) contains a set of components for each field point. Each set consists of contributions from a source point representing a region of polarization, U. This results in an $F \times S$ by $F \times S$ matrix of sets of entries, where F and S are respectively the number of field and source points. For the 3-D Cartesian space, each set comprises nine components representing the three coordinate directions of the field, in response to the three coordinates of the source field, nine elements in total.

3.6 The self term and its impact on solution stability

The self-term, which occurs when the source and field points coincide so that $r = 0$ and hence Eqn (3.45) is not defined, represents the field at the centre of the cell due to $\boldsymbol{E}_i$ alone. Harrington (1968) suggested that for approximate solutions, use of the field inside a dielectric sphere within a uniform field was appropriate. In this application, the approach is limited by the non-uniform $\boldsymbol{E}_i$ over the volume of the cell and the representation of the cell by a sphere. Analytical methods exist for calculating the field inside a dielectric sphere within a uniform field (Kip, 1969), however the calculation for a cubic cell within a non-uniform field requires numerical techniques. For this work, the sphere approximation has been utilised, but a possible two-step improvement would be:

1. Use the sphere approximation and the solution method to select an approximation that best matches a cubic cell in a uniform field followed by
2. Use of the improved approximation and the solution method to calculate the self-term in each cell with the impressed, non-uniform field distribution.

From Kip (1969), the field in a sphere is:

$$\boldsymbol{E}_{local} = \boldsymbol{E}_i - \frac{\boldsymbol{P}}{3\varepsilon_0} \tag{3.46}$$

and since the local field is $\dfrac{\boldsymbol{P}}{\varepsilon_0 \chi}$ where χ is the susceptibility,

$$E_i = P\left(\frac{1}{\varepsilon_0 \chi} + \frac{1}{3\varepsilon_0}\right) \tag{3.47}$$

as Harrington (1968) had suggested for the self term. Some instability has been observed when using pulse basis functions in modelling the field in high permittivity materials (Hagmann, 1978; Massoudi, 1984, Tsai et al., 1986; Qian and Boerner, 1995), and is most likely due to an imperfect summation of the field terms in Eqn (3.49). That expression relies on a sum to infinity of field contributions from each source point, and the approximations we have made by finite cell size, and basis functions that imperfectly represent the field of each cell (§2.3.3 - §2.3.4) and the approximation in the self term. These approximations result in an incomplete sum, and hence inequality in Eqn (3.49), and result in a poorly conditioned matrix K in Eqn (3.11), and its resultant instability. The instability is frequently referred to as poor convergence since direct and iterative methods of solution are equivalent, and is manifested in the iterative approach by a non-convergent solution. Figures 3.6 and 3.7 show the serious instability that develops in the MM solution for the field distribution between two parallel plates as ε_r is increased from a uniform $\varepsilon_r = 10$ to $\varepsilon_r = 100$ (Listing 1).

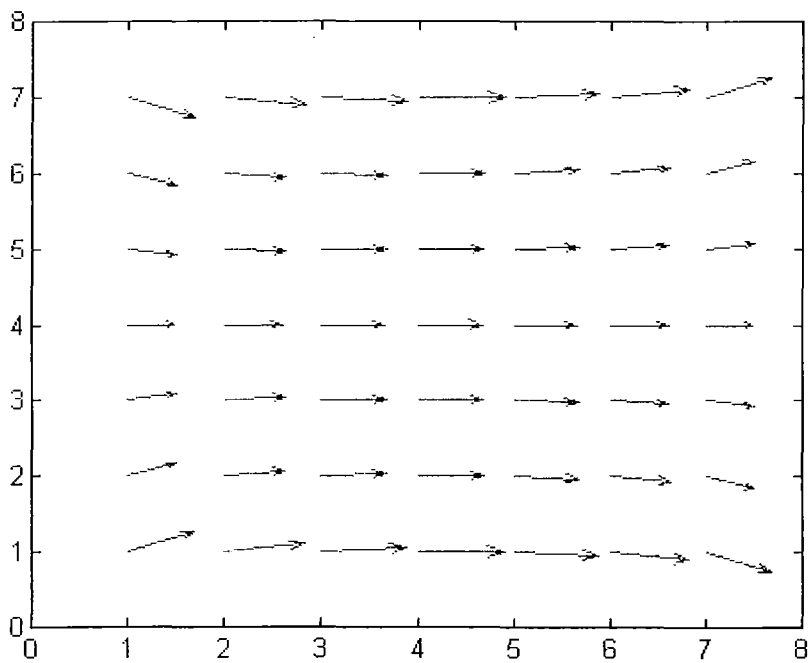

Figure 3.6 MM solution for field in a dielectric cube with $\varepsilon_r = 10$ in a uniform field.

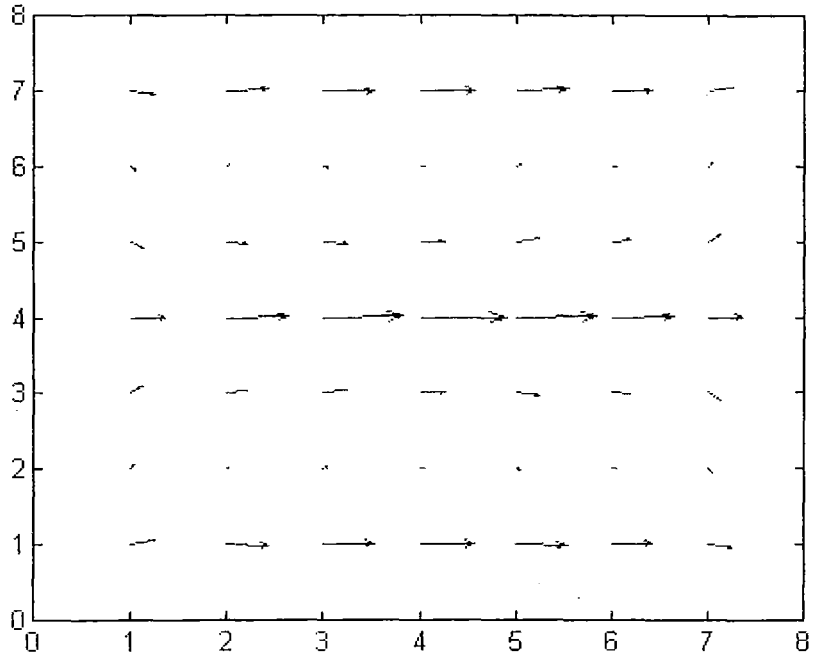

Figure 3.7 MM solution for field in a dielectric cube with $\varepsilon_r = 100$ in a uniform field.

We have been able to effect an improvement in the stability by manipulating the field due to the self-term. Figure 3.8 demonstrates the impact on stability of progressively increasing the self-term field $1/k\varepsilon_0$, from $k = 3$ to 2.8. The improved stability is a result of increasing the self term and providing compensation for the incomplete sum of field terms. However it may also be viewed in a different light. Tikhonov regularisation of an ill-conditioned matrix was shown in §2.4.6 to comprise:

$$K' = K + \lambda\xi \tag{3.48}$$

where in this case K' is the regularised K, λ is a stabilising factor (such as $1/42\varepsilon_0$ that adjusts k in the self term for a sphere from $k = 3$ to 2.8), and ξ is a stabilising functional which may, as in this case, be a unit matrix. Hence the stability has been achieved through a straightforward regularisation process. We could expect the use of higher order basis functions to also provide improved solution stability. For example Tsai et al. (1986) noted that higher order basis functions provide better accuracy and convergence, and it is likely that the effect of inaccurate estimation of the strongly non-uniform field in the boundary cells of Figure 3.7 by the pulse basis functions is responsible for the poor convergence.

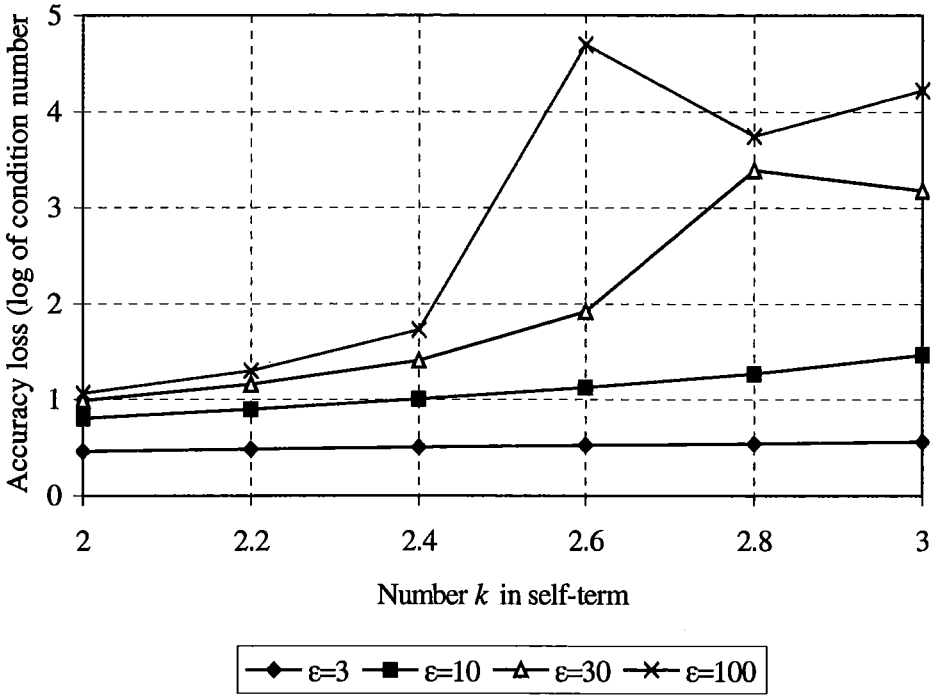

Figure 3.8 Convergence of MM with change in self-term.

3.7 Quasi 3-D method

Traditional EM methods generate large scattering matrices. In the case of the VIE approach, the scattering matrix is fully populated, and contrasts sharply with DE methods that produce larger but sparse (banded in this case) matrices (Binns et al., 1992). Using the example of a 3-D VIE method, the scattering matrix has dimensions $3n^3$ by $3n^3$, where n is the number of cells along the edge of the discretised zone. This arises from a typical formulation where each row of the scattering matrix represents the electric field within a cell, due to one polarization component (eg in the x dimension) of all cells. Each field cell has a scattering matrix entry for each of the three dimensions (x, y, z). Hence, a realistic problem that is discretised to 10 by 10 by 10 cells, produces a 3000 by 3000 element scattering matrix, requiring 72 MB of storage when double precision (8 byte) floating point numbers are used. Because the matrix is full, sparse matrix storage techniques, where only non-zero elements are stored along with their address within the matrix, provide no advantage.

In examining methods that could be used to decrease the memory use burden, the data redundancy in the z dimension or axial direction of the transmission line was noted. Along the z direction, ε_r variation cannot be easily resolved by the timing instrumentation used to measure v_p. Discontinuities have been used to generate reflections at intervals to achieve axial resolution (Topp and Davis, 1981), but few discontinuities can be used since the analysis becomes much more complex as the number of reflections increases. Full inversion techniques based on impedance changes have been employed and hold promise for invasive soil profiling

(Laurent, 1999; Hook et al., 1992). Nevertheless, the axial or z dimension represents an unusable degree of freedom that uses significant computing resources for the VIE method. To avoid this, an alternative method was developed by the author that retains the essential volume integration of the field terms, but relaxes the formal inclusion of the z dimension of the full VIE method. The approach includes integration of the field components in the z dimension at each cell in the transverse plane, effectively reducing the method's dimension from three to two.

It was expected that this approach would impact on the error since summation would be incomplete. For example, consider a series solution to the general linear inhomogeneous equation $L(f) = g$ (Harrington, 1968):

$$f = \sum \alpha_n f_n \tag{3.49}$$

represents the MM solution for the unknown f, which in this case represents the polarization. The domain of f is the anomalous region of the 3-D plane, so that n depicts all cells. α represents the polarization field of a dipole centred on a source cell (Harrington, 1968), and f is the basis function, in this case chosen as a Dirac delta function so that the contribution from only one cell is considered for each n. For a uniform axial polarization field and ε_r, and assuming zero z polarization, the sum is incomplete since no field contribution in the z direction is accounted for. Although the impressed field in the z direction is invariant (zero z component), the source cells do possess small z direction fields arising from the x and y excitation. Since these particular contributions from the field components in the z direction are not accounted for by the quasi 3-D method, they contribute to the modelling error. Nevertheless, the method was expected to provide a comparable solution to the full 3-D VIE approach. The method assumes a uniform axial ε_r distribution, and the output from the procedure is a description of the field in the chosen transverse plane, that is the same as the field in any transverse plane along the PTL.

The quasi 3-D method is implemented by constructing the scattering matrix **K** in 2-D, but including additional field contributions from all the axial or z cells at each calculation through the chosen transverse plane. For computational simplicity and speed, the transverse plane is located half way along the PTL so that symmetry may be used to calculate once, each pair of contributions on opposite sides of the transverse plane. The additional off-plane field contributions corresponding to each cell in the transverse plane at (x', y'), take the same form as elements in Eqn (3.45).

Consider a particular source cell position in the transverse plane, x' and y', and a field cell at x and y, where the resulting field is to be determined. Table 3.1 shows the components of the source field for each axial or z component. The $\hat{x}\hat{x}$ component is the field in the x direction, arising from the x-field at the source point. Similar expressions apply for the $\hat{y}\hat{y}$ components and the cross terms, $\hat{x}\hat{y}$.

Table 3.1 Contributions to a field cell from nearby cells in the transverse plane.

z	r_n	$\hat{x}\hat{x}$ contribution
0	$r_0 = \sqrt{(x-x')^2+(y-y')^2}$	$3(x-x')^2 - r_0^2$
± 1	$r_1 = \sqrt{(x-x')^2+(y-y')^2+1}$	$3(x-x')^2 - r_1^2$
± 2	$r_2 = \sqrt{(x-x')^2+(y-y')^2+4}$	$3(x-x')^2 - r_2^2$
± 3	$r_3 = \sqrt{(x-x')^2+(y-y')^2+9}$	$3(x-x')^2 - r_3^2$

Hence the calculation for the $\hat{x}\hat{x}$ field at (x,y) due to the dipole fields at (x',y'), for seven cells ranging from z = -3 cell lengths to z = +3 cell lengths, includes the geometric factor:

$$\frac{\Delta v}{4\pi\varepsilon_0}\left[\frac{(3x^2-r_0^2)}{r_0^5}+\frac{2(3x^2-r_1^2)}{r_1^5}+\frac{2(3x^2-r_2^2)}{r_2^5}+\frac{2(3x^2-r_3^2)}{r_3^5}\right] \tag{3.50}$$

where Δv is the cell volume and $r_n = \sqrt{(x-x')^2+(y-y')^2+(z-z')^2}$.

The reference or on-plane case where $(z-z')=0$ is represented by $n = 0$. For $n = 1$, $(z-z') = \pm 1$ cells distant from the reference plane, and for $n = 2$, $(z-z') = \pm 2$ cells from the reference plane.

The geometric factor of the field calculation for the $\hat{y}\hat{y}$ component is similar to that for $\hat{x}\hat{x}$:

$$\frac{\Delta v}{4\pi\varepsilon_0}\left[\frac{(3y^2-r_0^2)}{r_0^5}+\frac{2(3y^2-r_1^2)}{r_1^5}+\frac{2(3y^2-r_2^2)}{r_2^5}+\frac{2(3y^2-r_3^2)}{r_3^5}\right] \tag{3.51}$$

and in the $\hat{x}\hat{y}$ case the calculation is:

$$\frac{\Delta v}{4\pi\varepsilon_0}\left[\frac{3xy}{r_0^5}+\frac{6xy}{r_1^5}+\frac{6xy}{r_2^5}+\frac{6xy}{r_3^5}\right] \tag{3.52}$$

In general, all contributions from the z dimension will be included in the calculation so that n ranges from zero to $\frac{cells-1}{2}$, or $\frac{cells}{2}$ for an even number of cells. However where the contribution from cells with larger z-z' distances from the transverse plane is considered small in relation to the contribution from the on-plane value, a truncation may be applied to reduce calculation time.

In the 3-D model, there are nine electric field elements for each cell, representing the 3-D source field and the three field dimensions at the field point, resulting in a $3n^3$ by $3n^3$ scattering

matrix where n is the number of cells along the edge of the discretised zone. The pseudo 3-D method reduces the order of the matrix to $2n^2$ by $2n^2$, dramatically reducing both the storage requirements and calculation time. For the 10 by 10 by 10 case, the size of the scattering matrix is reduced from 3000 by 3000 to 200 by 200. The storage requirements of the scattering matrix reduce from 72 MB to 0.32 MB for the double-precision numbers used in this work. Thus the new method dramatically improves the resolution that may be used when modelling the field distribution of a PTL with a VIE approach.

For this work, calculating the field in the z-direction to a depth of $\pm$ 9 cells has provided accurate results, as shown by the experimental validation in §6. The actual error is dependent on the field distribution but a comparison of field strengths between the pseudo 3-D and full 3-D methods for a cube immersed in a uniform electric field provided differences less than 3% for a z-depth of $\pm$ 5 cells.

In geophysical EM modelling of earth structures, 2-D models are frequently used where the excitation source is an axially-invariant line charge (Torres-Verdín and Hashaby, 1994). Point source or dipole excitations are more amenable to subsurface investigations using bore holes, and the combination of the 3-D source and 2-D scatterer is commonly referred to as a quasi 2-D or 2.5-D problem (Torres-Verdín and Hashaby, 1994; Wilt et al., 1995). Consequently, the geophysical 2.5-D problem remains essentially 2-D, but accounts for a 3-D source and hence differs quite markedly from the quasi 3-D method described above.

3.8 Cell geometry

Choosing a cell size that closely resembles the cross-sectional dimensions of the PTL rods is appropriate. Typically, 5 mm diameter rods will be used, spaced between 10 and 20-rod diameters to achieve a reasonably large probing field yet still ensure TEM propagation. Hence the practical model size of 10 or 20 cells along the edge of the anomalous region (only this region needs to be included for IE methods), dictates that just one cell (of square cross-section) will be used to represent each rod. Although five cells could be used the resulting shape is little improved on a square cross-section. An alternative approach would be to use cells with hexagonal cross-section although this may adversely impact on discretisation of the anomalous region which may itself, be rectangular. It would also increase the complexity of the calculations since hexagonal packing doesn't conform regularly to Cartesian coordinates. For these reasons, cells with square cross-section have been chosen for this work.

3.9 Basis functions

The above derivations have used pulse or delta basis functions that provide a one to one correspondence between the polarization in each cell and the corresponding integral operator. Hill et al. (1983) noted that in relation to TE fields, pulse basis functions are inadequate in representing the resultant field near regions of high contrast and hence the method may fail to

converge to the correct solution. Linear or higher order basis functions provide for a smoother transition of the field across cell boundaries and a corresponding reduction in modelling errors (they provide a continuous field across cell boundaries, but discontinuous first derivatives).

Consider the MM applied to determining the polarization in the anomalous region within a 2-D space defined by x,y. Then:

$$L(\boldsymbol{P}(x,y)) = \boldsymbol{E}_i(x,y) \tag{3.53}$$

where in this case L is the linear operator defined by the dyadic of Eqn (3.45) and $\boldsymbol{P}(x,y)$ the unknown polarization. Then a series solution is:

$$\boldsymbol{P}(x,y) = \sum_n \alpha_n(x,y)P_n \tag{3.54}$$

where α_n are unknown constants representing the polarization at each point n in the x-y plane, and P_n are basis functions. $\boldsymbol{P}$ may be expressed in terms of delta or pulse basis functions:

$$\boldsymbol{P} = \sum_n \delta_n \left[\hat{x}(a_n(x-x_n) + b_n(y-y_n)) + \hat{y}(c_n(x-x_n) + d_n(y-y_n))\right] \tag{3.55}$$

where δ is the Dirac delta function, n is an index representing the cell number, $\hat{x}$ and $\hat{y}$ are unit vectors that represent the coordinate directions of the polarization, $a_n ... d_n$ are unknown coefficients, and x_n and y_n are the coordinates of the cell centroid. From Eqn (3.53):

$$\sum_n P_n L(\alpha_n(x,y)) = \boldsymbol{E}_i(x,y) \tag{3.56}$$

Weighting functions, w_1, w_2,... that lie within the range of L are used to define an inner product for $L(\alpha_n)$, $\langle w_m, L(\alpha_n)\rangle$, and for the inhomogeneous term $\boldsymbol{E}_i$, $\langle w_m, \boldsymbol{E}_i\rangle$.

If the Galerkin method of choosing w_m equal to P_n is employed then we may formulate as:

$$\sum_n \delta_n L(\delta_n(\alpha_n(x,y))) = \delta_n(\boldsymbol{E}_i(x,y)) \tag{3.57}$$

In matrix form, Eqn (3.57) may be written:

$$[l_{mn}][\alpha_n] = [\boldsymbol{E}_{i\,m}(x,y)] \tag{3.58}$$

so that:

$$[\alpha_n] = [l_{mn}^{-1}][\boldsymbol{E}_{i\,m}(x,y)] \tag{3.59}$$

If linear or higher order basis functions are employed, the one to one correspondence of the Galerkin approach is replaced by an interdependency. A simple example of this approach has been described (Qian and Boerner, 1995) using linear basis functions in a MM solution for electric current in a 1-D cylinder excited by a plane wave:

$$I(x_m < x < x_{m+1}) = I(x_m) + \frac{(x - x_m)[I(x_{m+1}) - I(x_m)]}{(x_{m+1} - x_m)} \tag{3.60}$$

When similarly applied to determining the polarization in this forward problem, there are additional unknowns so that $\boldsymbol{P}$ is:

$$\boldsymbol{P} = \sum_n \delta_n \left[\hat{x}(a_n + b_n(x - x_n) + c_n(y - y_n)) + \hat{y}(d_n + e_n(x - x_n) + f_n(y - y_n)) \right] \tag{3.61}$$

and the delta function is retained to define the range of each $(x - x_n)$. Hence there are six unknowns for each cell with linear basis functions compared with four in the case of delta functions. In the latter case, the physical interpretation is that the four unknowns represent the electric field in each of the two coordinate directions, in response to the two coordinate directions of the polarization in a source cell. For linear basis functions, the polarization in the source cell is represented by a plane, in turn defined by three coefficients for each of the two components (x and y) of the polarization in a source cell. However in this case, Eqn (3.61) possesses redundant information. Consider instead a so called "rooftop" function where the same number of data as used in the pulse basis functions is used to provide a linear interpolation between cell midpoints (Harrington, 1968). For a particular cell n, it may be shown that the value of the function P over the length of the cell is:

$$P = \frac{3}{4} x p_n + \frac{1}{8} x p_{n-1} + \frac{1}{8} x p_{n+1} \tag{3.62}$$

where x is the cell length and p_n the value of P at the centre of the cell. This may be extended to 2-D so that:

$$P = \frac{3}{4} x p_{n,m} + \frac{1}{16} x p_{n-1,m} + \frac{1}{16} x p_{n+1,m} + \frac{1}{16} x p_{n,m-1} + \frac{1}{16} x p_{n,m+1} \tag{3.63}$$

This forms a weighted, 2-D spatial average of cells in the x-y plane, and may be calculated using a convolution, which in discrete form represents polynomial multiplication.

This approach generates difficulties with the polarization method when using the calculated polarization to recover the electric field. The field is recovered using:

$$\boldsymbol{E} = \frac{\boldsymbol{P}}{\varepsilon_0 \chi} \tag{3.64}$$

and the use of linear or higher order basis functions applied to P, needs to be reflected in χ to obtain appropriate values of E. Preliminary work with linear basis functions was curtailed since the pulse basis functions were providing sufficiently accurate results with stability attained by alteration of the self-term, and the generation of the linear basis functions added significantly to the computational requirements. However, further investigation into use of linear or higher order basis functions is clearly warranted.

3.10 Integration of the electric field

The result of the MM calculation is a map of the electric field strength in each cell of the discretised zone. To achieve the objective of determining v_p on the PTL, the capacitance per unit length of line is calculated from the potential difference between the lines. The potential difference is in turn determined from a line integral of the field between the two PTL rods.

$$V = \int_{rod1}^{rod2} \boldsymbol{E} \cdot d\boldsymbol{l} \tag{3.65}$$

Here $\boldsymbol{E}$ is the electric field strength (a function of the space coordinates), and $\boldsymbol{l}$ the elemental length of the path between the two rods, in the direction of a straight line between the rods. In discrete form this is represented by:

$$V = \sum_{i=rod1}^{rod2} \boldsymbol{E}_i \Delta \boldsymbol{l}_i \tag{3.66}$$

where $\Delta \boldsymbol{l}_i$ is the length of a discrete element of the path $\boldsymbol{l}$ between the two rods. In practice, the most straightforward approach is to align the rods with the rectangular (in this case) discretisation grid to allow integration along one axis between the rods. This results in a straight line integral.

3.10.1 Geometry

The field generated by the transmission line rods is little different from that of a line charge, and the line may be chosen to be at the centre of a cell (Figure 3.9a), or at the intersection of cells (Figure 3.9b). In the former case the cell size may be conveniently chosen to match the size of the PTL rods, thereby assisting integration of the field. This also allows the anomalous region, to be very close to the rods (hatched cells in Figure 3.9a). When pulse basis functions are used, the field is assumed uniform over the area or volume of the cell, so that integration involves an integral number of cells. However, the field near the rods in particular, is far from uniform and has steep gradients, so assumptions about field uniformity are incorrect, and extrapolation from the cell centre to the cell boundary is required for best accuracy. Since the field on the surface of a PTL rod is conveniently represented by the field at the same distance from a line charge, prediction of the potential gradient becomes difficult due to the field

singularity that occurs on a line charge. When higher-order basis functions are used, field uniformity is not assumed and integration may usefully employ the chosen basis function and also conveniently finish at cell boundaries.

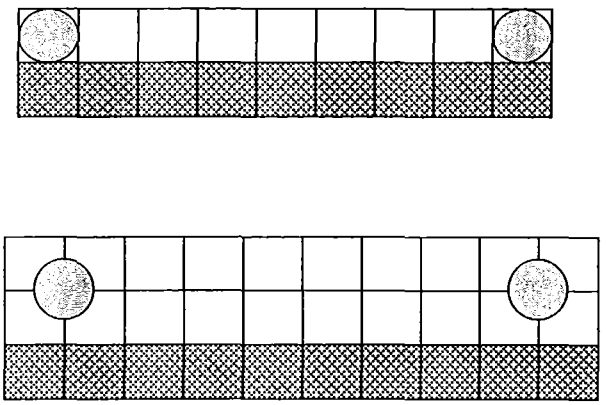

Figure 3.9 Alignment of PTL rods (a) concentric and (b) non-concentric with cells.

Conversely, an advantage of positioning the PTL rods at cell intersections is that self-consistency may be used to test the accuracy of the solution as described in §3.11 below. A further advantage of locating the centre of the rods at cell boundaries is that the singularities that occur at the centre of the line charge are relegated to cell boundaries, not the cell mid points where the fields are calculated when using pulse basis functions. In this case, the diameter (a) of the PTL rod may be chosen similar to the cell cross-section, again assisting integration. Further, since the rod surface may now coincide with a cell mid point where the field is calculated, extrapolation of the field is avoided. In practice, the forward model described here doesn't take account of loss within the material surrounding the PTL, so v_p is unaffected by the actual rod diameter, provided TEM propagation occurs.

If the rods are positioned at the centre of a cell, the anomalous region may in principle coincide with the edges of the rods, but practical considerations dictate that very close alignment is undesirable. The reasons include:

- Non-parallel or imperfectly straight rods resulting in non-uniform v_p
- Roughness in the surface of the anomalous region also resulting in non-uniform v_p
- Modelling errors arising from the very large potential gradients near the rods.

Prior to discussing various integration and interpolation techniques, mention will be made of cell geometry. In the MM implementation used here, cells with square cross-section have been used and since integration of the electric field is required from one rod surface to the other, the integration methods described below integrate to cell boundaries. However, the actual PTL rods have a circular cross-section, and a is used for calculation of PTL inductance. Since Guo et al. (1993) considered that volume mismatch was a significant contributing factor to their sphere discretisation and hence chose cell volumes to match the modelled sphere, a similar

approach was used here. Rod diameter a, used for the calculation of PTL inductance in Eqn (3.17), was 5.6 mm, providing a close match between the areas of the PTL rods and the 5 mm by 5 mm cells used in the model.

3.10.2 Coarse integration

All methods of improving the accuracy of the numerical integration involve an interpolation technique whereby an inference is made about the nature of the field distribution between the (assumed accurate) field at the cell mid points. The most trivial is that of linear interpolation, which may be easily shown to be identical to coarse integration. Coarse integration simply comprises a numerical line integral using the field points calculated from the forward model. A convenient approach is to align the rods parallel to the x-axis (as in Figure 3.1) so that the integration of Eqn (3.66) becomes:

$$V = \sum_{i=rod1}^{rod2} \boldsymbol{E}_i \Delta \boldsymbol{x}_i \tag{3.67}$$

While the integration accuracy may be easily improved by finer discretisation and hence smaller Δx_i, pragmatic aspects of the method and the experimental equipment apply constraints to this approach:

1. Extending the size of the forward model by finer discretisation greatly increases memory use and execution time.
2. This work is applied to measurement of v_p on a PTL, and requires a timing instrument with very high resolution to finely resolve the influence of discretised regions near the line. Hence, finer discretisation puts greater demands on the instrumentation required to solve the TDRI problem.

Following advances in computational capability and the performance of instrumentation, particularly over the last few years, there are excellent prospects in advancing technology enabling improved accuracy from "coarse" discretisation. Nevertheless, means of interpolating the discretised cells were sought with the aim of producing more accurate integration of the field.

3.10.3 Polynomial interpolation

One approach to improving field integration is to fit a polynomial to the field data from each cell, and integrate the fitted curve as representing a continuous function of field strength. As expected, polynomial curve fitting that requires continuous first derivatives produced overshoot near step changes in ε_r. These were exacerbated as the order of the polynomial was increased to better match the high rate of change in field strength, and hence improve the accuracy of the line integrals. Consequently, polynomials are inappropriate for field interpolation with inhomogeneous dielectric materials.

To circumvent the interpolation difficulties inherent with the polynomial fitting where there are discontinuities in the data, splines may be used. For example, the commonly used cubic polynomial may be fitted between adjacent data points to produce a continuous function. While cubic polynomials fitted between two points possess sufficient degrees of freedom to also permit continuous first derivatives, the option remains to separately apply cubic splines to each side of a discontinuity, to achieve a discontinuous first derivative. However, such approaches require careful analysis of the data to locate such discontinuities. Alternatively, a separate spline may be applied between the midpoints of adjacent cells.

3.10.4 Characteristic interpolation

An approach that is believed to be new, at least to this application, is to use existing knowledge of the nature of the field distribution of the PTL along with the calculated field values, to interpolate between the cells. The method, henceforth called characteristic interpolation, was evaluated by comparing a numerical method of calculating the capacitance of a PTL with the known analytical form. This comparison is only valid for an homogeneous dielectric. As shown in Eqn (3.22) for a rectangular grid in a Cartesian plane, the x component of the field is:

$$E_x = \frac{\hat{x}}{2\pi\varepsilon_0}\left(\frac{-\rho\left(x+\frac{b}{2}\right)}{\left(x+\frac{b}{2}\right)^2+y^2}+\frac{\rho\left(x-\frac{b}{2}\right)}{\left(x-\frac{b}{2}\right)^2+y^2}\right) \tag{3.68}$$

and for homogeneous permittivity and the PTL rods centred on the x-axis so that $y=0$:

$$E_x = \frac{-\rho\hat{x}}{2\pi\varepsilon_0\varepsilon}\left(\frac{1}{x+\frac{b}{2}}-\frac{1}{x-\frac{b}{2}}\right) \tag{3.69}$$

and $E_y = 0$. For convenience the PTL (Figure 3.3) is shifted to the right by $x = b/2$ so that:

$$E_x = \frac{-\rho\hat{x}}{2\pi\varepsilon_0\varepsilon}\left(\frac{1}{x}+\frac{1}{b-x}\right) \tag{3.70}$$

Then given a known E_x, an effective ε_r may be calculated to describe the field near the known value. In practice it is convenient to incorporate all the constants into one value k, so that:

$$E_x = k\left(\frac{1}{x} + \frac{1}{b-x}\right) \tag{3.71}$$

and hence

$$k = \frac{E_x}{\left(\frac{1}{x} + \frac{1}{b-x}\right)} \tag{3.72}$$

Then Eqn (3.71) may be used to estimate the field near the known E_x.

Initially, the method was evaluated by comparing a numerical method of calculating the capacitance of a PTL in a homogeneous dielectric with the known analytical form. The above procedure was tested using a MM (Listing 2) and a PTL with $b = 100$ mm, $a = 5$ mm, $\varepsilon_r = 1$, using 20 cells with cross-section 5 by 5 mm, and 10 subsamples within each cell. The numerical approach integrated the field between the cells using arbitrary ρ to obtain the voltage V, and then used $C = \rho/V$ to determine the line capacitance. The analytic form for the capacitance of a PTL is (Ramo et al., 1993):

$$C = \frac{\pi\varepsilon_0\varepsilon}{\cosh^{-1}\left(\frac{b}{a}\right)} \tag{3.73}$$

The calculated capacitance using a 20 cell numeric method changed from 8.36 pF/m to 7.58 pF/m when incorporating the subsampling, whereas the analytic solution was 7.538 pF/m (Table 3.2). As expected the method provided near perfect integration within the uniform ε_r since the known and exact analytic method was used to interpolate the numerically generated field. The characteristic interpolation was used for some of the initial work with the forward model. However, accuracy was limited when modelling non-uniform ε_r distributions that included large contrasts between adjacent cells, and arose from the non-linearity of the problem in such cases. The field distribution given by Eqn (3.71) assumes that the entire span between the PTL rods possesses a constant effective ε_r equal to that in this vicinity. The result is incorrect curvature and step changes at cell boundaries where a new constant k is calculated. As expected, the slope errors are more pronounced in or near anomalous regions.

Table 3.2 Comparison of characteristic interpolation with coarse integration.

Method	Calculated Capacitance (pF/m)
Analytic	7.538
20 cell numeric	8.36
20 cell numeric, 200 subsamples	7.58

3.10.5 Hybrid approach

While providing the expected enhanced accuracy in the above case, characteristic interpolation was less useful with an inhomogeneous ε_r due to discontinuous k. Instead, k was linearly interpolated between cell midpoints to provide a continuous field strength function, although the first derivative was still discontinuous. Figure 3.11 demonstrates the improvement. Polynomial interpolation of k resulted in deviations from the expected field distribution, as discussed below.

3.10.6 Comparison of interpolation methods

The results from the model with different integration methods and the measured values are given in Table 3.3 and represent the one-way travel time along the 300 mm PTL rods, where $a = 6$ mm and $b = 60$ mm. The conditions include no nearby phantom ($\varepsilon_r = 1$ in the region), a nearby water phantom ($\varepsilon_r = 80$, asymmetrically positioned), and a binary distribution where one rod was immersed in water and the other in air. For the asymmetric distribution, the geometric centre of the PTL was positioned 8 mm above the top corner of the container (Figure 3.10). Details of the experimental method and apparatus used to obtain the measurements are provided in §6.1 and §6.3.

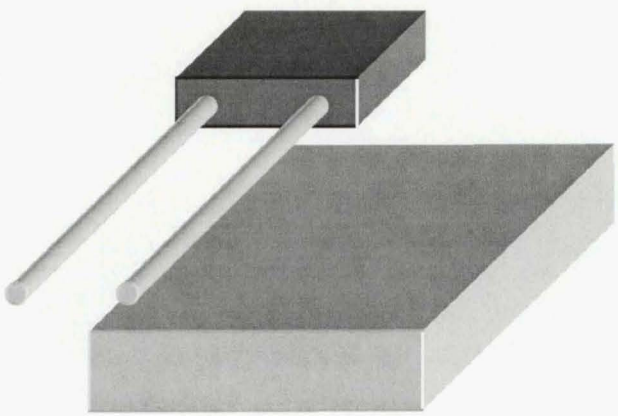

Figure 3.10 Arrangement of asymmetric permittivity distribution.

The data in the asymmetric and binary cases were corrected by subtracting the offset or time by which the air reading differed from 1.0 ns. No attempt was made to measure the travel time in a binary distribution, which was included to highlight the differences with ε_r distributions that are more extreme than those expected when externally probing a dielectric material. Although the better extrapolation performance of the characterisation methods is apparent from the air readings, there was no significant difference between the methods after the offset correction had been subtracted.

Table 3.3 Comparison of propagation times (ns) computed for different methods of interpolating the electric field along the integration axis.

Interpolation method	Air (ns)	Asymmetric (ns) (corrected)	Binary (ns) (corrected)
Linear	1.042	1.040	1.450
Spline	1.024	1.036	1.526
Characteristic	1.004	1.037	1.436
Hybrid linear	1.003	1.037	1.414
Hybrid polynomial	1.004	1.037	1.426
Measured	0.987	1.039	-

The difference in extrapolation (ie beyond an end cell) is apparent from the electric field distribution in Figure 3.10 where the spline method under-estimates the rapidly increasing field strength near the PTL rods. The discontinuities of the non-interpolated characteristic method are also apparent. Figure 3.11, although unrealistic for the probing application described here, indicates the expected poor extrapolation of the spline method and the larger steps in the non-interpolated characteristic method. However, what is more notable is oscillation of the polynomial-interpolated characteristic method, which adds deviations from the expected shape of the field strength distribution in the region between 3 and 5.5 cm. In this case, characteristic interpolation provided a fit that that most appropriately matched the expected shape, ie a uniform (for the linear scale of field strength) small field in water, a segmented exponential increase in air, and discontinuous field strength across the air-water interface at 2.5 cm. Using the linearly interpolated characteristic fit smoothed the small discontinuity at 1.5 cm, but also smoothed that across the air-water interface where a discontinuity is known to exist. Hence, the characteristic fit best represents situations where there are significant field discontinuities, but for a relatively smooth ε_r distribution, the linearly interpolated characteristic fit is suitable. The best option is to use *a priori* knowledge of the distribution to allow duality so that the linearly interpolated characteristic method is used across cell boundaries where there is no change in ε_r, otherwise the characteristic method is used.

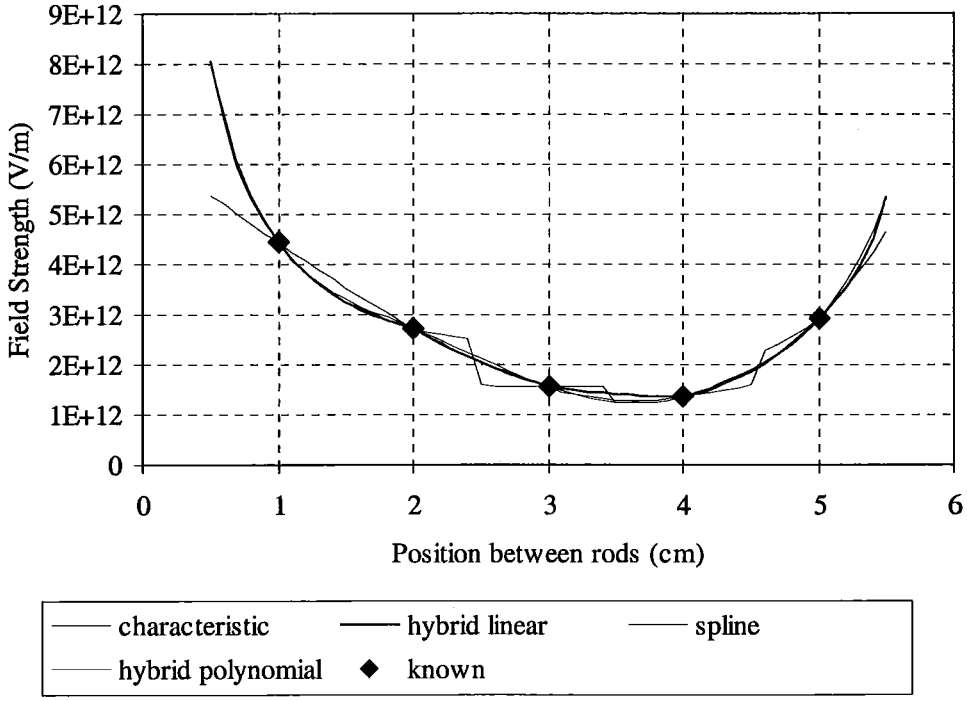

Figure 3.11 Comparison of field interpolation methods for the asymmetric ε_r distribution of Figure 3.10 and with b = 60 mm.

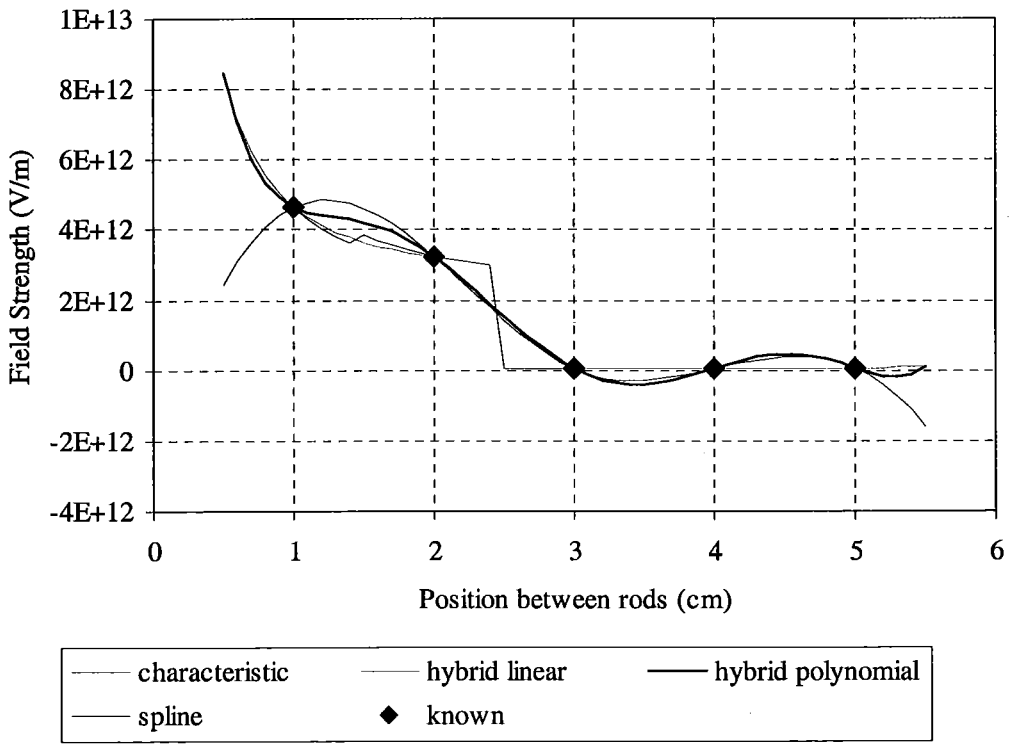

Figure 3.12 Comparison of field interpolation methods for the binary ε_r distribution.

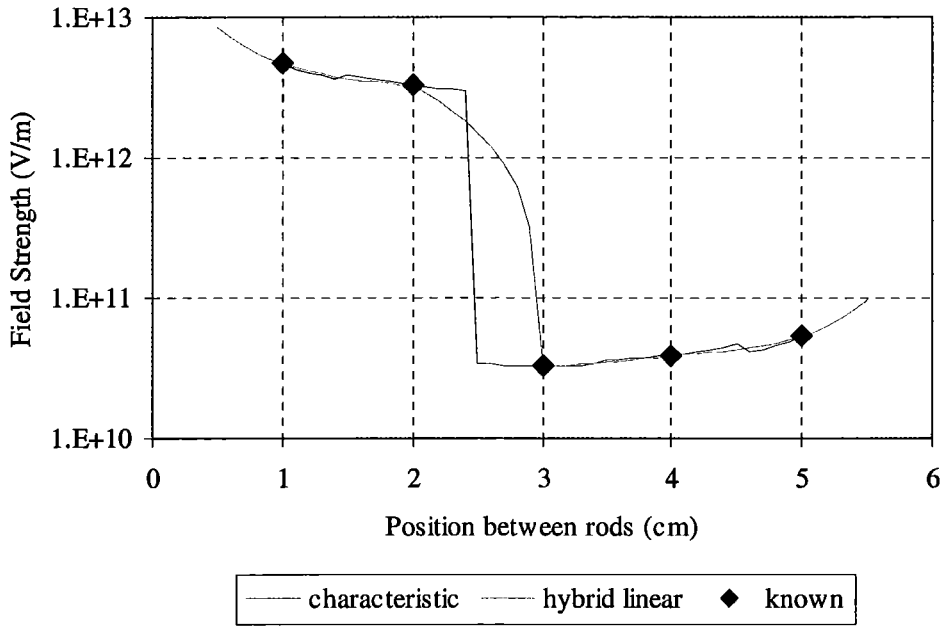

Figure 3.13 Comparison of characteristic and hybrid linear field interpolation with binary ε_r distribution.

3.10.7 Handling extrapolation

Whichever technique is used to perform the line integral, extrapolation is necessary to integrate that portion of the field between the surface or edge of the PTL rod, and the centre of the adjacent cell. In addition, the field near the rod rises rapidly in strength due to the 'virtual singularity' inside the rod. Linear or coarse integration extrapolation is relatively safe, if not particularly accurate. However extrapolating with polynomials, which have the sole aim of fitting a polynomial to known data, is known to be unsatisfactory. Outside the domain of the data, the polynomial usually diverges sharply from that which may be expected from visualising the data (Figure 3.). This characteristic is exacerbated where higher order polynomials are used.

Extrapolation using splines requires some *a priori* data to define the slope at the centre of the cell adjacent to the PTL rod. This could be accomplished by including a pseudo field point at the centre of each rod. Ignoring the proximity effect, the field near the rod is the same as it would be if the rod were replaced by a line charge of infinite field strength. However, as indicated by the theoretical development in §3.10.4 and shown by Figures 3.12 and 3.13, the characteristic method provides accurate extrapolation to the PTL rods.

3.11 Validation of the forward model

The forward model has been evaluated both by experiment, as described in §6.2 and §6.3, and theoretically, as described here. In the theoretical method, the model is used to simulate physical arrangements that have known or readily calculated solutions, and the results compared. Two approaches have been used, one for a uniform ε_r distribution, and the other for a heterogeneous distribution. The first validation method uses a uniform lossless ε_r distribution, and the predicted v_p using the known relationship: $v_p = c/\sqrt{\varepsilon}$ where c is the speed of light in a vacuum. The second validation method was to compare the model output with a symmetrical binary ε_r distribution with the same mean ε_r as an equivalent uniform distribution. The only arrangement that meets this criterion for a PTL, as pointed out by Knight et al. (1992), is a binary distribution where the separation plane is the *x-z* plane through the centre of both PTL rods. Knight et al. (1992), pointed out that there is no energy exchange between the two half spaces intersecting the axis through the centres of the rods of a PTL. Hence, provided ε_r in each half space is homogeneous, the equivalent ε_r of the PTL is the mean of the half plane values. The same values as Knight et al. (1992) were used, namely half-plane ε_r of 5 and 15 were compared with those of 10 and 10. The forward model used a pseudo 3-D MM, a transverse plane of 20 by 20 cells, $b = 8$ cells, and $a = 1$ cell. This arrangement provided a good compromise between the size of the model (total number of cells), rod size and spacing, and the distance from a rod to the boundary of the modelled region to ensure insignificant contribution to calculated v_p by the boundary cells. Table 3.4 shows the results from the verifications, which gave a 0.55 % error in v_p between the two ε_r distributions. The absolute error (first verification method) between the calculated v_p and the expected $c/\sqrt{10}$ m/s was 0.8 % for the course integration method used. Note that for the relatively large number of cells used, and the undistorted field distribution, the coarse integration method was appropriate.

Table 3.4 Self-consistency of the forward model.

ε_r **in half space 1**	ε_r **in half space 2**	**Expected** v_p **(m/s)**	**Model output (m/s)**
10-j0	10-j0	0.9487×10^8	0.9563×10^8
5-j0	15-j0	0.9487×10^8	0.9616×10^8

3.12 Concluding Remarks

In this chapter, a MM solution for the electric field in a heterogeneous, low loss dielectric (Harrington, 1968) has been adapted to provide rapid determination of v_p on a PTL, and several aspects of the solution method, including stability and field integration, have been investigated. The approach has been validated by comparison with known solutions, and comparison with measured data will be described in §6.1 to §6.4.

An initial assumption of the approach was that the dielectric material is isotropic and lossless. Materials with anisotropic ε_r in the transverse plane could be modelled by a procedure that calculates a provisional solution using the method described here, and then progressively refines it based on the field direction provided by the model output. Conceivably, lossy materials could be modelled by superimposing on the calculated polarization field, the imaginary components due to loss-related current filaments in a manner related to the approach of Xiong et al. (1995). They separately calculated the real and imaginary components for plane wave excitation of the earth, to improve geophysical modelling with high conductivity contrasts. However, resolution of both the above assumptions is beyond the scope of this work.

Chapter 4

A Solution to the Inverse Problem

The solution to the forward problem derived in Chapter 3 provides a prediction of the propagation velocity (v_p) on a parallel transmission line (PTL) surrounded by a prescribed, discretised, inhomogeneous distribution of relative permittivity (ε_r). We now turn to formulation of the inverse problem, which has the aim of quantifying the ε_r distribution given a set of v_p representing different physical positions of the PTL.

4.1 Overview

Although the forward solution is quite general and allows any physical arrangement of the PTL and ε_r distribution, practical constraints dictate that in this case the inverse solution should be constrained since the purpose of time domain reflectometry imaging (TDRI) is non-invasive probing of the interior of materials to determine the distribution of volumetric moisture content (θ_v). Hence, the PTL remains outside the physical body with the unknown ε_r distribution (Fig 4.1).

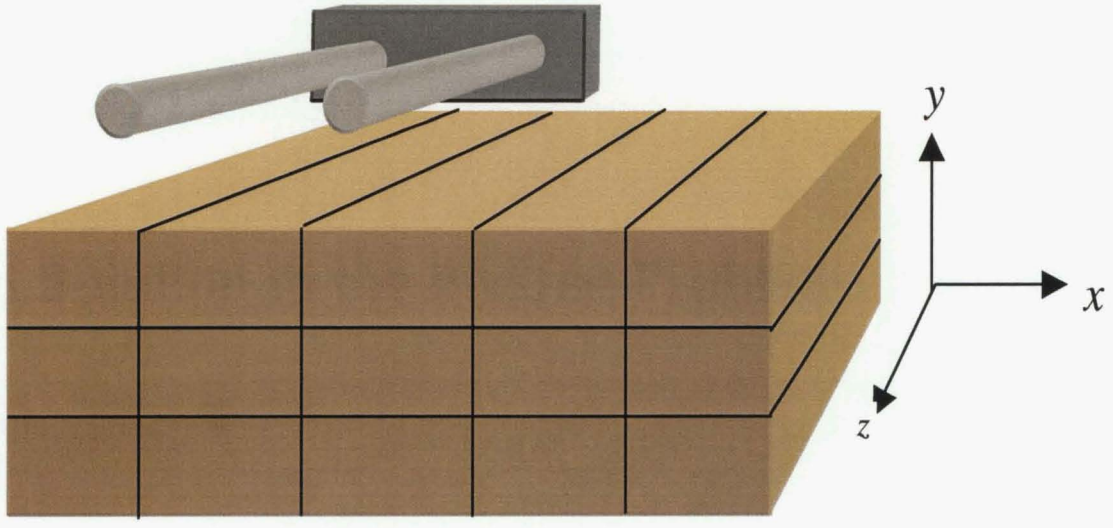

Figure 4.1 Physical arrangement of the PTL.

In §2.4, a review was given of appropriate methodologies and techniques for solving inverse problems related to quantitative imaging of electrical data. The outcome of the review was that iterative conjugate gradient (CG) optimisation would be appropriate and that the electric field

strength could form a useful surrogate for the Jacobian. Further, *a priori* data should be included through a suitable regularisation process to assist the resolution of under-determined problems. It was also noted that quantifying the moments of a probability distribution function (PDF) describing the solution errors would be useful for ascribing confidence levels to a solution.

A procedure for the inverse solution as presented in §2.4.4 is:

1. Select an objective function and stopping criterion to indicate completion
2. Choose an appropriate method for updating the solution
3. Select an initial solution set, such as *a priori* information
4. Solve the forward problem to calculate a trial data set (propagation times in this instance)
5. Calculate the objective function and exit if the stopping criterion has been met
6. Compute a search direction and step length
7. Update the provisional solution
8. Loop to Step 4.

In the solution method described in this chapter, CG optimisation is used with the Rabiere Polak direction vector (§2.4.7) and an electric field strength surrogate for the Jacobian. Several aspects are then refined to improve the inversion procedure. These include:

- A generalised format for the software to allow straightforward configuration of the procedure to suit both the problem and incorporation of *a priori* data
- A rapidly-calculated substitute for the CG line search
- A blocking method for speeding the convergence of buried cells
- A procedure that both quantifies the expected illposedness of the problem and provides direction to selecting additional data that could be obtained to improve the accuracy and specificity of the solution.

Details of experimental work are provided in §6.5, but here we detail the inverse method, the software, and results obtained using simulation. The simulations are enabled by choosing a ε_r distribution and set of PTL positions, and using the forward solution to produce a set of simulated data. Then the solution to the inverse problem is calculated using the simulated data, allowing comparison with the chosen ε_r distribution. Completion of the TDRI methodology uses a dielectric model to convert the calculated ε_r in each cell to θ_v. The dielectric model is in principle fully invertible so that a direct analytic relation exists between model inputs and outputs. Hence it does not limit the performance of the inversion, so will not be included in the simulations described here. Instead it will be described in Chapter 5.

4.2 Distributions describing errors

In order to apply a PDF to the solution of the inverse problem it is necessary to know the PDF's of two components: the transfer function g, and that of the measured data d. Here we focus just

on the PDF of g, since in the simulations, we may consider the data as 'perfect' even though they are derived using the forward solution. A difficulty in specifying the errors in g is that the forward problem is inexact, so that error estimates must inevitably rely on a combination of analysis, the results of validation through self-consistency (as in §3.11), and comparison with experimental results which are described in §6.2 and §6.2.

It was shown in §2.5.4 that a regularised objective function that incorporated weighting of data elements could take the form:

$$S = \frac{1}{1+\lambda}\left[(g(m)-d)' C_d^{-1}(g(m)-d) + \lambda(m-m_{prior})' C_m^{-1}(m-m_{prior})\right] \qquad (4.1)$$

where λ is the regularisation parameter, (m - m_{prior}) the distance between the first estimate or prior data vector m_{prior} and the current solution m, C_d the covariance of the data and C_m the covariance of m_{prior}. C_d and C_m are diagonal matrices with the data variances σ^2 on the diagonal. Where the PDF's describing d and m are non-Gaussian the situation is not clear-cut. Tarantola (1987) generalises the Gaussian distribution to arbitrary order so that a second order Gaussian is the normal distribution, and a Gaussian of order ∞ is the boxcar distribution. While the generalisation of the Gaussian allows for long-tailed distributions (order < 2), it doesn't accommodate skewed distributions, although supposedly this could be achieved by further generalisation incorporating a bi-modal order which differs depending on the sign of the deviation from the mean, $x-\mu$.

For TDRI, the forward problem may be described by $d = g(m)$, but there are two transformation processes g between the model space and the data space:

$$[\varepsilon] \rightarrow \textit{instrumentation} \rightarrow \textit{observations } (d_{obs}) \qquad (4.2)$$

$$[\varepsilon] \rightarrow \textit{forward model} \rightarrow \textit{predictions } (d) \qquad (4.3)$$

ε_r will subsequently be related to θ_v distribution via a dielectric model. In practice, we do not have perfect knowledge of the true transfer function, but just one estimate by the instrumentation as revealed through d_{obs}, and another by application of the forward model and revealed by the predicted data set d. Nonetheless, we only need to be concerned about the correspondence between the observations and the predictions since the intent of the inversion process is to alter [ε] until $d - d_{obs}$ is zero (or sufficiently small). Hence, the only contribution to a PDF describing the final model [ε] arises from the differences between the two transfer functions, coupled with the accepted error in $d - d_{obs}$ when iteration is complete. A further component that may be included is the intentional PDF from the regularisation process.

We conclude therefore that a PDF describing both instrumentation and forward model errors could be achieved by a sampling process. It is apparent that the distribution will be non-normal since many of the sources of error cannot be ascribed to a Gaussian distribution. Examples of error sources are:

- The forward model errors increase as the PTL nears the material under investigation and hence the field gradient becomes large
- Errors due to pseudo 3-D modelling that are expected to be dependent on the contrast within the θ_v distribution, transverse to the PTL
- The MM solution method errors increase as θ_v contrast increases
- Integration errors increase as the electric field gradient increases
- Timebase errors in the measuring equipment are at least partly Gaussian (§2.4.1) but a resultant *x-t* measurement is also likely to be influenced by fixed, non-random effects
- Determination of the travel time by a smoothing and slope-detection method (§6.1) will be influenced by discretisation (which may be approximated by Gaussian distribution) and errors in slope detection
- The isolation between the unbalanced and balanced sections of the measuring system, as provided by the balun, is imperfect and provides systematic differences between the influences by θ_v on each PTL rod
- Errors due to discretisation of the material under investigation, and measurement errors, could be described by Gaussian distributions.

Thus while some errors are random, others are fixed or systenatic errors that will depend on both the θ_v distribution and the PTL position. Consequently, a mixed model that defines the PDF of Δ (which describes the difference between the measured propagation times and those from the model) could take the form:

$$\Delta = \mu + \alpha(\theta) + \beta(r) + \gamma \tag{4.4}$$

where μ is the mean difference between the two readings, α the component that is a function of the θ_v distribution, β a PTL position-dependent error, and γ a random variable that explains the remaining errors that are assumed to be normally distributed. Both α and β are functions with more than one dimension, so that a large number of combinations of their variables exist. It is important when determining the moments of the α and β dependencies, that a systematic sampling process is used lest the central limit principle erroneously points towards normal distributions.

4.3 Determination of the Jacobian

The Jacobian or sensitivity matrix has elements, which in this instance describe the change in v_p due to a change in ε_r within a particular cell, and for a particular position of the PTL. Thus, the rows could represent changes in ε_r distribution, and the columns changes in PTL position, and provide a set of vectors that provide a distance and heading to the next solution iterate, but not the solution itself. The magnitude of the Jacobian elements provides a measure of the influence of a model parameter on the solution. For this class of non-linear solution methods, the Jacobian elements point towards the solution but assume linearity around the current solution estimate. In this instance, the Jacobian is defined as:

$$J = \begin{bmatrix} \frac{\partial t_{p_1}}{\partial \varepsilon_{r_1}} & \cdots & \frac{\partial t_{p_1}}{\partial \varepsilon_{r_n}} \\ \vdots & \ddots & \vdots \\ \frac{\partial t_{p_m}}{\partial \varepsilon_{r_1}} & \cdots & \frac{\partial t_{p_m}}{\partial \varepsilon_{r_n}} \end{bmatrix} \tag{4.5}$$

A finite difference (FD) method is typically used for the calculation of J, but forms the most computationally intensive step of the inversion process, since it requires a forward solution for each of the above nm approximations to the partial derivatives. As discussed in §2.4.8, approximations to the Jacobian may be employed since at least in the first instance, the accuracy of the sensitivity matrix affects just the convergence and not the target or solution. A new linear approximation to the Jacobian is now described. It combines the electric field and ε_r to form a Jacobian that suits this TDRI problem. It differs from approximations described by Farquharson and Oldenburg (1995) for example, who derived a Jacobian providing $\partial \boldsymbol{E}/\partial\sigma$, the rate of change of field strength with conductivity. Here, $\partial t/\partial \varepsilon_r$ is formed, directly indicating the rate of change of travel time with ε_r.

Knight (1992) showed that the sensitivity of v_p on a PTL to the properties of a small region, is a function of the stored energy of the electric field in that region. Prior to describing use of the surrogate, we briefly review the connection between sensitivity and field strength, and then compare the surrogate with the FD method using the forward model.

From Ramo et al. (1993), it is shown that the energy in an electric field surrounding a charged body can be derived from the work done to emplace the charge distribution. Thus

$$U = \frac{1}{2}\iiint \rho\phi \, d\tau \tag{4.6}$$

where ρ is the charge density, ϕ the electric potential, and $d\tau$ the volume over which the energy is to be calculated. By applying vector equivalence, the differential form of Gauss's law $\rho = \mathrm{div}(\boldsymbol{D}) = \nabla \cdot \boldsymbol{D}$, and

$$\nabla \cdot (\phi \boldsymbol{D}) = \phi \nabla \cdot \boldsymbol{D} + \boldsymbol{D} \cdot \nabla\phi \tag{4.7}$$

it can be shown (Ramo et al., 1993) that

$$U = \frac{1}{2}\iiint \nabla \cdot (\phi D) d\tau - \frac{1}{2}\iiint D \cdot (\nabla\phi) d\tau \tag{4.8}$$

and using the divergence theorem:

$$U = \frac{1}{2}\iint \phi \boldsymbol{D} \cdot d\boldsymbol{s} - \frac{1}{2}\iiint \boldsymbol{D} \cdot (\nabla \phi)\, d\tau \tag{4.9}$$

The first term approaches zero as the domain of the problem gets large (ie as argued by Ramo et al. (1993), D falls off at least as fast as $1/r^2$), and since $\nabla\phi = -\boldsymbol{E}$ and $\boldsymbol{D} = \varepsilon \boldsymbol{E}$:

$$U = \frac{1}{2}\varepsilon \iiint |E|^2 d\tau \tag{4.10}$$

and applying to a cell of the MM method using pulse basis functions where the field is considered uniform inside the cell:

$$U = \frac{1}{2}\varepsilon |E|^2 \tau \tag{4.11}$$

where τ is the volume of the cell. From the direct relationship between the field strength and energy, Eqn (4.11) can be used as the basis of an approximation to the true sensitivity matrix. However, the sensitivity is also dependent on the dimensionality of the problem. Hence to eliminate dimensional dependency, volume compensation in the form of cell area A and length of the PTL l could be included. When applied to the forward solution method described earlier the approximation J_a to the true Jacobian J is:

$$J_a = \left[k\varepsilon_i |\boldsymbol{E}|_i^2 lA \right]_{i=1..n} \tag{4.12}$$

where k is a scalar introduced to scale each $J_{a\,i}$ to closely match the expected value of each J_i. ε_i and E_i are respectively ε_r and the magnitude of the electric field within the ith discretised zone, l is the length of the PTL, A the cross-sectional area of the cuboid cells, and n the total number of discretised zones in the unknown ε_r distribution. The cuboid cells have the same cross-sectional area as the discretised zones or cells from the forward solution.

Next a comparison was made between Jacobian elements determined by a FD method, and those using the square of the local electric field strength as a surrogate. The procedure for the FD method was to perturb ε_r in a cell, and then use the forward model to calculate the impact on propagation time. The perturbation comprised individually adding $\varepsilon_r = 1$ to the existing $\varepsilon_r = 10$ of cells 1 and 12 (shown shaded in the model of Table 4.1 where the anomalous region is defined in the model by non-zero cells). The PTL positions used for the comparison covered the unperturbed cells above the anomalous region, and comprised nine positions with rod spacing of three cells, and four positions with rod spacing of four cells.

Table 4.1 Model test body with anomalous region (non-zero entries represent ε_r) for evaluating J'acobian surrogate.

0	0	0	0	0	0
0	0	0	0	0	0
0	0	0	0	0	0
0	10	10	10	10	0
0	10	10	10	10	0
0	10	10	10	10	0

The results of the comparison are shown in Table 4.2. Each entry in the 'FD method' row is the ratio of the difference between the perturbed and unperturbed travel times, and each entry in the 'surrogate' row is the ratio of the square of the electric field strengths. Tables 4.2 and 4.3 demonstrate the inconsistent discrepancy between the FD and surrogate methods. The mean discrepancy is of little concern.

Table 4.2 Comparison of Jacobian surrogate with FD method, and perturbing cells 1 and 12 (as shown in Table 4.1) by $\Delta\varepsilon_r = 1$.

Position (x,y)	1,1	1,2	1,3	2,1	2,2	2,3	3,1	3,2	3,3	1,2	2,2	1,3	2,3
FD method	18.4	10.6	4.6	40.1	12.0	2.8	347	14.0	0.39	16.4	8.2	24.8	10.6
Surrogate	13.2	8.6	4.2	23.5	10.7	3.4	82.2	12.8	1.1	12.0	7.9	11.1	13.8
Discrepancy (%)	28	18	9	41	10	-21	76	8	-193	27	4	55	-30

Table 4.3 Comparison of Jacobian surrogate with FD method, and perturbing cells 1 and 9 by $\Delta\varepsilon_r = 1$.

Position (x,y)	1,1	1,2	1,3	2,1	2,2	2,3	3,1	3,2	3,3	1,2	2,2	1,3	2,3
FD method	8.4	5.5	2.9	13.6	6.0	1.9	29.0	7.1	0.29	8.2	4.7	13.9	6.2
Surrogate	6.2	4.7	2.8	9.3	5.7	2.3	11.8	8.1	0.76	6.4	4.7	7.8	8.0
Discrepancy (%)	26	14	3	32	5	-23	59	-15	-158	22	0	44	-29

The discrepancy between the exact travel time using the FD method with the model (ignoring errors in the forward model) and that from the surrogate, is position dependent. The largest discrepancy occurs at position (3,3) where in Table 4.2 the surface cell lies far from the centre region of the PTL. In this case, the buried cell has a greater influence than the surface cell, but

this is not recognised by the surrogate method. The contention by Knight (1992) that the sensitivity of TDR is determined by the energy density of the field, and thereby the square of the field strength, was stated as being dependent on a nearly uniform ε_r distribution, as required for Eqn (4.11). The dependency also relied on the assumption of conformity to Laplace's equation. Hence, the comparison was repeated with $\varepsilon_r = 1.1$ in the anomalous region, and a perturbation of $\varepsilon_r = 0.1$ (Table 4.5). However, since the smaller step size could be expected to result in a different FD accuracy, another comparison was made with $\varepsilon_r = 10$ in the anomalous region, and a perturbation of $\varepsilon_r = 0.1$, to ensure a valid comparison with the smaller base ε_r (Table 4.4). It is apparent that there is a greatly improved consistency between the FD and surrogate methods when the ε_r contrast (between the anomalous region and the surrounding $\varepsilon_r = 1$) is reduced, leading to the conclusion that problem linearity has a strong influence on the accuracy of the surrogate method.

Table 4.4 Jacobian surrogate comparison using cells 1 and 12 with reduced perturbation of $\Delta\varepsilon_r = 0.1$.

Position (x,y)	1,1	1,2	1,3	2,1	2,2	2,3	3,1	3,2	3,3	1,2	2,2	1,3	2,3
FD method	18.0	10.9	4.7	37.3	12.6	3.1	217	14.9	0.55	16.7	8.6	25.3	11.3
Surrogate	13.2	8.8	4.2	22.9	11.2	3.6	66.2	14.3	1.3	12.3	8.1	12.1	14.3
Discrepancy	27	19	10	39	11	-16	70	4	-144	26	6	52	-27

Table 4.5 Jacobian surrogate comparison using cells 1 and 12 with perturbation of $\Delta\varepsilon_r = 0.1$, and reduced contrast of $\varepsilon_r = 0.1$.

Position (x,y)	1,1	1,2	1,3	2,1	2,2	2,3	3,1	3,2	3,3	1,2	2,2	1,3	2,3
FD method	11.6	7.5	4.2	21.0	10.7	4.3	52.0	17.3	3.7	11.9	7.2	20.8	10.9
Surrogate	8.4	5.5	3.1	13.8	8.0	3.4	25.4	16.4	3.7	8.1	5.5	11.5	10.9
Discrepancy	28	27	25	34	25	20	51	5.5	0.9	31	23	45	0.2

Hence we may conclude that for a nearly uniform ε_r distribution, the field energy forms a reasonably accurate surrogate for the Jacobian. Larger discrepancies exist for greater ε_r contrasts but as discussed in §2.4.8, this may be of lesser importance for nonlinear problems that require an iterative solution method.

4.3.1 Use of the surrogate

The value of k in Eqn (4.12) may be determined by calculating a Jacobian element using the more conventional FD calculation that provides a correctly scaled approximation to each partial derivative. Thus for some convenient term i,

$$k = \frac{\dfrac{\partial t_{p_i}}{\partial \varepsilon_{r_i}}}{\varepsilon_i \left|E\right|_i^2 lA} \tag{4.13}$$

and using a FD approximation to the Jacobian element $\dfrac{\partial t_{p_i}}{\partial \varepsilon_{r_i}}$,

$$k = \frac{G(\varepsilon_{r_i}) - G(\varepsilon_{r_i} + \delta)}{\varepsilon_{r_i} \left|E\right|_i^2 lA\delta} \tag{4.14}$$

where δ is a suitably small step in the value of ε, and G is the forward model. Combining Eqns (4.12) and (4.14) provides a surrogate J_a for the true Jacobian:

$$J_a = \left[\frac{G(\varepsilon_{i=0}) - G(\varepsilon_{i=0} + \delta)}{\varepsilon_{i=0} \left|E\right|_{i=0}^2 \delta} \varepsilon_{r_i} \left|E\right|_i^2 \right]_{i=1..n} \tag{4.15}$$

While the use of Eqn (4.15) provides a correctly scaled Jacobian element for the chosen term ε_{r_i}, the variation apparent from Table 4.2 results in uncertainty of the sensitivity. However it will become apparent that accurately determining a mean value for k is unnecessary since during the inversion process, the line search algorithm in the CG method will dynamically weight the Jacobian. Hence it is most expedient to avoid scaling the surrogate Jacobian and just use $\left|E\right|^2 \varepsilon_r$.

4.4 Execution of the inverse solution simulation

Much of the refinement of the inversion algorithm and the parameter testing used simulated data sets, in turn using a model ε_r distribution as the starting point. The model output was a ε_r distribution that ideally should match the initial model. Explanation of the development, testing and application of a dielectric model to the inverse solution is described in Chapter 5.

An essential component of the simulation is size consistency within all data structures used by the simulation. The initial process requires assigning the variables, and choosing a solution that will then be used to generate the simulated observation set using the forward solution. The initialisation procedure is:

1. Edit the initialisation routine, 'setup.m', to set parameters that control both the dimensionality of the problem, and inversion. Details are provided in Listing 2.
2. Run the program 'unpertrb.m' (Listing 3) to generate and save the L matrix on disc. This step is only necessary if the number of cells has changed since the previous run.
3. Edit 'mprior.dat' which is a structural representation of the problem. Cells in the unperturbed zone should be set to zero, and perturbed cells set to the *a priori* value of ε_r

for this ε_r-based inversion (which doesn't include the dielectric model). The top left cell is allocated the address (1,1).

4. Edit 'model.dat' to form a physical representation of the problem that includes target values of ε_r. This file is used to generate the simulated set of observations of travel time.
5. Edit 'readings.dat'. The data in the columns is respectively: rod1x, rod1y, rod2x, rod2y, and travel time, where the rod positions are defined by their location at cell centres. Simulations demand the existence of the travel time column, but its contents are immaterial. Unused rows must be deleted.
6. The final step is to execute 'make_t.m' (Listing 4) to overwrite any existing travel time data in 'readings.dat'. This step uses the forward solution method to generate simulated observations from the model distribution and the specified PTL rod positions.

After the model and *a priori* data files are loaded by the program, they are rotated to conform to the internal representation that the first array index x represents rows, and the second index y represents columns. The Matlab (The Mathworks Inc.) plotting routines that are used to show distributions require exchange of x and y (eg 'quiver (Ex, Ey)') to correctly represent the above convention, although the result will still be a (left) rotated representation.

The use of the quasi 3-D approach to speed up calculation of the forward solution was described in §3.7. However, one characteristic of the MM method that has been exploited to greatly speed up execution of the inverse solution is that the scattering matrix contains mathematical representations of the interactions between the field in each cell of the dicretised region of interest, but is quite independent of the strength and distribution of the impressed field. Hence the time-consuming effort in calculating the scattering matrix is expended just once for each iteration of the inverse solution. This contrasts with a DE method such as FD, where a complete forward calculation would be required for each position of the PTL, representing perhaps 20 or 30 forward calculations for every iteration of the inverse solution. Thus while IE methods are arguably more expensive than DE methods for a forward solve, once applied to tomographic inversion, the IE method is much faster. For example the MM method (§3.5) results in a vector of polarisation components $\boldsymbol{P}$ described by:

$$\mathbf{K}\boldsymbol{P} = \boldsymbol{E}_i \tag{4.16}$$

where $\mathbf{K}$ is the scattering matrix and $\boldsymbol{E}_i$ a vector of impressed field components. Hence,

$$\boldsymbol{P} = \mathbf{K}^{-1}\boldsymbol{E}_i \tag{4.17}$$

Then with the MM method, $\mathbf{K}^{-1}$ can be calculated for a particular set of model parameters and then a rapid matrix multiplication is used to determine $\boldsymbol{P}$ for each $\boldsymbol{E}_i$ that is defined by a PTL position.

A further significant time saving may be realised for the entire inversion process since the only elements of the scattering matrix that are dependent on the ε_r model parameter that is altered with each iteration, are those that lie on the main diagonal. Hence for a fixed geometry or

number and distribution of cells, the scattering matrix only needs to be calculated once. In practice, since the scattering matrix is symmetrical about both diagonals, only one quarter of the matrix needs to be calculated. The following pseudo code procedure was implemented for handling the scattering matrix in the inversion process:

- Retrieve stored scattering matrix K from disk
- For each iteration:
  - Recalculate main diagonal using current model
  - Calculate $\mathbf{L}$, the inverse of scattering matrix $\mathbf{K}$
  - For each PTL position:
    - Calculate $\boldsymbol{P} = \mathbf{L}\boldsymbol{E}_i$
    - End
  - End
- End

The above method provided a rapid inversion algorithm with minimal manipulation of the scattering matrix. For a 12 by 12 cell model, inversion of the scattering matrix took 6.98 s (Pentium 120) and multiplication 0.06 s. Conversely, back substitution took 0.93 s. Hence for the 12 by 12 model (used for inversion of measured data in §6.6), it is more rapid to use inversion of the scattering matrix than back substitution, when more than 8 PTL positions (and hence field distributions) are used.

4.5 Optimisation procedure

It was reported in §2.4.7 that a Quasi-Newton or CG method was most appropriate for updating the solution of the TDRI non-linear inverse problem. Early in development of the inverse solution method, a damped steepest descent approach was used while developing particular software modules. After the methodology was developed, the procedure was generalised and a CG method was formulated using the Polak-Ribière distance to the next iterate. However a disadvantage of the CG and quasi-Newton methods is that while the number of CG iterations may be quite small, the methods rely on a line search to determine the local minimum in the current direction. Where a FD method is used for construction of the Jacobian, and the problems are large, this is not a significant drawback, since one Jacobian suffices for each CG iteration incorporating the line search. Consider for example a modest 10 by 10 2-D inversion. Calculation of the Jacobian requires 100 forward calculations which should greatly exceed the number required for even a robust (but slow) line search. However for smaller problems such as will be typical with TDRI, and where a rapid Jacobian surrogate is used, the line search is a significant overhead. The line search requires a forward solution for each iteration, so may be just as expensive as slower methods that avoid 'minimisations within minimisations'.

All initial testing of the inversion procedure used simulation and avoided use of a dielectric model, instead working directly with values of ε_r. After initialisation, the inversion procedure (Listing 5) loads matrices representing the target ε_r distribution and the PTL positions, and

then uses the forward solution to calculate a simulated set of readings. The procedure then inverts the forward solution using the simulated observations, to provide a solution that ideally should match the initial ε_r distribution.

The key parameter in the CG method is the weighting factor α in the CG recurrence relation:

$$m_{i+1} = m_i - \alpha_i J_i \Delta t_i \tag{4.18}$$

where the new model m_{i+1} is derived from the previous ε_r model, corrected by the weighted product of the Jacobian J_i from the previous forward modelling, and the error in propagation time Δt_i. The magnitude of α_i controls the step size and its optimal value is dependent on the local curvature in the response function g of the forward model, the accuracy of J_i, and the distance to the solution. As with many optimisation methods, this is ideally determined dynamically, and is typically determined using a line minimisation procedure (Press et al., 1992, Tarantola, 1987, Zhdanov, 1993). Figure 4.2 maps the characteristics of the line minimisations for the first five iterations of the CG method of Listing 5. The first two or three CG iterations exhibit changes in the objective function of several orders of magnitude, and the position of each minimum is quite variable, ranging from CG weighting factor $\alpha_i = 0$ for the case where no further improvement is possible with the current heading, to $\alpha_i > 30$ for the third line minimisation. In later iterations the minimum frequently occurs at $\alpha_i = 0$ and is the result of some linear combination of CG headings that have already been explored and minimised.

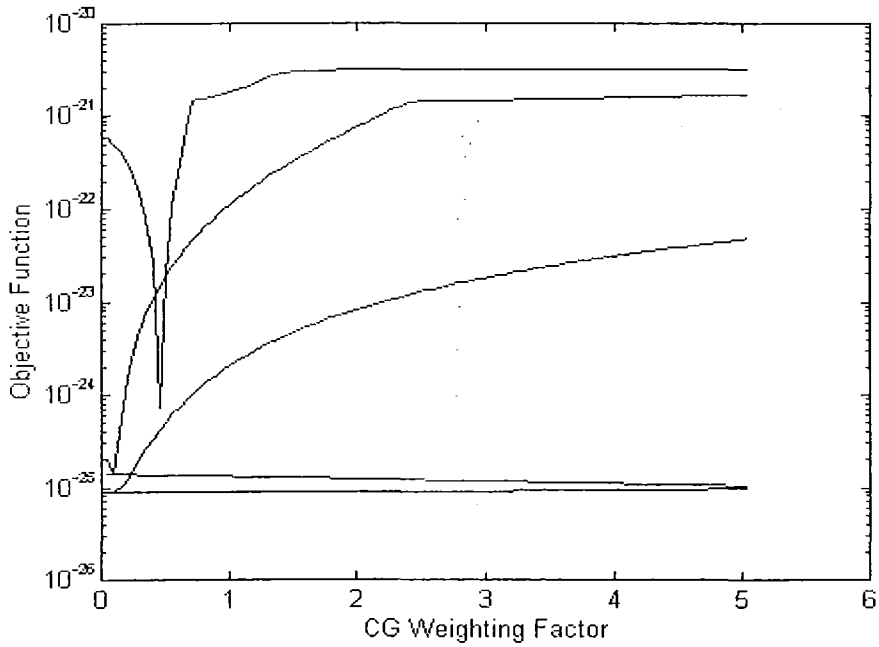

Figure 4.2 Line minimisations for the first 5 iterations of a CG inversion algorithm.

There are numerous procedures for line minimisations, and Press et al. (1992) recommend initially bracketing a minimum, and then using either gradient methods or Brent's method that uses either or both parabolic interpolation and golden section search. However in this case just a golden section method was used since the initial deep minima are insufficiently parabola-like to warrant the alternative parabola fitting that ideally detects the minimum in just one or two iterations. Later CG iterations are relatively efficient using the golden section searches, although derivative methods may be more rapid. A particular consideration is that the minimum for some search directions may occur at zero, so a trap in the initial bracketing procedure is required to detect this condition. Although the golden section minimisation method followed that of Press et al. (1992), a rapid bracketing method was used that chose as outer brackets, values of $\alpha_i = 0$ and $\alpha_i = 50$. Then beginning from $\alpha_i = 50$, α_i was progressively reduced by a factor of 50 until a bracketed value of objective function was obtained that was less than that of the outer brackets. Typically, three or four forward calculations were sufficient to provide the three bracketing values. Press et al. (1992) advise using a tolerance, or value of the error that forms the stopping criterion used in the minimisation, of $\sqrt{eps}$ where *eps* is the floating point accuracy, defined as the distance from 1.0 to the next largest floating point number. Here, a relaxed tolerance of $10^5\sqrt{eps}$ was used since it sped up the search process, and recognised the relatively flat minima that typify the objective function characteristics. This resulted in negligible effect on convergence provided the tolerance factor was no greater than 10^5, and gave a maximum distance between the actual minimum and the relaxed minimum of one part in 10^6. A rapid alternative to the use of line searches is described in §4.7.

For TDRI, prior knowledge of the distribution allows bounding ε_r or θ_v values to be included in the solution method. These were incorporated by scanning the model at each iteration, and substituting any model parameter outside the boundary, with the boundary value. This constraint made no judgement on the likelihood of a model parameter being on or near the boundary, just that it may not be outside.

4.6 Convergence

A standardised inversion method was chosen to compare inversion schemes and inversion parameters. The chosen target distribution (Table 4.6) exhibited several characteristics that were considered most appropriate for the comparisons:

- It is small (just 4 by 3 elements in the anomalous region) so that convergence and hence evaluation was rapid (approximately 0.3 seconds per forward calculation). The distribution nevertheless represents a useful spatial resolution for the distribution of θ_v in timber for example.
- The target distribution mirrors typical real-life situations where the internal θ_v distribution of a material is being measured during or after drying. The block could represent eg timber or a sample of soil, where there is a wet layer overlaid by a dry layer.

- The distribution is inherently problematic to a sub-surface inversion process since the higher ε_r layer is sandwiched between lower ε_r layers. In particular, the lowest layer is shielded to some extent by the high ε_r layer that reduces the field strength and hence influence of the lowest layer.
- The flat, initial or *a priori* distribution does not provide a starting point that assists inversion. Indeed ε_r of the lowest layer that has least influence on the PTL readings, must change by the same amount as the most influential top layer.
- The initial tendency is for the centre cells to converge more rapidly than the side bounding cells since they are always nearer the centre of the PTL rod positions and hence have a greater influence. The result is that in the first one or two iterations when all cells either increase or decrease in ε_r to reduce the mean error in propagation time, there is a tendency for some cell values to either overshoot the target (eg the highly influential surface cells), or to move in the wrong direction (the centre cells move to a smaller ε_r than their adjacent cells on the same layer, and against the required direction for the chosen target ε_r distribution).

Consequently, these characteristics provided a realistic set of conditions that proved difficult to invert compared with many other sets of conditions, and hence was useful for refining, evaluating and comparing inversion performance.

Table 4.6 *A priori* and target ε_r distributions for inversion comparisons.

1	1	1	1	1	1		1	1	1	1	1	1
1	1	1	1	1	1		1	1	1	1	1	1
1	1	1	1	1	1		1	1	1	1	1	1
1	10	10	10	10	1		1	5	5	5	5	1
1	10	10	10	10	1		1	5	10	10	5	1
1	10	10	10	10	1		1	5	5	5	5	1

The set of readings used for the comparisons is detailed in Table 4.7 where (x1, y1) and (x2, y2) are the coordinates of the two PTL rods, and the travel time reading was obtained by forward calculations using the target distribution of Table 4.6. The rod positions have been chosen to coincide with the centre of each cell since this assists both symmetry of the problem and visualisation through the plots of the results. However, this approach has precluded positioning the PTL rods in the row $y = 3$ since the very large field gradients around the cells in contact with the PTL rods caused sufficiently large errors in the Jacobian surrogate so that convergence failed. Hence for practical use of the inversion procedure, the PTL rods could alternatively be aligned with cell intersections.

Table 4.7 PTL positions used for inversion comparisons. x and y are cell positions from the top left of the discretised region.

x1	y1	x2	y2	Travel time (sec)
1	1	3	1	2.3046E-09
2	1	4	1	2.3078E-09
3	1	5	1	2.3078E-09
4	1	6	1	2.3046E-09
1	2	3	2	2.3262E-09
2	2	4	2	2.3417E-09
3	2	5	2	2.3417E-09
4	2	6	2	2.3262E-09
1	1	5	1	2.1478E-09
2	1	6	1	2.1478E-09
1	2	5	2	2.2028E-09
2	2	6	2	2.2028E-09

While there are the same number of readings as there are unknowns, the data in Table 4.7 do not adequately define a path that directs an inversion process to one unique solution (§2.4.1). Instead several different ε_r distributions provide a set of readings that nearly match the observed set. This aspect will be resolved later using more realistic *a priori* data, but here the performance of several inversion schemes will be compared using the ill-posed data.

The result of the CG inversion of simulated data using the readings in Table 4.7 is shown in Figure 4.3. Note that the representation of ε_r distribution by Figure 4.3 and subsequent figures employs the convention that a cell centroid and hence the ε_r of a cell is represented by a grid-intersection point. This means that the anomalous region of Mprior (the *a priori* distribution) in Figure 4.3 appears as a three by two set of cells whereas it is actually four by three. Returning to the CG convergence depicted in Figure 4.3, it is expected (Press et al., 1992) that the procedure should have converged to the solution in around 12 CG iterations, ie the number of unknowns. In this case, the procedure was halted after 16 CG iterations that included 885 forward calculations, so that each line search typically used 55 forward calculations. The performance of the CG method with this target, *a priori* distribution and set of readings is poor, as indicated by the solution in Table 4.8 and the objective function of 2.3×10^{-25}. Continuing the procedure provided no further significant change to the solution or the objective function. Indeed, almost all convergence took place within the first CG iteration, since the *a priori* distribution itself yields an objective function greater than 1×10^{-20}, and not indicated in Figure 4.3.

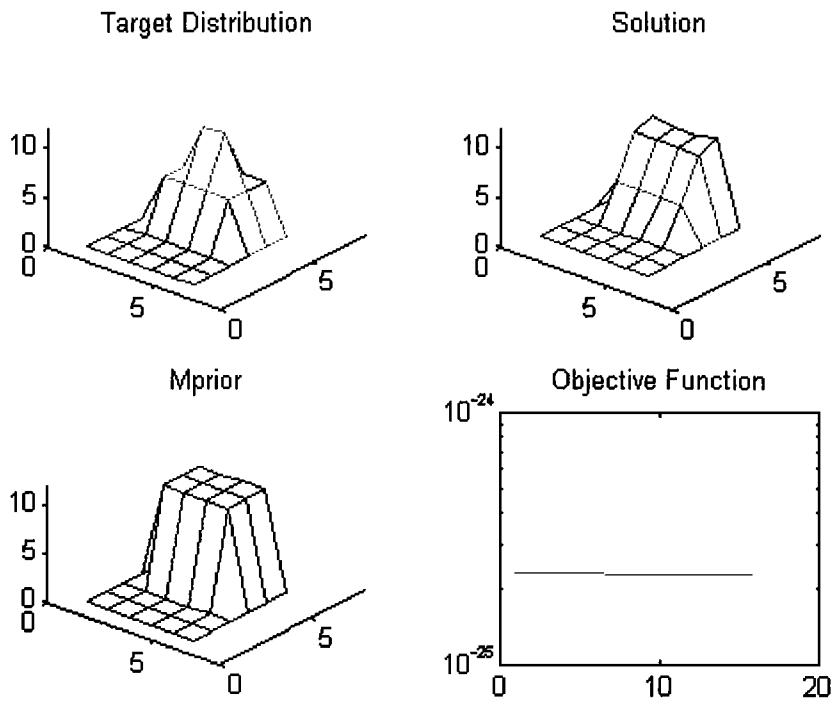

Figure 4.3 CG inversion using an electric field surrogate for the Jacobian ($|\boldsymbol{E}|^2 \varepsilon_r$).

Table 4.8 Solution of CG inversion using an electric field surrogate for the Jacobian (compare with target distribution of Table 4.6).

1	1	1	1	1	1
1	1	1	1	1	1
1	1	1	1	1	1
1	4.5	4.5	4.5	4.5	1
1	8.6	8.6	8.6	8.6	1
1	9.4	9.0	9.0	9.0	1

Once the surrogate Jacobian was applied to the CG method, it became apparent that buried cells were experiencing very slow convergence, although that of surface cells was quite satisfactory. This was not a result of errors in the Jacobian, but rather a peculiarity of the physical arrangement of the problem whereby buried cells have a very small influence on the measured travel time.

The Jacobian or sensitivity matrix describes the rate of change of v_p resulting from a change in ε_r of a cell. In the inversion process, the rate of change of ε_r of a cell during a particular iteration, is proportional to the magnitude of its respective element in the Jacobian. Since the elements of the Jacobian are directly proportional to the square of the electric field strength, a cell will have less influence on v_p the further it is from the PTL, resulting in a slower, perhaps

much slower, convergence rate. There are further influences that will result in slow convergence of surface cells, and these relate strongly to the resolving power of the individual PTL positions, their zones of influence, and the resulting discrimination of the ε_r of individual cells.

The use of a 'flatter' Jacobian than the surrogate described earlier would give greater weight to the buried cells that otherwise get only a small score at update time, and hence converge only slowly. Consequently, $|\boldsymbol{E}|\varepsilon_r$ was chosen for the Jacobian surrogate rather than $|\boldsymbol{E}|^2\varepsilon_r$, yet although convergence of the buried cells was accelerated, there did not appear to be a negative impact on the accuracy of convergence or the propensity to converge on a particular local minimum. This strongly supports the contention of Farquharson (pers comm. 1999) and Zhdanov (pers comm. 1999) that the accuracy of the sensitivity matrix is not critically important in an iterative method. Clearly, provided the Jacobian usually points in a direction that leads to a reduced objective function, the process will converge. Furthermore, the distance component of the Jacobian is factored by the error, so that corrections reduce in magnitude provided the process is converging. Consider the following correction h_i for a CG iteration.

$$h_i = \alpha_i \left[\Delta t_{p_1} \cdots \Delta t_{p_m}\right] \begin{bmatrix} \frac{\partial \varepsilon_{r1}}{\partial t_{p_1}} & \frac{\partial \varepsilon_{r2}}{\partial t_{p_1}} & \cdots & \frac{\partial \varepsilon_m}{\partial t_{p_1}} \\ \frac{\partial \varepsilon_{r1}}{\partial t_{p_2}} & \frac{\partial \varepsilon_{r2}}{\partial t_{p_2}} & & \vdots \\ \vdots & & \ddots & \vdots \\ \frac{\partial \varepsilon_{r1}}{\partial t_{p_m}} & \cdots & \cdots & \frac{\partial \varepsilon_m}{\partial t_{p_m}} \end{bmatrix} = \alpha_i \left[\Delta \varepsilon_{r1} \cdots \Delta \varepsilon_m\right] \qquad (4.19)$$

The correction in ε_r for a particular cell comprises the sum of the t_p errors for all PTL positions, each weighted by the corresponding sensitivity. Errors in individual sensitivities will lead to incorrect weighting for a cell given a particular set of travel time errors. In the worst case, it may tip the sign of the correction to a cell's ε_r, but unless the sign of the error is constant and pervasive, it will not propagate for many iterations. Instead, the inappropriate correction will increase the error in the cell's ε_r, thereby increasing the cell's weighting and hence the opportunity for the error to be ultimately corrected.

Thus, while an incorrect Jacobian is expected to influence the convergence, unless it is seriously in error, it is unlikely to prevent convergence to a solution. Indeed, satisfactory convergence rates have been noted by the author for Jacobians using surrogates ranging from $|\boldsymbol{E}|\varepsilon_r$ to $|\boldsymbol{E}|^2\varepsilon_r$. Jacobians that are flatter than $|\boldsymbol{E}|\varepsilon_r$ provide sufficient distortion to adversely affect convergence. Figure 4.4 and Table 4.9 indicate the improved inversion performance obtained by the use of the flatter Jacobian, as indicated by smaller ε_r on the lowest layer, and closer values on the centre layer. Note that there are two important indicators of convergence performance with this target distribution:

1. Whether ε_r of the centre cells has reversed the initial trend and exceeded that of their neighbours on the same layer. As noted earlier, these cells have a higher ε_r target than their neighbouring cells but are quickly moved to a lower value during the first few iterations.
2. Whether ε_r of the lowest and least influential layer is less than the centre cells, against both the small influence of the buried cells and the 'shielding effect' of the centre cells with higher ε_r.

On both the above counts, convergence is more advanced when using $|E|\varepsilon_r$ as the Jacobian surrogate. This influence would also apply to use of the FD Jacobian which would be expected to be similarly crippled by poor convergence of buried cells. The objective function for Figure 4.4 and Table 4.9 is a much improved 2.45×10^{-26}, and an average of 25 forward calculations was required for each of the 16 CG iterations. However a straight comparison of the number of forward calculations required for the CG methods would be misleading since the search ranges for the minimisation within each iteration were not optimised. A search range of 0 to 1 was used for the $|E|\varepsilon_r$ surrogate, and a range of 0 to 50 for the $|E|^{\wedge}\varepsilon_r$ surrogate. Nevertheless, both approaches required a large number of forward calculations, and produced quite mediocre results.

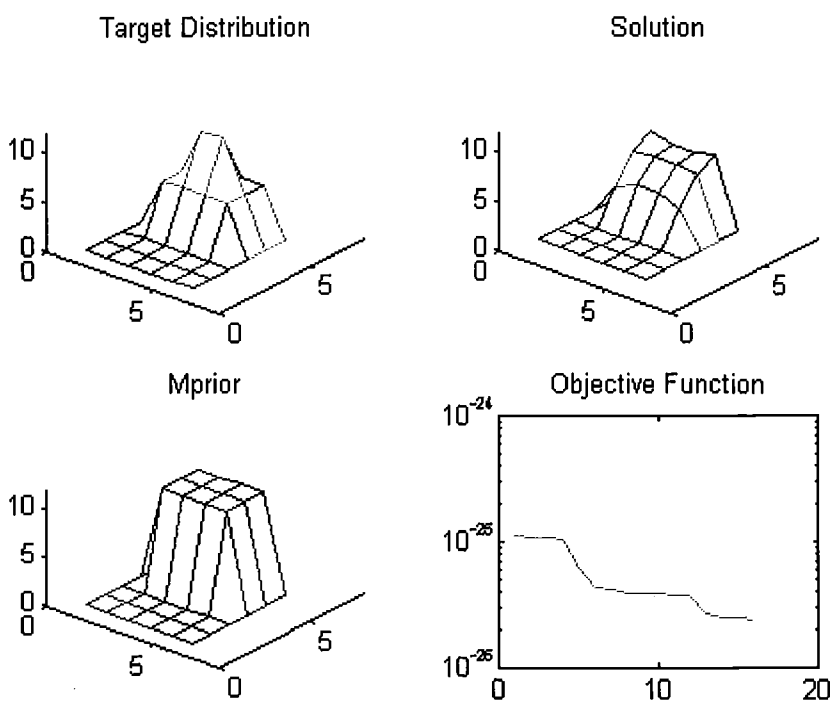

Figure 4.4 CG inversion with flatter surrogate Jacobian ($|E|\varepsilon_r$ in place of $|E|^2\varepsilon_r$).

Table 4.9 CG inversion solution with flatter surrogate Jacobian (compare with target distribution of Table 4.6).

1	1	1	1	1	1
1	1	1	1	1	1
1	1	1	1	1	1
1	4.3	5.3	5.3	4.3	1
1	7.0	7.2	7.2	7.0	1
1	8.1	7.4	7.4	8.1	1

While a more efficient line search could reduce this number, the relaxed tolerance described above has enabled the golden section search to retain its robustness yet provide reasonably rapid convergence. However, it is unreasonable to expect such a line minimisation to even approximately locate a turning point in less than five or so iterations, even when beginning near the known turning point as would be the case for all but the first of the CG iterations. Consider then a CG optimisation method for an inverse solution with just 12 unknowns. We would expect at best (Press et al., 1992) that 12 iterations of the CG method would be required to converge to the optimal solution, assuming a complete set of observations to make up a well-posed solution. This would require a minimum of 60 computations of the forward solution. However, despite the convergence rate, the solution still fails to provide a sufficiently satisfactory solution. This situation could be attributed to several reasons:

1. The inversion procedure has become trapped at a local minimum – typical of underdetermined problems
2. There is insufficient accuracy in the Jacobian to correctly guide the inversion procedure that consequently dithers around the broad area of a minimum. This is notwithstanding the earlier comment that convergence did not seem adversely affected by using $|\boldsymbol{E}|\varepsilon_r$ for the Jacobian surrogate. At some magnitude of the objective function, modelling and Jacobian errors will result in dithering.
3. The inversion procedure converges to a deep minimum that satisfies the objective function but which is known to be an incorrect solution. This too is typical of underdetermined problems.
4. The correct minimum of the problem is located, but even when the objective function is satisfyingly small, there are parameters that are still distant from their target values. In this case the poorly converged parameters are not sufficiently influential to attract much attention from the inversion procedure.

For minimisation procedures that explore the model space using manual guidance, human observation and intervention in the solution method can greatly speed convergence. Such methods are difficult to automate since they are likely to be a combination of the application of mechanistic understanding and heuristic processing. Hence observing the progress of the minimisation procedure along with how the variables change provides strong intuition about the convergence process, although subtle aspects may be difficult to define. This may, incidentally,

point towards combining different techniques for difficult inversion problems, such as using a neural net to select parameters for a mechanistic method. For the current problem however, it seems that the poor convergence demonstrated in the above implementations fits within category 4 above, and hence requires a further method to accelerate convergence.

For this reason, methods of dynamically determining α_i that avoid line searches were sought, combined with approaches that would hasten the expected slow convergence of buried cells whose influences on the propagation time are significantly less than those of surface cells that are close to the PTL.

4.7 Alternative selection of CG weighting factor

A convenient and computationally expedient method of dynamically selecting the CG weighting factor is adjusting it to provide a suitable alteration in ε_r distribution. Hence within the first iteration but before a correction was made to the ε_r distribution, the value of α_i in Eqn (4.18) was repeatedly decreased until the maximum correction in any cell was less than a preset threshold, typically $\varepsilon_r = 3$. This straightforward method was very rapid, requiring no additional forward calculations (see Figure 4.5 and Table 4.10).

Using $|E|\varepsilon_r$ as the Jacobian surrogate, this method provided a creditable inversion performance considering the crude approach. At 7.02×10^{-26}, the objective function was worse than the true CG method, and although this was achieved with 100 iterations, just 100 forward calculations were required. Since the forward calculations completely dominate the execution time, the method was four times faster than the CG method using line minimisations, although provided poorer results.

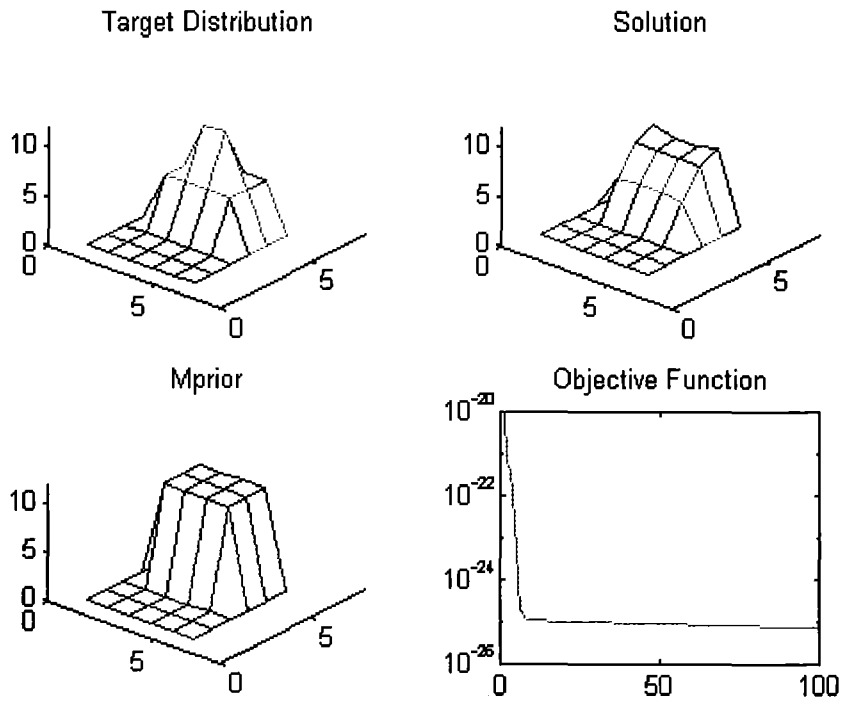

Figure 4.5 CG inversion using threshold limited weighting factor.

Table 4.10 CG inversion solution using threshold limited weighting factor (compare with target distribution of Table 4.6).

1	1	1	1	1	1
1	1	1	1	1	1
1	1	1	1	1	1
1	4.6	4.9	4.9	4.6	1
1	7.3	7.3	7.3	7.3	1
1	8.3	7.7	7.7	8.3	1

As convergence of the CG method proceeds, changes in the model, J_i, and the distance to the solution influence its optimal value, but these are overshadowed by the change in influence of $\alpha_i J_i \Delta t_i$ in Eqn (4.18) due to the shrinking time error, Δt_i. Hence, the static α_i provides a slow convergence as shown in Figure 4.5. Methods to address this issue have been integrated with others that circumvent the expected slow convergence of buried cells, and will now be described.

We note that the line search algorithm of the CG method minimises the objective function at each step and hence essentially ensures that that particular direction need not be revisited. However while this calculates the optimal α_i at each step, and hence optimal CG convergence, it doesn't help the poor convergence of buried cells that have little contribution to the v_p.

While it may be appreciated that from a pragmatic viewpoint, the accuracy of measurement of v_p means that the influence of a buried cell is below the noise floor of the instrument reading, we nevertheless wish to resolve this issue to ensure that the inversion procedure itself does not impose constraints on the performance of inversion from measured data.

Despite the more rapid convergence from the use of $|\boldsymbol{E}|\varepsilon_r$ rather than a more accurate form of the Jacobian such as from a FD formulation, convergence is slow given disparate and highly variable *a priori* and target distributions. We note that the two distributions should not be too dissimilar given a regularised inversion process, since there is significant weight applied to the *a priori* data that should in turn provide a strong lead in the inversion process.

In an attempt to resolve the slow convergence, several techniques for speeding convergence under these difficult conditions were devised and evaluated. The principle behind the techniques is to increase the CG weighting factor to accelerate the convergence of buried cells, yet without unduly disturbing the underlying CG process. The methods include the following:

1. Biasing the weighting factor. This technique slowly, iteration by iteration, increased the CG weighting factor α_i until a certain number of iterations was reached, and was then followed by a slow decrease. α_i continued to be constrained to provide a maximum change in ε_r per iteration of typically $|\Delta\varepsilon_r| = 3$. The positive bias was reversed after typically 30 iterations to allow the final convergence. This approach supported a degree of divergent behaviour particularly in the surface cells, but under control of the constraining approach. In contrast to the blocking method, the jockeying of buried cells was not limited by surface cells over-shooting their target values. Indeed the initial jockeying is not dissimilar to that in the simulated annealing method where in the initial stages, the method "wanders freely among local minima" (Press et al., 1992), and only later as gain is fixed, does it descend to a local, and demonstrably more global, minimum. However the method of biasing the weighting factor was frequently unsuccessful, in those cases leading to a worsening objective function that did not recover.

2. Stall detection. This adaptive technique tracks the progress of CG convergence as measured by improvement in the objective function, and increases the value of α_i, typically by a factor of two, if the rate of improvement falls below a preset limit, typically 10%. To counter excessive increases in the value of α_i, the constraint discussed at the beginning of §4.7 applies. The tracking was implemented by an exponential filter, and when it fell below the threshold, the CG weighting factor was increased and the filter reset. This procedure was more successful than the weighting factor bias, but was still quite dependent on the conditions and parameters and hence demonstrated insufficient robustness. Nevertheless, performance was frequently better than other methods described above.

3. Prediction. It is apparent from plots of ε_r for each cell, that successful convergence results in somewhat exponential change to ε_r in each cell. Initially, the inversion procedure converges normally while initial convergence stabilises and any misdirection of cell ε_r has reversed. The misdirection occurs when highly influential cells overshoot or undershoot

their target values to compensate for the slow convergence of less influential cells. The prediction method then fits to each cell's convergence history, an exponential curve and hence determines the asymptotic value. This approach was unsuccessful, seemingly too much influenced by the errors inherent in accurately determining second derivative information from the small slopes of the cell convergence. Instead such information could be gained directly from the Jacobian and extrapolated much like a Newton method. This idea is extended in the next method.

4. Blocking. The principle of blocking is to perturb α_i so that rapid changes are made to the current model during one iteration, and then redistribution of ε_r in each cell occurs by normal CG convergence over the next few iterations. Changes to ε_r of highly influential cells are blocked during the perturbed iteration, so that the cells with small influence are favoured. This method has demonstrated very good gains in convergence performance, with the odd flash of brilliance. It will now be described in more detail.

4.8 Blocking

Convergence in the above CG variants was rapid provided the difference in ε_r between the *a priori* model and the solution was small in buried cells. However, if they differed significantly, convergence of the buried cells that had only a small influence on the v_p, was very slow. Thus, the concept of blocking was to increase the magnitude of all Jacobian elements, but to mask or block the most influential cells from changing. The intention was to repeat the blocking process several times during the convergence. The following procedure was used:

1. Set α_i to one.
2. Begin CG convergence and during the first iteration, α_i will be scaled to limit the maximum change in ε_r per iteration.
3. For a blocking iteration, α_i is increased in value until the blocking limit is reached. This condition is met when the maximum correction to any cell exceeds the block threshold, typically $|\Delta\varepsilon_r| = 2$.
4. Block (assign a ε_r change of zero) the most influential row of cells (row one) where the prospective change in ε_r would be expected to be close to the blocking threshold, and which will converge quickly without blocking.
5. Update the model in the unblocked cells.
6. Return to step 2 until the stopping criterion is met.

The principle of blocking relies on several factors.

1. The weighting on buried cells is increased so that any pending correction is greatly amplified, but the signs of individual cell corrections are unaffected. The sign of the correction at a blocking step is determined in the usual manner but uses an alternative Jacobian that is exponentially smoothed from previous Jacobians, and weighted by the propagation time errors. Then after the individual corrections have been calculated, their

size distribution is distorted by the blocking scheme so that the multivariate heading is altered.

2. For several iterations following blocking, the objective function normally worsens, often quite dramatically. It is critical that normal iteration proceed to again allow the objective function to reduce by the usual rapid changes in the high influence cells, and for all cells to again settle down to changing in a direction that reduces the objective function. Although this has been achieved by allowing blocking to occur only at intervals of greater than the number of unknowns, a better method is to rely on the Jacobian smoothing to provide a reliable blocking direction.

3. The maximum allowable change in ε_r during blocking needs to be constrained to avoid significant overshoot. This requirement is analogous to step size selection in the Newton method.

4. Blocking should be precluded when the objective function has reached a near satisfactory level that may still be somewhat larger than the target objective function. Blocking when near a deep minimum has been observed to direct the process away from the minimum since at this stage only small changes to ε_r in each cell are required. Blocking may appear to be advantageous when near a deep but incorrect minimum, but apart from the current use of simulated inversions, any deep minimum which is within the constraints of the problem and is near to the *a priori* distribution must be considered a valid solution.

5. While the method does allow more rapid convergence of cells with small influence, it is limited by noise and inconsistency in the observed data.

In general, the blocking scheme (Listing 5) has driven the inversion process into deeper minima than the other methods, however the located minimum may not correspond with the target distribution. Consider the results of convergence in Figure 4.6. The procedure used blocking and converged to an objective function value of 2.5×10^{-29} in just 30 iterations, with a maximum error in propagation time of 2.6×10^{-15} sec. This deep minimum is well beyond the reach of current TDR instrumentation that cannot resolve better than about 1×10^{-13} sec. Despite the very small error, the solution (Table 4.11) is still quite distant from the target distribution (Table 4.6).

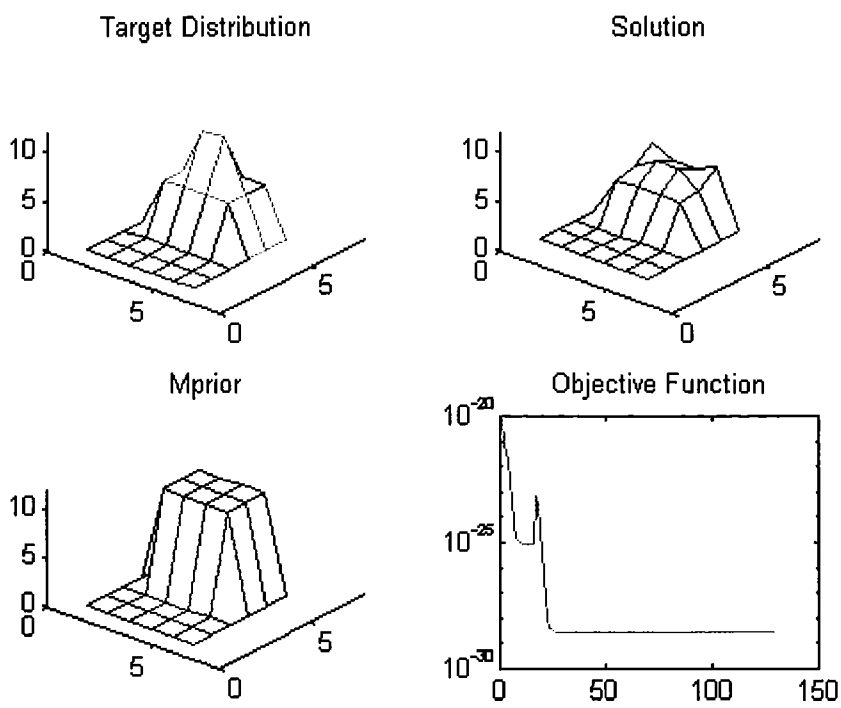

Figure 4.6 Rapid CG convergence using blocking.

Table 4.11 CG inversion using blocking (compare with target distribution of Table 4.6).

1	1	1	1	1	1
1	1	1	1	1	1
1	1	1	1	1	1
1	5.0	5.2	5.2	5.0	1
1	5.3	6.8	6.8	5.3	1
1	6.9	5.8	5.8	6.9	1

Figure 4.7 is a map of the convergence process and demonstrates the effectiveness of the blocking scheme given the set of inversion parameters in Table 4.12. The traces represent the ε_r of the cells. In this instance, just one blocking procedure was implemented before the objective function fell below the blocking limit intended to avoid the situation described in point four above. The results from this inversion clearly demonstrate the necessity of meaningful *a priori* distributions where the problem is under-determined and there is insufficient accuracy in the measurements to adequately define the deepest minimum, assuming that the inversion time to search all minima was not an issue.

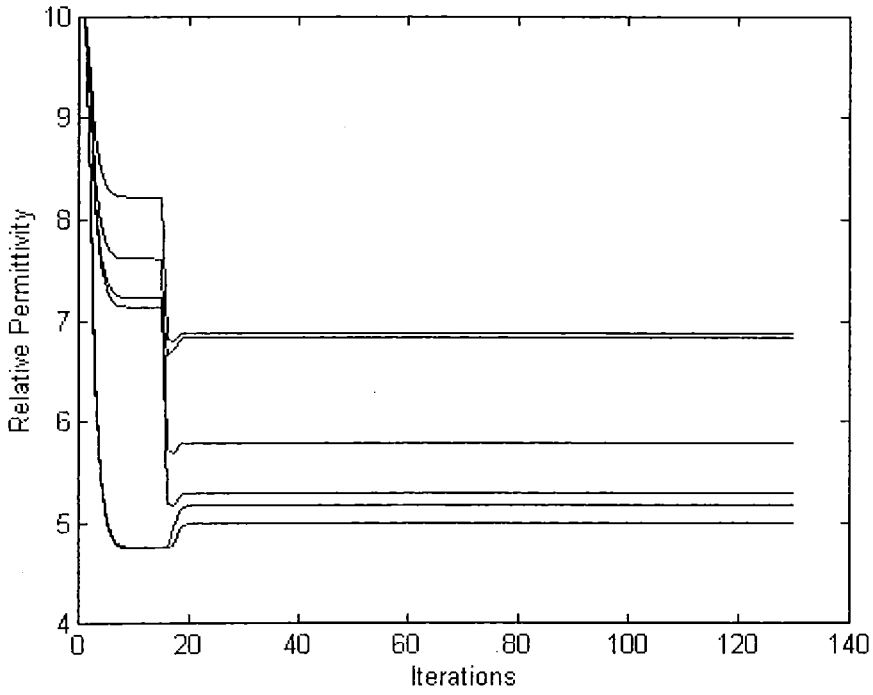

Figure 4.7 Map of convergence of CG inversion using blocking. Each trace follows ε_r of a particular cell.

Table 4.12 Typical CG inversion parameters used with blocking.

Parameter and value	Description of parameter
max_iterates = 130	maximum passes through inversion process
target = 1E-29	target misfit as sum of squares
gamma = 0	Tikhonov regularisation parameter
max_corr = 2	largest change in ε, constrains CG sensitivity
Er_min = 2	no dry material will have ε less than this
Er_max = 30	maximum ε of wet material
turnover = 105	sensitivity is increased until 'turnover' iterations
blocking = true	Switch to turn blocking on or off
block_count = 15	blocking occurs every 'block count' iterations
block_limit = 2	maximum change in ε during blocking
block_target = 2×10^{-27}	no blocking if objective function S < block target
max_terr = 1×10^{-15}	target as maximum propagation time error (sec)

Mention has already been made of how observing the inversion process enables inversion and blocking parameters to be intuitively selected to favour convergence towards a known minimum. For example, the convergence to the solution of Table 4.13 and Figure 4.9 used a blocking interval of just eight and provides an intuitively closer solution with an objective

function of 7.9×10^{-28}, and a maximum error in propagation time of 1.7×10^{-14} sec, yet the minimum is shallower than the previous solution. However, observing the convergence progress in Figure 4.8 indicates that although the solution is close to the target, there were unnecessary blocking events, and blocking might just as well have been halted after 20 iterations.

Table 4.13 Solution of CG inversion using a blocking frequency of eight (compare with target distribution of Table 4.6).

1	1	1	1	1	1
1	1	1	1	1	1
1	1	1	1	1	1
1	5.0	5.0	5.0	5.0	1
1	4.7	12.5	12.5	4.7	1
1	6.3	3.5	3.5	6.3	1

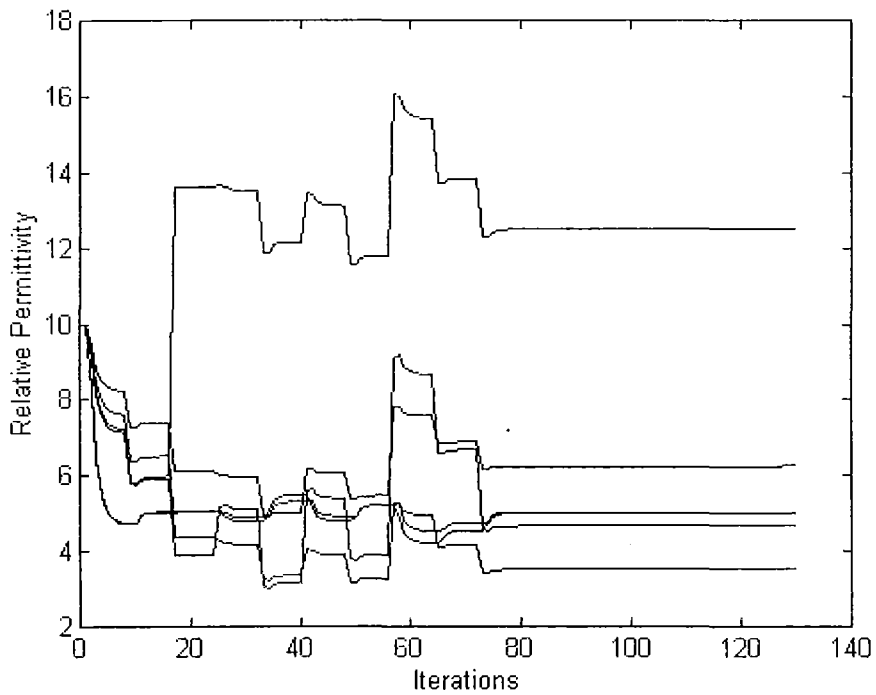

Figure 4.8 Map of convergence of CG inversion using blocking frequency of eight iterations. Each trace follows ε_r of a particular cell.

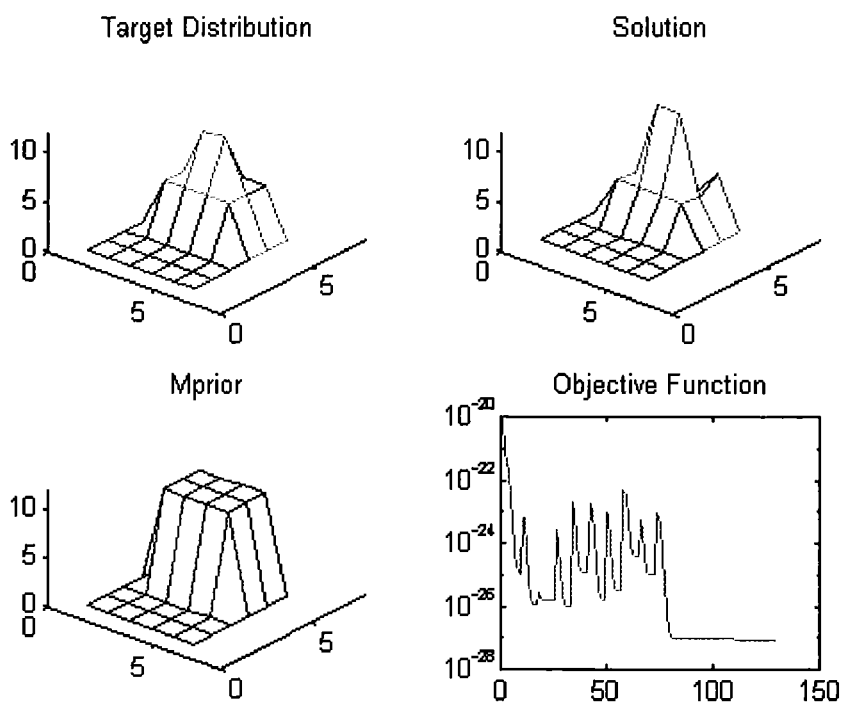

Figure 4.9 Rapid CG convergence using blocking frequency of eight.

The robustness of a set of inversion parameters is easily tested by altering the *a priori* or target distributions. In this case we demonstrate robustness with a different target since the *a priori* distribution that has been worked with until now (Table 4.6), does not assist convergence. Table 4.14 represents the cross-sectional θ_v distribution in a block of material that has been non-uniformly dried. This could for example occur in timber that has a sector of heart wood, a so-called mixed board that is difficult to dry uniformly due to aspirated cells in the heartwood. This distribution too has resulted in a satisfactory convergence as indicated by the similarity of the solution to the target distribution (Table 4.15 and Figure 4.10). The objective function was 1.3×10^{-27} and the maximum error in propagation time was 2.8×10^{-14} sec.

Table 4.14 Altered target ε_r distribution.

1	1	1	1	1	1
1	1	1	1	1	1
1	1	1	1	1	1
1	5	5	5	5	1
1	10	10	10	5	1
1	10	10	5	5	1

Table 4.15 Solution to altered target distribution.

1	1	1	1	1	1
1	1	1	1	1	1
1	1	1	1	1	1
1	5.2	5.1	5.1	5.0	1
1	9.1	8.1	7.1	5.4	1
1	10.8	9.3	6.3	5.9	1

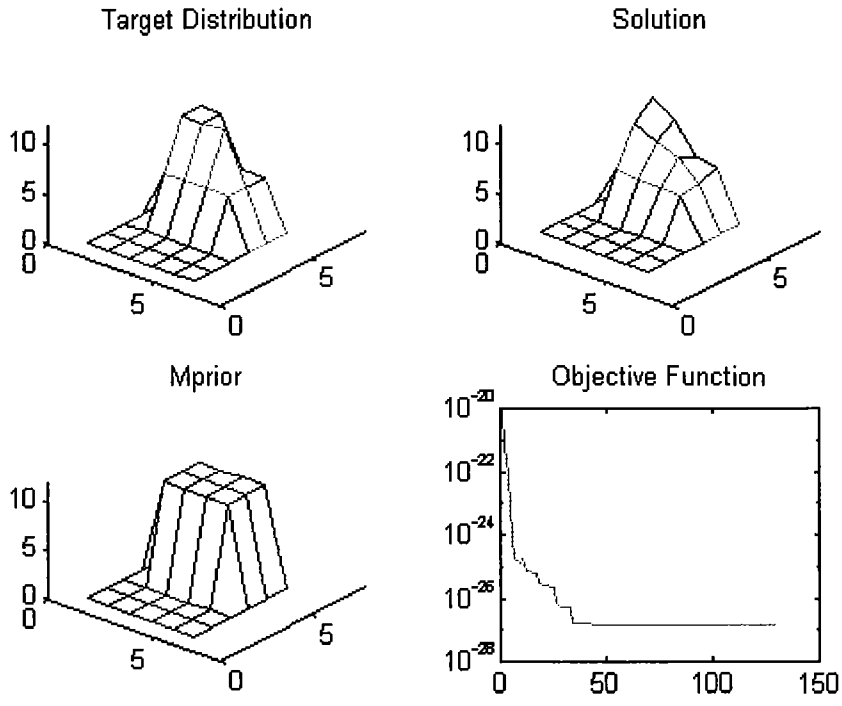

Figure 4.10 Rapid CG convergence to the altered target distribution (Table 4.14).

4.9 Bayesian inversion

From the above, it is apparent that acceptable convergence may be obtained from simulated inversion that effectively minimises errors in the forward model and assumes perfect instrumentation. Despite the idealised simulation conditions, it has been shown that convergence to a solution that is quite distant from the true solution (which is normally unknown) may occur. In the more realistic situation where a TDR instrument provides a (noisy) set of readings of an unknown distribution, the performance will be degraded. Hence to

reduce the likelihood of the inversion procedure stepping down into an inappropriate minimum, and to accommodate reduced confidence of both the model and the instrumentation, *a priori* data in the form of a starting distribution needs to be applied, along with regularisation to include any alternative data that may assist convergence to a solution that is close to the target. Fundamental to this process is a reliable *a priori* distribution. In the Bayesian tradition, the *a priori* data is updated or refined by observations, and the weighting applied to each is a measure of the respective confidence in the measured and *a priori* data sets. In the previous sections, the flat starting distribution (Table 4.6) could be considered as null *a priori* data, but now we introduce *a priori* distributions that are intended to prompt the inversion towards a likely minimum.

In §2.5.4, reference was made to the feasibility of using time varying *a priori* data. This would be particularly applicable to monitoring the drying of a material, where the solution of one inversion procedure could form the *a priori* distribution of the next solution. However more likely is the scenario that there are many items such as blocks of cheese or boards on a production line, and the objective is to gain a measure of the θ_v distribution of each. In that case a single starting distribution would be appropriate. In the cheese application, a flat distribution would form a likely starting distribution, that could be updated to the long term mean of the measured distributions. For timber that has recently dried in a kiln, the *a priori* distribution should take account of the likely wetter central region as a remnant of the θ_v gradient during drying. Again, the *a priori* distribution could be iteratively improved by earlier solutions.

Returning to the first target distribution (Table 4.6), the convergence was tested using the *a priori* distribution in Table 4.16, that could represent the mean distribution over the previous 100 measurements.

Table 4.16 Realistic *a priori* distribution for dried timber.

1	1	1	1	1	1
1	1	1	1	1	1
1	1	1	1	1	1
1	6	6	6	6	1
1	6	8	8	6	1
1	6	6	6	6	1

Using an *a priori* distribution that is close to the target solution did, as would be expected, require smaller values of the maximum correction per iteration both during CG iterations and during blocking. For this distribution they were reduced to $|\Delta\varepsilon_r| = 0.5$. Then the inversion procedure rapidly converged to a solution near to the target (Table 4.17 and Figure 4.11) with

an objective function of 1.0×10^{-27} and a maximum propagation time error of 2.1×10^{-14} sec. Given more appropriate stopping criteria (which had been selected here to indicate the effect of continuing the inversion process), the inversion could have been completed with approximately 20 iterations that include just 20 forward calculations. For this situation, the stopping criteria could be:

- maximum propagation time error of 2×10^{-14} sec, OR
- objective function less than 2×10^{-27}, OR
- iterations greater than 50.

Table 4.17 CG solution using the realistic *a priori* distribution of Table 4.16 (compare with target distribution of Table 4.6).

1	1	1	1	1	1
1	1	1	1	1	1
1	1	1	1	1	1
1	4.9	5.0	5.0	4.9	1
1	5.0	10.8	10.8	5.0	1
1	5.4	5.3	5.3	5.4	1

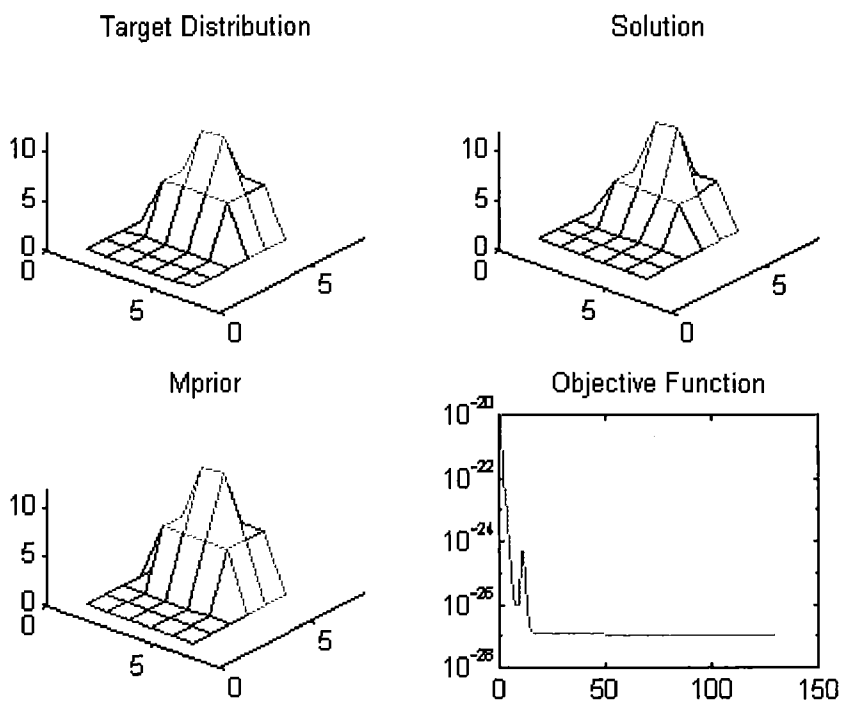

Figure 4.11 CG convergence using nearby *a priori* distribution.

The methodologies described here have demonstrated rapid convergence with simulated data and this has obviated the need to employ regularisation methods described in §2.4.6 and Eqn (4.1). This is contingent on a reasonably well-posed set of observations and if necessary, for reasons of noise, instrumentation accuracy etc, additional linearly-independent measurements may be obtained by positioning the PTL on more than one side of the anomalous region, as pointed out by Oldenberg pers comm. (1999). The influence of measurement noise on the inversion process was only briefly considered and, as expected, merely altered the solution ε_r (the effect of the noise was to change the value of each measured propagation time). However given an overdetermined observation set, the resulting inconsistencies would be expected to result in a shallower and less well-defined true minimum, but could also give rise to deeper false minima.

4.10 An indicator for convergence rate

Non-linear inversion from experimental data is not a recipe-driven process. For example in the case of inverting geophysical data, difficulties such as too few data enforce a manual, interventionist approach to inversion that demands the addition of *a priori* data and Bayesian techniques (Ellis and Oldenburg, 1994). In the present case, although there is less restriction on the number and choice of measurements that may be included, there are measurement time and convenience overheads with implications for inversion time. A method has been developed to formalise the assessment of the inversion process and to provide a qualitative indication of the likely rapidity and ultimate accuracy of convergence.

A hypothetical transfer function T that maps the ε_r distribution to the propagation time on the PTL, and which incorporates the geometry of the problem, could be viewed as having the structure:

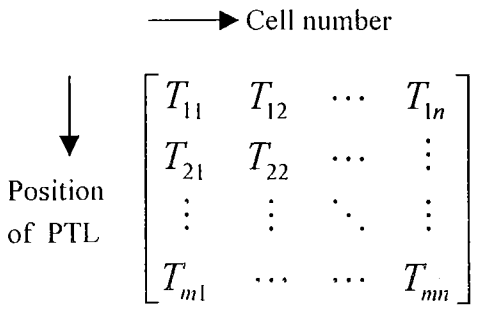

$$\begin{bmatrix} T_{11} & T_{12} & \cdots & T_{1n} \\ T_{21} & T_{22} & \cdots & \vdots \\ \vdots & \vdots & \ddots & \vdots \\ T_{m1} & \cdots & \cdots & T_{mn} \end{bmatrix}$$

Each T_{mn} is, for a particular position m of the PTL, a measure of the influence of a cell on the propagation time, ie $\partial t/\partial \varepsilon_r$ as in the Jacobian. The condition number of matrix T is the ratio of largest to smallest singular value, and provides an indication of the linear dependence of T. The elements of the diagonal matrix resulting from a singular value decomposition (SVD) of T provide all the singular values. To provide discrimination of ε_r in each cell, the value of T_{mn} needs to be distinctly different between at least two of the rows. Hence if T is of full rank, then the inverse problem will be at least fully-determined. The question that remains is how the rank is defined, that is what tolerance is applied to determine whether a singular value should

contribute to the solution. Here we draw on the calculation described earlier, to quantify the relationship between the scaled value of $|E|^2$ and the FD calculation, and relating to the smallest time resolvable by the instrumentation. Without prejudice to the instrumentation, we apply a limit of 0.05 ps, since the range of propagation time errors for a well converged, fully determined, simulated inversion was from less than 0.01 ps to around 0.3 ps. Then, the change in $|E|^2$ due to a perturbation of $\varepsilon_r = 0.1$, normalised to the unperturbed value, was 0.0119, with a corresponding change in predicted propagation time of 0.0126 ps. Hence, a threshold in the normalised change in $|E|^2$ of 0.05 was chosen as the tolerance for calculation of the rank, or equivalently, the threshold singular value that would be used for calculation using singular value decomposition.

A procedure to formalise the process was developed, and involved constructing T where each element represents the field strength as a surrogate for the actual transfer function for each cell in the perturbed region. By determining the number of linearly independent data, the linearly dependent rows may be identified and removed. Then the condition number of the resulting matrix provides an indication of the likely precision from the inversion process, while the difference between the rank and the total number of unknowns provides a measure of the illposedness.

Hence the procedure is:

1. Form a transfer function matrix from the data – the electric field was used as a surrogate.
2. Normalise each row, ie each set of sensitivities for a particular PTL position.
3. Report on the rank and condition number of the matrix.
4. Search row pairs for the largest difference between the pairs in one column (indicating the discrimination available between the pair).
5. Reconstruct the transfer function matrix, omitting the row with the smaller sensitivity of the pair identified above, and remove that column.
6. Progressively remove columns and rows as in steps 4 and 5.
7. Identify rows and cells where the normalised value is less than the above preset limit.

The rank indicates the number of unknowns that can be determined, and the condition number η is a measure of the illposedness. If R is less than the number of unknowns, either regularisation is required, or additional linearly independent observations are needed. Similarly, if η is larger than about 10^4, the Jacobian and hence the problem is poorly conditioned, and regularisation will be required. However the major benefit arises from steps 4-7 above. They identify which cells are poorly discriminated and hence likely to have larger errors, and which rows or readings contribute little new information, hence not contributing to the rank.

The above makes no assumption about linearity of the problem, and differs from standard techniques such as factor analysis that quantify the influence on the model, of a particular variable or group of variables. Here we have a known set of influencing factors, the cells with their unknown ε_r, and a set of observations that are influenced by all the factors to a greater or

lesser extent. The relationships are non-linear, and we wish to exclude observations that do not contribute significantly to the information encapsulated in the remaining observation sets.

4.11 Concluding remarks

An inversion methodology based on a CG technique has been developed for inverting TDRI measurements of a composite material, and evaluated using simulation. A rapidly calculated electric field strength surrogate was used for the Jacobian and proved adequate for the CG convergence process. Rather than employing a computationally intensive line search for each CG iteration, an approximate method of determining the CG weighting factor was used and significantly reduced the number of forward calculations required for an inversion. Then to accelerate the convergence of buried and less influential regions of the composite material, a blocking scheme was devised that provided further improvement in inversion performance. Coupled with introduced *a proiri* starting distributions, this scheme resulted in rapid convergence, typically requiring just 20 forward calculations. Finally, a procedure was described that provides a measure of the illposedness of a set of observations for TDRI, and indicates which observations are redundant.

These developments have resulted in an inversion scheme that by all accounts is robust, and provided the actual solution is the nearest deep minimum to the *a priori* data, rapidly converges to the actual solution.

Chapter 5

A Generic Dielectric Model

Time domain reflectometry imaging (TDRI) is a new technique for predicting the distribution of volumetric moisture content (θ_v) in a composite material (such as soil or wood). Any measurement using relative permittivity (ε_r) as a surrogate for θ_v, requires a dielectric model to translate measured ε_r to θ_v. For TDRI, the dielectric model is used first to translate the *a priori* θ_v distribution to a distribution of ε_r, and after the inverse problem is solved (as described in Chapter 4), it translates the solution back to a distribution of θ_v (Figure 5.1). Hence a dielectric model for TDRI must be invertible since both forward and inverse application of the model is required.

It was concluded from §2.5.1 that separate parameters should be incorporated to account for tightly held water, molecular relaxation, and temperature. Although the literature describes numerous dielectric models that have been formulated for specific uses and materials (Jacobsen and Schjonning (1995) for example, summarise and compare several models), a new model was synthesised by the author for TDRI to meet the following requirements.

- Accommodate a range of composite materials.
- Include a compensation to adjust the response according to the volume fraction of tightly held water (this issue was discussed by Wang and Schmugge (1980) and others).
- Include a parameter to accommodate the reduction in the real ε_r of the included water due to Debye relaxation.
- Adjustment of ε_r for the water fraction to accommodate changes in temperature.

Not included in the model was:

- Adjustment for dielectric loss. The forward model did not accommodate dielectric loss, and it was considered that at the measurement frequency of around 1 GHz, the impact of loss on the real ε_r for typical target materials (water phantoms, timber and soil) was considered small (§6.1). However the model does not specifically exclude the loss component, which is calculated if complex ε_r is allowed for.
- Relaxation of water inclusions or interfacial components. These loss effects usually occur at frequencies well below 1 GHz (§ 2.1.1 and §2.1.2).

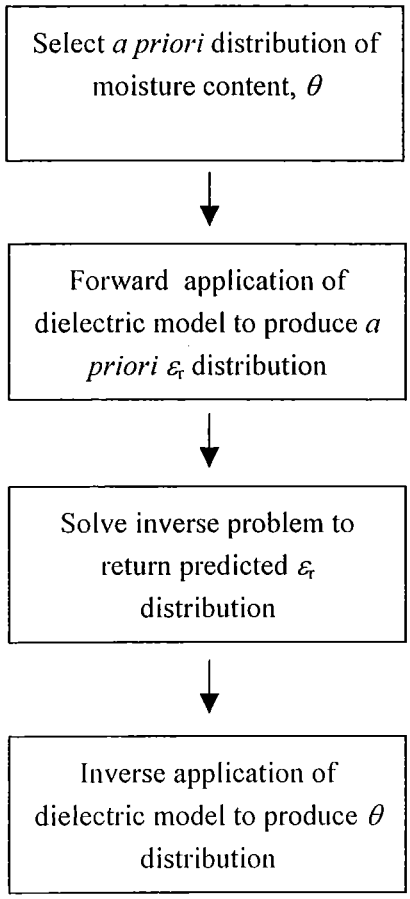

Figure 5.1 Procedure for applying a dielectric model to the inverse solution.

5.1 Synthesis of a generic dielectric model

A dielectric model was formulated to meet the above requirements. It is based on a general two phase model:

$$\varepsilon_m = [\varepsilon_h^\alpha + P(\varepsilon_{inc}^\alpha - \varepsilon_h^\alpha)]^{\frac{1}{\alpha}} \tag{5.1}$$

where ε_m, ε_h, and ε_{inc} are respectively the complex ε_r of the mixture, the host (eg soil, timber) and the inclusion (water), α is a shape factor ($\frac{1}{3}$ for the spherical particle model of Looyenga, 1965), and P is the volume fraction of the inclusion. A θ_v dependency was included for the bound water component so that

$$\varepsilon_{inc} = \begin{cases} \varepsilon_b, & \theta_v \le \theta_t \\ \dfrac{\theta_t}{\theta_v}\varepsilon_b + \dfrac{(\theta_v - \theta_t)}{\theta_v}\varepsilon_w, & \theta_v > \theta_t \end{cases} \tag{5.2}$$

where ε_b is the relative permittivity of the ice-like initially adsorbed or bound water, ε_w the relative permittivity of liquid water, and θ_t the transition water content between the two states. A term accounting for the Debye relaxation (Debye, 1950, cited in Hastead, 1973) of free water defines a new ε_w, ε_w':

$$\varepsilon_w' = \varepsilon_\infty + \frac{\varepsilon_w - \varepsilon_\infty}{1+\omega^2\tau^2} \tag{5.3}$$

where ω is the angular frequency, $\varepsilon_\infty = 3.2$ the high frequency ε_r of water (Hastead, 1973), and τ the relaxation time. Finally, ε_w may be corrected for temperature by:

$$\varepsilon_w = 89 - 0.37T \tag{5.4}$$

where T is the temperature in degrees Celsius (Wobschall, 1977). Synthesis of the complete model results in:

$$\varepsilon_m = \begin{cases} \left\{(1-\theta_v)\varepsilon_h^{\alpha} + \theta_v \varepsilon_b^{\alpha}\right\}^{\frac{1}{\alpha}}, & \theta_v \le \theta_t \\ \left\{\left[\varepsilon_h\right]^{\alpha} + \theta_v \beta\left[\frac{\theta_t}{\theta_v}\varepsilon_b + \frac{(\theta_v - \theta_t)}{\theta_v}\left(3.2 + \frac{85.8 - 0.37T}{1+\omega^2\tau^2}\right)\right]^{\alpha} - \theta_v \varepsilon_h^{\alpha}\right\}^{\frac{1}{\alpha}}, & \theta_v > \theta_t \end{cases} \tag{5.5}$$

An empirically-derived term β was included to allow fitting independent from the curvature adjustment by α. Although modelling complex permittivity was specifically excluded in Eqn (5.5), Dobson et al. (1985) also used a 'semi-empirical' mixing model with a similar derivation, and included the loss components. The performance of the model will now be evaluated for soil and timber.

5.2 Applying the dielectric model to soil data

The empirically derived equation commonly used in TDR measurement of soil water content (Topp, 1980) is widely accepted as an accurate model for coarse-grained soils (Hallikainen et al., 1985; Dirksen and Dasberg, 1985; Jacobsen and Schjønning, 1995), and hence forms a useful comparison for the generic model.

Table 5.1 Model parameters for a coarse-grained soil.

Parameter	Value	Source
ε_h	3	Topp (1980) equation
α	$\frac{1}{3}$	Looyenga (1965)
β	1.18	Selected to match Topp (1980)
θ_t	0.017	Dirksen and Dasberg (1985)
ε_b	3.2	Dirksen and Dasberg (1985)
T	15 °C	Assumed
ω	$2\pi\times10^9$ s^{-1}	Heimovara (1994)
τ	9.3×10^{-12} s	Hastead (1961)

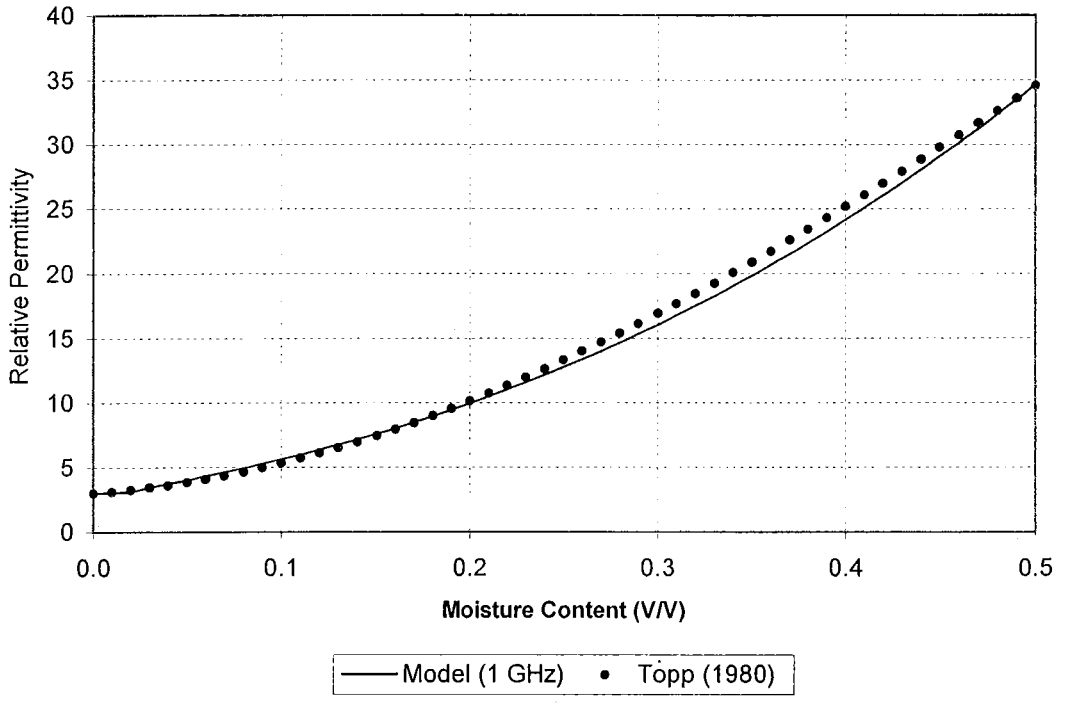

Figure 5.2 Comparison of the dielectric model of Eqn (5.5) with that of Topp (1980), for a coarse-grained soil.

The close fit with the Topp equation is not surprising since the grains in coarse soils are roughly spherical and hence modelled appropriately with $\alpha = \frac{1}{3}$ (Looyenga, 1965), and the other parameters have a physical basis. In the case of θ_t, the hygroscopic water content for the Wichmond sandy-loam from Dirksen and Dasberg (1985) was used. A frequency of 1 GHz was chosen since this is similar to the effective measurement frequency of TDR using a Tektronix 1502 (Hiemovara, 1994) and software that determines the reflection point y tangents to the

slope (also refer to §6.3). At this frequency, the impact on ε_r due to free water relaxation is negligible.

Dirksen and Dasberg (1985) comment on the departure of Topp's equation from the actual dielectric properties of finer-grained soils. Their bentonite data for example, exhibit an apparent bimodal characteristic with a slope of $d\varepsilon_r/d\theta_v \approx 12$ for $0 < \theta_v < 0.22$, followed by a slope of $d\varepsilon_r/d\theta_v \approx 90$. The generic model accommodates these characteristics (Figure 5.3). The parameters which were altered from those for sandy-loam values were $\theta_t = 0.19$ as proposed by Dirksen and Dasberg (1985) and typical of the wilting point for clays (Wang and Schmugge, 1980), $\varepsilon_b = 20$, the lower end of the range for the clays, and $\beta = 1.4$. Although it may be difficult to rigorously assign a physical meaning to the empirically-determined factor β, it could be considered to complement the shape factor α by altering the contribution or rate of ε_r/θ_v for free water. Dirksen and Dasberg (1985) used ε_b as a free parameter for fitting their model to the clays, yet their fit for bentonite was notably inferior to that of Figure 5.3. They also commented on the assumption of the Dobson et al. (1985) version of the Maxwell-De Loor model that the soil particles were flake-like. A further interesting facet of the Dirksen and Dasberg (1985) work is their early rejection of the α model (they mistakenly referred to it as the Birchak α model, but Birchak et al. (1974) didn't develop the model) because of its critical dependency on the value of α, which was also soil-type dependent. Yet the α model is quite similar to the Looyenga model which, as has been demonstrated here for both a near-ideal and a difficult soil type (bentonite), gives a reasonable fit when a distinct bound water phase is included instead of the additional phase included Looyenga-style, in the α model. The prediction of ε_r is significantly better than Dirksen and Dasberg's (1985) fit of the Maxwell-De Loor model to bentonite.

Note that the intention in this work has been to configure a flexible, predominantly mechanistic model, broadly applicable to a range of materials, not to accurately fit to specific materials. Nevertheless it appears that the model could usefully be employed as a soil model based on physically determined soil parameters, and considering the many sets of soil permittivity data that have been published, there is scope for much further work.

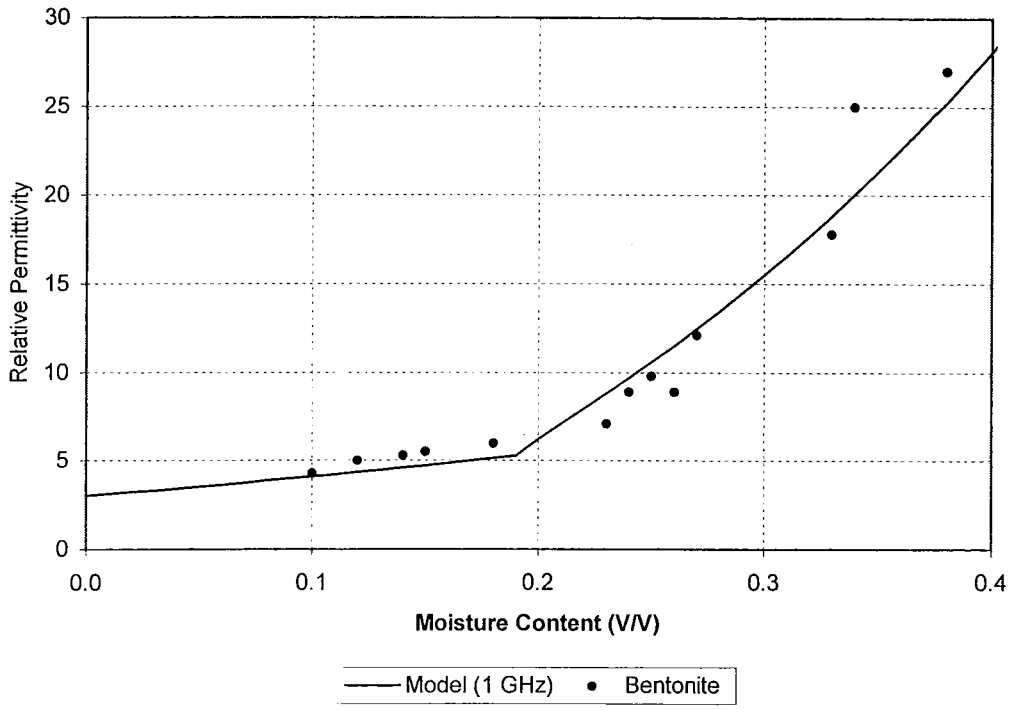

Figure 5.3 Fit of the dielectric model of Eqn (5.5) to ε_r of bentonite clay.

5.3 Applying the dielectric model to wood data

Use of the model for predicting ε_r of wood will now be considered, although there are few published sets describing ε_r of wood at microwave frequencies. The model has been fitted to data presented by Torgovnikov (1993, Appendix 3) but the genus of the wood for this data set was not stated. To make a valid comparison of the model with published data, it was necessary to convert from the 'native TDR' volumetric moisture content to gravimetric moisture content against which the comparisons are made (eg Torgovnikov 1993 – Fig 2.5). Ignoring density change of the water itself, $\theta_v = \theta_g \rho / \rho_w$ where θ_v is the volumetric moisture content, θ_g the gravimetric moisture content, ρ the dry density of the wood, and ρ_w the density of water. The effect of density on ε_h was ignored since the contribution to the total ε_r would be small, as was the effect of shrinkage which does not appear to have been compensated for in any dielectric models. As in the case with the soil data, physically based properties of the materials were used to specify most model parameters. The data used were for measurements taken with the electric field perpendicular to the grain, which provides lower ε_r than measurements parallel to the grain (Torgovnikov, 1993).

As shown in Figure 5.4, the alignment between the model and data results in a worst case error of approximately 10%. This unsatisfactory error seems likely to have arisen through errors in either the θ_g measurement or in recording ε_r since they are not reflected in similar data from the same source but for named genera (Figure 5.5). It is likely that the readings at $\theta_g = 0.3$ should have been for $\theta_g = 0.4$. It is also apparent that better alignment of the model and data would be achieved if θ_t was greater for the higher frequency measurements, but there seems little physical basis to support this notion.

Table 5.2 Model parameters for wood of unknown genus (from Torgovnikov, 1993).

Parameter	Value	Source
ε_h	1.8	Torgovnikov (1993)
α	$\frac{1}{3}$	Looyenga (1965)
β	0.85	Selected for fit (Figure 5.4)
θ_t	0.05	Monomolecular (Torgovnikov, 1993)
ε_b	3.2	Taken as ice (Hastead, 1961)
T	20 °C	Torgovnikov (1993)
ω	$2\pi \times 10^9$ s^{-1}	Torgovnikov (1993)
τ	9.3×10^{-12} s	Hastead (1961)
ρ	0.5	Torgovnikov (1993)

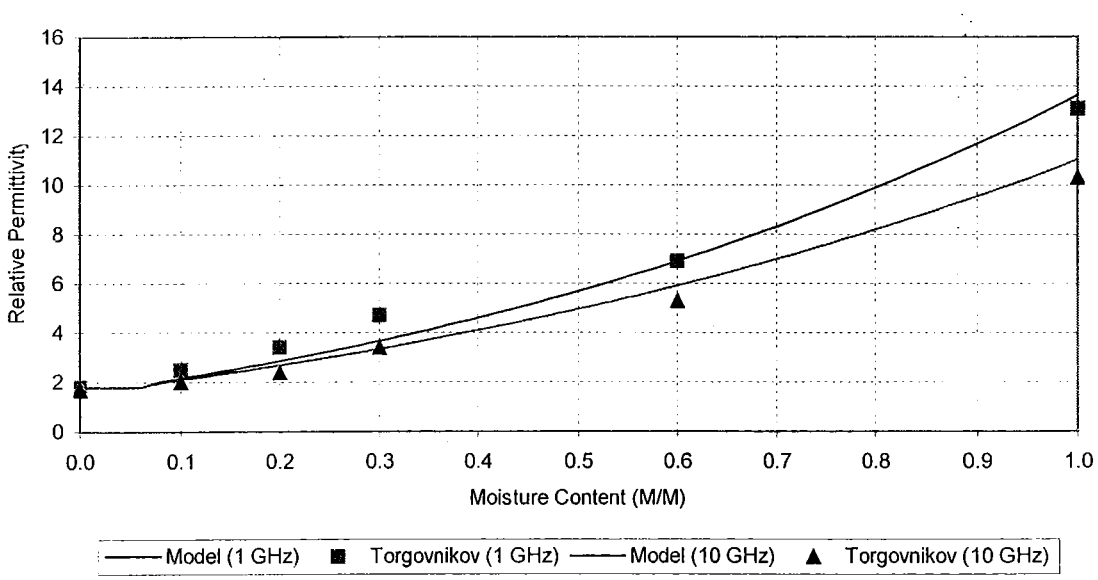

Figure 5.4 Fit of the dielectric model of Eqn (5.5) to ε_r for an unknown wood genus at 1 and 10 GHz.

Other data for specific wood types at measurement frequencies of 0.915 GHz and 2.375 GHz were also presented by Torgovnikov (1993). To compare changes in genus, the model was used with the above parameters (Figure 5.5), except that the density was altered to reflect the data quoted by Torgovnikov (1993), 0.47 g/cm^3 for aspen and 0.6 g/cm^3 for birch. β was also changed from 0.9 for the unnamed genus and suspect data point at $\theta_g = 0.3$, to 0.85 for aspen and birch. As with the soils data, only β was altered to optimise (by eye) the fit.

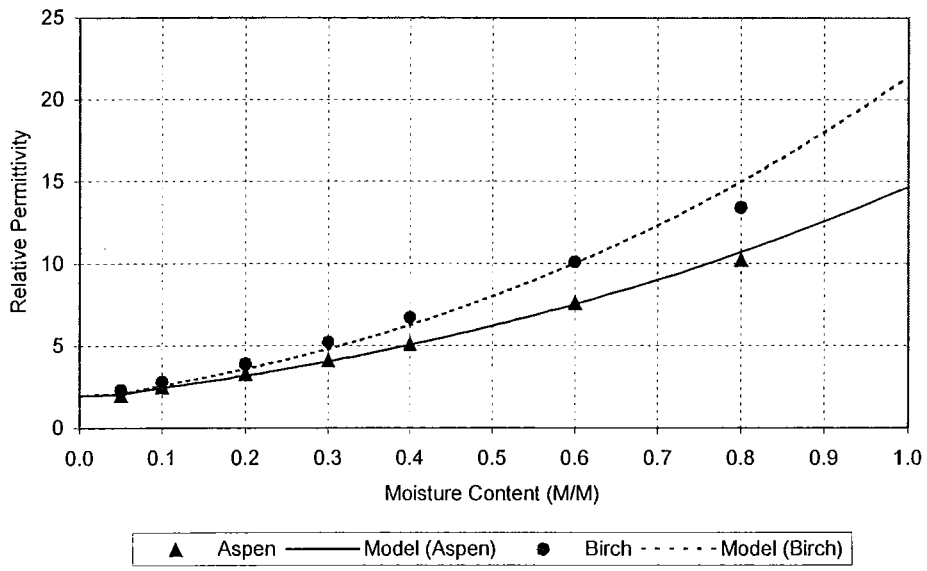

Figure 5.5 Fit of the dielectric model of Eqn (5.5) to ε_r for aspen and birch.

While a deeper study of the influence of physical properties on the performance of the model is beyond the scope of this work, further refinement would seem likely to result in a quite comprehensive dielectric model that apart from one factor (β), may be configured using physical measurements. The observations in §5.4 should be considered in such work.

5.4 The assumptions of the Looyenga model

The derivation of the Looyenga dielectric model is fundamentally different from that of Böttcher (1952) or Bruggeman (1935) in that it although it was derived for spherical particles, it does not rely on that shape for the derivation (Looyenga, 1965). The model was derived by making small changes to the permittivity of the composite material through addition of sub-particles of the inclusion (water in our case) around the host particles. Using Taylor expansions and some manipulation, a differential equation is formed:

$$3\varepsilon_r v''(\varepsilon_r) + 2v'(\varepsilon_r) = 0 \tag{5.6}$$

where $v(\varepsilon_r)$ is the volume fraction of the inclusion. Solving Eqn (5.6) and evaluating the constants leads directly to Eqn (5.1). Although it is claimed that the model is independent of the particle shape (Looyenga, 1965), this is not so. Eqn (5.6) assumes that the addition of a subparticle has the same impact on the total permittivity wherever it is placed in a volume surrounding a host particle, and this is true for a large number of inclusions distributed relatively uniformly around the host particle. Consider however the layered, plate-like or flake structure of clay where the flakes are arranged parallel to an electric field. If a water molecule is added at a random position near one flake, it has a much higher probability of being positioned along a face than at an edge. The local magnitude of the electric field is reduced further when the water molecule is placed near the face than at an edge, so $1/v'(\varepsilon_r) = \partial\varepsilon_r/\partial\theta_v$ is greater than for a near-spheroidal host particle. For a random arrangement of clay flakes or the edge-to-face electrostatic bonding described in Hillel (1980), the porosity is high and there is proportionately less low ε_r mineral for a given path length than the same distance through more regularly shaped particles. This forms one of several possible mechanisms that explain why the $\partial\varepsilon_r/\partial\theta_v$ of bentonite beyond θ_l (Figure 5.3) is greater than that for the coarse-grained soil (Figure 5.2). Consider then a clay soil where the above argument requires that $\partial\varepsilon_r/\partial\theta_v$ is greater than that for a coarse-grained soil. From the general solution to Eqn (5.6):

$$v = c_1\varepsilon_r^{\frac{1}{3}} + c_2 \tag{5.7}$$

$\partial v/\partial\varepsilon_r$ is only reduced if the exponent of ε_r is less than 1/3. In a similar manner for the fixed orientation of tracheids in wood, ε_r could be expected to be modelled more accurately if α of Eqn (5.1) were less than 1/3 for measurements along the grain, and greater than 1/3 for measurements across the grain. Hence it is proposed that a rather more comprehensive version of Looyenga's dielectric model could include shape factors through analysis of the volume distribution surrounding a host particle. Friedman (1997) alluded to the potential of this approach in future development of the statistical model of the soil-air-water matrix.

5.4.1 Distribution of water binding site strength

One area that could be investigated further to achieve better accuracy with a wide range of composite materials is that of dispersion. For example, ε_r of moist larch is significantly higher than that of moist spruce, aspen or birch (Torgovnikov, 1993) and is not accounted for by density. The mean rate of change of ε_r over the θ_v range 20 to 80 % is 0.43 (% V/V)$^{-1}$ for larch, 0.21 for spruce, 0.27 for birch, and 0.26 for aspen. It also has a strong temperature coefficient of -0.21 °C^{-1}, but only above a water content of about 20%. This implies that this threshold θ_v is the fibre saturation point of the wood, above which free water is considered to exist (Skaar, 1988), and hence could be considered to possess the temperature coefficient of water, -0.37 °C^{-1} (Eqn (5.4)). It also implies (rather surprisingly) that the other genera (aspen, birch and spruce) do not have free water at the maximum quoted water content of 80%, and hence ε_r of the included water would be somewhat less than 80. Although these differences

could be accounted for by the free parameter β, a more representative compensation would be to reflect the differences in ε_r of the included water and also in its relaxation time that is greater than that of free water (Trapp and Pungs, 1956, cited in Skaar, 1988).

5.4.2 Temperature coefficient of bulk water

Following on from the above discussion on the temperature coefficient of moist wood, the modelled coefficient needs to reflect that of the bulk water above θ_t, which may differ from that of free water as given by Eqn (5.4).

5.4.3 Distribution of θ_t

A further area for a deeper treatment would be consideration that while θ_t may be well-defined for a particular water molecule binding site, there will normally be a range of binding strengths that would be better modelled by a distribution of θ_t that avoids the abrupt knee indicated by Figure 5.3. However, the knee may be relatively sharp, as indicated by the measured ε_r of bovine serum albumin (Rosen, 1962) at 10 MHz.

5.5 Inversion of the dielectric model

It was noted earlier that both forward and inverse application of the dielectric model is required. If $\theta_v < \theta_t$, Eqn (5.5) is simply rearranged to give:

$$\theta_v = \frac{\varepsilon_m^\alpha - \varepsilon_h^\alpha}{\varepsilon_b^\alpha - \varepsilon_h^\alpha} \tag{5.8}$$

However for $\theta_v > \theta_t$, there is no analytic solution for θ_v, so an approach such as described by Eqn (4.11) was used. These inversions have been incorporated into Listing 6 that is used to recover θ_v from the dielectric and other physical properties.

The procedure used to invert the dielectric model was to solve using Eqn (5.8) and then if $\theta_v > \theta_t$, discard that solution and invert by using Eqn (5.5) for the forward solution, and solve using a damped Newton's method:

$$\theta_v = \theta_0 + J^{-1}\left(\varepsilon_m - g(\theta_t)\right) \tag{5.9}$$

where the *a priori* θ_0 was taken as the transition moisture θ_t, J the rate of change of θ_v with respect to ε_m, and $g(\theta_t)$ the resultant relative permittivity ε_m, at θ_t. Evaluating Eqn (5.5) at $\theta_v = \theta_t$:

$$\varepsilon_m = \left(\varepsilon_h^\alpha + \theta_t \beta \varepsilon_b^\alpha - \theta_t \varepsilon_h^\alpha\right)^{\frac{1}{\alpha}} \tag{5.10}$$

and differentiating:

$$J^{-1} = \frac{\partial \varepsilon_m}{\partial \theta_t} = \frac{\varepsilon_m^{1-\frac{1}{\alpha}}}{\alpha}\left(\beta\varepsilon_b^{\alpha} - \varepsilon_h^{\alpha}\right) \tag{5.11}$$

Thus the recurrence relation is:

$$\theta_{i+1} = \theta_i + \frac{\varepsilon_m^{1-\frac{1}{\alpha}}}{\alpha}\left(\beta\varepsilon_b^{\alpha} - \varepsilon_h^{\alpha}\right)\left(\varepsilon_m - g(\theta_t)\right) \tag{5.12}$$

The inversion method (Listing 6) was not optimised since it is relatively trivial and executes rapidly and reliably.

5.6 Concluding remarks

In this chapter, a generic dielectric model has been formulated with the intention of representing physical influences on ε_r that are relevant to the loss-less and relatively narrow frequency range of TDRI. Despite its simplicity, choosing physical parameters from the literature and just one empirical fitting factor has enabled the model to represent the character of published data sets for coarse-grained soil, a swelling clay (bentonite), wood (of unknown genus) at 1 and 10 GHz, and further data for two different (known) genera of wood. The model translates θ_v to ε_r for the *a priori* distribution required by the TDRI inverse solution, and a damped Newton method was used to invert the model and hence enable translation of the TDRI inversion output from a distribution of ε_r, to θ_v.

Chapter 6

Experimental Validation

In earlier chapters, a forward model was described that predicted propagation velocity (v_p) on a transmission line surrounded by an inhomogeneous distribution of relative permittivity (ε_r). Then using simulated data, an inversion procedure was developed to re-create the ε_r distribution from a set of observations of propagation velocity (v_p) on a parallel transmission line (PTL) at several nearby locations. In this chapter, the experimental equipment is described, and earlier findings and determinations are evaluated by comparison with measured data.

Specifically, predicted edge propagation times (t_p) using the forward model are compared with measurements using phantom dielectric bodies, a physical PTL, and a time domain reflectometer (TDR). Next a phantom is employed for evaluating the inverse solution and the performance is compared with that of the simulations.

6.1 Experimental method (Tektronix 1502C)

Initially, physical verification of the forward solution was accomplished using a Tektronix 1502C TDR and PTL positioned over a water phantom. With a length of 300 mm, the PTL was significantly shorter than the phantom, to enable constant propagation velocity v_p along the PTL. The diameter and spacing of the stainless steel rods were respectively 6 mm and 60 mm, chosen to match that used for the common TDR interrogation of soil moisture. Since very precise measurement of v_p was required, a reference PTL was included so that the difference in path length between the reference and measuring lines was 300 mm. Figure 6.1 shows the arrangement of the measuring and reference lines. The printed circuit board held a can-type relay (similar to Teledyne 172 that has an insertion loss of 0.3 dB at 1GHz and ostensibly identical internal path lengths) that switched the incoming balanced signal to either the reference or measuring PTL. Although impedance matching to the PTL was impractical, earthed lines guarded the relay coil wiring and provided matching dummy guards in all quadrants of the circuit board (Figure 6.2) to ensure similar capacitances and hence impedances to ground for each signal line.

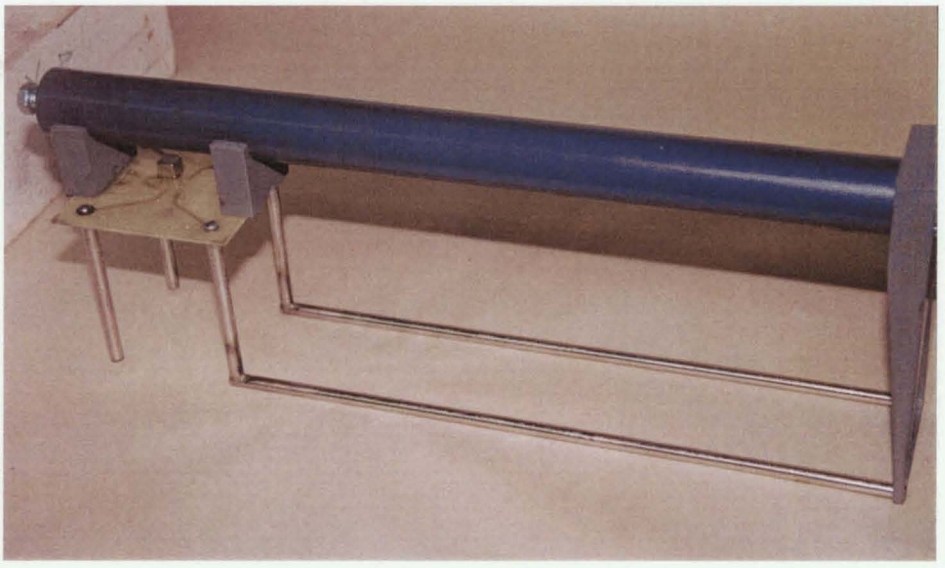

Figure 6.1 Initial PTL assembly showing reference and measuring rods.

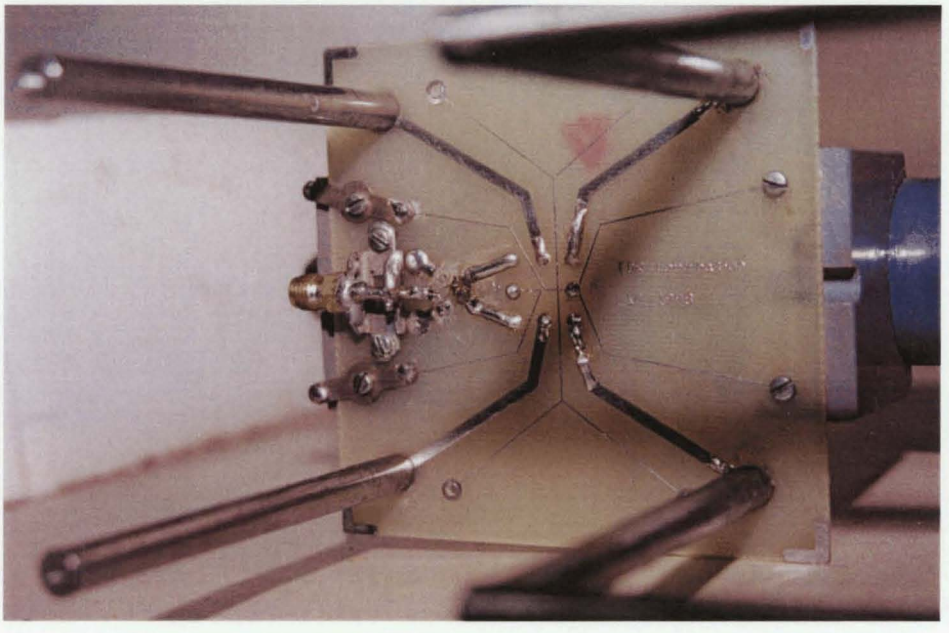

Figure 6.2 Detail of balun, printed circuit board and reference PTL.

A Tektronix 1502C TDR was used to measure t_p. It operates by repeatedly transmitting a voltage step of risetime (t_r) less than 200 ps and recording the resultant time domain (TD) waveform within a window of adjustable position and width. The PTL assembly was connected to the 1502C by 0.8 m of URM 43 (50 Ohm) coaxial cable, and a 1:4 balun mounted on the circuit board converted the unbalanced signal from the 50 Ohm source impedance of the 1502C to a balanced signal for the PTL. The characteristic impedance Z_0 of a PTL is (Ramo et al., 1993):

$$Z_0 = \sqrt{\frac{\mu}{\pi^2 \varepsilon_0 \varepsilon_r}} \cosh^{-1}\left(\frac{b}{a}\right) \tag{4.1}$$

where μ is the permeability (for TDR measurements this is usually taken as the free space value, $4\pi \times 10^{-7}$ H/m), ε_0 is the free space permittivity, b the PTL rod spacing and a the diameter of the PTL rods. z_0 in air is 359 Ohms for $b:a$ of 10:1 for the PTL dimensions used here (and commonly used for TDR measurements in soil where the impedance is lower). Perfect matching (200 Ohm PTL impedance) to the 50 Ohm source through a 4:1 balun would require $\varepsilon_r = 3.2$. This effective permittivity would not be attained with typical TDRI operation ($\varepsilon_r \approx 1.5$ when the PTL is spaced 5 mm from a water phantom). Three methods to improve the matching were considered but were impractical and hence avoided.

1. Change the ratio $b:a$ from the current 10:1 to 2.74:1. This would have resulted in an unacceptably cumbersome PTL.
2. Balun winding arrangements providing higher ratios than 4:1 are uncommon and would further compromise the high frequency performance of the existing balun by additional inductance.
3. A passive impedance matching network could be used but would result in unwanted signal attenuation.

Consequently, the mismatch was accepted, since no characteristics of the TDR waveform could be attributed to the resulting mismatches (Figure 6.3), and Hook and Livingstone (1995) reported no difficulties with such mismatches. Balun construction followed Spaans and Baker (1993) but omitted the initial 1:1 transformer, and used a single, 3.5 mm diameter, grade S3 ferrite toroid. Three turns of 0.125 mm enamelled wire formed each winding. The design was selected as a reasonable compromise between inadequately balanced lines when using a simple transmission line transformer (Hale, 1989), and the degraded t_r of the incident voltage step when the two-transformer balun was used. An HP54121T TDR oscilloscope was used to record t_r at the beginning of the PTL of 250 ps for the above balun, compared with 370 ps for a commercial TDR head used for soil moisture measurement.

The PTL assembly was attached to a manually adjustable x-y mounting to which 10-turn wire wound potentiometers had been fitted to measure position. Potentiometer outputs were measured by an Advantech PCL711S analogue card and provided on-screen readout of position, accurate to 1 mm. The PTL could be moved in a vertical measurement plane under which was located the test body (the PTL was parallel to the surface of the test body and interrogated it using the transverse evanescent field).

For measurement of volumetric moisture content (θ_v) in soil, TDR rods have an open circuit at the end (naturally this facilitates insertion into the soil and causes less soil disturbance). However, short circuit termination provided sharper and better-defined reflections than unterminated lines. Consequently, 6 x 1 mm shorting straps were used to terminate the PTLs.

After propagation along the PTL, t_r of the reflected edge was approximately 500 ps, representing an upper frequency component of 700 MHz. Since this was well below the 17.1 GHz primary relaxation frequency of water (Hastead, 1973), compensation for dispersion or loss was not required in the modelling (Table 6.3 provides measured bandwidths and predicted errors due to relaxation, using a later version of the PTL and balun). Waveform data were retrieved from the Tektronix 1502C, and smoothed and differentiated using 25 point least squares fitting routines (Savitzky and Golay, 1964). Calculating the intersection between the tangents to the maximum negative slope and the immediately preceding inflection point, defined the time of reflection (Figure 6.3). t_p for the reference and measuring PTL was defined by the time between the peak due to the balun (marked + in Figure 6.3 and Figure 6.4) and point of reflection (Figure 6.3 and Figure 6.4). Subtracting the reference time from the measurement time provided the actual t_p of the edge, and ignored end effects which decrease propagation velocity due to end capacitance.

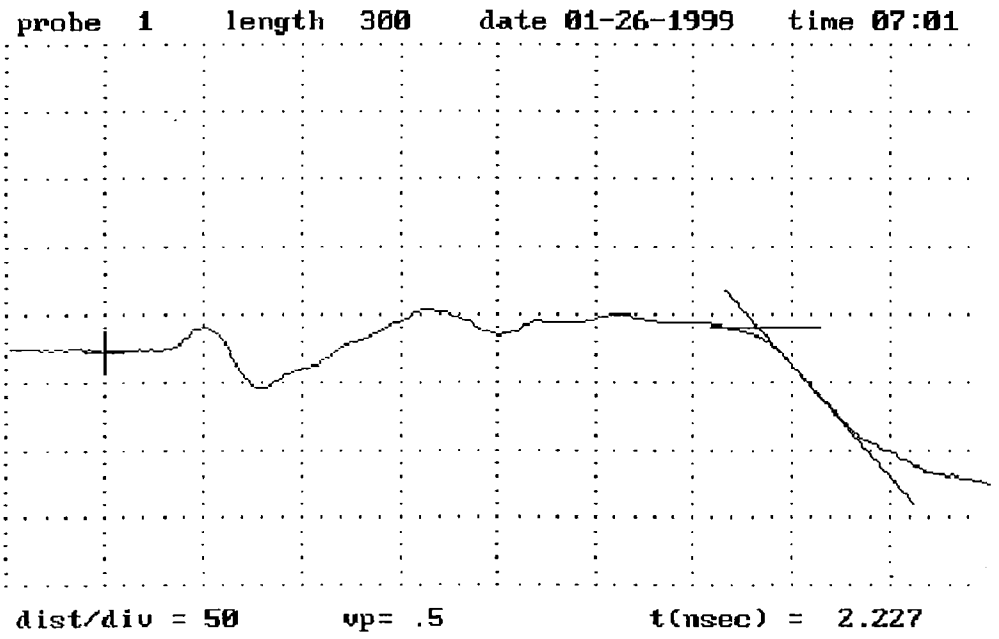

Figure 6.3 TDR measuring waveform with calculated reflection point. The time base is 0.33 ns per division.

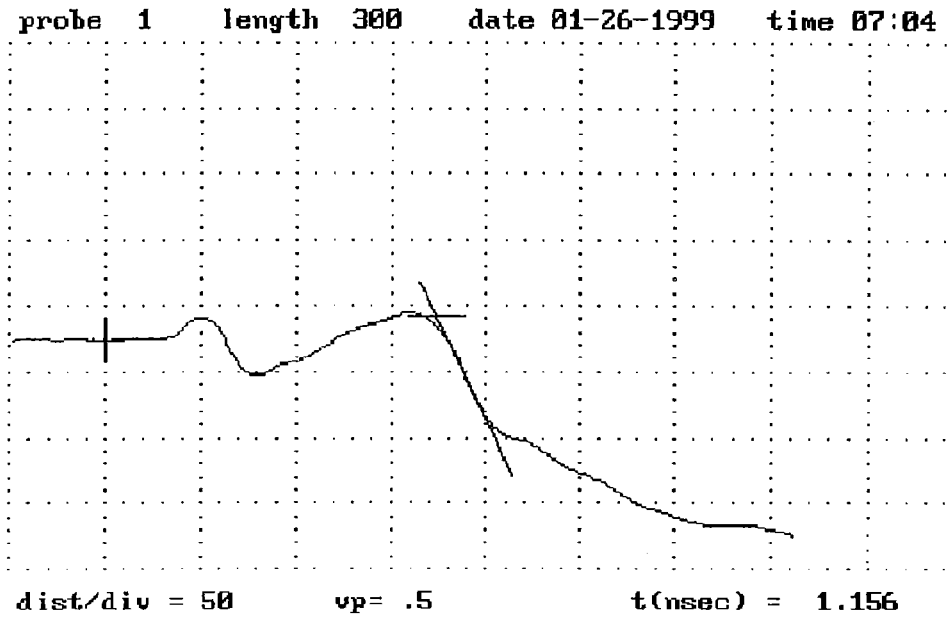

Figure 6.4 TDR reference waveform with calculated reflection point. The time base is 0.33 ns per division.

6.2 Results (Tektronix 1502C)

A rectangular thin walled plastic container 150 mm wide by 500 mm long by 80 mm deep filled with water formed the phantom dielectric body, and the PTL was positioned over the phantom (Figure 6.5). The position (Table 6.1) was defined as the (x, y) distances (mm) between the top edge of the container and the geometric centre of the PTL (Figure 6.5). A 'distant' separation provided a reference reading that was used for comparison with the theoretical 1.001 ns, and to compensate (offset) the discrepancy in the last column of Table 6.1. Model predictions were calculated using 5 mm cubic cells and the pseudo 3-D approach that included the influence of the neighbouring cells in the z direction within the 2-D (xy) matrix (Listing 7). The value of ε_r selected for the water phantom used the relation $\varepsilon_r(water) = 87 - 0.37T$ where T was the water temperature in degrees Celsius. Since there were small differences (20 ps at $y = 5$ mm) between t_p when the PTL was positioned at $x = 0$ mm compared with the opposite position $x = 150$ mm, the table entries for $x = 0$ mm were the mean of the two measurements. The compensated discrepancy values in the table were offset from the discrepancy column by the 'distant' or free space discrepancy.

Table 6.1 Comparison of measured (Tektronix 1502C) and calculated t_p.

Position (mm)	Measured (ns)	Model (ns)	Discrepancy (ps)	Compensated Discrepancy (ps)
0, 5	1.061	1.073	12	-10
0, 10	1.011	1.044	33	11
0, 20	0.997	1.022	25	3
0, 30	0.992	1.014	22	0
75, 5	1.172	1.196	24	2
75, 10	1.047	1.108	61	39
75, 20	1.009	1.046	37	15
75, 30	0.998	1.025	27	5
distant	0.987	1.009	22	0

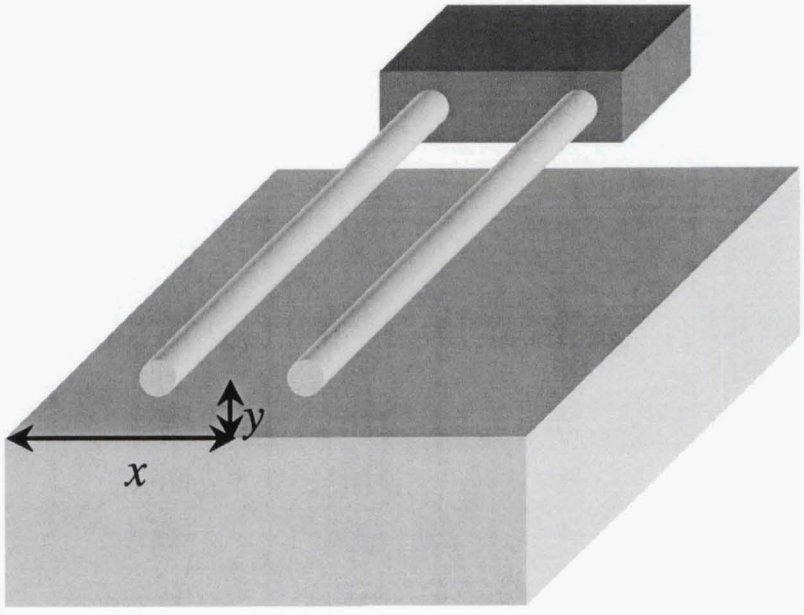

Figure 6.5 Position of PTL and phantom dielectric body (a water-filled container).

Although the compensated discrepancies were small in relation to the total t_p, the errors are significant when compared with the change in t_p from the distant ($\varepsilon_r = 1$) case to the $y = 5$ mm case. Although the most significant discrepancy (which occurred at position (75,10) mm) could be attributed to model errors as summarised in §2.5.3, we would expect greatest model errors when the rods were near the phantom, and hence the field gradients were large. More likely is that the repeatable discrepancy of 39 ps for (*x*,*y*) = (75,10) mm was due to measurement error. The differencing technique using the reference PTL was intended to remove consistent errors from the measurements, but instrument errors would still be expected to dominate. Note that the resolution of 12 ps (0.004 feet/0.66c, Tektronix (1996), where c is the free-space speed of light) was not a fundamental limitation since following a smoothing process, values of t_p were obtained from the intersection of tangents that linearly interpolate between data points. One source of error is small perturbations in the time-base ramps of the Tektronix 1502C due to non-linearity or ripple (Hook and Livingston, 1995). A series of measurements were made using the Tektronix 1502C and different lengths of connecting cable (Table 6.2).

Table 6.2 Measured time base errors for the Tektronix 1502C.

Position (mm)	Additional cable (mm)	Additional time (ns)	Propagation time (ns)
75,5	0	0	1.147
75,5	100	0.33	1.203
75,5	200	0.66	1.166
75,5	300	1	1.177
75,10	0	0	1.065
75,10	100	0.33	1.091
75,10	200	0.66	1.051
75,10	300	1	1.046

The 'additional time' column in Table 6.2 assumes $v_p = 0.8c$ in the URM43 cable. Since, for the $y = 5$ mm case, the t_p varied by 56 ps between 0 and 333 ps, we could infer (linear interpolation) that the error is at least 17% for a relative change in reading. Hence for the readings in Table 6.2 at positions (75,5) and (75,10), the error could be expected to be at least 15 ps. The observed discrepancy was 39 ps.

6.3 Experimental method (HP54121T)

To further improve the precision of physical measurements, a higher precision TDR instrument and preferably a voltage step with more rapid t_r would be required. A Hewlett Packard (HP but now renamed Agilent) HP54121T digitising oscilloscope provided a measurement time resolution of 10 ps on the 500 ps/div scale used, and an accuracy of 0.4 ps (however note from

§2.4.1 that amplitude or x-axis accuracy is also an influence on time measurement accuracy for non-ideal signals or signals with finite t_r), and a voltage step with t_r of less than 50 ps. The HP54121T also incorporates software for deconvolving the resultant waveform by the incident trace that incorporates the voltage step, a process included within the instrument's 'normalisation' (Hewlett Packard, 1989). The deconvolution reverses (subject to limitations due to noise and nonlinearity) the instrument limitation whereby the ideal step function $H(t)$ is convolved with the instrument response $r(t)$ (Boyce and DiPrima, 1976). In this case, it describes the degradation of $H(t)$ by the HP54121T's pulse generator and measuring circuits:

$$s(t) = \int_0^t H(t-\tau)r(\tau)d\tau \tag{4.2}$$

where $s(t)$ is the resultant TDR waveform. The normalisation process employs calibration using a precision short circuit and 50 Ohm (non-reflective) termination at the reference plane and is attributed to Bracewell (Hewlett-Packard, 1989). Simulation of voltage steps with t_r as short as 12 ps is possible with normalisation, which also removes other artefacts that occur prior to the measurement plane, such as changes in cable impedance and spurious reflections from connectors.

While improving the performance of the instrumentation, it was necessary to reconsider the limitations imposed by the balun and PTL. Although the balun was imposing significant limitations on t_r with the HP54121T step generator, there was a compromise between t_r from the balun and the symmetry of the signal from the balun, which is translated to the individual sensitivity of each PTL rod. Limitations also became apparent when using the faster HP54121T TDR. Measurement of the reflections from shorts placed along the PTL revealed that degradation in t_r from series loss of the stainless steel PTL rods, exacerbated by the skin effect, was also limiting performance of the TDR system. A new PTL made from brass rod rendered negligible, the 100 ps t_r degradation along the stainless steel PTL rods. To enhance signal symmetry, a 1:1 isolating balun (Spaans and Baker, 1993) was added between the TDR and the Guanella balun (Figure 6.6).

A further change from the previous arrangement was to dispense with the reference PTL. Instead, a reference comprising a HP5082-3188 PIN diode (on-resistance $R_s = 0.6\,\Omega$ at a diode current $I_d = 10$ mA, and reverse bias capacitance $C_t < 1$ pF at 20 V) at the beginning of the measuring portion of the PTL, was used in a manner similar to Hook et al. (1992). A bias network (Figure 6.6), enabled the PIN diode to be switched on for a reference measurement. However, contrary to the findings of Hook et al., (1992) for the lower sensitivity measurements in soil, the effect of changing the reverse bias on the diode was apparent up to 20 volts, although the forward current had little effect once the diode was forward biased. Consequently, plus 5 V was applied to Vs (Figure 6.6) to select the reference measurement mode ($I_d \cong 10$ mA) and minus 20 V to measure total t_p. The variable resistance was used to balance, as far as practicable, the sensitivity of each PTL rod.

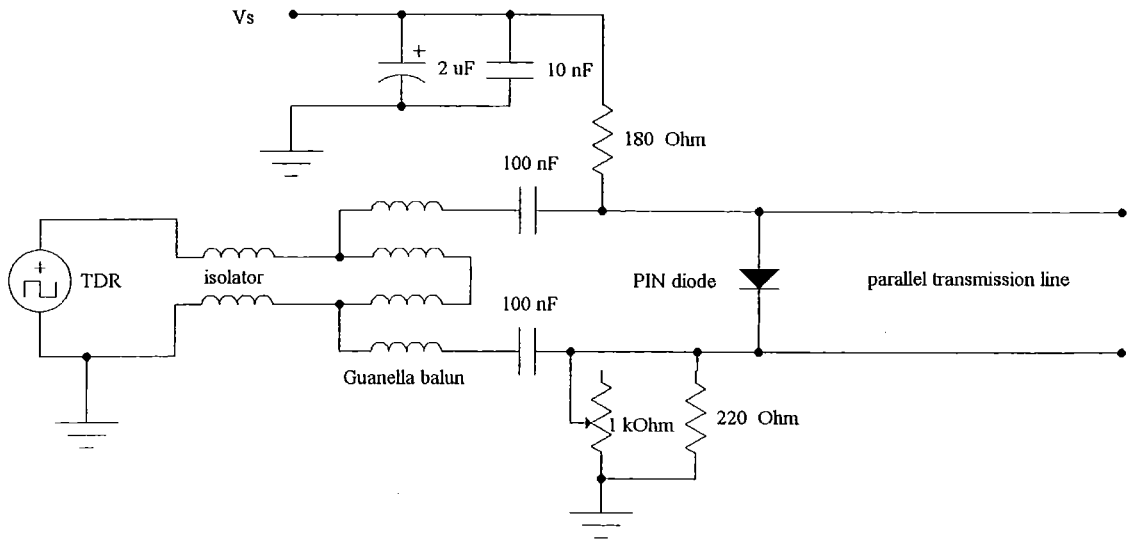

Figure 6.6 Circuit of balun, PIN diode bias and balancing network.

The IEEE488 interface on the HP54121 was connected to an HPIB (IEEE488 communication standard) card and measurement data (comprising *x-t* pairs) were normalised, retrieved and filed. The data were then imported into a Matlab routine (Listing 8) that calculated t_p. In this instance, the waveform with the diode shorted was subtracted from that with the unshorted diode, providing both perturbations in one data set, and cancelling perturbations due to changes in cable impedance and spurious reflections from connectors. The HP54121T output was normalised with the reference plane located at the connector between the cable and the balun. Normalisation was also evaluated with the reference plane located at the PIN diode, and using a 270 Ohm resistor at the end of the PTL as the '50 Ohm load' (determined experimentally as providing the flattest response at the end of the PTL rods). However the resulting t_p deviated significantly from both the output from the forward model and from previous readings (Table 6.1). This is assumed to be due to minor errors in the normalisation process, also apparent in Hewlett Packard (1989), where the time between the leading corners of the pulse pairs change when normalisation is applied.

The point of reflection was determined from the intersection of tangents to the maximum slope of the returned edge and the preceding plateau in a manner similar to that used by van Gemert (1973) and Or et al. (1998). The effective frequency that is most influential in determining the position of the returned edge is that with the same slope as the tangent, ie the highest frequency component. The usual method of determining the highest frequency is (Brazee, 1968) $bw = 0.35/t_r$ where the bandwidth (bw) actually refers to the highest frequency component present assuming the lowest is zero, and t_r is defined as the time for the signal to change from 10% to 90% of the amplitude of the step function. These were determined for the PTL positions used with the water phantom (Table 6.3). In this case the method overestimates the frequency for the $x, y = (75, 5)$ position since the tail of the waveform was beyond the range of the 500ps/div HP54121T timebase setting (chosen to maximise the time resolution). The method differed from the approach used by Heimovara (1994) who calculated the standard

deviation of the scatter function versus frequency using three separate measurements in demineralised water. Since the standard deviation increased above 1.5 GHz, that was considered to be the bandwidth of the measuring system (a 7-wire probe without balun was employed). Table 6.3 also indicates the expected error in ε_r due to the relaxation of free water where $\lambda_r = 1.8$ cm (Hastead, 1973). The calculation used a single Debye relaxation (Debye, 1929), at the effective measurement frequency for each position of the PTL. A maximum error of $\varepsilon_r = 0.21$ or approximately 0.3 % suggests relaxation generates no significant error for the balun used here. The HP54121T digitising oscilloscope was normalised at the balun connector and set for $t_r = 40$ ps (normalised t_r).

Table 6.3 Characteristic measurement frequency and ε_r error due to free water relaxation.

Position (mm)	Effective Frequency (GHz)	Error in ε_r
0, 5	0.62	0.11
0, 10	0.72	0.14
0, 20	0.84	0.19
0, 30	0.87	0.21
75, 5	0.59	0.1
75, 10	0.66	0.12
75, 20	0.81	0.18
75, 30	0.88	0.21
distant	0.9	0.22

It became apparent from the analysis of readings from the enhanced instrumentation that the readings deviated significantly from those obtained previously with the 1502C, and those generated from the model when the PTL was positioned near the water phantom. The deviations coincided with significant deviation between the maximum slope of the reflected edge and that from the shorted reference edge. Although the tangent intersection method was similar to that commonly used for measuring travel times with TDR (van Gemert, 1973; Or et al., 1998), the method induced limitations due to changes in slope. The effect of a reduction in slope is to move the intersection point back towards the start point, thus to some extent, masking the slower v_p when near the phantom. These discrepancies could have been masked in previous TDR measurements. First, van Gemert (1973) was working with small samples so the impact on slope would have been quite small. In measurements of soil moisture, the accuracy demanded from measurement of t_p in soil is much lower than for this work.

Measurements of t_p employed here use the difference between two edges (shorted diode and non-shorted diode) and are dependent for accurate measurement on the exact timing of the highest frequency component in the edge. Table 6.3 indicates the almost 2:1 t_r difference for different positions of the PTL, and Figure 6.7 illustrates the effect using Fourier reconstructions of an edge comprising the fundamental and first harmonic in the frequency-limited trace, and a further two harmonics for the broader band trace.

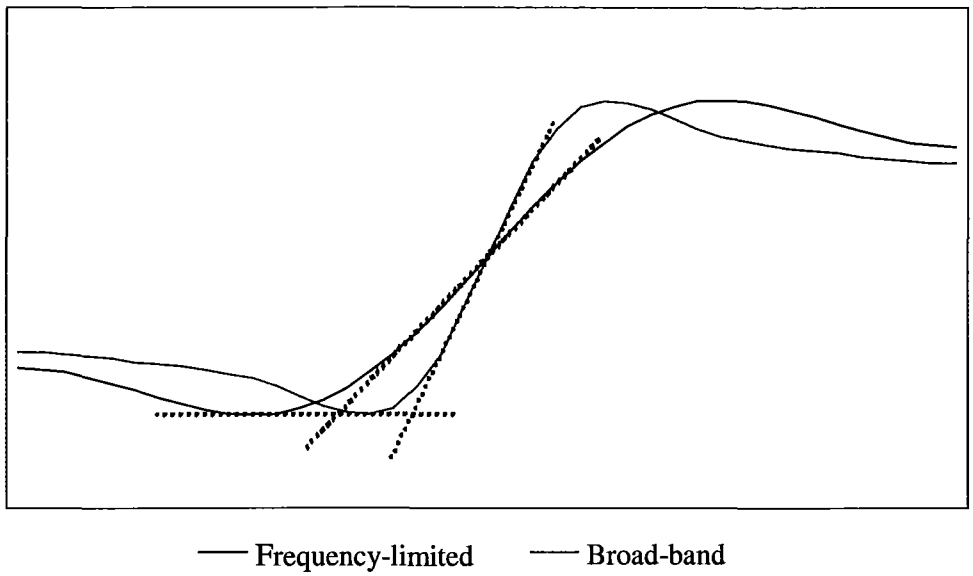

Figure 6.7 Typical reflected edges with differing slope using Fourier reconstruction with a) fundamental and first harmonic only (frequency-limited trace), and b) a further two harmonics. The hand-drawn tangents indicate the different edge positions using conventional TDR analysis.

The method used here to circumvent the effect of changing slope was to calculate the slope of the tangent with the diode unshorted, and use the same tangent slope for the shorted diode reference. The tangent representing the reduced bandwidth edge is positioned at the point of maximum slope on the reference waveform (Figure 6.8 and Figure 6.9). The above tangent technique could be applied to improve the accuracy for TDR measurements in soil and other materials. It is expected that some of the discrepancies that have been noted in the literature for clays and electrically conductive soils (eg Jacobsen and Schjonning, 1995) and attributed to modelling error, could result from waveform interpretation error.

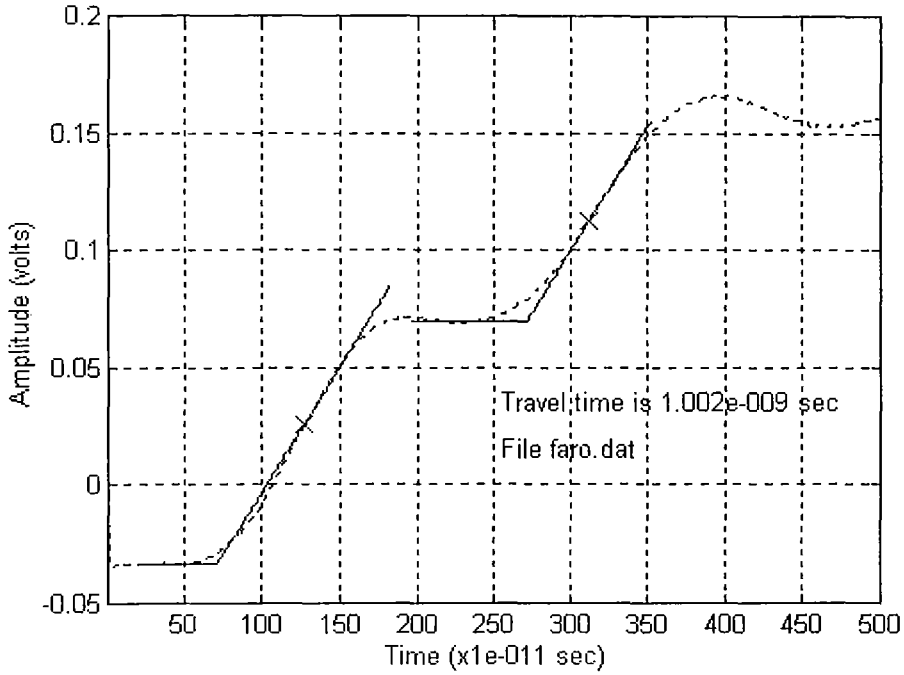

Figure 6.8 Difference waveform and same-slope tangents for TDR measurement with no phantom.

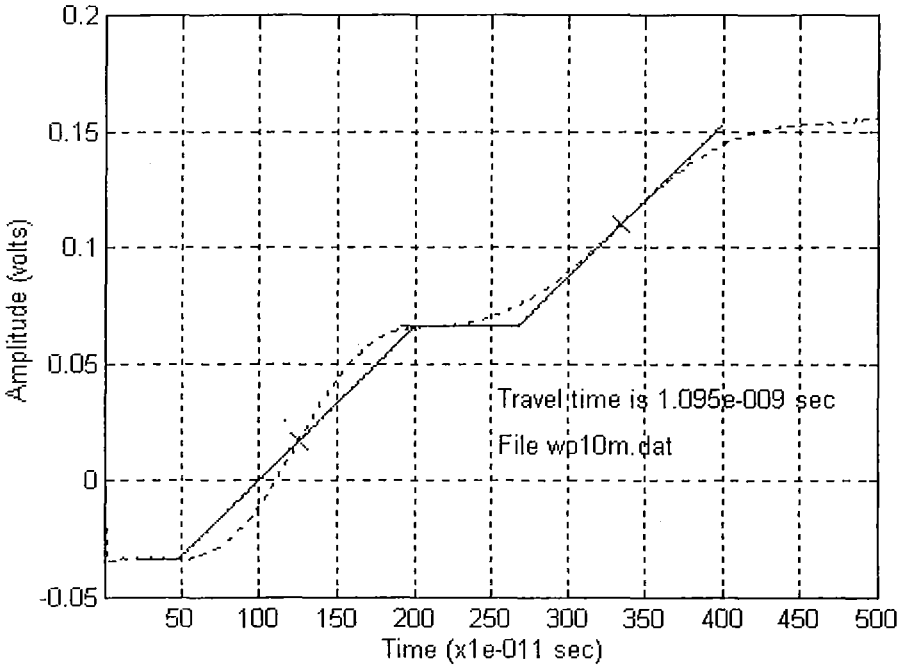

Figure 6.9 Difference waveform and same-slope tangents for PTL centred 10 mm above a water phantom.

Using the above approach, travel times were calculated from measurements obtained using the brass PTL with the same phantom and positions measured earlier (Figure 6.5). As with the Tektronix 1502C trial, PTL end effects were ignored. Using the dominant frequency

component of Table 6.3 and the guidelines of Hale (1989) for a dipole antenna, an end effect correction of 4% is suggested. Quantification of this value would ideally be incorporated in future improvements to the forward model.

6.4 Results (HP54121T)

The readings recorded when the PTL was positioned over an edge of the phantom were averaged with the reading from the opposite edge. With the exception of the (75,5) reading, the measurement errors reported with the enhanced instrumentation (Table 6.4) are more consistent than the previous readings (Tektronix 1502C, Table 6.1), supporting the notion that the observed scatter in the readings from the latter were primarily instrumentation errors and that these have been substantially reduced. The error in reading (75,5) is most likely due to measurement error since it is very sensitive to height of the PTL above the water phantom (the reading changed from 1.095 to 1.252 between 10 and 5 mm, and is not a linear function). Note that the physical position measurements were not replicated but the HP54121T measurements were. Some doubt also remains on the model accuracy at such high rates of change of field strength across cell boundaries as discussed in §2.3.3 and §2.3.4, and will form the basis of future work by the author. The impact of the discrepancy between the model and the measurements on TDRI is discussed in §4.7.

Table 6.4 Comparison of measured (HP54121T) with calculated t_p.

Position (mm)	Measured (ns)	Model (ns)	Discrepancy (ps)	Compensated Discrepancy (ps)
0, 5	1.077	1.073	4	11
0, 10	1.043	1.044	-1	6
0, 20	1.026	1.022	4	11
0, 30	1.005	1.014	-9	-2
75, 5	1.252	1.196	56	63
75, 10	1.095	1.108	-13	-6
75, 20	1.028	1.046	-18	-11
75, 30	1.014	1.025	-11	-4
distant	1.002	1.009	-7	0

To further improve measurement accuracy and enable a better comparison between the model predictions and measured values, further improvement would be required to interface the

balanced PTL with the unbalanced signal from the HP54121T oscilloscope. Possibilities include:

1. Further improve the balun. For example, the model 5315 balun from Picosecond Pulse Labs of Colorado USA, comprises a passive splitter, a 1:1 inverting transformer driving the 50 Ohm inverting output, and a short length of coaxial cable to delay the non-inverting output to match propagation times. The performance is stated as having a maximum risetime of 25 ps and an insertion loss of 8 dB. However this approach does not provide a balanced, differential signal back to the TDR instrument.
2. Dispense with the balun and use a three-pronged transmission line with a centre signal rod and two grounded rods. The issues with this arrangement are to confirm that propagation along the rods remains TEM, and that the dielectric model for the PTL can be adequately adapted to suit the altered field distribution. The same caution as above would apply since an unbalanced signal is potentially subject to error from asymmetric impedance to ground.
3. Design and construct a balanced step generator in place of the HP54121's own unbalanced generator, and use two channels of the 54121T or other TDR to digitise each of the balanced lines. There would be significant work with this approach including the design of the step generator, and arranging for normalisation.

6.5 Evaluating TDRI

6.5.1 Timber Phantoms

Phantoms made from stacked cuboid timber billets were used for verifying the complete TDRI procedure. To prepare the timber cuboids, both wet and dry straight-grained *Pinus radiata* sticks were cut to a length of 400 mm and sectioned to 20 by 20 mm, forming cuboid-shaped billets. They were dipped in molten wax to provide a thin coating that has been shown to greatly reduce moisture loss or gain from the air (Fuller pers. comm., 2000), and stacked to form composite sticks of timber for use as phantoms. The discarded portions of the original sticks were used to determine moisture content and density. θ_g, the gravimetric moisture content was determined for each discarded billet by drying at 105 °C until no further weight loss occurred (typically 12 hours for the small billets used here). Dry density ρ, was then determined by using the known dimensions of the billets (Table 6.5). The dielectric model described by Eqn 5.5, was configured for birch but with the measured density of the *pinus radiata* billets, and used as a predictor of ε_r for Table 6.5.

Table 6.5 Measured θ_g, dry density (ρ), and calculated ε_r (from Eqn 5.5) of wooden billets. The billets were cut from two sticks of timber, one at $\theta_g = 0.15$ and $\rho = 0.37$ g/cm^3, and the other at $\theta_g = 0.32$ and $\rho = 0.41$ g/cm^3.

Billet	θ_g	ρ (g/cm^3)	ε_r
1	0.15	0.37	2.6
2	0.32	0.41	3.7

6.5.2 Automatic positioning of PTL

Since TDRI requires a number of measurements from an accurately positioned PTL, automatic positioning apparatus was designed. 1 mm pitch lead screws driven from 7.5° stepper motors were used to provide accurate positioning within the *x*-*y* plane (Figure 6.10).

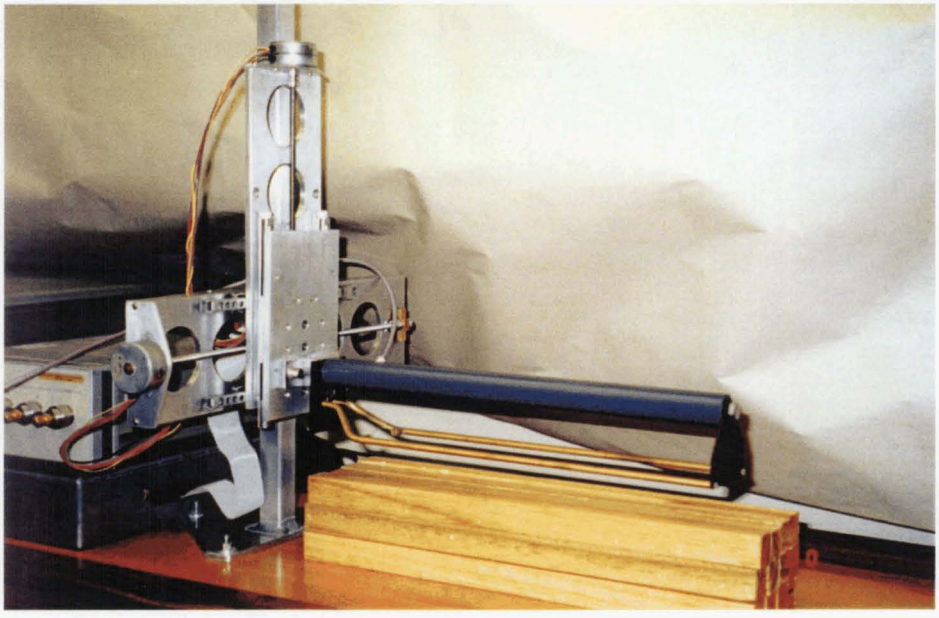

Figure 6.10 *x*-*y* positioning apparatus with PTL.

Two stepper motor driver boards (Radio Spares part number 217-3611) were used with 47 Ohm, 5W resistors to set the current in each 25 Ohm stepper motor (Panasonic PJJ027ZA-P) windings to 0.22 A. The boards require a clock and direction input, and these were provided from a standard PC printer port via open-drain level shifters using 2N7000 field effect transistors. The driver unit was powered from an external 16.5 V, 2A power supply.

Provision was made for incorporating optical sensors to enable positioning the PTL at a 'home position' when powering-on (stepper motors only provide relative positioning). However for the tests described here, initial positioning was achieved manually. A computer was used to control the PTL position through the clock and direction lines for the two driver boards, allocated to data lines 0 through 3 of the parallel printer port. Given a particular moisture distribution, measurements were recorded for each position in the *x-y* plane. The sequence was:

1. Move to the next *z-y* position of the PTL
2. Normalise the current TDR trace on the HP54121 oscilloscope, pass to memory #1, and then retrieve the *x-t* oscilloscope readings and write to a local file.
3. Retrieve *x-t* data from the local file and determine the t_p as the difference between t_p for the shorted diode and t_p for non-shorted diode, each defined by the intersection of tangents as described in §6.3.
4. Compile an array with PTL position and t_p in the same format as required for the inversion procedure.

6.6 Validation of TDRI

The final step in the development of TDRI is validation of the entire process using measured data. This comprised the experimental arrangement described in §6.3, a configurable phantom using timber as the composite material, the forward model of §3.7 with the blocking CG inversion scheme of §4.3 to §4.9, and the dielectric model of section §5.1 using parameters for cross-grain measurement of timber.

The billets were stacked to form a phantom similar to the shape of the target distribution in Table 4.14, and although the shape of the distribution was known *a priori*, the values were chosen before θ_g and hence ε_r of the billets (Table 6.5) were known. The parameters of Table 5.2 were used with the dielectric model for wood with the respective measured densities to convert the *a priori* distribution in θ_g to ε_r (Table 6.6). θ_g rather than θ_v is used since it is the prevalent form for representing θ in wood. Table 6.7 shows the actual distribution assembled from *Pinus radiata* billets. Had the size of the cells been chosen to coincide with the 20 by 20 mm billets, very coarse discretisation would have resulted. In the zone between the PTL rods, just two entire cells plus a portion of the rod cells would have represented the potential difference. Hence the size of the model was expanded to cells of 10 mm by 10 mm cross-section, and each timber billet was represented by four cells.

Table 6.6 The *a priori* distribution chosen for TDRI validation with wooden (*Pinus radiata*) billets, in units of (a) θ_g and (b) ε_r.

0.2	0.2	0.2	0.2	0.2	0.2
0.2	0.2	0.2	0.2	0.2	0.2
0.2	0.2	0.5	0.5	0.5	0.5
0.2	0.2	0.5	0.5	0.5	0.5
2.7	2.7	2.7	2.7	2.7	2.7
2.7	2.7	2.7	2.7	2.7	2.7
2.7	2.7	5.7	5.7	5.7	5.7
2.7	2.7	5.7	5.7	5.7	5.7

Table 6.7 Actual distribution in wooden phantom used for validation of TDRI, in units of (a) θ_g and (b) ε_r.

0.15	0.15	0.15	0.15	0.15	0.15
0.15	0.15	0.15	0.15	0.15	0.15
0.15	0.15	0.32	0.32	0.32	0.32
0.15	0.15	0.32	0.32	0.32	0.32
2.5	2.5	2.5	2.5	2.5	2.5
2.5	2.5	2.5	2.5	2.5	2.5
2.5	2.5	3.9	3.9	3.9	3.9
2.5	2.5	3.9	3.9	3.9	3.9

The collected data were compensated by subtracting an offset. A distant (no phantom) reading using the same reference waveform as the readings in Table 6.8, provided a t_p reading of 1.009 ns, 8 ps higher than the theoretical free space propagation over the 300 mm length of the PTL. Hence the Table 6.8 readings comprise the original reading minus 8 ps.

Table 6.8 Measured TDR data from the timber phantom of Table 6.7.

x1	y1	x2	y2	Measured Travel time (sec)	Discrepancy with solution (ps)
3	8	9	8	1.090e-009	-2.1
6	8	12	8	1.045e-009	2.8
1	7	7	7	1.019e-009	-2.6
3	7	9	7	1.022e-009	4.3
6	7	12	7	1.018e-009	-0.8
1	6	7	6	1.005e-009	2.2
3	6	9	6	1.012e-009	-1.5
6	6	12	6	1.008e-009	-0.5

Then the CG blocking method described in §4.8 with the inversion parameters of Table 4.12 but with max_corr = 0.5 and block_limit = 0.5 as described in §4.9, and the measured data of Table 6.8, were used to predict the ε_r distribution of Table 6.7. The results of the inversion process (Figure 6.11) show the actual and predicted ε_r distributions. It is apparent that the inconsistent data in Table 6.8 (revealed by the discrepancies with the model predictions) has lead to a relatively shallow minimum with an objective function of 2.65×10^{-23} (a discrepancy of 1 ps between corresponding measured and model values of t_p provides an objective function of 8×10^{-24}).

Table 6.9 TDRI solution in units of (a) θ_g and (b) ε_r (compare with the actual phantom data of Table 6.7).

0.12	0.1	0	0	0.16	0.17
0.16	0.13	0	0.13	0.1	0.07
0.16	0.11	0.41	0.4	0.43	0.42
0.15	0.16	0.45	0.44	0.42	0.46

2.3	2.2	1.7	1.6	2.6	2.7
2.6	2.3	1.8	2.4	2.2	2.0
2.6	2.2	4.8	4.7	4.9	4.8
2.5	2.6	5.2	5.0	4.8	5.3

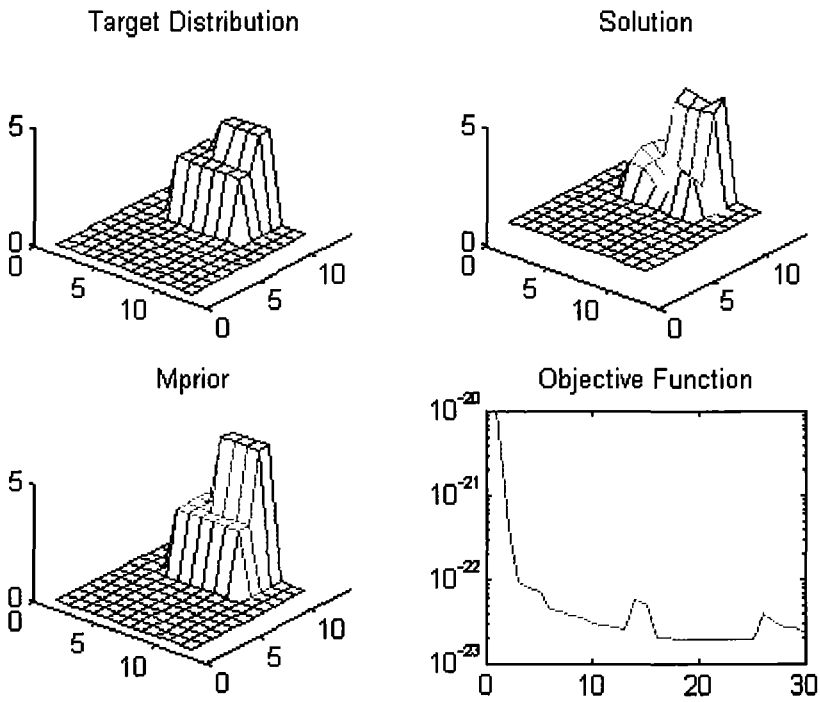

Figure 6.11 Results from inversion of measured data in Table 6.8.

The zero values of θ_g in Table 6.9 are a direct result of the limits imposed by the inversion process. Hence an appropriate lower bound for ε_r when used in industrial measurement with the dielectric model for wood, corresponds to $\theta_v = 0$, in this case $\varepsilon_r = 1.8$. It is also apparent that the near-zero $\frac{d\varepsilon_r}{d\theta_g}$ for wood when θ_g is small (Fig 5.4), constrains the accuracy.

6.7 Concluding remarks

The experimental work described here has provided validation of the dielectric model for distances between a water phantom and the PTL of 10 mm or more. For spacing less than 10 mm, errors may have been contributed by either the model, or by the experimental equipment and techniques. Model errors are most likely a result of the steep field gradients, and it is expected that those errors would be reduced by the use of higher order basis functions than the pulse basis functions used here. However, a different approach to the problem would be required than that described in §3.9. Work currently in progress (by the author) uses a hybrid approach where pulse basis functions are retained, but the field due to the polarisation in nearby cells, is integrated over the volume of each field cell. The integration recognises the non-linear field distribution over the field cell and provides an "effective" distance between source and field cell to compensate for the non-linearity. Although incomplete, the procedure provides significantly smaller discrepancies when used with the water phantom than the model used for

generating the figures in Tables 6.1 and 6.4. Measurement errors would need to be addressed by reducing t_r, in order to reduce errors in measuring t_p, in turn addressed by an improved balun or alternative means to generate and detect a balanced, fast t_r step. An active step generator with complementary outputs using for example, two step-recovery diodes with matched storage times could achieve this.

As expected, introducing a small amount (< 1ps) of Gaussian noise to simulated data perturbed the solution, but increasing noise amplitude produced increasingly inconsistent data and shallow solution minima. However, as noted in §4.2, forward modelling errors and measurement errors are not distinguished by TDRI, but any discrepancies result in an inconsistency between observed and predicted t_p. For use in an industrial environment, a probability distribution function (PDF) quantifying the errors would enable some inconsistency to be mitigated through weighting by the covariance matrices (C_d and C_m in Eqn (4.1) which were unit matrices to provide uniform weighting for this work).

Although there remains further work on improving both model accuracy and measurement accuracy, inversion of measured data has been successful and hence has validated the TDRI principle. Discrepancies between the actual and predicted θ_g for a binary distribution in wood provided a mean error of + 0.11 and –0.09 for the wet ($\theta_g = 0.32$) and dry ($\theta_g = 0.15$) billets. Although the current error level is barely adequate for measurements in wood (an accuracy in θ_g of 0.02 to 0.04 is required), the greater $\frac{d\varepsilon_r}{d\theta_v}$ of soil (approximately four times that for wood), indicates that the technique would already be useful in its current form.

Chapter 7

Conclusions and Suggestions for Future Work

The objective of this research was to develop a new technique to enable non-invasive, non-destructive measurement of moisture content (θ_v) distribution in composite materials. The result of this work is time domain reflectometry imaging (TDRI), a new method for non-invasive, non-destructive imaging of the moisture content of composite materials. It features shallow probing within the composite material (typically to 100 mm), quantitative measurement of θ_v distribution, and instrumentation-dependent spatial resolution.

7.1 Conclusions and achievements

A moment method (MM) solution for the electric field in a heterogeneous dielectric has been adapted to model the propagation velocity (v_p) on a parallel transmission line (PTL) immersed in a heterogeneous permittivity distribution. A pseudo-3-D variant was devised to greatly speed up the calculation, and significantly reduce the memory required to execute the model. These developments have provided a rapid, quantitative modelling technique that is ideally suited to form the forward model of an inverse problem. In this application, the technique has overcome the main drawback of volume integral equation (IE) modelling (ie large, full matrices), without impacting on its significant advantage of only requiring modelling within the anomalous region. Hence for inverse solutions, the benefit of an IE forward model wherein recalculation is not required for a new source position (ie for a change in position of the PTL) and only the anomalous region requires modelling, has been achieved while avoiding the penalties of a large and full scattering matrix.

A new integration technique was devised to provide accurate interpolation of the electric field between the PTL rods. The method used the theoretical field relationship to define the shape of the curve between calculated points, along with the predicted permittivity (ε_r), to quantitatively define the field. Discontinuities at cell boundaries are accommodated by the approach. The method has provided demonstrably improved accuracy, and improved extrapolation near the virtual singularity within the rod cells.

The dielectric model described in Chapter 5 was intended as a broadly applicable but not necessarily very accurate model. However it is usefully based on measurable or predictable physical parameters, and has demonstrated that straightforward inclusion of a single bound water component is able to account for the atypical dielectric behaviour of a swelling clay, while using

one empirically-determined fitting parameter. Inversion of the model has enabled its use for TDRI.

A conjugate gradient (CG) inversion method was developed for inverting TDRI measurements of a composite material and included several new or alternatively applied techniques.

- Rather than using the computationally intensive line search for each CG iteration, an approximate, dynamically-determined CG weighting factor was used. This approach reduced by a factor four, the number of forward calculations required for an inversion.
- A rapidly calculated electric field strength surrogate was used for the Jacobian. It provided a direct relationship between the electric field and the propagation time, and hence differed from use by others of an electric field surrogate. It was also factored by the dynamically determined CG weighting factor.
- To accelerate the convergence of buried and less influential regions of the composite material, a blocking scheme was devised that further improved inversion performance. When coupled with introduced *a priori* starting distributions, blocking provided rapid convergence, typically requiring just 20 forward calculations.

Development of the above techniques has resulted in an inversion scheme that by all accounts is robust and, provided the *a priori* solution is the nearest deep minimum to the actual solution, it converges rapidly (typically within 20 iterations for 12 unknowns).

The techniques described here have been validated by the use of simulation and self-validation, and also by measurement on a physical PTL. It was also shown that to achieve accurate measurement of the very short travel-times on the 300 mm PTL, very high speed instrumentation, and PTL rods with high electrical conductivity are required. The balun is also critical. It must allow short risetimes, preferably no greater than the 50 or so picoseconds of a high speed TDR pulse, yet effectively convert the typically unbalanced source to a well-balanced signal to avoid asymmetrical sensitivity from the PTL. Finally, determination of the propagation time must account for the significant changes in slope of the returned edge. In this work, this was achieved by recording the slope of the slower edge (which occurs during normal measurement) for use as a tangent slope in the reference or shorted diode measurement.

The consequence of the advances listed above is that the fundamental theory and practical aspects of TDRI have been explored and developed to provide a new method for quantitative, non-invasive measurement of moisture content distribution in composite materials. Although further enhancement of instrument accuracy will be required for useful measurement of moisture distribution in timber (§6.6), the greater $d\varepsilon_r/d\theta$ for soil suggests that the techniques would already be useful for monitoring moisture distribution in soil.

Assuming an improvement in measurement accuracy to enable θ measurement accuracy of 2%, TDRI would have immediate use in the following industrial and soil science related applications:

- Tracking diurnal, near-surface changes in soil moisture content
- Mapping spatial distribution of soil moisture
- Detecting moist areas beneath chip seal that may lead to pothole formation
- Control of drying (eg in a timber drying kiln)
- On-line measurement of moisture distribution in kiln-dried timber
- Measurement of moisture distribution in unpeeled logs for prediction of sapstain susceptibility
- Detecting possible moist regions in packed materials such as powders and grains
- Measurement of moisture distribution in textiles (eg wool cones).

7.2 Suggestions for future work

TDRI has been shown to be a viable technique for non-invasive measurement of moisture content distribution, but further improvements in both instrumentation and model accuracy are required for useful application for measurement of profiles in timber and other materials where ε_r changes with θ_v are relatively small. Here, suggestions are made for further work to improve accuracy and applicability.

- TDRI demands very high-speed instrumentation, but rapid advances are expected as semiconductor switching speeds increase (for example indium phosphide transistors are now switching at frequencies beyond 100 GHz). Hence the development of custom instrumentation for highly accurate TDR and TDRI would provide a useful research direction. Such development could focus on the requirement for well-balanced signals to the PTL, achievable by a balanced step generator and TDR sampling circuit.

- Several researchers have observed that linear or other basis functions of higher order than the pulse basis functions used here, provide better modelling of the field, particularly near large discontinuities in the electrical properties (permittivity in this case) of the material. Although the best choice is a balance between increased cells using pulse basis functions or reduced discretisation and higher order basis functions, further work investigating this aspect would be a valuable addition to this modelling work. In a similar vein, a Galerkin approach has been used here but some researchers have called into question the universality of Galerkin advantages. The author considers that evaluating Galerkin and non-Galerkin methods using an integral quantity such as in the present forward model, could yield new insights into model accuracy.

- A technique was introduced that provides a measure of the illposedness of a set of inversion data, and a similar approach could be employed to discard redundant data and point towards data (in this case from particular PTL positions) that would reduce problem illposedness. Development and evaluation of a formalised approach would provide a useful advance to inversion practice.

- Transmission line end effects were ignored when translating calculated propagation velocity to total travel time within the forward model. While an approximate correction could be made based on empirical results, a better approach would be to model the impedance at the end of the PTL, and make a correction to the near-end propagation velocity and hence total travel time.

- An initial assumption of the forward model was an isotropic and lossless dielectric. Materials with anisotropic permittivity in the transverse plane could be modelled by a procedure that calculates a provisional solution using the method described here, and then progressively refines it based on the field direction provided by the model output. Conceivably, lossy materials could be modelled by superimposing on the calculated polarisation field, the imaginary components due to loss-related current filaments in a manner related to the approach of Xiong et al. (1995).

In addition to further effort in advancing TDRI, the work described here has identified a number of factors that could also be applied to related disciplines.

- The forward model also has application to TDR methodology since it enables calculation of the propagation velocity from electrical properties of the heterogeneous region surrounding the PTL, and the PTL geometry. For example, parallel work is underway in use of the model to quantify the response of TDR in soil to an invading wetting front. This related work has application to infiltration and percolation studies.

- Several new techniques have been applied to the inverse problem of TDRI, and are likely to be applicable to other inverse problems. The blocking technique in particular appears to possess some attributes of the simulated annealing algorithm that provided the first reliable solution to the travelling salesman problem. Hence an interesting future direction would be the application of these inversion techniques to other inverse problems that are plagued by numerous local minima and/or slow convergence of less influential parameters.

- Deficiencies in the conventional means of determining v_p in TDR measurements have been identified by the demanding TDRI application. Further work in the use of matched tangents could improve the performance of TDR measurement of θ_v in soils that have a significant clay content and/or high salts content and hence a high electrical loss. The degraded TDR bandwidth in these circumstances could be compensated for by the matched tangent approach, although higher dispersion (and hence lower v_p of the reduced bandwidth signals) will still result in some errors.

References

Alharthi, A., Lange, J. 1987. Soil water saturation: dielectric determination. *Water Resources Research* 23:591-595

Ansoult, M., De Backer, L. W., Declercq, M. 1985. Statistical relationship between apparent dielectric constant and water content in porous media. *Soil Sci. Soc. Am. J.* 49:47-50

Baker, J. M., Lascano, R. J. 1989. The spatial sensitivity of time-domain reflectometry. *Soil Science* 147:378-384

Baker, J. M., Lascano, R. J. 1991. Discussion of "The spatial sensitivity of time-domain reflectometry". *Soil Science* 151:254-257

Bartley, P., Nelson, S. O., McClendon, R. W., Trabelsi, S. 1999. Determination of moisture content in wheat using an artificial neural network. *Third Workshop on Electromagnetic Wave Interaction with Water and Moist Substances,* USDA, Athens, GA

Berryman, J. 1991. *Nonlinear inversion and tomography.* Retrieved April 2001 from: http://utam.geophys.utah.edu/~jingchen/ebooks/lecture_notes.pdf

Bertero, M. 1992. Sampling theory, resolution limits and inversion methods. *IOP Publishing Ltd*

Bhattacharyya, G. K., Johnson, R. A. 1977. *Statistical concepts and methods.* 1 ed. New York: John Wiley and Sons

Binns, K. J., Lawrenson, P. J., Trowbridge, C. W. 1992. *The analytical and numerical solution of electric nd magnetic fields.* 1 ed. Chichester: John Wiley and Sons Ltd

Birchak, J. R., Gardiner, C. G., Hipp, J. E., Victor, J. M. 1974. High dielectric constant microwave probes for sensing soil moisture. *Proceedings of the IEEE* 62:93-98

Bolomey, J. C., Pichot, C. 1992. Some application of diffraction tomography to electromagnetics - the particular case of microwaves. *IOP Publishing Ltd.*:319-344

Bones, P. 1981. *Contributions to electrocardiographic science.* PhD. University of Canterbury

Borup, D. T., Johnson, S. A., Kim, W. W., Beggren, M. J. 1992. Nonperturbative diffraction tomography via Gauss-Newton iteration applied to the scattering integral equation. *Ultrasonic Imaging* 14:69-85

Bottcher, C. J. F. 1952. *Theory of electric polarisation.* Amsterdam: Elsevier

Boyce, W. E., DiPrima, R. C. 1976. *Elementary differential equations and boundary value problems.* 3 ed. New York: John Wiley and Sons, Inc

Brazee, J. G. 1968. *Semiconductor and tube electronics*. 1 ed. Holt, Rinehat and Winston

Brown, T. L. 1968. *General chemistry*. 2 ed. Columbus: Charles E Merrill Publishing Company

Bruce, M. Personal communication 1997

Bruggeman, D. A. G. 1935. Berechnung verschiedener physikalischer kostanten von heterogenen substanzen. *Annalen der Physik* 5:636-664

Campbell, J. E. 1988. *Dielectric properties of moist soils at RF and microwave frequencies*. PhD. Dartmouth College

Campbell, J. E. 1990. Dielectric properties and influence of conductivity in soils at one to fifty megahertz. *Soil Sci. Soc. Am. J.* 54:332-341

Chew, W. C., Jin, J.-M., Lu, C.-C., Michielssen, E., Song, J. M. 1997. Fast solution methods in electromagnetics. *IEEE Transactions on Antennas and Propagation* 45:533-543

Chew, W. C., Wang, Y. M. 1990. Reconstruction of two - dimensional permittivity distrubution using the distorted born iterative method. *IEEE Transactions on Medical Imaging* Vol. 9:218-225

Cole, R. H. M., Satoru and Windsor, Paul. 1980. Evaluation of dielectric behavior by time domain spectoscopy. *The Journal of Physical Chemistry* Vol.8:786-793

Conte, S. D., de Boor, C. 1980. *Elementary numerical analysis*. 3 ed. McGraw-Hill

Dasberg, S., Dalton, F. N. 1985. Time domain reflectometry field measurements of soil water content and electrical conductivity. *Soil Sci. Soc. AM. J.* 49:293-297

Dasberg, S., Hopmans, J. W. 1992. Time domain reflectometry calibration for uniformly and nonuniformly wetted sandy and clayey loam soils. *Soil Sci. Soc. Am. J.* 56:1341-1345

de Loor, G. P. 1968. Dielectric properties of heterogeneous mixtures containing water. *The Journal of Microwave Power 3 - 2*:67-73

Devaney, A. J. 1992. Current research topics in diffraction tomography. pp. 47-58 *IOP Publishing Ltd.*

Dirksen, C., Dasberg, S. 1994. Four-component mixing model for improved calibration of TDR soil water content measurements. *Soil Sci Soc.Am. J.* 57:660

Dobson, M. C., Ulaby, F. T., Hallikainen, M. T., El-rayes, M. A. 1985. Microwave dielectric behaviour of wet soil - Part II: Dielectric mixing models. *IEEE Transactions on Geoscience and Remote Sensing* GE-23:35-46

Dudley. 1997. Comment on "Variational nature of Galerkin and non-Galerkin moment method solutions". *IEEE Transactions on Antennas and Propagation* AP45

Dudley, D. G. 1994. *Mathematical foundations for electromagnetic theory.* 1 ed. Piscataway: Oxford University Press and IEEE Press

Ellis, R. G. 1995. Joint 3D EM inversion, *An International Symposium on Three-Dimensional Electromagnetics,* Schlumberger-Doll Research, Ridgefield, CT

Ellis, R. G., Oldenburg, D. W. 1994. Applied geophysical inversion. *Geophysics* 116:5-11

Farqhuarson. Personal communication 1999

Farquharson, C. G., Oldenburg, D. W. 1995. Approximate sensitivities for the multi-dimensional electromagnetic inverse problem, *An International Symposium on Three-Dimensional Electromagnetics,* Schlumberger-Doll Research, Ridgefield, CT

Fellner-Feldegg, H. 1972. A thin sample method for the measurement of permeability, permittivity, and conductivity in the frequency and time domain. *The Journal of Physical Chemistry* 76:2116-2122

Ferre, P., Hook, W., Livingston, N., Bassey, C. 1999. Errors in TDR-determined water content in a saline soil. *Third Workshop on Electromagnetic Wave Interaction with Water and Moist Substances*, USDA, Athens, GA.

Ferre, P. A., Rudolph, D. L., Kachanoski, R. G. 1996. Spatial averaging of water content by time domain reflectometry: Implications for twin rod probes with and without dielectric coatings. *Water Resources Research* 32:271-279

Franks, F., ed. 1972. *Water: a comprehensive treatise. Vol. 1. The physics and physical chemistry of water.* ed. J. B. Hasted. London: Plenum Press

Friedman, S. P. 1997. Statistical mixing model for the apparent dielectric constant of unsaturated porous material. *Soil. Sci. Soc. Am. J.* 61:742-745

Fuller, P. Personal communication 2000

Ghodgaonkar, D. K., Gandhi, O. P., Hagman, M. J. 1983. Estimation of complex permittivities of three-dimensional inhomogeneous biological bodies. *IEEE Transactions on Microwave Theory and Techniques* MTT-31:442-447

Giese, K., Tiemann, R. 1975. Determination of the complex permittivity from thin-sample time domain reflectometry improved analysis of the step response waveform. *Advances in Molecular relaxation process,* 7:45-59

Gill, P., Murray, W., Wright, M. H. 1981. *Practical optimisation* London: Academic Press

Glisson, A. W. 1989. Recent advances in frequency domain techniques for electromagnetic scattering problems. *IEEE Transactions on Magnetics* 25:2867-2871

Glisson, A. W., Wilton, D. R. 1980. Simple and efficient numerical methods for problems of electromagnetic radiation and scattering from surfaces. *IEEE Transactions on Antennas and Propagation,* AP-28:593-603

Grewal, K. S., Buchan, G D and Sherlock, R R. 1991. A comparison of three methods of organic carbon determination in some New Zealand soils. *J. of Soil Science* 42:251-257

Grivet, P. 1976. *The physics of transmission lines at high and very high frequencies.* London: Academic Press,

Guo, T. C., Guo, W. W., Oguz, H. N. 1993. A technique for three-dimensional dosimetry and scattering computation of vector electromagnetic fields. *IEEE transactions on magnetics* 29:1636-1641

Hager, N. E. 1994. Broadband time-domain-reflectometry dielectric spectroscopy using variable-time-scale sampling. *Rev. Sci. Instrum.* 65:887-891

Hagmann, M. J. 1981. Convergent tests of several moment method solutions. *IEEE Transactions on Antennas and Propagation* AP-29:547-550

Hagmann, M. J. 1985. Comments on "limitations of the cubical block model of man in calculating SAR distributions. *IEEE Transactions on Microwave Theory and Techniques* MTT-33:347-350

Hagmann, M. J., Gandhi, O. P., Durney, C. H. 1978. Improvement of Convergence in Moment - Method Solutions by the Use of Interpolants. *IEEE Transactions on Microwave Theory and Techniques* MTT-26:904-908

Hale, B. S., ed. 1989. *The ARRL handbook.* The American Radio Relay League

Hallikainen, M. T., Ulaby, F. T., Dobson, M. C., El-rayes, M. A., Wu, L. K. 1985. Microwave dielectric behaviour of wet soil - Part 1: Empirical models and experimental observations. *IEEE Transactions on Geoscience and Remote Sensing* GE-23:25-34

Harrington, R. F. 1968. *Field computation by moment methods.* New York: MacMillan

Hastead, J. B. 1973. *Aqueous dielectrics* London: Chapman and Hall

Heimovaara, T. J. 1994. Frequency domain analysis of time domain reflectomtry waveforms: 1. Measurement of the complex dielectric permittivity of soils. *Water Resources Research* 30:189-199

Hewlett Packard. 1989. *HP 54121T digitising oscilloscope.* 1 ed. Hewlett-Packard Company

Hilhorst, M. A. 1998. *Dielectric characterisation of soil.* PhD. Wageningen Agricultural University

Hilhorst, M. A., Groenwold, J., de Groot, J. F. 1992. Water content measurements in soil and rockwool substrates: dielectric sensors for automatic in situ measurements. *Acta Horticulturae* 304:209-217

Hill, S. C., Durney, C. H., Christensen, D. A. 1983. Numerical Calculation of low-frequency TE feilds in arbitrarily shaped inhomogeneous lossy dielectric cylinders. *Radio Science* 18:328-336

Hillel, D. 1980. *Fundamentals of soil physics.* 1 ed. San Diego: Academic Press

Hoekstra, P., Doyle, W. T. 1970. Dielectric relaxation of surface absorbed water. *Journal of Colloid and Interface Science* 36:513-521

Hohmann, G. W. 1975. Three-dimensional induced polarization and electromagnetic modelling. *Geophysics* 40:309-324

Hook, W. R., Livingston, N. J. 1995. Propagation velocity errors in Time Domain Reflectometry measurements of soil water. *Soil Sci. Soc. Am. J.* 59:92-96

Hook, W. R., Livingston, N. J., Sun, Z. J., Hook, P. B. 1992. Remote diode shorting improves measurement of soil water by time domain reflectometry. *Soil Sci. Soc. Am. J.* 56:1384-1391

Jacobsen, O. H., Schonning, P. 1993. A laboratory calibrationof time domain reflectometry for soil water measurement including effects of bulk density and texture. *Journal of Hydrology* 151:147-157

Jofre, L., Hawley, M. S., Broquetas, A., De Los Reyes, E., Ferrando, M., Elias-Fuste, A., R. 1990. Medical Imaging with a Microwave Tomographic Scanner. *IEEE Transactions on Biomedical Engineering* 37:303-311

Johnson, S. A., Borup, D. T., Berggren, M. J., al, e. 1996. *Report on Collaboration by the Center for Inverse Problems, TechniScan, Inc. and Others in Application of Inverse methods to Practical Acoustic and EM Imaging Problems.* Retrieved 1996 from http://www.collab.htm

Keey, R. 1998. *Understanding kiln-seasoning for the benfit of industry* Christchurch: Wood Technology Research Centre, University of Canterbury.

Kent, M. 1987. *Electrical and Dielectrical Properties of Food Materials*, ed. R. Jowitt. 5 vols. Great Yarmouth, UK: Galliard Printers

Kent, M., Meyer, W. 1984. Complex permittivity spectra of protein powders as a function of temperature and hydration. *J. Phys. D: Applied Physics.* 17:1687-1698

Kip, A. F. 1969. *Fundamentals of Electricity and Magnetism.* 2 ed. McGraw-Hill

Knight, J. H. 1992. Sensitivity of time domain reflectometry measurements to lateral variations in soil water content. *Water Resources Research* 28:2345-2352

Knight, J. H., Ferre, P. A., Rudolph, D. L., Kachanowski, R. G. 1997. A numerical analysis of the effects of coatings and gaps upon relative dielectric permittivity measurement with time domain reflectometry. *Water Resources Research,* 33:1455-1460

Kraszewski, A. S., Maria; and Stuchly, Stanislaw. 1983. ANA Calibration Method for Measurement of Dielectric Properties. *IEEE Transactions on Instrumentation and Measurement* Vol, IM-32:385-387

Laurent, J. P. 1998. Profiling water content in soils with TDR: experimental comparison with the neutron probe technique. *IAEA-Meeting*, Vienna. Accessed 2001 from: http://lthent1.hmg.inpg.fr/~laurent/#Publications

Leschinik, W., Schlemm, U. 1999. Measurement of the moisture and salt content of building materials. *Third Worksop on Electromagnetic Wave Interaction with Water and Moist Substances,* USDA, Athens, Georgia

Looyenga, H. 1965. Dielectric Constants of Heterogeneous Mixtures. *Physica* 31:401-406

Mackie, R. L., Madden, T. R. 1993. Three-dimentional magnetotelluric inversion using conjugate gradients. *Geophysics* 115:215-229

Magnusson, P. C. 1965. *Transmission lines and wave propogation.* 4 ed. Boston: Allyn and Bacon

Mashimo, S., Kuwabara, S., Yagihara, S., Higasi, K. 1987. Dielectric relaxation time and structure of bound water in biological materials. *J. Phys. Chem.* 91:6337-6338

Massoudi, H., Durney, C. H., Iskander, M. F. 1984. Limitations of the Cubical Block Model of Man in Calculating SAR Distributions. *IEEE Transactions on Microwave Theory and Techniques* MTT-32:746-751

Mei, K. K., Van Bladel, J. G. 1963. Scattering by perfectly-conducting rectangular cylinders. *IEEE Transactions on Antennas and Propagation* AP11:185-192

Misra, D. K. 1987. A Quasi-Static Analysis of Open-Ended Coaxial Lines. *IEEE Transactions on Microwave Theory and Techniques* Vol. MTT - 35:925-928

Morison, K. Personal communication 1994

Nelson, S. O. 1973. Electrical Properties of Agricultural Products (A Critical Review). *ASAE Special Publication SP-05-73.* St. Joseph, MI: ASAE

Oldenburg, D. Personal communication 1999

Oldenburg, D. W., Yaoguo, L. 1994. Inversion of induced polarization data. *Geophysics* 59:1327-1341

Or, D., Fisher, B., Hubscher, R. A., Wraith, J. 1998. *WinTDR 98 V4.0 - users guide.* Logan: Utah State University. Accessed 2001 from: http://psb.usu.edu/wintdr99/

Or, D., Wraith, J. M. 1999. Temperature effects on soil bulk dielectric permittivity measured by time domain reflectometry: a physical model. *Water Resources Research* 35:371-383

Peterson, A. F., Klock, P. W. 1988. An improved MFIE formulation for TE-wave scattering from lossy, inhomogeneous dielectric cylinders. *IEEE Transactions on Antennas and Propagation* Vol. 36:45-49

Peterson, A. F., Wilton, D. R., Jorgenson, R. E. 1996. Variation nature of galerkin and non-galerkin moment method solutions. *IEEE Transactions on Antennas and Propagation* 44:500-503

Pichot, C., Jofre, L., Peronnet, G., Bolomey, J.-C. 1985. Active Microwave Imaging of Inhomogeneous Bodies. *IEEE Transactions on Antennas and Propagation* AP-33:416-425

Pichot, C., Lobel, P., Dourthe, C., Blanc-Feraud, L., Barlaud, M. 1997. Microwave Inverse Scattering: Quantitative Reconstruction of Complex Permittivity for Different Applications. *IEICE Trans. Electron.* E80-C:1343-1348

Plonsey, R., Collin, R. E. 1961. *Principles and applications of electromagnetic fields.* 1 ed. McGraw Hill

Portniaguine, O., Zhdanov, M. S. 1999. Focusing geophysical inversion images. *Geophysics* 64:874-887

Press, W. H., Teulolsky, S. A., Vetterling, W. T., Flannery, B. P. 1992. *Numerical recipes in C: the art of scientific computing,* Cambridge University Press

Price, C. 1997. Personal communication

Qian, W., Boerner, D. E. 1995. Basis functions in 1D EM integral equation modelling, *An International Symposium on Three-Dimensional Electromagnetics,* Schlumberger-Doll Research, Ridgefield, CT

Ramo, S., Whinnery, J. R., Van Duzer, T. 1993. *Fields and Waves in Communication Electronics.* 3 ed. New York: Wiley

Richmond, J. H. 1965. Scattering by a dielectric cylinder of arbitrary cross section shape. *IEEE Transactions on Antennas and Propagation* 334-341

Richmond, J. H. 1966. TE-Wave scattering by a dielectric cylinder of arbitrary cross-section shape. *IEEE Transactions on Antennas and Propagation* 14:460-465

Rosen, D. 1962. Dielectric Properties of Protein Powders with Absorbed Water. *Trans. Faraday Soc.* 59:2178-2191

Roth, C. H., Malicki, M. A., Plagge, R. 1992. Empirical evaluation of the relationship between soil dielectric constant and volumetric water content as the basis for calibrating soil moisture measurements. *Journal of Soil Science* 43:1-13

Savitsky, A., Golay, M. J. E. 1964. Smoothing and Differentiation of Data by Simplified Least Squares Procedures. *Analytical Chemistry* 36:1627-1639

Schaubert, D. H., Meaney, P. M. 1986. Efficient computation of scattering by inhomogeneous dielectric bodies. *IEEE transactions on antennas and propagation* AP-34:587-592

Schaubert, D. H., Wilton, D. R., Glisson, A. W. 1984. A Tetrahedral Modeling Method for Electromagnetic Scattering by Arbitrarily Shaped Inhomogeneous Dielectric Bodies. *IEEE Transactions on Antennas and Propagation* AP-32:77-85

Schmugge, T. J., Jackson, T. J., McKim, H. L. 1979. Survey of in-situ and remote sensing methods for soil moisture determination. *Satellite Hydrology*, June:333-352

Schwan, H. P., Schwarz, G., Maczuk, J., Pauly, H. 1962. On the Low-Frequency Dielectric Dispersion Of Colloidal Particles in Electrolyte Solution. *J. Phys. Chem.* 66:2626-2635

Sheen, N. I., Woodhead, I. M. 1999. An Open-ended Coaxial Probe for Broad-Band Permittivity Measurement of Agricultural Products. *J. agric. Engng Res.* 74:193-202

Skaar, C. 1988. *Wood-water relations* Berlin: Springer-Verlag

Smith, R. W. M., Freeston, I. L., Brown, B. H. 1995. A real-time electrical impedance tomography system for clinical use- design and preliminary results. *IEEE Transactions on Biomedical Engineering* 42:133-140

Spaans, E. J. A. a. B., John M. 1993. Simple Baluns in Parallel Probes for Time Domain Reflectometry. *Soil Science Society American Journal* Vol. 57:668-673

Spiegel, R. J. 1984. A Review of Numerical Models for Predicitng the Energy Deposition and Resultant Thermal Response of Humans Exposed to Electromagnetic Fields. *IEEE Transactions on Microwave Theory and Techniques* MTT-32:730-746

Stuchly, M. B., Michael M.; Stuchly, Stanislaw; and Gajda, Gregory. 1982. Equivalent Circuit of an Open-Ended Coaxial Line in a Lossy Dielectric. *IEEE Transactions on Instrumentation and Measurement* Vol. IM-31:116-118

Takashima, S. 1962. Dielectric Properties of Water of Adsorption on Protein Crystals. *Journal of Polymer Science* 62:233-240

Tarantola, A. 1987. *Inverse problem theory,* Amsterdam: Elsevier

Tektronix. 1996. 1502C MTDR User Manual. Beaverton, OR: Tektronix

Tikhonov, A. N., Arsenin, V. Y. 1977. *Solutions of ill-posed problems* Washington DC: V H Winston and Sons

Topp, G. C., Davis, J. L. 1981. Detecting infiltration of water through soil cracks by time-domain reflectometry. *Geoderma* 26:13-23

Topp, G. C., Davis, J. L., Annan, A. P. 1980. Electromagnetic determination of soil water content: measurements in coaxial transmission lines. *Water Resources Research* 16:574-582

Torgovnikov, G. I. 1993. *Dielectric properties of wood and wood-based materials*, ed. T. E. timell Berlin: Springer-Verlag

Torres-Verdin, C., Habashy, T. M. 1994. Rapid 2.5-dimentional forward modeling and inversion via a new nonlinear scattering approximation. *Radio Science* 29:1050-1079

Torres-Verdin, C., Habashy, T. M. 1995. A Two-Step Linear Inversion of Two-Dimensional Electrical Conductivity. *IEEE Transactions on Antennas and Propagation* 43:405-415

Tsai, C.-T., Massoudi, H., Durney, C. H., Iskander, M. 1986. A Procedure for Calculating Fields Inside Arbitrarily Shaped, Inhomogeneous Dielectric Bodies Using Linear Basis Functions with the Moment Method. *IEEE Transactons on Microwave Theory and Techniques* MTT-34:1131-1139

Tsukerman, I. 1997. Stability of the Moment Method in Electromagnetic Problems. *IEEE Transactions on Magnetics* 33:1402-1405

van der Standen, J. 1999. Personal communication

van Gemert, M. J. C. 1973. High frequency time domain methods in dielectric spectroscopy. *Philip Res. Repts.* 28:530-572

Wang, J. J. H. 1991. *Generalized moment methods in electromagnetics: Formulation and computer solution of integral equations*. John Wiley & Sons.

Wang, J. R. 1980. The dielectric properties of soil-water mixtures at microwave frequencies. *IEEE Transactions on Geoscience and Remote Sensing,* 15:977-985

Wang, J. R., Schmugge, T. J. 1980. An empirical model for the complex dielectric permittivity of soils as a function of water content. *IEEE Transactions on Geoscience and remote sensing.* GE18:288-295

Weaver, J. T., Agarwal, A. K., Pu, X. H. 1995. Recent developments in three-dimensional finite difference modelling of the magnetic field in geo-electromagnetic induction, *An*

International Symposium on Three-Dimensional Electromagnetics, Schlumberger-Doll Research, Ridgefield, CT

Weidelt, P. 1995. Three-dimensional conductivity models: implications of dielectric anisotropy, *An International Symposium on Three-Dimensional Electromagnetics,* Schlumberger-Doll Research, Ridgefield, CT

Wexler, A., Fry, B., Neuman, M. R. 1985. Impedance-Computed Tomography Algorithm and System. *Applied Optics* 24:3985-3992

White, I., Zegelin, S. J. 1995. Electric and Dielectric Methods for Monitoring Soil-water Content. 1995 ed. In *Handbook of vadose zone charcterization & monitoring*, ed. L. G. Wilson, e. al, pp. 343-385. Boca Raton, FL: Lewis Publishers, CRC Press

Williams, W. E. 1980. *Partial Differential Equations* Oxford: Oxford University Press

Wilt, M., Spies, B., Alumbaugh, D. 1995. Measurement of surface and borehole electromagnetic fields in quasi two- and three-dimensional geology, *An International Symposium on Three-Dimensional Electromagnetics,* Schlumberger-Doll Research, Ridgefield, CT

Wobschall, D. 1977. A theory of the complex dielectric permittivity of soil containing water: The semidisperse model. *IEEE transactions on Geoscience electronics* GE-15:49-58

Woodhead, I., Buchan, G., Kulasiri, D. 1999. Modelling TDR response in heterogeneous composite materials, *Third Workshop on Electromagnetic Wave Interaction with Water and Moist Substances,* USDA, Athens, Georgia

Woodhead, I., Buchan, G., Kulasiri, D., Christie, J. 2000. A new model for the response of TDR to heterogeneous dielectrics. *Subsurface Sensing Technologies and Applications*, 1:473-487

Woodhead, I., Buchan, G., Kulasiri, D. 2001. Non-invasive measurement of moisture distribution using TDR, *Fourth Workshop on Electromagnetic Wave Interaction with Water and Moist Substances,* Weimar, Germany (accepted for oral presentation)

Woodhead, I. M., Buchan, G. D. 1996. Determination of moisture content profiles in composite materials using dielectric computed tomography. In *WISPAS*

Woodhead, I. M., Buchan, G. D. 2000. Non-invasive determination of subsurface moisture distribution. In *WISPAS*

Woodhead, I. M., Buchan, G. D., Kulasiri, D. 2001. Pseudo 3-D moment method for rapid calculation of electric field distribution in a low loss inhomogeneous dielectric. *IEEE Transactions on Antennas and Propagation,* 49:1117-1122

Wraith, J. M., Or, D. 1999. Temperature effects on soil bulk dielectric permittivity measured by time domain reflectometry: Experimental evidence and hypothesis development. *Water Resources Research* 35:361-369

Xie, C. G., al, e. 1991. Tomgraphic imaging of industrial equipment - development of system model and image reconstruction algorithm for capacitive tomography. *Sensors: Technology, Systems , and Applications*:203-208

Xiong, Z. 1992. Electromagnetic modelling of a 3-D structure by the method of system iteration using integral equations. *Geophysics* 57:1556-1570

Xiong, Z., Raiche, A., Sugeng, F. 1995. A new integral equation formulation for electromagnetic modelling, *An International Symposium on Three-Dimensional Electromagnetics,* Schlumberger-Doll Research, Ridgefield, CT

Yagihara, S., al, e. 1999. Observation of changes in dynamicd of water molecules in various aqueous systems using time domain relectometry, *Third Workshop on Electromagnetic Wave Interaction with Water and Moist Substances,* USDA, Athens GA

Zeff, C. Personal communication 1995

Zegelin, S. Personal communication 1995

Zegelin, S. J., White, I., Jenkins, D. R. 1989. Improved field probes for soil water content and electrical conductivity measurement using time domain reflectometry. *Water Resources Research* 25:2367-2376

Zhdanov, M. Personal communication 1999

Zhdanov, M. S. 1993. *Tutorial: Regularization in Inversion Theory.* Golden, CO: Center for Wave Phenomena, Colorado School of Mines

Zhou, R., Shafai, L. 1997. Study on the convergence of volume integral equation method. *Antennas and Propagation Society International Symposium 1997* 3:1830-1833

Appendix 1

A Comparison of Moisture Content Imaging Techniques

There are a number of imaging techniques that are potentially useful for generating images of moisture content (θ_v) distribution. Here the techniques, including time domain reflectometry imaging (TDRI), are compared (Table A1.1) for their suitability for measuring moisture content distribution in an industrial or environmental situation. The assessment is of necessity rather qualitative since a thorough comparison would require full study within itself.

A number of the techniques, including electrical impedance tomography, electrical resistance tomography, electromagnetic (EM) conductivity imaging, and capacitance tomography, may be considered variants of dielectric tomography. The classification arises since these methods determine one or both of the components of the complex permittivity of the material under examination. Note that there are some inconsistencies in classification of imaging techniques. For example the term diffraction tomography is commonly used for both microwave imaging Devaney (1992) and sonic imaging (Borup et al., 1992). However, the common and more generic classification by source or measured variable has been adopted here rather than by a particular methodology or variant.

Table A1.1 Qualitative comparison of imaging techniques for measuring moisture content distribution.

Technique	Spatial Resolution	Moisture (θ_v) Resolution	Cost	Safety	Further Comment
Magnetic Resonance Imaging	Excellent, depends on coil geometry	Excellent	Moderate to high	Safe	Requires strong magnetic fields
Gamma Ray Imaging	Better than 1 mm, sensor-dependent	Excellent	High	Ionising radiation	
X-ray Computed Tomography	Better than 1 mm	Excellent	High	Ionising radiation	Bulky, retired medical systems available
Electrical Resistance Tomography	Dependent on electrodes, 1mm should be attainable	Likely to be poor at low θ_v	Low	Safe	
Electromagnetic Conductivity Imaging	Poor, dependent on coil size	Good	Moderate	Safe	Usually applied to large, geophysical structures
Electrical Impedance Tomography	Dependent on electrodes, 1mm should be attainable	Likely to be poor at low θ_v	Low	Safe	
Electrical Capacitance Tomography	Dependent on electrodes, 1mm should be attainable	Qualitative, uses low sensing frequencies	Low	Safe	
Magnetic Source Imaging	Probably poor with current technology	Unknown	Low	Safe	Is an indirect method, medical advantages
Sonic Imaging	Moderate, wavelength dependent	Poor, relies on moisture-density interaction	Low	Considered safe	Coupling transducer to material may be problematic
Microwave Imaging	Potentially good, scattering impacts on precision	Good, relies on a dielectric model	Moderate	Low level signals considered safe	May be difficulties launching the signal into the material
Terahertz imaging	Excellent, << 1mm	Good, relies on absorption bands	High	Low level signals considered safe	Small penetration < 1mm in water
Time Domain Reflectometry Imaging	Satisfactory, depends on geometry and measurement precision	Good, relies on a dielectric model	Moderate	Safe	Penetration < λ

Appendix 2

Non-linearity of the Forward Problem

The forward problem for time domain reflectometry imaging (TDRI) has been defined as calculation of the propagation velocity (v_p) of a pulse on a parallel transmission line (PTL) in an arbitrary inhomogenous permittivity (ε_r) distribution. Here, a proof is derived to show the non-linearity of the forward problem (and hence the associated inverse problem).

Consider two small regions of identical size and shape with susceptibilities χ, within a space of $\chi = 0$, and under the influence of a uniform impressed field $\boldsymbol{E}_i$ (Figure A2.1). A point C is positioned equidistant (for convenience) from A and B.

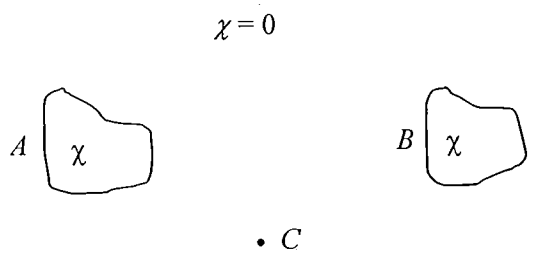

Figure A2.1 A dielectric region with two small sub-regions of susceptibility χ immersed in a space with $\chi = 0$.

We wish to verify the non-linearity of the problem by considering a doubling of χ in A and B, and then showing that $\boldsymbol{E}_C(2\chi) \neq 2\boldsymbol{E}_C(\chi)$ where $\boldsymbol{E}_C$ is the field at C. However since $\boldsymbol{E}_C$ comprises both $\boldsymbol{E}_i$ and the polarisation field of A and B, we will show that:

$$\boldsymbol{E}_C(2\chi)\text{-}\boldsymbol{E}_i \neq 2\left[\boldsymbol{E}_C(\chi)\text{-}\boldsymbol{E}_i\right] \tag{A2.1}$$

$\boldsymbol{E}_C$ is defined as:

$$\begin{aligned}\boldsymbol{E}_C(\chi) &= \boldsymbol{E}_i + \text{field due to polarisation at } A + \text{field due to polarisation at } B \\ &= \boldsymbol{E}_i + f(\boldsymbol{E}_A\chi) + f(\boldsymbol{E}_B\chi)\end{aligned} \tag{A2.2}$$

where f is a function incorporating distance, permittivity, etc., and describes the influence of the polarisation of region A or B on the field at C. Then using symmetry, and since $\boldsymbol{E}_A = \boldsymbol{E}_B = \boldsymbol{E}$:

$$\boldsymbol{E}_C(\chi) = \boldsymbol{E}_i + 2f(\chi[\boldsymbol{E}_i + g(\boldsymbol{E}\chi)]) \tag{A2.3}$$

Here g describes the functional influence of the polarisation of region A on B, or vice versa. Assuming f and g are linear functions:

$$\boldsymbol{E}_C(\chi) = \boldsymbol{E}_i + 2f(\boldsymbol{E}_i\chi) + 2f(\chi g(\boldsymbol{E}\chi)) \tag{A2.4}$$

Then doubling the susceptibility in the regions A and B to 2χ and noting that we are just concerned with the polarisation component of $\boldsymbol{E}_P$ rather than the incident $\boldsymbol{E}_i$ which remains constant:

$$\boldsymbol{E}_C(2\chi) = \boldsymbol{E}_i + 2f(2\boldsymbol{E}_i\chi) + 2f(2\chi g(2\boldsymbol{E}\chi)) \tag{A2.5}$$

and again assuming linearity of f and g:

$$\boldsymbol{E}_C(2\chi) = \boldsymbol{E}_i + 4f(\boldsymbol{E}_i\chi) + 8f(\chi g(\boldsymbol{E}\chi)) \tag{A2.6}$$

so that

$$\boldsymbol{E}_C(2\chi) - \boldsymbol{E}_i = 2[\boldsymbol{E}_C(\chi) - \boldsymbol{E}_i] + 4f(\chi g(\boldsymbol{E}\chi)) \tag{A2.7}$$

and hence the problem is non-linear. The non-linearity is quantified by the right hand term. For a heterogeneous permittivity where $\varepsilon = \varepsilon(x, y, z)$, the interaction between polarised regions will be more complex, again leading to non-linearity.

Appendix 3

Differential and Integral Equation forms for the Potential

For an inhomogenous permittivity $\varepsilon(x,y)$, Maxwell's first equation $\nabla \cdot \boldsymbol{D} = \rho$ becomes;

$$\nabla \cdot (\varepsilon(x,y)\nabla\Phi) = -\rho \tag{A3.1}$$

In this application, the domain of Eqn (A3.1) may include the source and sink of flux (the PTL) represented in an idealised manner (provided $a \ll b$) by a dipole described by two, 2-D Dirac delta functions, in which case:

$$\nabla \cdot (\varepsilon(x,y)\nabla\Phi) = \delta(x-x_1, y-y_1) - \delta(x-(x_1-b), y-y_1) \tag{A3.2}$$

In Eqn (A3.2), (x_1, y_1) and $(x_1 - b, y_1)$ are the positions of the two PTL rods, and b their spacing. If the homogenous part of Eqn (A3.2) is expanded, and the convention that a subscripted variable represents the partial derivative is adopted, we obtain:

$$(\varepsilon\Phi_x)_x + (\varepsilon\Phi_y)_y = \delta(x-x_1, y-y_1) - \delta(x-(x_1-b), y-y_1) \tag{A3.3}$$

ie

$$\varepsilon(\Phi_{xx} + \Phi_{yy}) + \varepsilon_x\Phi_x + \varepsilon_y\Phi_y = \delta(x-x_1, y-y_1) - \delta(x-(x_1-b), y-y_1) \tag{A3.4}$$

Since the determinant of Eqn (A3.4) is less than zero, it is an elliptic equation for all $\varepsilon(x,y)$ providing $\varepsilon \geq \varepsilon_0$ and is real. Two approaches to evaluating Φ are to discretise the plane to zones of uniform ε and solve Laplace's equation numerically in each zone, a FD approach, or use an IE method that instead presents Eqn (A3.2) in integral form. Using the approach of Dudley (1994):

$$\nabla\Phi = \frac{-1}{\varepsilon(x,y)} \boldsymbol{L}^{-1}\rho(x,y) \tag{3.5}$$

where L^{-1} is the inverse of differential operator ∇. Assuming L^{-1} is adequately represented by an integral with kernel G, we obtain the elementary integral form:

$$\begin{aligned} -\nabla\Phi(r) &= \boldsymbol{E}(r) \\ &= \frac{1}{\varepsilon(x,y)} \iiint_{region} \boldsymbol{G}(r)\rho(x,y)\,dr \end{aligned} \tag{A3.6}$$

where r is a 3-space dimension, and $G(r)$ is a Green's function that incorporates the boundary conditions of the problem.

Appendix 4

The 3-D Electromagnetic Scattering Problem

The common 3-D electromagnetic (EM) scattering problem comprises a dielectric body that is illuminated by a plane wave source, and the required solution is the resultant field over the region. Richmond (1965, 1966) presented the theoretical basis for this class of scattering problem that is typically used in microwave imaging. The VIE solution method may be formulated from the Helmholtz equation:

$$\boldsymbol{E}(r) = -\omega\mu \int_{v} J(r')\boldsymbol{G}(r,r')dv \tag{A4.1}$$

where J is the volume distribution of electric current and where the Green's function G that uses the problem geometry to describe the field between field point r and source point r', is defined as:

$$\boldsymbol{G}(r,r') = \frac{1}{4j}\boldsymbol{H}_0^{(2)}(\omega\sqrt{\mu\varepsilon}\ \ |r-r'|) \tag{A4.2}$$

and $\boldsymbol{H}_0^{(2)}$ is the zero order Hankel function of the second kind (Xiong et al., 1995; Harrington, 1968). Much of the effort in solving Eqn (A4.1) is focussed on circumventing the strong singularity where $r = r'$. Wang (1990) describes several approaches that may be used. Note that the above method is formulated using the transverse magnetic component of the plane TEM wave and conveys some advantages over the TE formulation in terms of simplicity (Harrington, 1968) and convergence (Peterson and Klock, 1988).

Program Listings

1 Stability of 3-D moment method with high permittivity contrast

```
% unstable.m
% Linear field (parallel plate capacitor)
% Demonstration of instability of moment method with large Er.


% Break entire plane into a cells by cells grid of total size 1cm^2

clear
format compact

E0 = 8.85e-12;          % permittivity of free space, epsilon zero
size = 1e-2;            % dimension (m), A is size^2, d is size.
cells =7;               % number of cells along edge
length = size/cells;    % cell edge dimension (capacitor 1cm square)
vol = length^3;         % vol of cell (m^3)
part= vol/(4*pi*E0);
half = floor(cells/2);


% First, establish some conventions to keep everything in order.
% The first array index is x and represents horizontal position
% the second is y and represents vertical position.
% Zero is lower left corner.


% Now set up the impressed field and permittivity distribution

Er=100*ones(cells);          % uniform permittivity distribution

qm = 1;                      % charge density on plates (C/m^2)
q = qm*size^2;               % charge on one plate



% Set up the vector of impressed field components

for m=1:cells                % ie for x
for n=1:cells                % for y
for o=1:cells                % for z

Ei(3*((m-1)*cells^2+(n-1)*cells+(o-1))+1)=1;    % x direction only
Ei(3*((m-1)*cells^2+(n-1)*cells+(o-1))+2)=0;
Ei(3*((m-1)*cells^2+(n-1)*cells+(o-1))+3)=0;

end
end
end



% Now work out the polarization

for field_x=1:cells          % for each field point
for field_y=1:cells
for field_z=1:cells

for source_x=1:cells         % contributions from each source point
for source_y=1:cells
```

```
for source_z=1:cells

% make matrix indices

field  = 3*((field_x-1)*cells^2+(field_y-1)*cells+(field_z-1))+1;
source = 3*((source_x-1)*cells^2+(source_y-1)*cells+(source_z-1))+1;

% calculate the dyadic

if (field==source)              % remember the x is columns, y rows


      L(field,source) = 1/(3*E0) + 1/(E0*(Er(field_x,field_y)-1) );
      L(field+1,source+1) = L(field,source);
      L(field+2,source+2) = L(field,source);
      L(field+1,source) = 0;
      L(field+2,source) = 0;
      L(field,source+1) = 0;
      L(field+2,source+1) = 0;
      L(field,source+2) = 0;
      L(field+1,source+2) = 0;

      else

      x = (field_x - source_x)*length;
      y = (field_y - source_y)*length;
      z = (field_z - source_z)*length;
      R = x^2 + y^2 + z^2;
      mod = -part/R^2.5;

      L(field,source)   = (3*x^2-R)*mod;
      L(field,source+1) = 3*x*y*mod;
      L(field,source+2) = 3*x*z*mod;
      L(field+1,source) = 3*y*x*mod;
      L(field+1,source+1) = (3*y^2-R)*mod;
      L(field+1,source+2) = 3*y*z*mod;
      L(field+2,source)   = 3*z*x*mod;
      L(field+2,source+1) = 3*z*y*mod;
      L(field+2,source+2) = (3*z^2-R)*mod;
      end


end
end
end


end
end
field_x                 % report progress on screen
end

Pf = L\Ei';             % back-solve


                        % now calculate field

for i=1:cells           % x
for j=1:cells           % y
for k=1:cells           % z

      m= 3*((i-1)*cells^2+(j-1)*cells+(k-1));% + half*cells;

      if (k==2)         % select a z-plane for which to retrieve field

            Ex(i,j) = Pf(m + 1) /(E0*(Er(i,j) - 1));
            Ey(i,j) = Pf(m + 2)/(E0*(Er(i,j) - 1));
```

```
            end

        end
        end
        end

hold off
quiver(Ex,-Ey)                  % show field distribution
axis([0,cells+1,0,cells+1]);    % sort axis scaling
print -dbitmap                  % copy graph to clipboard

end
```

2 Configuration file for TDRI inversion

```
% Sets constants and the size of the tomography problem. Called by
% TOMOGn.M. The number of positions of rods is set up in
% observe.m.  The a priori data in Mprior.dat must be edited.  It must
% be consistent with size of entire zone specified by the number of
% cells (cells).  Also ensure that positions of the tx line rods
% specified in observe.dat are consistent with perturbed zone setup in
% Mprior.dat although recall that the tx line rod positions are at the
% top left corner of rod cell, so rod posn may just infringe perturbed
% zone.

% initialisation

clear
format short
format compact
cd c:\progra~1\mwork\inverse;       % set current directory for file
read/write
true = 1;
false = 0;


% forward problem parameters

block_size = 0.12;          % dimension of block (m).
cells = 12;                 % # of cells along edge of discretised zone
width = 6;                  % line spacing (in cells)
%b = 6*length;              % line spacing (in metres)
a=0.006;
rod_length = 0.3;           % line length in metres
E0 = 8.85e-12;              % permittivity of free space
U0 = 4*pi*1e-7;             % permeability of free space, mu zero
length = block_size/cells;     % cell edge dimension
vol = length^3;             % volume of cell (m^3)
part = vol/(4*pi*E0);       % these speed up later calculations


% inverse problem parameters

max_iterates = 30;          % maximum passes through inversion process
target = 1E-27;             % target misfit as sum of squares
gamma = 0;                  % Tikhonov regularisation parameter
max_corr = 0.5;             % used for constraining CG sensitivity
min_corr = 0;               % this stuffs up convergence, even 001
Er_min = 1.5;               % no dry material will be less than this
Er_max = 20;                % maximum Er of wet material
progress = false;           % increase of gain if average progress low
blocking = true;            % set blocking on or off
block_count = 12;           % blocking every block count iterations
block_limit = 0.5;          % maximum change in Er during blocking
block_target = 2e-26;       % no blocking if S less than this
max_terr = 1E-14;           % target as max error (sec)
constraint = 1;             % factor for constraining the CG slope
S = 1E-20;                  % startup value of objective function
S_old = 2E-20;              % startup for sum of squared deviation
beeta = 1;                  % startup for CG regularising parameter
first = 1;                  % true for first entry to refine
iteration = 1;              % initialise main inverse problem loop
fit = 0;                    % boolean, whether at target or not
better = 0;                 % boolean, whether fit better or worse
damping_factor = 1;         % used for the damped  method
illposed_limit = 0.2;       % warning if normalised Ei-Ej below this
avg_progress = 1;           % a measure of the progress of S

end
```

3 Generation of unperterbed scattering matrix

```
% This generates and saves the unperturbed (Er=1) L matrix as L.mat.

% It obtains the required geometry etc from SETUP.M

% Utilise the similarity of the L matrix despite changes in Er(x,y).
% Pre-calculate the matrix but omit the Er term on leading diagonal
% Leading diagonal elements added later as required for different Er.
% The diagonal elements are also saved for refreshing.

% Uses impressed field (and polarization calculations) in 3D,
% third (z) dimension invariant.  This implementation calculates field
% contributions from invariant third dimension and sums for each cell
% in 2-D array.  This allows faster execution and smaller cell size
% than from the full 3-D implementation.

clear

format compact

setup;


% First, let's establish some conventions to keep everything in order.
% The first array index is x and represents horizontal position and
% the second is y and represents vertical position.
% Zero is lower left corner.

% calculate the linear operator

for field_x=1:cells          % for each field point
for field_y=1:cells


for source_x=1:cells         % and contributions from each source
point
for source_y=1:cells
                             % make matrix indices

field  = 2*((field_x-1)*cells+(field_y-1))+1;
source = 2*((source_x-1)*cells+(source_y-1))+1;

% calculate the dyadic, remember the x is columns, y rows

      x = (field_x - source_x)*length;
      y = (field_y - source_y)*length;

  if (field==source)


L(field,source) = 1/(2.7*E0) - 2*(length^2)*(-part)/length^5 -
2*(2*length)^2*(-part)/(2*length)^5 - 2*(3*length)^2*(-
part)/(3*length)^5;
      L(field+1,source+1) = L(field,source);

  else

      R = x^2 + y^2;                 % the part of r in 2-space

      R1 = R + (length)^2;           % 3-space modulii of R
      R2 = R + (2*length)^2;         % all R are squared versions
      R3 = R + (3*length)^2;
      mod = -part/R^2.5;
```

```
L(field,source)   = (3*x^2-R)*mod + 2*(3*x^2-R1)*(-part)/(R1^2.5) +
2*(3*x^2-R2)*(-part)/(R2^2.5) + 2*(3*x^2-R3)*(-part)/(R3^2.5);

L(field,source+1) = 3*x*y*mod + 2*3*x*y*(-part)/(R1^2.5) + 2*3*x*y*(-
part)/(R2^2.5) + 2*3*x*y*(-part)/(R3^2.5);

L(field+1,source) = L(field,source+1);

L(field+1,source+1) = (3*y^2-R)*mod + 2*(3*y^2-R1)*(-part)/(R1^2.5) +
2*(3*y^2-R2)*(-part)/(R2^2.5) + 2*(3*y^2-R3)*(-part)/(R3^2.5);

  end

end
end

end
end

diagonal = diag(L);

save L.mat L diagonal

disp(' Unperturbed matrix saved as L.mat')

end
```

4 Routine to generate simulated data set (uses routines from Listing 5)

```
% Makes set of observations from Er distribution in model.dat which
% should have the same zero (unperturbed) elements as Mprior.dat.


setup                           % clears workspace, sets constants,
dimensions, etc
load readings.dat -ascii
load Mprior.dat -ascii
Mprior = rot90(Mprior);         % LHS is top of region
Mprior = flipud(Mprior);        % 0,0 is lower left
prior = Mprior;                 % make clean copy, keep Mprior as a mask
load L                          % load unperturbed matrix
load model.dat -ascii           % load artificial distribution
model = rot90(model);           % LHS is top of region
model = flipud(model);          % 0,0 is lower left

% Alter the model and prior arrays to eliminate the zero entries

for m=1:cells
for n=1:cells

      if prior(m,n)<1
            prior(m,n) = 1 + eps;
            end

      if model(m,n)<1
            model(m,n) = 1 + eps;
            end

      end
      end

Er = model;                     % make useable by existing matrix.m

% Calculate forward solution for matrix Er.

matrix;                         % calculate matrix L for the current
model

for position = 1:size(readings,1)    % the number of  observations
(rows)

            impress;            % calculate impressed field
            Pf = L\Ei';         % get polarisation matrix
            time;               % propagation time in t(position)

            end                 % position

readings(:,5) = t';             % save generated observations

save readings.dat readings -ascii

end                             % end of program
```

5 Inverse program and routines

5.1 Main

```
% Tomography - uses a pseudo 3-D forward solution and
% solves for different positions of the transmission line.


% Initialise

setup                   % sets constants, dimensions, etc
load L                  % load unperturbed matrix and its diagonal
apriori;                % load a priori data (first guess at Er)
observe;                % load matrix of observations
%illposed               % report on problem
%noise;                 % add measurement noise

% Main inverse problem loop

while ~fit & (iteration < max_iterates)

% Calculate forward solution and sensitivity matrix
% for the current model, ie for current matrix Er.

      forward;

      refine            % generate update of model

      regular           % regularise the update

      Er                % report on progress
      S

      objectiv          % Calculate the objective function and
                        % arrange to quit if a satisfactory fit.
      update

      iteration = iteration+1;

      record1(iteration,:)=Erv;
      record2(iteration,:)=terr;
      record3(iteration,:)=S;

end                             % end while

Er = rot90(rot90(rot90(flipud(Er))));     %get Er to input format
results                         % plot image
pause
figure
plot(record1,'w')
xlabel('Iterations')
ylabel('Relative Permittivity')
print -dbitmap
end                             % end of program
```

5.2 Forward

```
% Forward modelling stage providing a time vector and sensitivity
% matrix given a permittivity distribution Er.

% Calculate forward solution and  sensitivity matrix for the current
% model, ie for current matrix Er.

matrix;                  % calculate matrix L for current model Er

% Ll = inv(L);

for position = 1:size(readings,1)    % # of observations (rows)

      impress;                  % calculate impressed field
      Pf = L\Ei';               % get polarisation matrix
      time;                     % propagation time in t(position)

      sensitiv;                 % calculate the Jacobian J(position)

      end                       % loop on tx line positions ends here
end
```

5.3 Matrix

```
% Calculates the perturbed matrix, given the permittivity distribution
% and unperturbed matrix L (loaded by SETUP).  Assumes the third (z)
% dimension is invariant.  It calculates field contributions from the
% third dimension and sums for each cell in 2-D array.  This allows
% faster execution and more cells than for full 3-D implementation.


% First, establish some conventions to keep everything in order.
% The first array index is x and represents horizontal position
% the second is y and represents vertical position.
% Zero is lower left corner.


% Now work out the matrix.  On diagonal, we just add the
% perturbation due to Er to the geometric values for the
% 2.5D case.


for field_x=1:cells              % for each field point
for field_y=1:cells


for source_x=1:cells             % contributions source points
for source_y=1:cells
                                 % make matrix indices

field  = 2*((field_x-1)*cells+(field_y-1))+1;
source = 2*((source_x-1)*cells+(source_y-1))+1;

% calculate the dyadic, remember the x is columns, y rows

      x = (field_x - source_x)*length;
      y = (field_y - source_y)*length;

  if (field==source)     % get original from diagonal, add Er term


L(field,source) = diagonal(field) + 1/(E0*(Er(field_x,field_y)-1) );
      L(field+1,source+1) = L(field,source);

  end


end
end


end
end
```

5.4 Impress

```
% Calculates impressed field of parallel transmission line given the
% coordinates of the rod positions.

% Format in readings.dat is: rod1x, rod1y, rod2x, rod2y, travel time.
% Current row in array readings is set by 'posn', set in forward.m.
% The actual rod position is at cell centroids.

qm = 1;                                 % charge density on lines (C/m)
const = -qm/(2*pi*E0);                  % precalculate the constant

spacing = readings(position,3) - readings(position,1);

for m=1:cells                           % x
for n=1:cells                           % y

x1 = (m-readings(position,1))*length;     % x distance to rod1 etc
y1 = (n-readings(position,2))*length;
x2 = (m-readings(position,3))*length;
y2 = (n-readings(position,4))*length;

R1 = x1^2 + y1^2;                       % square of distance to rod1
R2 = x2^2 + y2^2;                       % and rod2

addr = 2*((m-1)*cells+(n-1));           % vector base address

if R1==0                                % avoid singularities
      R1=1000;                          % in rod cells and cause
      end                               % a small field there.

if R2==0
      R2=1000;
      end

Ei(addr+1) = const*(x1/R1 - x2/R2);       %Ex
Ei(addr+2) = const*(y1/R1 - y2/R2);       %Ey

Eix(m,n)=Ei(addr+1);
Eiy(m,n)=Ei(addr+2);

end
end

end
```

5.5 Time

```
% Calculates vel on parallel transmission line, give a polarisation
% vector, number of cells along edge of the 2-D array, qm the charge
% density on ine, transmission line rod positions, line length (m),
% size of each cell and in this case rod diameter, and U0,
% permeability of free space.

% Columns in readings.dat is: rod1x, rod1y, rod2x, rod2y, travel time.
% Current row in array readings is set by 'posn', set in forward.m.
% The actual rod position is at cell centroids.


% First calculate the field in each cell

for m=1:cells                                   % x
for n=1:cells                                   % y

  addr = 2*((m-1)*cells+(n-1));
  Ex(m,n) = Pf(addr + 1) /(E0*(Er(m,n) - 1));
  Ey(m,n) = Pf(addr + 2)/(E0*(Er(m,n) - 1));
  E(m,n) = sqrt(Ex(m,n)^2 + Ey(m,n)^2);

end
end

      % integrate the field to get voltage on lines.  We'll just
      % integrate in the x dirn, but interpolate using curve
      % for better accuracy.

V=0;
clear efield
rod1x = readings(position,1); % get rod positions
rod1y = readings(position,2); % assume rod y's the same
rod2x = readings(position,3);

for i=1:rod2x-rod1x-1                   % except that rod
  cell=i+rod1x;                         % posn at cell intersections,
  efield(i)=Ex(cell,rod1y);             % integrate BETWEEN rod posns.
end

V = sum(efield)*length;                 % summed field, no fitting
Cm = -0.92*qm/V;                        % capacitance per metre of line

b = (rod2x-rod1x)*length;               % rod spacing (m)

vel = sqrt(pi/(Cm*U0*acosh(b/length)));   % tx line vel (m/s)

t(position) = (rod_length)/vel;         % time (sec) for 2 way trip

end
```

5.6 Sensitiv

```
% Calculates sensitivity matrix for given position of the transmission
% line.  Currently uses simplified, rapid method based on the square
% of calculated electric field strength. Expect a maximum
% slope of around ((10 Er)^0.5)E-9 *rod_length*sec/Er for one cell.


addr = 0;

for m=1:cells
for n=1:cells

      if Mprior(m,n) > 0            % if a perturbed cell then
            addr = addr+1;          % next address(1-(S<5E-24)*0.5)

            Esquare = (Ex(m,n)^2 + Ey(m,n)^2);

J(position,addr) = (Esquare^0.5)*Er(m,n);       % ~dEr/dt
            J1(position,addr) = Esquare;        % this for illposed
            end


      end
      end

end
```

5.7 Refine

```
% Refine model, alter the model using the correction and the
% current value of the damping factor


% get Er and Mprior into vector form and make up a matrix (Erm)
% of (position x Erv)

% we've swapped indices

addr = 0;                              % we'll index just the perturbed
cells

for m=1:cells
for n=1:cells

      if Mprior(m,n) > 0               % if a perturbed cell
            addr = addr+1;             % then advance index address
            Erv(addr) = Er(m,n);       % vectorise the current model
            end
      end
      end

if iteration==1
      record1(iteration,:)=Erv;
      record2(iteration,:)=t;
      record3(iteration,:)=S;
end

for i = 1:addr
      Erm(i,:) = Erv;                  % make model Er into matrix
      end

if first
      terr = t - tobs;                 % don't have a tprior
      tprior = t;
else
      terr = t - tobs + gamma*(t-tprior); % model - measured
end

% dirn is current direction, old_dirn is that from previous loop

dirn = terr*J;


if first
      correction = terr*J;
      Jmean = J;
      first = 0;
else                                   % calculate Polak-Ribiere direction

      beeta = norm(dirn)*norm(old_dirn)/norm(old_dirn)^2;

if iteration<1
beeta=0;
end
      correction = dirn + beeta*old_dirn;
      Jmean = 0.7*Jmean + 0.3*J;
      end


old_dirn = dirn;

%
```

```
%     NOTE constraint is adjusted upward inside update.m
%
constraint = constraint +

while max(abs(correction*constraint))>max_corr  % constrain constraint
= constraint/1.2;
      end


while max(abs(correction*constraint))<min_corr  % constrain constraint
= constraint*1.2;
      end


iteration
if S>1e-24 & ~rem(iteration,block_count)
%     Erv=Erv-(0.5-rand(size(Erv)));
      end

      Erv = Erv - correction*constraint;


% BLOCKING

                                % every block_count iteration:

if ~rem(iteration,block_count) & blocking & iteration<turnover &
S>block_target

      block = terr*Jmean*constraint;
      while abs(max(block))<block_limit %/iteration*30
            block=block.*1.2;
            end
%     block=block.*1.5;

      for i=1:size(block,2)
%           block(i)=sign(block(i)*sqrt(abs(block(i))));
            if    ~rem(i-1,3) %abs(block(i)) > block_limit
                  block(i) = 0;
            end
      end


Erv = Erv - block;
end

addr = 0;

for m=1:cells                         % don't alter unperturbed cells
for n=1:cells

      if Mprior(m,n) > 0                  % if a perturbed cell
            addr = addr+1;                % then next base address

            Erv(addr) = max([Erv(addr),Er_min]);      % keep Er in
            Erv(addr) = min([Erv(addr),Er_max]);      % limits
            Er(m,n) = Erv(addr);                % reconstruct model
            end

      end
      end


end
```

5.8 Regular

```
% regularise the model update, operate on square Er
      alpha = 0.2;
% first get solution norm

Ermean = sum(sum(Er));
Ernorm = 0;

for m=1:cells
for n=1:cells

      Ernorm = Ernorm + (Er(m,n) - Ermean)^2;          % 2 norm
      end
      end
```

5.9 Objectiv

```
% formulates and calculates the objective (or misfit) function.


% calculate the misfit (sum of squared deviations)


S=0.5*((t-tobs)*inv(Cd)*(t-tobs)' + gamma*(t-tprior)*inv(Cm)*(t-
tprior)');
      better = (S <= S_old);        % looking for a smaller S


fit = max(abs(terr))<max_terr | S<target;       % (S < target);
max_err=max(abs(terr));                    % indicate max error

end
```

5.10 Update

```
% Updates model once we've found a correction that reduces objective
% function.


better = 0;              % set for next overall iteration

damping_factor = 1;

if S<S_old

      avg_progress = 0.7*avg_progress + 0.3*(S_old-S)/S;

      if avg_progress < 0.02 & progress
            constraint = constraint*2;
            avg_progress=3;
            end
      end

S_old = S;               % update S_old
Er_old = Er;
```

5.11 Results

```
% show the results

scale = [0 14 0 14 0 5];
load model.dat                  % get the model distribution
figure
subplot(2,2,1)
mesh(model)                     % what we should get
view(40,40)
title('Target Distribution')
axis(scale);                    % keep last axis scale
subplot(2,2,2)
mesh(Er)                        % what we got
axis(scale)
view(40,40)
title('Solution')
subplot(2,2,3)
Mprior = flipud(Mprior);        % align with (0,0) at lower left
Mprior = rot90(Mprior);
Mprior = rot90(Mprior);
Mprior = rot90(Mprior);
mesh(Mprior)                    % plot starting distribution
axis(scale)
view(40,40)
title('Mprior')
subplot(2,2,4)
semilogy(record3,'g')           % show the objective function
title('Objective Function')


print -dbitmap                  % copy graph to clipboard
```

6 Inversion of dielectric model

```
% Inversion of dielectric model, global Eh, Ei, T, tc, w

% First calculate assuming theta < theta_t

format compact
theta_t = 0.07;
a=1/3;
Eb=4;
b=1;
Eh = 3;
w = 1e9;
tc=1e-15;
T=20;
for theta=0:0.01:1
theta

% first generate Em using the forward model

if theta>theta_t

      Em = (Eh^a + theta*b*(theta_t*Eb/theta+(theta-theta_t)/theta*
      (3.2+(85.8-0.37*T)/(1+w^2*tc^2)))^a - theta*Eh^a)^(1/a);
else
      Em = ((1-theta)*Eh^a + theta*(Eb)^a)^(1/a);
end

% now invert to get back to theta

theta = (Em^a-Eh^a)/(Eb^a - Eh^a);

if theta > theta_t                    % have to invert the full form
      obj = 10+eps;
      old_obj = 10;
      theta_m = theta_t;              % first model
      iteration=0;
      while obj>1e-3 & iteration<300

g = (Eh^a + theta_m*b*(theta_t*Eb/theta_m+(theta_m-theta_t)/theta_m*
      (3.2+(85.8-0.37*T)/(1+w^2*tc^2)))^a - theta_m*Eh^a)^(1/a);

G = (Eh^a+theta_m*b*Eb^a-theta_m*Eh^a)^(1/a-1)/a*(b*Eb^a-Eh^a);

      beeta = 5;
      i2=0;
    . while obj>=old_obj & i2<300

            beeta = beeta/2;
            theta_next = theta_m + beeta/G*(Em-g);          % next

pred = (Eh^a + theta_next*b*(theta_t*Eb/theta_next+(theta_next-
theta_t)/theta_next*(3.2+(85.8-0.37*T)/(1+w^2*tc^2)))^a -
theta_next*Eh^a)^(1/a);

            obj = abs(Em-pred);
            i2=i2+1;
      end
      old_obj=obj;
      theta_m = real(theta_next);
      theta = theta_m;        % might get imag part in beeta loop
      iteration = iteration+1;

      end   %while
end
end
```

7 Forward model

```
% Field calculation using a dipole source


clear

format compact

E0 = 8.854e-12;                 % permittivity of free space, epsil zero
U0 = 4*pi*1e-7;                 % permeability of free space, mu zero
c = 2.998;                      % speed of light in vacuum
cells = 20;                     % number of cells along edge
length = 0.005;                 % cell edge dimension
dimension = length*cells;       % dimension of block (m).
spacing = 12;                   % line spacing (rods at 1,4 or 2,5)
b = spacing*length;             % actual spacing
a = 0.0056;                     % rod diameter (m)
vol = length^3;                 % area of cell (m^2)
part = vol/(4*pi*E0);
half = ceil(cells/2);


format short

linear = 0;

% First, let's establish some conventions to keep everything in order.
% The first array index is x and represents horizontal position and
% the second is y and represents vertical position.
% Zero is lower left corner.


% Set up the permittivity distribution (Ei is 2D)

Er=1.00001*ones(cells);         % unperturbed Er distribution


%Er(5,7)=1e6;
%Er(11,7)=1e6;


% calculate the linear operator

for field_x=1:cells              % for each field point
for field_y=1:cells


for source_x=1:cells            % and contributions from each source
point
for source_y=1:cells
                                % make matrix indices

field  = 2*((field_x-1)*cells+(field_y-1))+1;
source = 2*((source_x-1)*cells+(source_y-1))+1;

% calculate the dyadic, remember the x is columns, y rows

      x = (field_x - source_x)*length;
      y = (field_y - source_y)*length;


  if (field==source)
```

```
        L(field+1,source) = 0;
        L(field,source+1) = 0;

    else
        % adjust for dipole at centre of cell

        R = x^2 + y^2;                          % the part of r in 2-space
        R1 = R + (length)^2;                    % 3-space modulii of R
        R2 = R + (2*length)^2;                  % all squared versions
        R3 = R + (3*length)^2;
        R4 = R + (4*length)^2;

% now calculate off plane components, no compensation

L(field,source) = 2*(3*x^2-R1)*(-part)/(R1^2.5)...
+ 2*(3*x^2-R2)*(-part)/(R2^2.5) + 2*(3*x^2-R3)*(-part)/(R3^2.5)....
+ 2*(3*x^2-R4)*(-part)/(R4^2.5);

L(field,source+1) = 2*3*x*y*(-part)/(R1^2.5) +
2*3*x*y*(part)/(R2^2.5)....
+ 2*3*x*y*(-part)/(R3^2.5) + 2*3*x*y*(-part)/(R4^2.5);

L(field+1,source+1) = 2*(3*y^2-R1)*(-part)/(R1^2.5)....
+ 2*(3*y^2-R2)*(-part)/(R2^2.5) + 2*(3*y^2-R3)*(-part)/(R3^2.5)....
+ 2*(3*y^2-R4)*(-part)/(R4^2.5);


        if R < 1.5*length^2             % trap adjacent cells,
              x = x*0.9;
              y = y*0.9;

        elseif  R >  3*length^2 & R < 7*length^2 %

              x = x*0.93;
              y = y*0.93;

        elseif R < 16*length

              x = x*0.98;
              y = y*0.98;
        end

        R = x^2 + y^2;              % recalculate part of r in 2-space

                                    % add corrected 2-space components

L(field,source) = L(field,source) + (3*x^2-R)*(-part)/R^2.5;
L(field,source+1) = L(field,source+1) + 3*x*y*(-part)/R^2.5;
L(field+1,source+1) = L(field+1,source+1) + (3*y^2-R)*(-part)/R^2.5;
L(field+1,source) = L(field,source+1);


    end


end
end


end
end



% Now to calculate the perturbed elements of L

% First set up Er
```

```
for x=1:cells            % actual x and y in their normal sense
for y=8:cells%6          % defines height of tx line above water

if (x>10)                % defines lateral position of tx line, 11
Er(x,y)=80;              %*********
end

end
end

X=Er-1;                  % get susceptibility Chi



%Er(3,4)=1.0001;         % unnecessary if rod cell field forced small
%Er(9,4)=1.0001;


for field_x=1:cells      % for each field point
for field_y=1:cells


for source_x=1:cells     % and contributions from each source point
for source_y=1:cells
                         % make matrix indices

field  = 2*((field_x-1)*cells+(field_y-1))+1;
source = 2*((source_x-1)*cells+(source_y-1))+1;

% calculate the dyadic, remember the x is columns, y rows

      x = (field_x - source_x)*length;
      y = (field_y - source_y)*length;

  if (field==source)

% Calculate the surface charge influence

      % each cell face, 1 is in the direction
      % of increasing source_y, 2 increasing x,
      % 3 decreasing y and 4 decreasing x.


self = 1/(3*E0) + 1/(E0*X(field_x,field_y) ) +
2*2*(length^2)*part/length^5 + 2*2*(2*length)^2*part/(2*length)^5 +
2*2*(3*length)^2*part/(3*length)^5+2*2*(4*length)^2*part/(4*length)^5;

L(field,source) = self;
L(field+1,source+1) = self;

  end

end
end

end
end



G = inv(L);

%save v4

for rod_row = 1:6        % we'll do this for each transmission line
for rod_col = 4:4        % position, one spacing (4) and two rows
```

```
% Impressed field: +/- q is the linear charge density on each line.

qm = 1.4055;                          % charge density on lines (C/m)

% now for MM we require a column vector of components of the
% impressed field.  Two elements for each point, representing the
% x and y components at that point.

const = qm/(2*pi*E0);

for m=1:cells                         % rows, y
for n=1:cells                         % columns, x

  x = (m-rod_col)*length-b/2;  % origin is geometric centre of tx line
  y = (n-rod_row)*length;      %************

  if (abs(x+b/2)<1e-6)&(abs(y)<1e-6)
    % disp('altered1')
    x=x+a/2+1000;                     % rods have radius of a
  end

  if (abs(x-b/2)<1e-6)&(abs(y)<1e-6)
    % disp('altered2')
    x=x-a/2+1000;                     % rods have radius of a
  end


  denom1 = (b/2+x)^2 + y^2;
  denom2 = (b/2-x)^2 + y^2;

  addr = 2*((m-1)*cells+(n-1));       % vector base address

  Ei(addr+1) = const*((x+b/2)/denom1 + (b/2-x)/denom2);      %x
  Ei(addr+2) = const*(y/denom1 - y/denom2);                  %y
  Einc(m,n)=sqrt(Ei(addr+1)^2+Ei(addr+2)^2);
  Eix(m,n)=Ei(addr+1);
  Eiy(m,n)=Ei(addr+2);


end
end


%hold on
%axis([0,cells+1,0,cells+1]);


Pf = G*Ei'; % polarisation matrix



            % now calculate field in each cell

for i=1:cells                         % y, rows
for j=1:cells                         % x, columns

  m= 2*((i-1)*cells+(j-1));
  n= (i-1)*cells+j;

  Ex1(i,j) = Pf(m + 1) /(E0*(Er(i,j) - 1));
  Ey1(i,j) = Pf(m + 2)/(E0*(Er(i,j) - 1));
  Px(n)=Pf(m+1);
  Py(n)=Pf(m+2);
```

```
end
end


% form Px and Py into square matrices

Px1=Px;
clear Px
Py1=Py;
clear Py

for i=1:cells                    % x
for j=1:cells                    % y

      m= 2*((i-1)*cells+(j-1));
      n= (i-1)*cells+j;

      Px(i,j) = Px1(n);
      Py(i,j) = Py1(n);

end
end



Ex=Ex1;
Ey=Ey1;



% integrate the field to get voltage on lines.  We'll just
% integrate in the x direction, but interpolate for better
% accuracy.


% integrate from one line to next by curve fitting
% first determine the constant in each cell
% However we cannot use the rod cells since we do not accurately
% calculate the field in them (the singularity interferes with
% calculation of distribution since it is effectively in the cell
% centre, or at the singularity).  Instead extrapolate field
% from the adjacent cells, not large error since we are only
% extrapolating in to the rod surface.


method=1;          % LINEAR FIT

V(method)=length*sum(Ex(rod_col+1:rod_col+spacing-1,rod_row));



                %CALCULATE THE PROPAGATION TIMES


Cm(method) = qm/V(method);                          % C per metre of line
vel(method) = sqrt(pi/(Cm(method)*U0*acosh(b/a)));    % velocity (m/s)
t(rod_row) = (0.3)/vel(method);                     % time (sec) for 1 way



end          % loop on different tx line positions ends here
end
```

```
t

hold off

quiver(rot90(Ex),-rot90(Ey),1,'w')
axis([0,cells+1,0,cells+1]);
print -dbitmap

end
```

8 Calculate edge travel time

8.1 Tdr1

```
% Loads up file for TDR

clear
format compact

measure=input('Enter filename of short circuit waveform (.dat) ','s');
ext='.dat';
fid=fopen([measure,ext])
if fid < 3
      'file not found'
      return
      end
narrative=fscanf(fid,'%c',40)        %preamble
data=fscanf(fid,'%c',29);            %column headers
data=fscanf(fid,'%g %g',[2,500]);
ref=data';
fclose('all');

measure=input('Enter filename of open circuit waveform (.dat) ','s');
ext='.dat';
fid=fopen([measure,ext])
if fid < 3
      'file not found'
      return
      end
narrative=fscanf(fid,'%c',40)        %preamble
data=fscanf(fid,'%c',29);            %column headers
data=fscanf(fid,'%g %g',[2,500]);
data=data';
fclose('all');
TRUE = 1;
false = 0;

diff=data(:,2)-ref(:,2);

% show the plot
      figure
      plot(diff,'w:')
      axis([1,500,-.05,0.2])
      hold on

status=0;
window=[180,250,450];
travel1
oc=travel_time;
status=1;                            % 1 to use short circuit slope
mslope=max_slope;

window=[30,100,200];

travel1
t=oc-travel_time

      text(255,0.015,['File ',measure,'.dat']);
      text(255,0.035,['Travel time is ',num2str(t),' sec '])
      grid
      hold off
      print -dbitmap
      end
```

8.2 Travel1

```
% MODIFICATION:   on line 26
% the max positive slope is ignored instead a horizontal
% line is drawen from the minima point and the intersection
% between this line and the min_slope line is taken as the
% start point.
% Passed time/voltage pairs and calculates travel time.
% Pass variable name comprising rows of time and voltage.
% Start of trace is ref since with the 1:1 and guanella balun
% the inflection is lost.  Uses diode and the difference method
% Waveform is signal - short which then has two rising portions.
% window(2) for locating rising portions of the waveform.


      [average,slope] = smooth(diff);     % smooth, differentiate
      x_inc = data(2,1)-data(1,1);  % extract time step
      raw = data(:,2);

reference = 1;                              % measure time from here

%look for open circuited end

      % value of maximum slope
      [max_slope,max_slope_x] = max(slope(window(2):window(3)));

% x coord of maximum slope
max_slope_x = max_slope_x + window(2) - 1;

if status
      max_slope=mslope;
      end

% now look backwards for zero slope

      [zero_slope,x] = min((slope(window(1):max_slope_x)));
      zero_slope_x = window(1) + x;

range=10;
slope1 = 0;              %zero_slope;
intercept1 = mean(diff(zero_slope_x-range:zero_slope_x+range))-
slope1*(zero_slope_x);  % c=y-mx

% find the point of intersection using x=(y-c)/m
% get c for tangent to max slope

      intercept = diff(max_slope_x)-max_slope_x*max_slope;
% intersection x=(c1-c2)/(m2-m1)

      x = (intercept-intercept1)/(slope1-max_slope);

% y values of zero slope line
      tangent=[(max_slope)*(x:2*max_slope_x-x)+intercept];

% x values for neg slope line
x1=round(zero_slope_x)-20:round(x);
y1=slope1*(x1-x1(1)-20) + ones(1,size(x1,1))*diff(zero_slope_x);

% travel time is that between the reference and intersection

      travel_time = (x-reference)*x_inc/2
      plot(max_slope_x,diff(max_slope_x),'wx')
      plot(x:2*max_slope_x-x,tangent,'w')
      plot(x1,y1,'w')
      xlabel(['Time (x',num2str(x_inc),' sec)'])
      ylabel('Amplitude (volts) ')
```